The Dissertation Committee for Douglas Allen Dalton Certifies that this is the approved version of the following dissertation:

Fast Rate Fracture of Aluminum Using High Intensity Lasers

Committee:

Todd Ditmire, Supervisor

Mike Downer

Ken Shih

John Keto

Eric Taleff

Fast Rate Fracture of Aluminum Using High Intensity Lasers

by

Douglas Allen Dalton, B.S.

Dissertation

Presented to the Faculty of the Graduate School of

The University of Texas at Austin

in Partial Fulfillment

of the Requirements

for the Degree of

Doctor of Philosophy

The University of Texas at Austin

August, 2009

ACKNOWLEDGEMENTS

I would first like to thank my wife Ashley, for her love and support through these years in graduate school and for her patience during the times that I stayed in Albuquerque, NM, while performing experiments. When I had discouraging days, she was always there encouraging me. I would also like to thank my parents (Doug and Barbara) and my brothers (Blake, Jesse and Scott) for their encouragement and support throughout my early education and through college and graduate school.

I would like to especially recognize Dr. Todd Ditmire, my research advisor, for his patience and guidance as I learned to become a valuable researcher. I would like to thank him for his encouragement and support throughout my time at the University of Texas. He has always challenged me to think beyond my current comfort level.

I would like to thank Dr. Eric Taleff for the long discussions that we had regarding material response. His patience and ability to discuss topics clearly greatly helped increase my understanding regarding fast rate material response.

I would like to thank Dr. Aaron Bernstein for the conversations we had regarding optical diagnostic design. I would also like to thank Aaron for his innovation in designing a pulse stacker, which was vital for the completion of our experiments. I learned a great deal from Aaron on how to go about designing the VISAR.

I would also like to thank Dr. Will Grigsby, Despina Milathianaki, Dr. Hernan Quevedo, and Franki Aymond for their hard work and support in implementing shocked materials experiments at both Sandia and Texas. Will, as a senior graduate student, taught me many of the laboratory skills needed to perform these laser-induced shock experiments. As a junior researcher, I was very fortunate to have someone as patient and knowledgeable as Will to answer my many questions. Despina contributed a great deal to the initial VISAR design and has been a great resource in performing these experiments. Hernan, as a postdoctoral fellow, helped me a great deal in the shocked materials experiments at Texas and Sandia. Hernan has been an invaluable resource when trying to diagnose timing and electronic problems. I would also like to thank Hernan for reading this dissertation and suggesting revisions. I would also like to thank Franki Aymond for all of her hard work in helping with the THOR spall experiments. As an undergraduate, Franki has proven to be an extremely hard worker. She also helped revise this dissertation. I will greatly miss the support and help that these people have given me during my time as a researcher here as they have helped shape the way that I think about experimental design, implementation and analysis. I would also like to thank Brendan Murphy, Alex Belolipetski, and Parrish Brady for being such great office mates.

I would like to thank Jonathan Brewer, Sean Steuck, Evan Jackson, Dan Worthington, Paul Sherek, and Nick Pedrazas in Mechanical Engineering. Each of these guys played a pivotal role in designing and manufacturing target specimens and in the post-shot analysis. We had a lot of valuable conversations that helped paint a clear picture between the dynamic results and post shot analysis. Without their hard work, we would not have been able to understand the role of various microstructural effects in fast rate material response.

I would also like to thank the Z-Beamlet and Z-Petawatt staffs at Sandia National Laboratories (specifically Richard G. Adams, Patrick Rambo, Matthias Geissel, Jens Schwarz, Ian Smith, Briggs Atherton, Jon Porter, and Jon Shores). I would like to give a special thanks to Jon Shores for his tireless efforts to get us as many laser shots as possible.

Fast Rate Fracture of Aluminum Using High Intensity Lasers

Publication No._____________

Douglas Allen Dalton, Ph.D.
The University of Texas at Austin, 2009

Supervisor: Todd Ditmire

Abstract: Laser induced shock experiments were performed to study the dynamics of various solid state material processes, including shock-induced melt, fast rate fracture, and elastic to plastic response. Fast rate fracture and dynamic yielding are greatly influenced by microstructural features such as grain boundaries, impurity particles and alloying atoms. Fast fracture experiments using lasers are aimed at studying how material microstructure affects the tensile fracture characteristics at strain rates above 10^6 s^{-1}.

We used the Z-Beamlet Laser at Sandia National Laboratories to drive shocks via ablation and we measured the maximum tensile stress of aluminum targets with various microstructures. Using a velocity interferometer and sample recovery, we are able to measure the maximum tensile stress and determine the source of fracture initiation in these targets. We have explored the role that grain size, impurity particles and alloying in aluminum play in dynamic yielding and spall fracture at tensile strain rates of $\sim 3 \times 10^6$ s^{-1}. Preliminary results and analysis indicated that material grain size plays a vital role in the fracture morphology and spall strength results.

In a study with single crystal aluminum specimens, velocity measurements and fracture analysis revealed that a smaller amplitude tensile stress was initiated by impurity particles; however, these particles served no purpose in dynamic yielding. An aluminum-magnesium alloy with various grain sizes presented the lowest spall strength, but the greatest dynamic yield strength. Fracture mode in this alloy was initiated by both grain boundaries and impurity particles. With respect to dynamic yielding, alloying elements such as magnesium serve to decrease the onset of plastic response. The fracture stress and yield stress showed no evidence of grain size dependence. Hydrodynamic simulations with material strength models are used to compare with our experiments. In order to study the strain rate dependence of spall in aluminum we used a shorter pulsed laser and thinner targets. From these experiments we do not observe an increase in spall strength for aluminum up to strain rates of $\sim 2x10^7$ s^{-1}.

TABLE OF CONTENTS

LIST OF TABLES

LIST OF FIGURES

CHAPTER 1. INTRODUCTION

High pressure material research can be achieved using both static and dynamic methods. High pressure static research is commonly conducted using diamond anvil cells. This research is often pursued to reach the high pressures that are relevant to planet interiors, such as the Earth's, and other novel material phases (Chen, Weidner and Vaughan 2002). Dynamic high pressure research is performed using gas guns, explosives and lasers to explore various shock induced processes such as fast rate fracture and phase transitions. In this dissertation, I present work in fast rate fracture and compressive yielding of aluminum and aluminum alloys initiated by laser induced shocks.

1.1 REASONS FOR STUDYING FAST RATE MATERIAL FRACTURE

The study of fast rate fracture has several defense applications. When a high velocity projectile impacts a piece of armor, it may not be the projectile itself that breaches the armor, but rather the debris that exits the non-impacted or rear surface. Metals tend to have roughly the same resistance to plastic flow in tension as they do in compression. In this dissertation I will focus on how metals fail (yield and fracture) under impulsive loads. Our experiments investigated how microstructural variations affected fracture mode and fracture stress at the fast strain rates achievable by lasers.

Another application of fast rate fracture and yield strength is the role that they play in nuclear weapons. Verifying the integrity of an aging nuclear arsenal is an area of national security. Hixson, et al. discovered that low purity (high carbon) uranium and high purity depleted uranium have approximately the same spall stress (Hixson, et al. 1998); however, at higher stresses, the higher purity uranium exhibited longer time to spall. Veeser, et al. stated that plutonium and other weapon components are not resistant to effects of oxidation and radioactivity (Veeser 1999). These examples are evidence that specimen purity and long term storage may present obstacles in ensuring the integrity of nuclear materials.

Another, albeit less practical, reason for examining fast rate fracture is to determine peak stress conditions that will fracture a given material. It has been shown that the peak stress needed to fracture metals, like copper and aluminum, is greater at faster strain rates (Moshe, Eliezer and Dekel, et al. 1998).

1.2 SUMMARY OF KEY SPALL RESULTS AT FAST STRAIN RATES

Spall is the fast rate fracture that occurs when a shock pulse reflects from a free surface which puts the material into tension. When the tensile strength of the material is exceeded, the material will fracture. Figure 1 shows various tensile tests that are applicable at different strain rates. Within the context of this dissertation, I will refer to strain rates of 10^4 to 10^6 s^{-1} as slow strain rates, while strain rates > 10^6 s^{-1} will be referred to as fast strain rates.

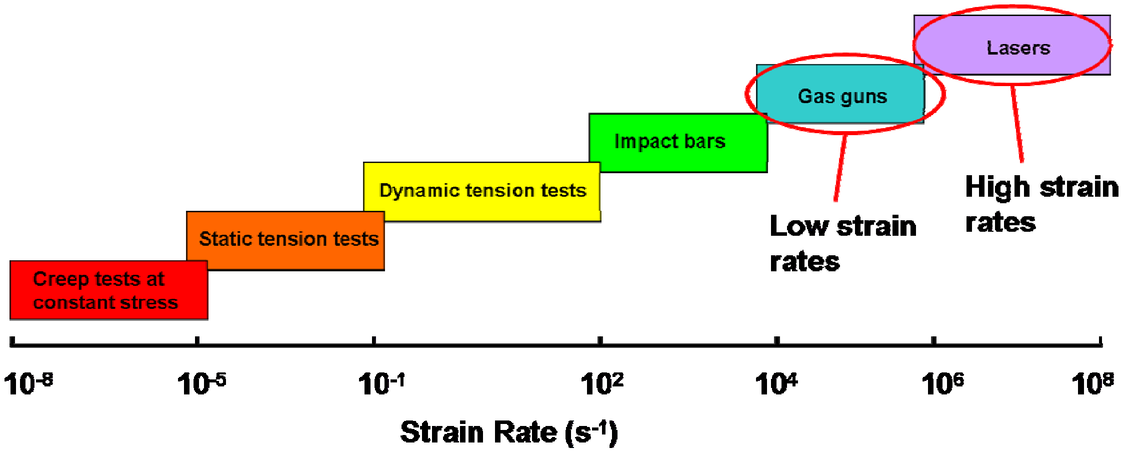

Figure 1: Various tensile test methods versus strain rate.

An extensive amount of experimental work has been performed measuring the maximum fracture stress of materials with different microstructures over the strain rates accessible with gas guns and flyer plates, specifically at strain rates of 10^4 up to 10^6 s^{-1}. These studies have examined a plethora of influences on spall strength including grain size, second-phase particles, alloying and grain orientation. Studies have shown that certain traditional yield strengthening mechanisms do not necessarily lead to fracture resistance at strain rates above 10^4 s^{-1} (Minich, et al. 2004). Early laser-induced spall studies involved post-shot target analysis with a concentration on examining the spall surface morphology (Cottet and Boustie, 1990), (Eliezer, Gilath and Bar-Noy 1990), (Gilath, et al. 1988). These studies were limited in that they did not determine the spall strength of materials dynamically. More recently, using a velocity interferometry probe coupled with lasers of a wide range of pulse durations, E. Moshe, et al. were able to study spall strength over a range of fast strain rates. They showed that laser-driven foils of aluminum and copper exhibited spall strength that dramatically increased with strain rate (Moshe, Eliezer and Henis, et al. 2000). This result implies a change in spall failure mechanism at strain rates of about 10^7 s^{-1}. Our experiments involved varying the microstructure of materials and investigating how fracture mode and fracture stress were affected at fast strain rates achieved by lasers.

In this dissertation, I will report experimental studies of the spall strength and fracture morphology of aluminum slabs subject to strain rates of 2 to 8 x 10^6 s^{-1}. Slabs of pure aluminum and various aluminum alloys were shock-driven using the high energy, nanosecond pulsed Z-Beamlet Laser at Sandia National Laboratories. A velocity interferometry diagnostic was used to infer the spall strength of the materials, and post-shot target analysis explored the microscopic fracture mode. We observed a slow increase in the spall strength for all materials as the strain rate is increased. We also found significantly greater spall strength for the large-grained, recrystallized high-purity aluminum, with post-shot target analysis showing the dominant failure mode was ductile transgranular. The spall strength for Al+3% Mg alloys were lower, by nearly a factor of two, than in the high purity aluminum, though strengths were similar in both the recrystallized and cold-worked alloyed targets. Comparison of this strength data with post-shot analysis indicated that grain size is the important differentiating factor at these strain rates.

Recent experiments were designed to look at the effect of single crystals on spall. The results from these experiments indicate an inverse relationship between the dynamic yield stress and spall fracture stress. Accordingly, the high purity single crystal aluminum samples had the highest spall fracture stress and exhibited a ductile fracture mode with no particle impurities present. A single crystal aluminum alloy (Al-1100) showed the second highest spall strength and its fracture mode was also ductile, but possessed particle impurities. Another alloy, Al+3 wt. % Mg, with fine, intermediate, and coarse grain sizes exhibited the lowest spall fracture stress, but showed no obvious trend in terms of spall strength versus grain size. However, there was a trend in the fracture mode as the finer grain size materials exhibited more brittle intergranular fracture. The coarser grained material possessed a ductile transgranular fracture with impurity particles at the center of the ductile dimples. These results suggest that the impurities greatly affect the fracture strength.

In contrast to the spall results, the Al+3Mg alloy exhibited the highest dynamic yield strength when compared to both the high purity single crystal aluminum and the single crystal Al-1100. Both the high purity aluminum and the Al-1100 exhibited the lowest dynamic yield stress. The inverse relationship between dynamic yield strength and spall fracture stress is supported by static results (Courtney 2000); however, it is interesting to point out that the single crystal Al-1100 shows nearly the same dynamic yield stress as the single crystal high purity aluminum.

1.3 PLAN FOR THIS DISSERTATION

In Chapter 2, the concept of shock waves will be introduced, along with a description of how lasers can produce plasma driven shocks. I will also discuss how shocks and rarefactions are formed, which is important to understanding how high pressure waves interact with materials. Laser ablation also gives rise to thermal waves which can complicate comparison with more traditional shock methods (i.e. gas gun and explosive techniques).

In Chapter 3, I will discuss the concepts of stress and strain and describe various ways in which materials respond to a given load. The two primary types of experiments explored, melt and spall, will be discussed. An in depth summary will be presented of how other groups have varied material microstructure and wave profile characteristics to study spall fracture. I will summarize the materials desired for the preliminary fast rate fracture experiments and provide a strong motivation for studying these materials.

In Chapter 4, a brief description is given of both the large scale and table top lasers used in this dissertation. A description of the laser diagnostics used in these experiments, along with a description of the experimental setup will be provided. Also, a summary of the hydrodynamic code, HYADES, along with relevant yield and spall models will be presented.

In Chapter 5, the experimental results that were briefly summarized in this introduction will be provided in more detail. Results will be discussed in the context of how microstructural changes such as grain size and alloying affect fast rate fracture and plastic response. Hydrocode simulations will be presented to compare the dynamic experimental results with fracture and yield models.

In Chapter 6, I will discuss shocked silicon experiments which resulted in a change to the linear reflectivity signal, but no change in the third harmonic signal. In

Chapter 7, this dissertation will be summarized and concluded. I will also discuss how these laser induced shock experiments can be continued and improved.

CHAPTER 2. SHOCK WAVE PHYSICS

2.1 SHOCK PHYSICS

In this chapter I discuss the introductory shock wave physics, first deriving the conservation equations for mass, momentum, and energy. The Rankine-Hugoniot equation is then introduced, which describes the thermodynamic condition of the final shock state. A description of the equation of state (EOS) is provided in order to describe the manner in which shocks and rarefactions are formed. Understanding shocks and rarefactions is needed to interpret how waves decay. The concept of wave splitting is described in relation to phase transitions and elastic-plastic material response. A description is given of pressure transmission across a boundary which relates to our melt and spall experiments. A discussion of laser absorption mechanisms and their role in shock wave generation will be provided. Many of the descriptions in this chapter are found in the following references ((Zel'dovich and Raizer 1966), (Ditmire 2004), and (Boslough and Asay 1993)).

2.1.1 Conservation Equations

I first derive the equations for conservation of mass, momentum and energy across a discontinuity jump (i.e. shock). For a gas filled shock tube (Figure 2) with initial thermodynamic properties P_0 (pressure), ρ_0 (mass density), E_0 (internal energy), and $U_{p,0}=0$ (particle velocity) a shock can be driven in the gas by a piston. A shock will propagate faster than the piston. The properties of the gas behind the shock are P, ρ, E, and non-zero particle velocity U_p.

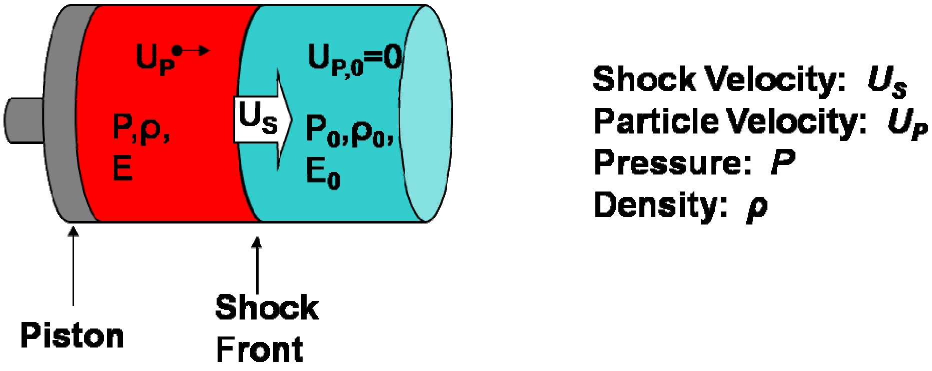

Figure 2: The piston model illustrates shock propagation through a gas with initial properties ($U_{p,0}$, P_0, ρ_0, E_0) ahead of the shock front (with velocity U_s) and behind shock at U_p, P, ρ, E.

I first derive the conservation of mass equation. The mass of material which crosses the shock front is given by the mass density and the change in volume, which is determined by the difference in shock and particle velocities. The mass change across the shock front is:

$$\rho_0 A(U_S - U_{p,0})\cdot \Delta t = \rho A(U_S - U_p)\cdot \Delta t \, , \tag{2.1}$$

where A is the cross-sectional area of the cylinder and Δt is the change in time. Setting $U_{p,0}$ to zero and then rearranging variables yields the equation for conservation of mass:

$$\boxed{\frac{\rho}{\rho_0} = \frac{U_S}{U_S - U_p}} \, . \tag{2.2}$$

Thus the compression of the gas can be described using only the shock and particle velocities.

I now derive the conservation of momentum equation. The impulse, I, is the momentum transfer across the shock front. The impulse is the difference in pressure behind and ahead of the shock front times the cross-sectional area times the incremental time.

$$I = (P - P_0)A \cdot \Delta t \tag{2.3}$$

The momentum change, Δp, is the difference in mass times velocity before and after the shock front.

$$\Delta p = \lfloor \rho A(U_S - U_p)\Delta t \rfloor U_p - \lfloor \rho_0 A(U_S - U_{p,0})\Delta t \rfloor U_{p,0} \tag{2.4}$$

Equating the impulse with the momentum change and using the conservation of mass gives the equation for conservation of momentum: ($U_{p,0}=0$)

$$\boxed{P - P_0 = \rho_0 U_S U_p}. \tag{2.5}$$

This equation describes the pressure of the gas behind the shock front.

I now derive the conservation of energy equation. The work due to the shock is the change in kinetic energy plus the change in potential energy:

$$W = \Delta KE + \Delta PE. \tag{2.6}$$

The change in kinetic energy upon shock loading is given by:

$$\Delta KE = \frac{1}{2} m(v_f{}^2 - v_i{}^2) = \frac{1}{2}\lfloor \rho_0 A(U_S - U_{p,0})\Delta t \rfloor (U_p{}^2 - U_{p,0}{}^2). \tag{2.7}$$

The change in potential energy of the gas due to the shock is given as the difference in specific internal energy (E-E_0) times the mass:

$$\Delta PE = (E - E_0)\rho_0 A(U_S - U_{p,0})\Delta t. \tag{2.8}$$

Additionally, the positive work is done as volume of the compressed material expands and negative work is done when the initial material contracts.

$$W = P\Delta V = PAU_p\Delta t - P_0 A U_{p,0}\Delta t \tag{2.9}$$

Combining these equations and then simplifying produces the conservation of energy equation: ($U_{p,0}=0$, $P_0=0$)

$$\boxed{PU_p = \frac{1}{2}\rho_0 U_S U_p{}^2 + \rho_0 U_S (E - E_0)}. \tag{2.10}$$

Using the conservation equations of mass, momentum and energy and eliminating the variables U_p and U_S yields a new equation called the Rankine-Hugoniot equation (or simply Hugoniot):

$$\boxed{(E - E_0) = \frac{1}{2}(P + P_0)(V_0 - V)}. \tag{2.11}$$

This equation describes a jump in specific internal energy as a function of pressure and specific volume. The Hugoniot is the locus of all points that describe the final shocked state from the initial state. The equation describes the specific internal energy (i.e. temperature) in terms of pressure and volume states. In a similar manner, the pressure can be described as a function of volume and specific internal energy states.

2.1.2 Equation of State

In order to solve the Rankine-Hugoniot equation, an equation of state (E(P,V)) must be known or assumed for a gas, liquid, or solid. The equation of state for a perfect gas with adiabatic index, γ, is given by:

$$E(P,V)=\frac{1}{\gamma-1}PV\ . \tag{2.12}$$

An equation of state for solids is the Mie-Gruneisen equation:

$$E(P,V)=E_k(V)+V(P-P_k(V))/\Gamma(V), \tag{2.13}$$

where E_k is the reference internal energy curve, P_k the reference pressure curve, and Γ is the Gruneisen parameter which is a function of specific volume. The equation of state of many materials is commonly expressed as a linear equation (Eq. 2.14) in which the shock speed depends on the particle velocity and the constants A and B which are characteristic of the material.

$$\boxed{U_S = A + BU_p} \tag{2.14}$$

The three jump conditions (Equations 2.2, 2.5 and 2.10) along with the equation of state, gives four equations, but five unknowns meaning that there is one independent variable. Some commonly used representations of the equation of state are U_s-U_p, P-U_p and P-V. Equation of state data for aluminum and lithium fluoride (a window commonly used in melt experiments) is given below, where both particle and shock velocities are in units of km/s (Trunin 2001).

Aluminum: $U_s=5.33+1.356\ U_p$ $0 \leq U_p \leq 6.10$

Aluminum: $U_s=6.541+1.158\ U_p$ $6.10 \le U_p \le 22$

LiF: $U_s=5.130+1.310\ U_p$ $0 \le U_p \le 10.10$

Figure 3 shows various representations of the equation of state of aluminum.

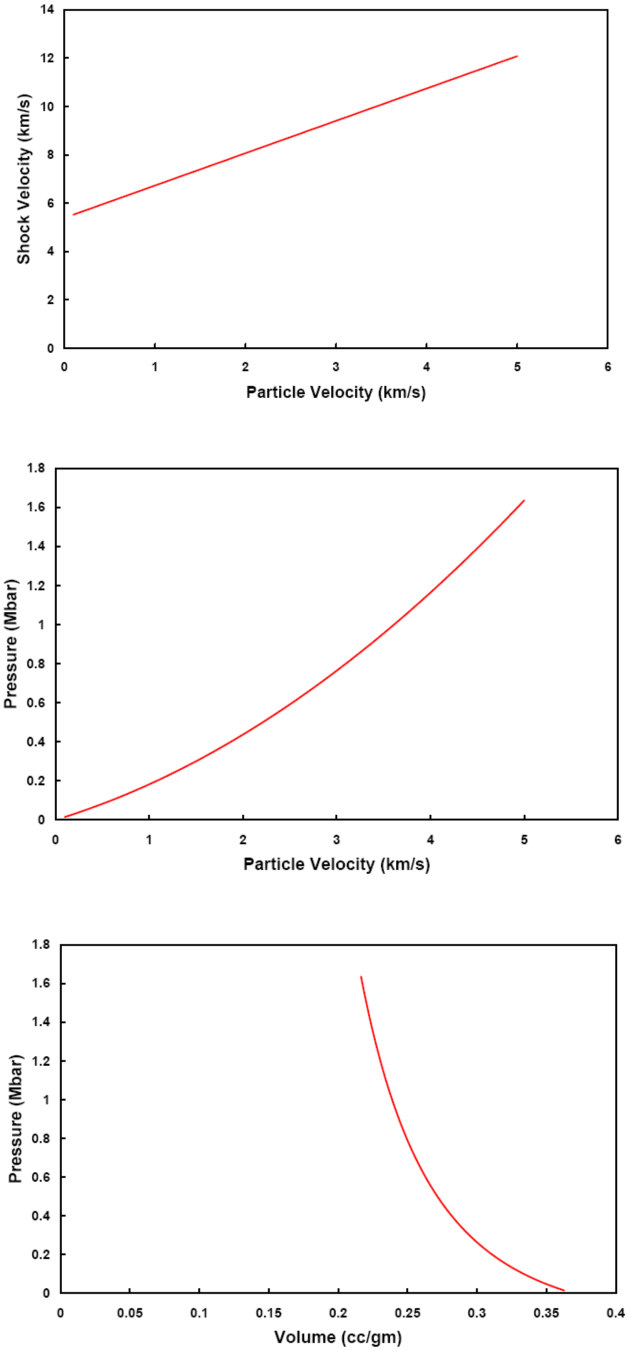

Figure 3: Various representations of the Hugoniot of aluminum: shock velocity versus particle velocity, pressure versus particle velocity, and pressure versus specific volume.

Experimentally, the equation of state is determined by measuring the particle velocity and the shock velocity. For materials that are well characterized, one may use published data for this equation and just measure the particle velocity. Substituting equation (2.14) in the mass and momentum conservation equations allows one to determine the peak pressure upon shock breakout in addition to the material compression. The pressure and compression are given below:

$$P = \rho_0 (A + BU_p) U_p = \frac{A^2 (V_0 - V)}{(B-1)^2 V^2 \left[\frac{B}{B-1} - \frac{V_0}{V} \right]^2}, \tag{2.15}$$

$$\frac{\rho}{\rho_0} = \frac{A + BU_p}{A + (B-1)U_p}. \tag{2.16}$$

One of the more highly debated equations of state is the case of deuterium which is relevant to fusion research ((Da Silva, et al. 1997), (Collins, et al. 1998), (Knudson 2001)). Figure 4 shows the equation of state for deuterium from various studies. The figure shows that there are differences in the measured equation of state above ~40 GPa. The laser studies show the greatest compressions (ρ/ρ_0) approaching ~ 6, while the magnetic flyer plate studies show compression asymptotically approaching ~ 4.

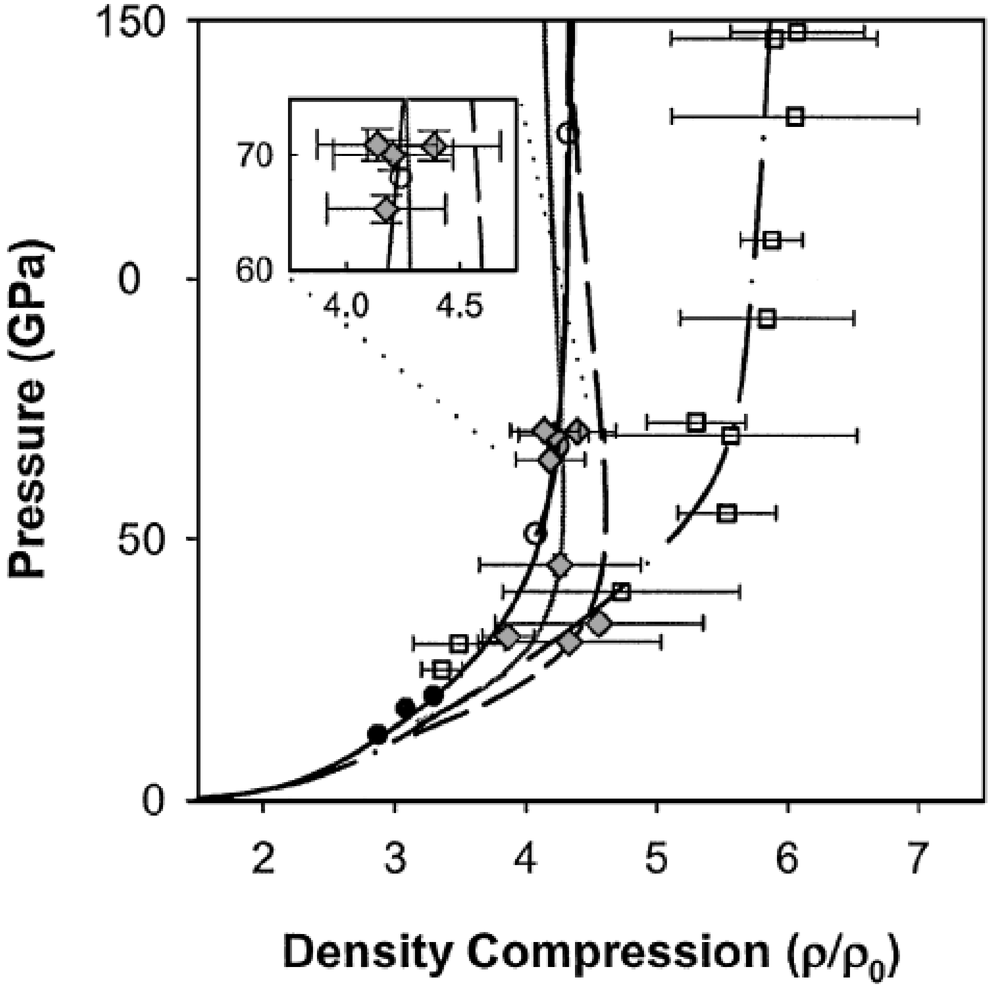

Figure 4: Equation of state of deuterium (Knudson, et al. 2001). The laser data is represented by open squares and the filled diamonds represent magnetic driven flyer plate data. Reprinted figure with permission from Knudson, M.D., Hanson, D.L., Bailey, J.E., Hall, C.A., Asay, J.R., and Anderson, W.W. "Equation of State Measurement in Liquid Deuterium to 70 GPa", Physical Review Letters, 87 (2001): 225501. Copyright (2001) by the American Physical Society. http://prola.aps.org/abstract/PRL/v87/i22/e225501

As introduced previously in Section 2.1.1, the Hugoniot describes the locus of all end states, not the thermodynamic path of initial and final states. In the next section, I will describe the thermodynamic path of a shocked material and how the Hugoniot gives rise to shock and rarefaction waves.

2.1.3 Rayleigh Line and Shock, Rarefaction

Consider the P-V diagram for the equation of state in Figure 5. The Rayleigh line connects the initial and final states in the P-V diagram. The slope of the Rayleigh line, *m*, is:

$$m = \frac{P - P_0}{V_0 - V} = \left(\frac{U_S}{V_0}\right)^2, \tag{2.17}$$

where the shock and particle velocities are described in terms of pressure and volume states:

$$U_S = V_0 \sqrt{\frac{P - P_0}{V_0 - V}} \tag{2.18}$$

and

$$U_P = \sqrt{(P - P_0)(V_0 - V)}. \tag{2.19}$$

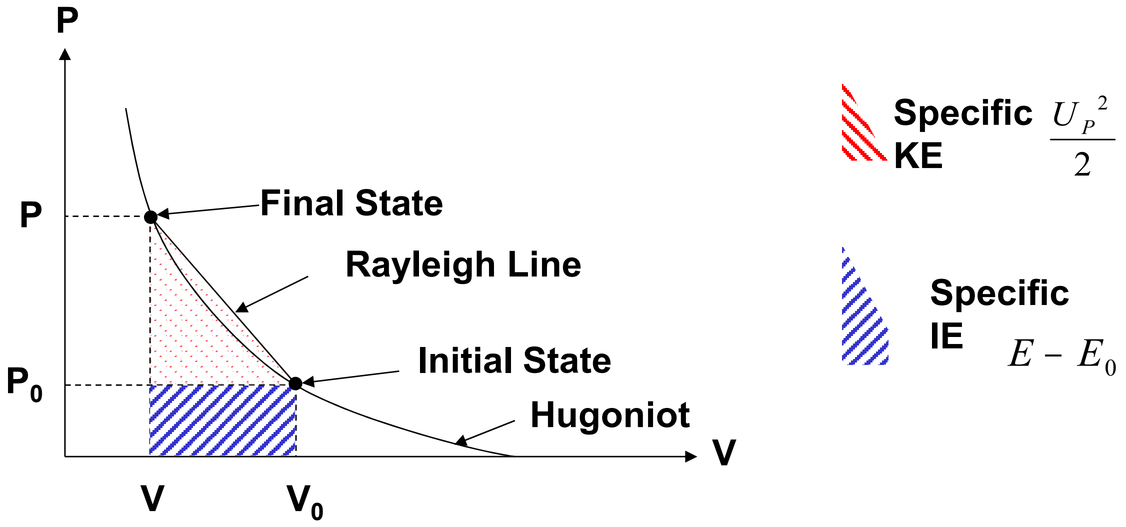

Figure 5: Schematic of a pressure versus specific volume diagram showing the Hugoniot with initial and final states. These states are connected by a chord, termed the Rayleigh line.

If the Hugoniot curve is concave up, then the shock velocity is an increasing function of shock pressure. Several dissipative mechanisms, such as viscosity and heat transport, ensure that the thermodynamic path of the shocked material is along the Rayleigh line, not the Hugoniot which is only the locus of final states. This means that the Rayleigh line is above the Hugoniot curve. The specific kinetic energy, ${U_p}^2/2$, is the triangular area bounded by V, P_0, and the Rayleigh line. The specific internal energy, $E-E_0$, is the trapezoidal area bounded by P=0, V, V_0, and the Rayleigh line.

There are three conditions that must be met for stable shock propagation:

1. The sound speed, *a*, must be an increasing function of pressure.

$$\frac{da}{dP}>0 \quad \text{where} \quad a=V\sqrt{-\left(\frac{\partial P}{\partial V}\right)_S} \tag{2.20}$$

2. The shock speed, U_s, must be supersonic with respect to the material in front of the shock, or the unshocked material, where a_0 is the initial state sound speed.

$$U_S>a_0 \tag{2.21}$$

   In other words the slope of the Rayleigh line (Eq. 2.17) must be greater than the Hugoniot slope at initial conditions.

$$\frac{P-P_0}{V_0-V}>-\left(\frac{\delta P}{\delta V}\right)_{S,0} \tag{2.22}$$

3. The shock must be subsonic compared to material behind the shock.

$$a+U_p\geq U_S \tag{2.23}$$

   Or equivalently, the Rayleigh line must be less steep than the Hugoniot at the final state.

$$\frac{P-P_0}{V_0-V}\leq-\left(\frac{\delta P}{\delta V}\right)_S \tag{2.24}$$

There are few instances in which materials do not satisfy these conditions. For example, at low pressures fused silica cannot support shocks because it does not satisfy these conditions (Barker and Hollenbach 1970). Elastic-plastic materials and materials that undergo phase changes also do not satisfy these conditions. This will be discussed in detail in section 2.1.5.

Satisfying these three stability conditions ensures that shocks and rarefactions can be formed in a material. Figure 6 illustrates how two wavelets (points 1 and 2) on compression and expansion waves give rise to shocks and rarefactions. Since the sound speed is an increasing function with pressure (Eq. 2.20), the higher pressure point 2 will travel faster than the lower pressure point 1. In a compression wave, Figure 6a, point 2 will eventually catch up to point 1 and form a discontinuity, or shock. In an expansion wave, Figure 6b, point 2 outruns the lower pressure point 1 and forms a rarefaction wave.

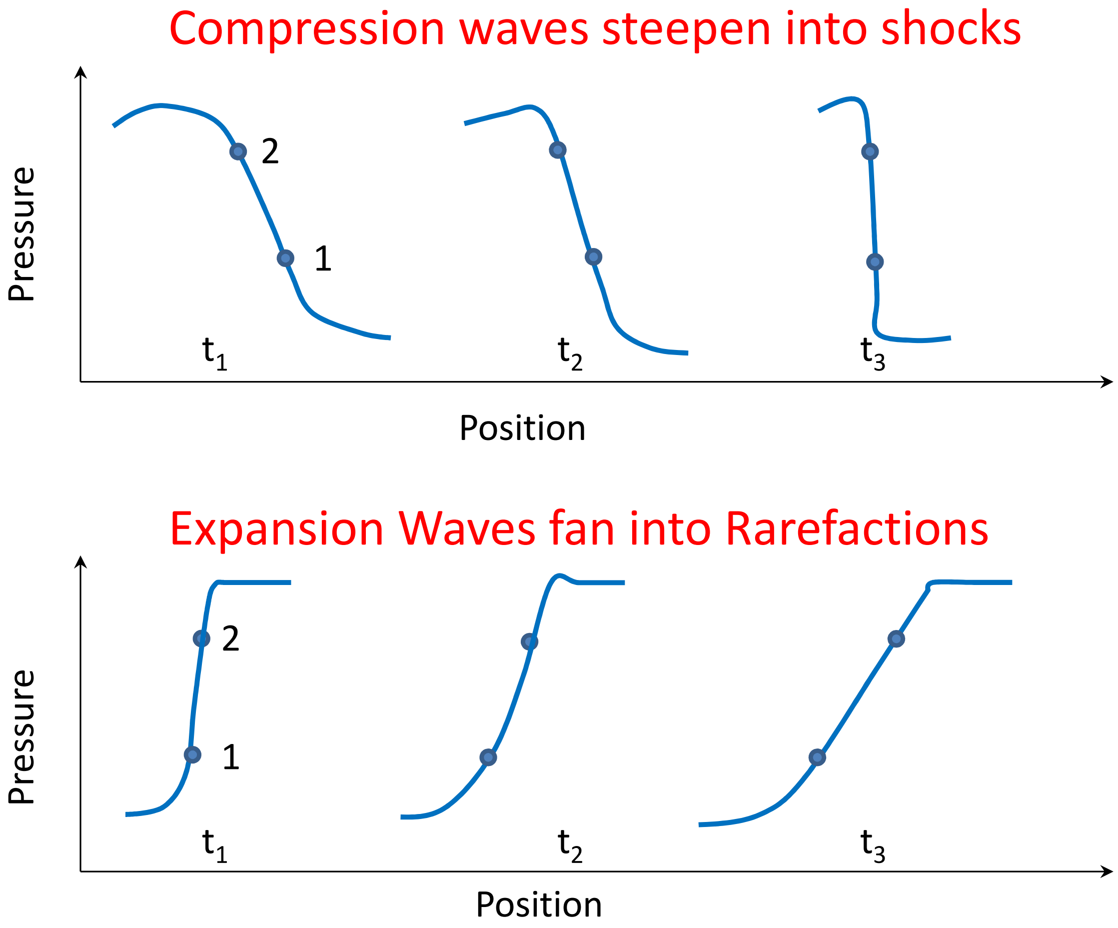
Compression waves steepen into shocks

Expansion Waves fan into Rarefactions

Figure 6: Sound speed as an increasing function of pressure results in (a) compression waves steepening into shocks and (b) expansion waves fanning into rarefactions.

2.1.4 Pressure Decay and Blast waves

For the case in which a compression pulse is short compared to the specimen thickness (as in many of our experiments) or the length of gas, the situation of a decaying shock occurs. Figure 7 shows x-t and P-x diagrams for the case of a decaying shock. At time t_1, the pulse has a constant peak pressure. As time progresses (t_2), the rarefaction begins to catch up with the shock. At time t_3, the rarefaction fan catches the shock front. At time t_4, the rarefaction eats away at the shock causing the pressure to decay and the shock speed to decrease. This type of pressure decay is referred to as a Taylor wave or a blast wave. A blast wave can be thought of as a point like explosion, where there is no continuous drive pulse.

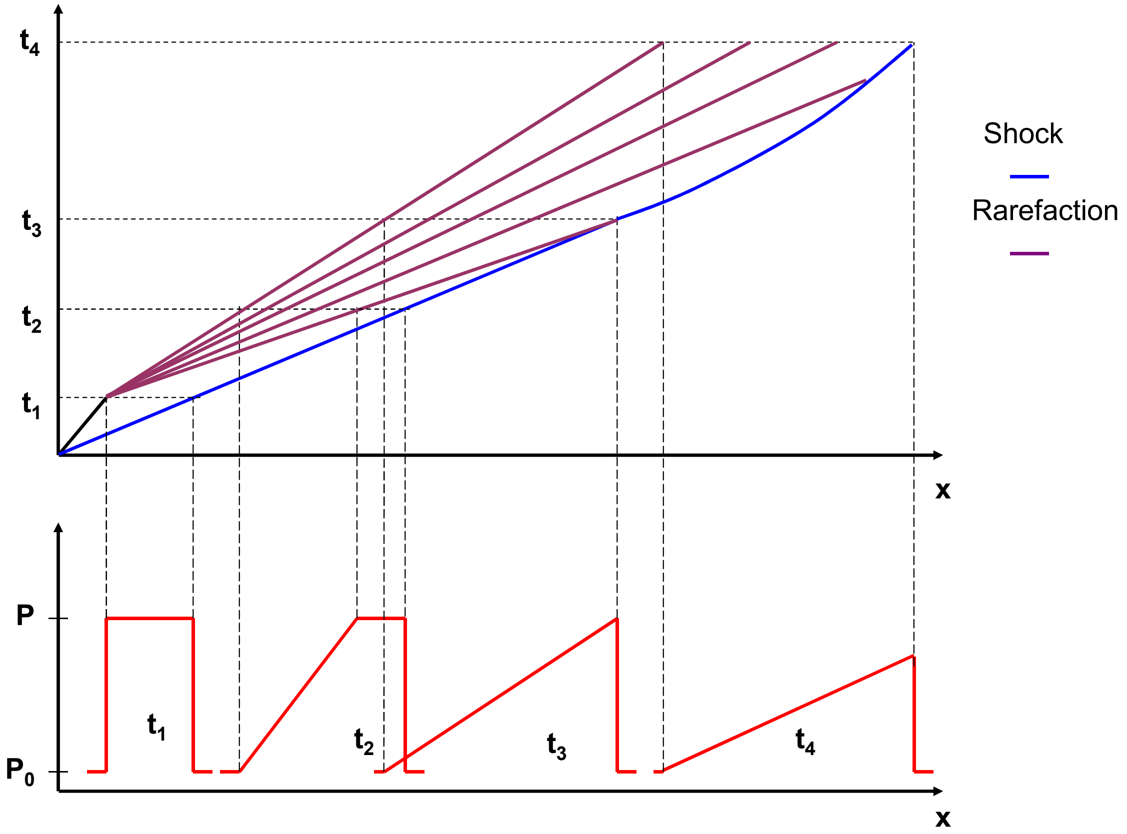

Figure 7: x-t and P-x diagrams illustrating the process of a decaying shock. (Figure not drawn to scale)

Zel'dovich and Raizer presented a derivation for the blast wave displacement in time (Zel'dovich and Raizer 1966). It is assumed that all mass of the ideal gas encountered by the blast wave is contained in a very thin layer, ΔR. The mass (M) swept by the blast wave is given by:

$$M = \frac{4}{3}\pi R^3 \rho_0 , \tag{2.25}$$

where ρ_0 is the initial gas density and R is the blast wave radius. The mass of gas within the thin shell is given by the shocked density, ρ_1, times the shell volume (surface area times shell thickness):

$$M_{shell} = 4\pi R^2 \Delta R \rho_1 . \tag{2.26}$$

In the strong shock limit ($P \gg P_0$), the following equations for density, pressure, and particle velocity are valid (using Equations 2.12, 2.11, and 2.5):

$$\frac{\rho_0}{\rho_1} = \frac{\gamma - 1}{\gamma + 1},\ p_1 = \frac{2}{\gamma + 1}\rho_0 D^2,\ u_1 = \frac{2}{\gamma + 1} D , \tag{2.27}$$

where D is the velocity of the front and γ is the adiabatic index:

$$D = \frac{dR}{dt} . \tag{2.28}$$

Via mass conservation, the shell mass is equal to the mass of gas swept by the blast wave:

$$4\pi R^2 \Delta R \rho_1 = \frac{4}{3}\pi R^3 \rho_0 . \tag{2.29}$$

Solving for the shell thickness yields:

$$\Delta R = \frac{R}{3}\frac{\rho_0}{\rho_1} = \frac{R}{3}\frac{\gamma - 1}{\gamma + 1} . \tag{2.30}$$

Since the shell is very thin, the gas velocity is somewhat constant and is the same as the velocity of gas behind the blast wave front. For mass in the shell, it is assumed that the shocked density is very large and the shell width is infinitesimally small. So M_{shell} is finite and approximately equal to M, the mass swept by the blast wave.

From momentum conservation, we derive the equation:

$$\frac{d}{dt}\left(Mu_1\right) = 4\pi R^2 p_c\,, \tag{2.31}$$

where p_c is the pressure at the inside of the layer and is the fraction, α, of the pressure p_1 behind the blast front. Substituting equations 2.25 and 2.27 yields:

$$\frac{d}{dt}\left(\frac{4}{3}\pi R^3 \rho_0 \frac{2}{\gamma+1} D\right) = 4\pi R^2 \alpha \frac{2}{\gamma+1}\rho_0 D^2 \tag{2.32}$$

Simplifying yields:

$$\frac{1}{3}\frac{d}{dt}\left(R^3 D\right) = R^2 \alpha D^2 \tag{2.33}$$

Using the chain rule to convert the time derivative to a spatial derivative and then integrating gives:

$$\begin{gathered}\frac{1}{3}D\frac{d}{dR}\left(R^3 D\right) = \alpha D^2 R^2 \\ 3DR^2 + R^3\frac{dD}{dR} = 3\alpha D R^2 \\ \int \frac{1}{D}dD = \left(3\alpha - 3\right)\int \frac{1}{R}dR \\ D = aR^{-3(1-\alpha)}\,,\end{gathered} \tag{2.34}$$

where a is an integration constant. We now have D, but need to determine a and α. Using energy conservation, the total energy is given by the kinetic energy of the gas and the internal energy of the gas inside the thin layer:

$$E = \frac{1}{\gamma-1}\frac{4}{3}\pi R^3 \alpha p_1 + M\frac{u_1^{\;2}}{2} \tag{2.35}$$

In the strong shock limit (Eq. 2.27) and substituting for D (Eq. 2.34), the total energy becomes:

$$E = \frac{4\pi}{3}\rho_0 a^2\left[\frac{2\alpha}{\gamma^2-1} + \frac{2}{\left(\gamma+1\right)^2}\right]R^{3-6(1-\alpha)} \tag{2.36}$$

Since energy is conserved, the energy dependence of R disappears, so

$$R^{3-6(1-\alpha)} = R^0\,, \tag{2.37}$$

$$\alpha = \frac{1}{2}$$

Substituting α into Eq. 2.36 and then solving for a yields:

$$a = \left[\frac{3}{4\pi} \frac{(\gamma - 1)(\gamma + 1)^2}{(3\gamma - 1)} \right]^{1/2} \left(\frac{E}{\rho_0} \right)^{1/2}. \qquad (2.38)$$

In spherical coordinates, the scaling for front velocity, pressure and blast radius are:

$$D \sim R^{-3/2},\ P \sim D^2 \sim R^{-3},\ R \sim t^{\,2/5} \qquad (2.39)$$

In cylindrical coordinates, the scaling of the blast wave radius with times goes as:

$$R \sim t^{1/2} \qquad (2.40)$$

In planar coordinates, the scaling of the blast wave radius with time goes as:

$$R \sim t^{2/3} \qquad (2.41)$$

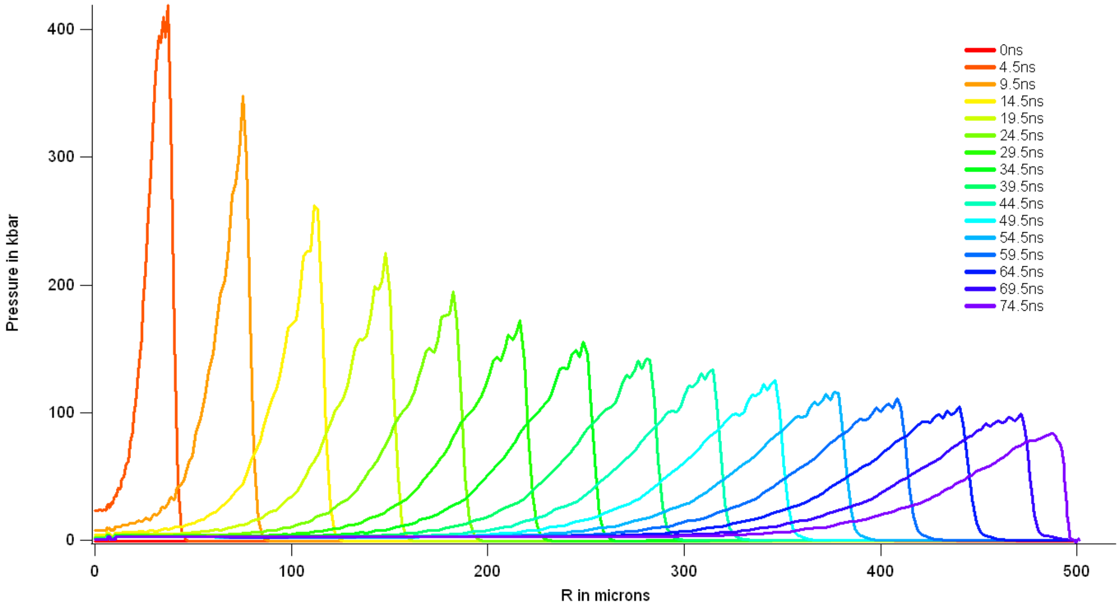

Figure 8: Simulation shows pressure versus Lagrangian coordinate at discrete intervals in time for a laser induced blast wave in aluminum.

Hydrodynamic simulations were used to roughly determine the blast wave radius and pressure scaling in a solid. Figure 8 shows the shock pressure (in kbar) versus Lagrangian coordinate (in microns) in aluminum at discrete intervals in time (ns). The displacement versus time scaling is $R \sim t^{0.92}$, whereas the pressure versus displacement scaling is $P \sim x^{-0.62}$.

2.1.5 Elastic and Plastic Waves and Phase Transitions

In this section, I will discuss the role that phase transitions and the elastic-plastic response of materials have on the equation of state and how they give rise to waves of different speeds. An excellent reference that discusses first and second order phase transitions is Duvall and Graham (Duvall and Graham 1977). Polymorphic materials possess first order phase transitions (i.e. α to ε transition in iron), whereas second order phase transitions include melting and freezing. Phase transitions often result in the presence of kinks or discontinuities in a Hugoniot.

Figure 9a shows an example Hugoniot for a material with a polymorphic phase transition. A material initially at state 0 will exhibit a single wave when shocked to state 1. In a similar manner, a material initially at state 0 shocked to state 4 will undergo a solid-solid phase transition, but will have single wave structure. For the intermediate pressure case, a material initially at state 0 shocked to state 3 will exhibit a two wave structure due to the phase transition: the first wave from state 0 to state 2 (steeper slope corresponding to a faster wave) and the second wave from state 2 to state 3 (shallower slope corresponding to a slower wave).

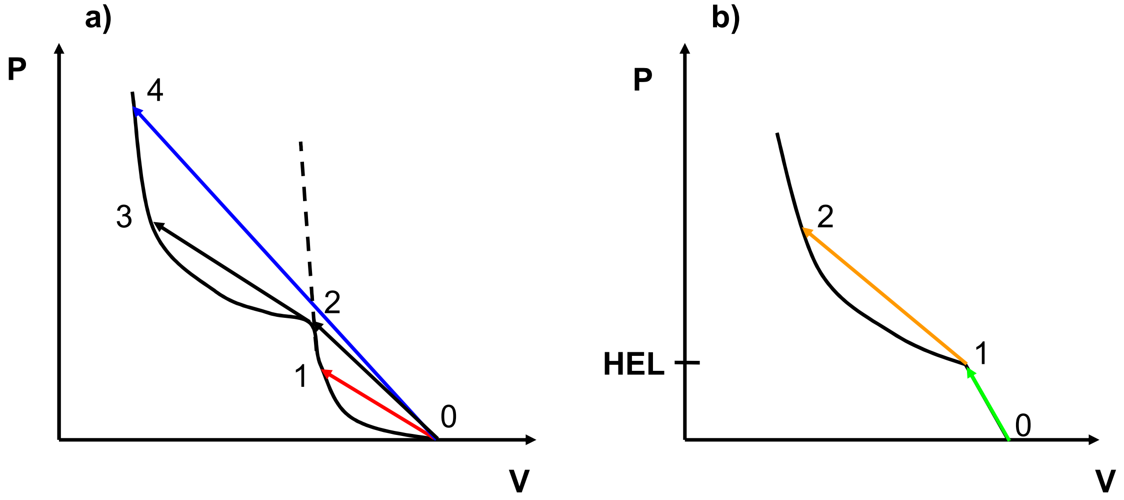

Figure 9: (a) Polymorphic phase transitions and (b) elastic-plastic materials give rise to wave splitting.

Wave splitting is also of interest in materials with an elastic-plastic response (Figure 9b). For small strains, the material deformation is linear with pressure (Hooke's law) meaning that the response is elastic. In this case, there is no deformation in the plane perpendicular to the direction of wave propagation. An elastic wave will travel at the longitudinal sound speed, c_l, which depends on both the bulk (K) and shear (G) moduli:

$$c_l = \left(\frac{K + \frac{4}{3} G}{\rho} \right)^{1/2}, \tag{2.42}$$

where the corresponding pressure is given by:

$$P = \frac{-\Delta V}{V} \rho c_l^{\,2}. \tag{2.43}$$

The bulk modulus is a measure of a material's ability to resist a uniform pressure, whereas the shear modulus is a measure of a material's response to shear. The Hugoniot elastic limit (HEL) is the maximum stress associated with the material's elastic response.

For deformation above the linear response, the material will respond with a two wave structure. In this case there is deformation in the plane perpendicular to the wave propagation, or in a plastic manner. A plastic wave will propagate at the bulk wave speed:

$$c_b = \left(\frac{K}{\rho}\right)^{1/2} , \qquad (2.44)$$

where the corresponding stress is given by:

$$P = \frac{-\Delta V}{V} \rho c_b{}^2 + const. \qquad (2.45)$$

For sufficiently high pressures, or in the strong shock case, there will be no elastic wave ahead of the shock.

2.1.6 Impedance Matching

Shock impedance, *Z*, is defined as the product of the density and shock velocity, $Z \equiv \rho U_S$. The impedance is a measure of the ability of the material to generate pressure under given loading conditions. Given the interface between two materials, A and B, (Figure 10) one can determine the reflection and transmission of waves at an interface. The incident wave with stress or pressure, σ_i and velocity v_i must satisfy two conditions at the boundary.

1. Pressure must be continuous across the boundary between the two materials.

$$\sigma_i + \sigma_r = \sigma_t \qquad (2.46)$$

2. The velocity of materials is continuous across the discontinuity

$$v_i - v_r = v_t \qquad (2.47)$$

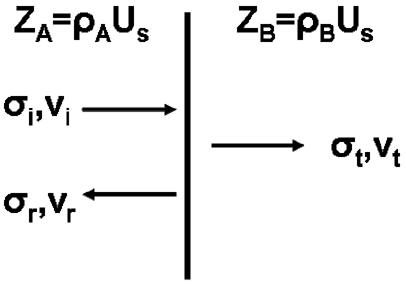

Figure 10: Shock impedance (Z_A and Z_B) of two materials at an interface along with the stresses and velocities associated with incident, transmitted and reflected waves.

Four conditions can then be derived for velocity and stress relating the ratio of transmitted to incident wave in addition to the ratio of reflected to incident wave. The ratio of reflected/transmitted velocity to incident wave velocity at the interface is given by:

$$\frac{v_r}{v_i} = \frac{Z_t - Z_i}{Z_t + Z_i} \tag{2.48}$$

$$\frac{v_t}{v_i} = \frac{2Z_i}{Z_t + Z_i} \tag{2.49}$$

Equations for the ratio of reflected/transmitted stress to incident stress at the interface are given by:

$$\frac{\sigma_r}{\sigma_i} = \frac{Z_t - Z_i}{Z_t + Z_i} \tag{2.50}$$

$$\frac{\sigma_t}{\sigma_i} = \frac{2Z_t}{Z_t + Z_i} \tag{2.51}$$

There are two special cases which we will discuss, a free surface interface and an impedance matched interface.

First, for the free surface case, which would be applicable to spall experiments, the second material or vacuum has an impedance of zero. This yields:

$$\frac{v_r}{v_i} = -1 \qquad \frac{v_t}{v_i} = 2 \qquad \frac{\sigma_r}{\sigma_i} = -1 \qquad \frac{\sigma_t}{\sigma_i} = 0 \tag{2.52}$$

From the second result, we see the transmitted (free surface) velocity is equal to twice the incident (particle) velocity. It is this condition that says that the free surface velocity is ~2U$_p$, which will use later in analysis. From the third result, the reflected stress is the negative of the incident stress, which means that if the incident wave is a compression wave (positive stress) then upon reflection the reflected wave becomes tensile (negative stress). The fourth result shows that the transmitted stress is zero which means that a stress wave must release to zero stress (or pressure) at the free surface.

Secondly, for the impedance matched case, which would be applicable for some melt experiments (i.e. aluminum on LiF, Figure 11), impedance of the second material has an impedance equal to the impedance of the first material. This yields:

$$\frac{v_r}{v_i} = 0 \qquad \frac{v_t}{v_i} = 1 \qquad \frac{\sigma_r}{\sigma_i} = 0 \qquad \frac{\sigma_t}{\sigma_i} = 1 \qquad (2.53)$$

From the first and third results, we see that there is no reflected wave across an impedance matched interface. From the second result, we see that the transmitted velocity is equal to the incident velocity. This means that if we probed the velocity at the interface then that would be the particle velocity. The fourth result shows that the transmitted stress is equal to the incident stress which means that a compressive initial stress remains a compressive transmitted stress across the boundary. In general, for an interface that has two materials of different impedance, there will be some percentage of the wave that is transmitted and then some percentage of the wave that is reflected. Using this same technique allows one to determine these percentages and thus the corresponding particle velocity or stress related to the measurement quantity.

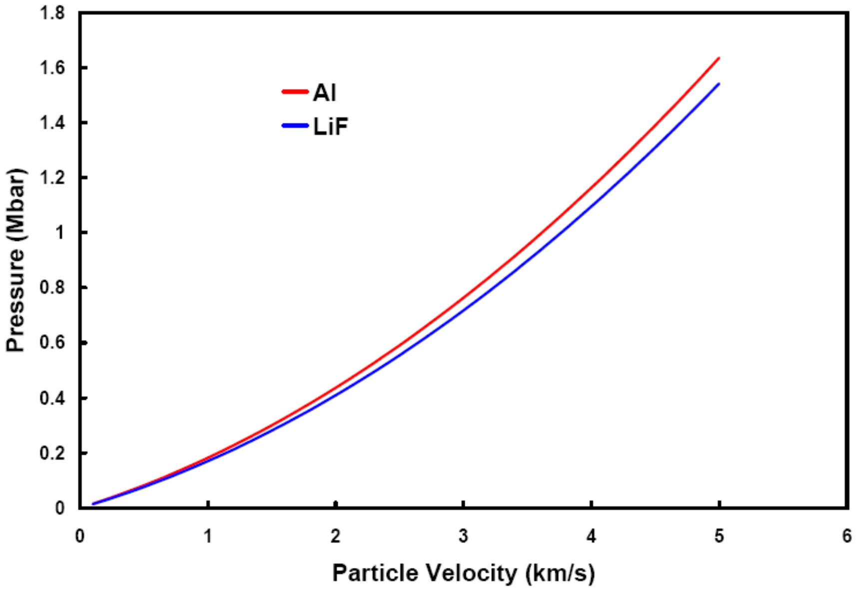

Figure 11: Pressure versus particle velocity for Al and LiF. The slope is the shock impedance, Z. The EOS's are from (Trunin 2001).

2.2 LASER MATTER INTERACTIONS

In this section I discuss laser interactions with matter and specify their role in inducing shocks in materials. I also explore the potential complicating factor of heat conduction.

2.2.1 Inverse Bremsstrahlung

When the laser interacts with the specimen it ionizes material, creating a low density plasma which expands into vacuum. The critical density surface is the density at which the plasma frequency equals the laser frequency, thus no laser light can pass. It is given by:

$$n_{crit}[cm^{-3}] = \frac{1.1x10^{21}}{\lambda[\mu m]}, \tag{2.54}$$

where λ is the laser wavelength. Bremsstrahlung (German for "braking radiation") is the process by which a particle such as an electron emits radiation when it encounters or collides with another particle (Figure 12a). Inverse Bremsstrahlung or collisional absorption is the process in which a photon is absorbed by a free electron under the influence of a nucleus (Figure 12b). Inverse Bremsstrahlung is the primary process of laser absorption at our relevant intensities. Resonance absorption is another process by which an electron plasma wave is driven at the critical density.

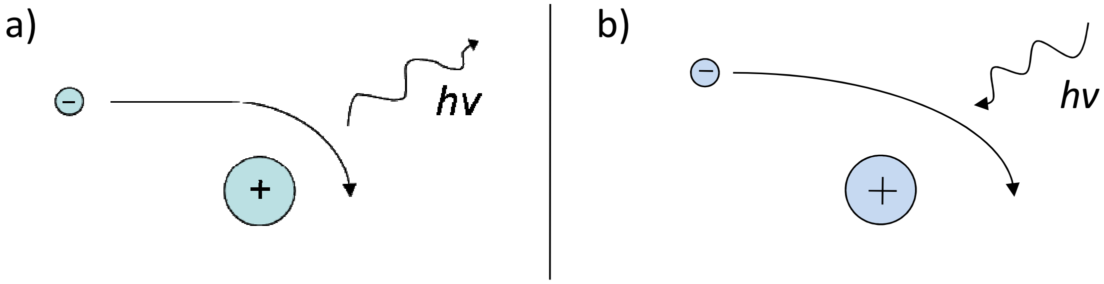

Figure 12: (a) Bremsstrahlung process: an electron encounters a nucleus and emits a photon. (b) inverse Bremsstrahlung process: an electron encounters a nucleus and absorbs a photon.

For an exponential density profile:

$$n_e = n_{crit} \exp\left(\frac{-z}{L}\right), \tag{2.55}$$

the fractional absorption at normal incidence due to inverse Bremsstrahlung is given by (Kruer 1988):

$$f_a = 1 - \exp\left(\frac{-8\nu_{crit} L}{3c}\right), \tag{2.56}$$

where ν_{crit} is electron ion collision frequency at the critical density and L is length of the plasma. This equation holds for the case where the electron-ion collision frequency, ν_{ei}, is density dependent:

$$\nu_{ei} = \nu_{crit} \frac{n_e}{n_{crit}}. \tag{2.57}$$

In a similar manner, for a linear density profile:

$$n_e = n_{crit}\left(1 - \frac{z}{L}\right) \tag{2.58}$$

the fractional absorption due to inverse Bremsstrahlung is given by:

$$f_a = 1 - \exp\left(\frac{-32}{15} \frac{\nu_{crit} L}{c} \right) . \qquad (2.59)$$

2.2.2 Shock Pressure via Laser Ablation

The coupling of laser light into a compression wave in a material occurs by laser ablation. Laser ablation of the material sends plasma into vacuum. This high velocity plasma induces a positive pressure wave into the bulk material, via a rocket-like effect. As previously discussed, laser light is absorbed by inverse Bremstrahlung. A simple scaling law can be derived for how the ablation pressure scales with laser intensity. Assuming that some fractional, *α*, laser intensity is absorbed, this is then equal to the rate of energy deposition per unit area. Rearranging this equation for velocity in terms of the laser intensity, *I*,

$$\alpha \cdot I = \frac{E}{At} = \frac{1}{2} \rho v^2 \cdot v \qquad (2.60)$$

Rearranging for the velocity *v* yields:

$$v = \left(\frac{2\alpha I}{\rho} \right)^{1/3} \qquad (2.61)$$

The ram pressure is approximately given as the density times the velocity squared. Inputting the velocity from above (Eq. 2.61) and rearranging produces the scaling for the ram pressure with laser intensity:

$$P_{ram} = \rho v^2 = \rho^{1/3} (2\alpha)^{2/3} I^{2/3} \qquad (2.62)$$

Clearly, the ablation pressure scales with laser intensity to the two-thirds power. Others have derived empirical relationships to estimate the ablation pressure. The scaling law for maximum ablation pressure induced in aluminum for a 1 μm laser is given by:

$$P_{\max}(kbar) = 120 \left(\frac{I_a \left(W / cm^2 \right)}{10^{11}} \right)^{2/3} , \qquad (2.63)$$

(Cottet and Boustie 1989) where I_a is the absorbed intensity. In a similar manner, an ablation pressure scaling law for various materials is given by Phipps, et al. (Phipps, et al. 1988):

$$P_{\max}(kbar) = 230\,A^{7/16} Z^{-9/16} \lambda^{-1/4} \tau^{-1/8} \frac{I^{3/4}}{10^{9}}, \qquad (2.64)$$

where A is atomic number, Z is ionication number, λ (μm) is laser wavelength, I is laser intensity (W/cm^2), and τ (ns) is pulse length. Figure 13 shows the plot of ablation pressure in aluminum versus laser intensity using Equations 2.63 and 2.64.

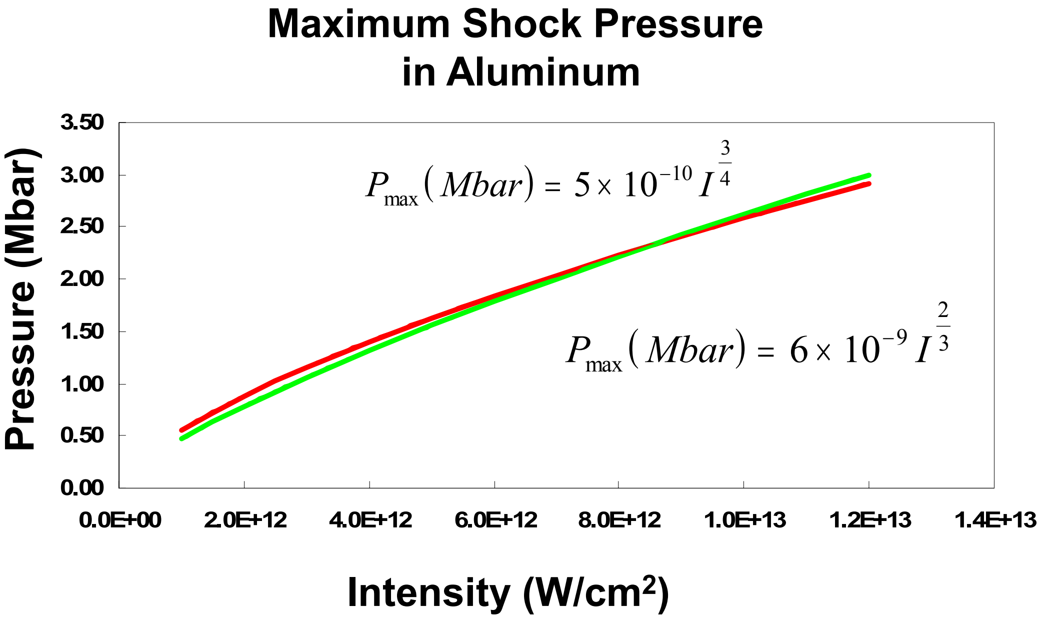

Figure 13: Ablation pressure versus laser intensity for λ=1.06 μm. The red curve is the scaling law from Cottet and Boustie (Eq. 2.63) and the green is the scaling law from Phipps, et al. (Eq. 2.64).

2.2.3 Thermal Waves

One problem with using laser induced plasmas to produce shocks is the occurrence of a thermal wave that propagates through a material. When a high intensity laser interacts with the surface of a material, the laser is absorbed within the material skin depth. A larger thermal gradient is then induced, which launches a thermal wave into the bulk material (Figure 14).

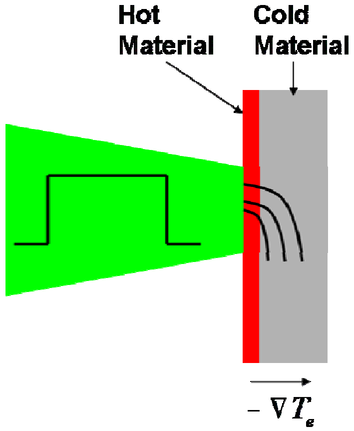

Figure 14: When a laser impacts materials a large thermal gradient is created near the front surface. This thermal gradient induces a thermal wave which propagates into the material.

Heat conduction advances energy diffusion and temperature equilibration:

$$\rho \cdot c_p \frac{\partial T}{\partial x} = -\nabla \bullet \vec{S} + W \tag{2.65}$$

where c_p is the specific heat at constant pressure, T is the temperature, S is the conductive heat flux, and W is the energy release per unit volume per unit time from external sources. The conductive heat flux can be considered proportional to the temperature gradient,

$$\vec{S} = -\kappa \nabla T \tag{2.66}$$

where $\kappa = a(k_B T_e)^{5/2}$ is the coefficient of thermal conductivity. Considering a one-dimensional problem, ∇T becomes dT/dx and then approximating dT/dx as T/x$_f$ (linear), where x$_f$ is the heat front:

$$\begin{gathered} S = a(k_B T_e)^{5/2} \frac{\partial T_e}{\partial x} \\ S \approx a(k_B T_e)^{5/2} \frac{T_e}{x_f} = a' \frac{(k_B T_e)^{7/2}}{x_f} \end{gathered} \tag{2.67}$$

.

Using energy conservation, the heat energy density can be equated with the thermal energy density of an ideal gas:

$$\frac{S}{x_f}t = \frac{3}{2}n_e k_B T_e$$
$$k_B T_e = \frac{2St}{3x_f n_e} \tag{2.68}$$

Substituting Eq. 2.68 into 2.67 and rearranging for the heat front x_f yields:

$$x_f \approx \frac{\left(\frac{2}{3}\right)^{7/9} a'^{7/9} S^{5/9} t^{7/9}}{n_e^{7/9}} \tag{2.69}$$

Notice that the thermal heat front scales as $t^{7/9}$. The shock front can be approximated by the product of the shock velocity and time, $x = U_s t$.

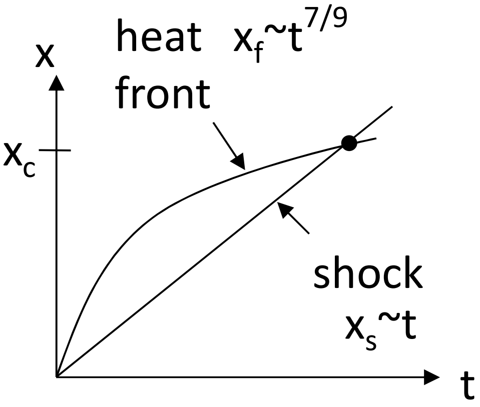

Figure 15: Displacement versus time showing the scaling of the thermal heat front propagation and the shock front propagation. The distance where they intersect is the critical distance, x_c.

The critical distance, x_c, is the distance needed for the shock front to catch up to the heat front. By rearranging the shock front distance for t, and inserting into the equation for the heat front distance (Eq. 2.68), the critical distance becomes:

$$x_c = \frac{\left(\frac{2}{3}\right)^{7/9} a'^{7/9} S^{5/9} \left(\frac{x_c}{U_S}\right)^{7/9}}{n_e^{7/9}}$$
$$x_c = \frac{\left(\frac{2}{3}\right)^{7/2} a'^{7/2} S^{5/2}}{n_e^{7/2} U_S^{7/2}} \tag{2.70}$$

One issue that was raised was whether the heat wave generated at the ablation surface could increase material temperature near the spall plane. To answer this question, I approximated the shock propagation to be linear in time. I also assumed that the shock speed is rather slow (U_s~6 km/s). Experimentally, this is a good approximation for the purposes of determining the importance of thermal waves since the spall signal does not occur later than 100 ns for a 500 µm target. There is also a heat front associated with a strong shock. I roughly assumed (based on previous experiments) that for a 500 µm target the spall plane would be about 100 µm from the rear surface. This means that the shock front would end up traveling about 600 µm (after being reflected from the rear surface) and the heat front would only need to travel about 400 µm. In the time of 100 ns, the shock traveled about 600 µm, but the heat wave only traveled 142 µm (Figure 16).

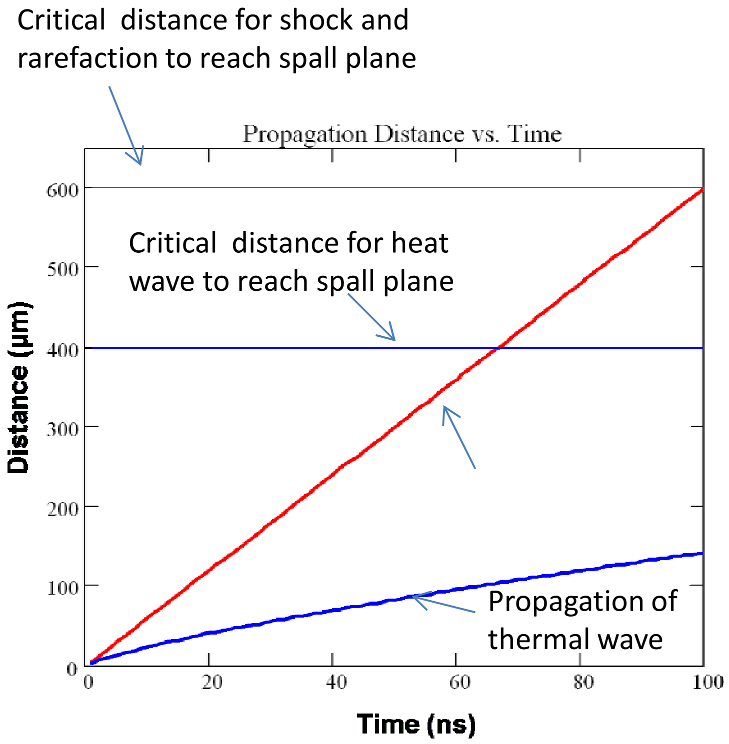

Figure 16: Propagation distance versus time for a weak shock (red) and a strong heat wave (blue) for a 500 um target.

In a similar manner for 200 µm targets, it is roughly assumed, but with experimental basis, that the spall thickness will be about 50 µm. The shock front must travel about 250 µm and the heat front must travel only about 150 µm. It takes 41.5 ns for the shock front to travel 250 µm. In the same amount of time, the heat front has traveled ~72 µm (Figure 17). It can be concluded that for these examples the heat wave does not seem to play a role in additional heating of material at the spall plane.

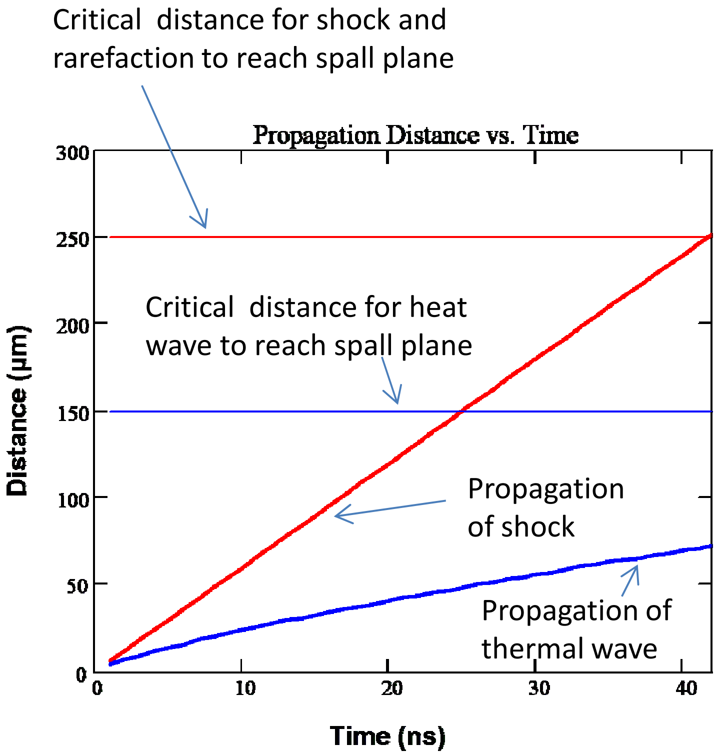

Figure 17: Propagation distance versus time for a weak shock (red) and strong heat wave (blue) for a 200 µm target.

CHAPTER 3. MECHANICAL RESPONSE OF MATERIALS

3.1 INTRODUCTORY ENGINEERING CONCEPTS

In this chapter, the concepts of stress and strain are introduced since they are vital quantities needed for interpreting material response. A description is provided for the way that materials respond, both elastically and plastically, before fracture. Several yield mechanisms are described to detail how microstructural changes can provide resistance to plastic deformation. A general description of the melt and spall experiments discussed in this dissertation are provided. The effects on fracture due to material microstructure and loading rate are discussed to motivate fast rate fracture studies of various aluminum based materials at the fast strain rates accessed by high intensity lasers. This chapter is concluded with a description of the preliminary plan of research.

3.1.1 Stress and Strain

When one puts a material under external forces, the load applied can cause the material to respond in various ways, which are discussed below. When a force per unit area is applied to a material it is called stress and it can be applied normal to the material (i.e. compressive or tensile) or in shear. Changes in shape are referred to as distortion, whereas, changes in volume are referred to as dilatation. Two references which present a strong foundation for understanding the mechanical response of materials are Dieter (Dieter 1976) and Courtney (Courtney 2000).

Consider a bar of length l_0 and cross-sectional area A_0. If one exerts a force F on the ends of the rod it lengthens the rod a distance Δl as in Figure 18.

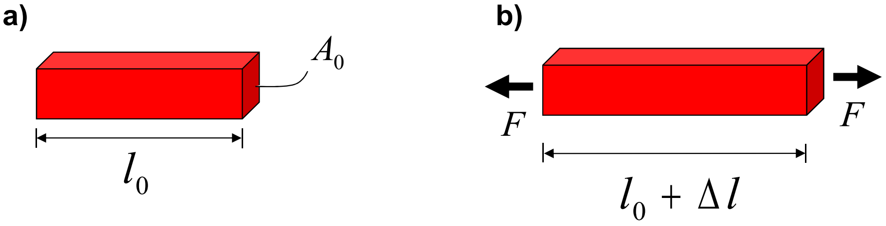

Figure 18: (a) Bar of initial length l_0 and cross-sectional area A_0. (b) Tensile force applied to the bar results in the bar extended a length Δl.

Engineering definitions are based upon the original dimensions of the specimen. Hence, the engineering strain, e, is defined as an incremental change in length over the original rod length.

$$e = \Delta l / l_0 = \frac{l - l_0}{l_0} \tag{3.1}$$

The engineering stress, s, is defined as the ratio of the force applied to the rod over the initial cross-sectional area.

$$s = F / A_0 \tag{3.2}$$

This means that the engineering definitions do not take into account the material changing (e.g. necking of ductile material). The true stress is defined as the applied load to the instantaneous cross section A. Assuming no change in volume ($A \cdot l = A_0 l_0$) the true stress is:

$$\sigma = \frac{F}{A} = \frac{F}{A_0}\frac{l}{l_0} = s(1+e) \tag{3.3}$$

As strain gets large and A of the specimen decreases, the true stress can get much larger than the engineering stress. The sum of the instantaneous engineering strains is the true strain.

$$\varepsilon = \int_{l_0}^{l_f} \frac{dl}{l} = \ln\left(\frac{l_f}{l_0}\right) = \ln\left(\frac{l_0 + \Delta l}{l_0}\right) = \ln(1+e) \tag{3.4}$$

3.1.2 Elastic versus Plastic Response and the Stress-Strain Curve

Starting with an atomic description of potential energy versus interatomic distance allows one to understand how atoms respond to an applied force. Figure 19 shows a potential energy curve versus interatomic spacing.

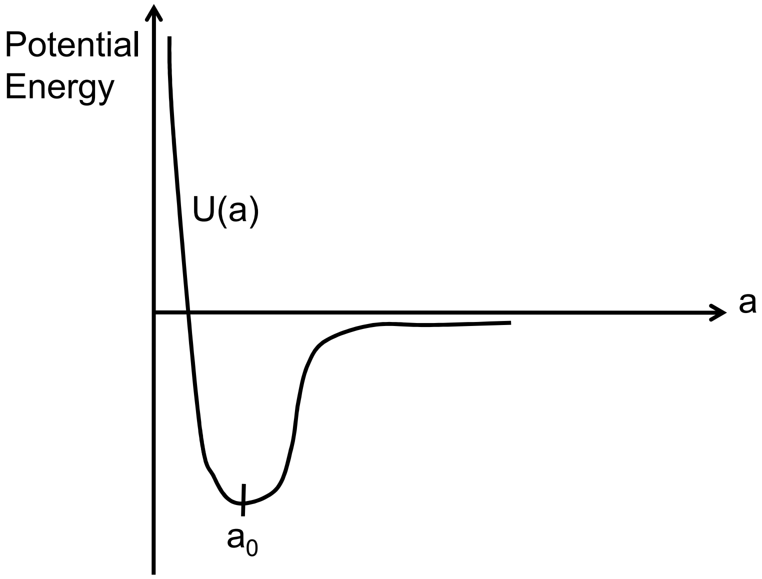

Figure 19: Potential energy curve versus interatomic spacing.

An external force applied to a crystal results in pulling atoms apart or pushing them together. The atoms act to oppose the applied force. For a null force applied, the atoms are at their equilibrium distance (a_0). For the case of a small, yet non-zero compressive force, the atoms act to repel each other, while for a tensile applied force, the atoms act to attract each other. The force is the derivative of the potential energy curve with respect to displacement ($x=a-a_0$).

$$F = -\frac{dU}{dx} \tag{3.5}$$

Assuming that the potential energy curve is continuous in x and representing it as a Taylor series gives:

$$U(x) = U_0 + \left(\frac{dU}{dx}\right)_{x=0} x + \frac{1}{2}\left(\frac{d^2U}{dx^2}\right)_{x=0} x^2 \tag{3.6}$$

Differentiating this form of the potential energy with respect to x yields:

$$F = \frac{-dU(x)}{dx} = -\left(\frac{d^2U}{dx^2}\right)_{x=0} x \tag{3.7}$$

This is the general form of Hooke's Law as the stiffness is the curvature of the energy-distance curve at zero displacement.

I now continue with a continuum description of stress and strain. An elastic response is one in which a body is deformed a small amount by an external force and upon release of that external force the body returns to its original stress-strain state (Figure 20). A material will respond elastically if the stress and strain have a linear relationship, given by:

$$\sigma = E\varepsilon, \tag{3.8}$$

where E is Young's (elastic) modulus. A material with a higher elastic modulus has a stiffer response. In general the response of material is anisotropic and Hooke's Law can be described in tensor notation:

$$\sigma_{ij} = C_{ijkl}\varepsilon_{kl}, \tag{3.9}$$

where σ_{ij} and ε_{kl} are the stress and strain tensors and C_{ijkl} is the stiffness tensor.

In a plastic response, the deformation is so large the body can not return to its original state, resulting in some permanent deformation. The yield strength is the stress at which materials begin to deform in a plastic manner. Atomically, this means that bonds are breaking and are able to re-arrange.

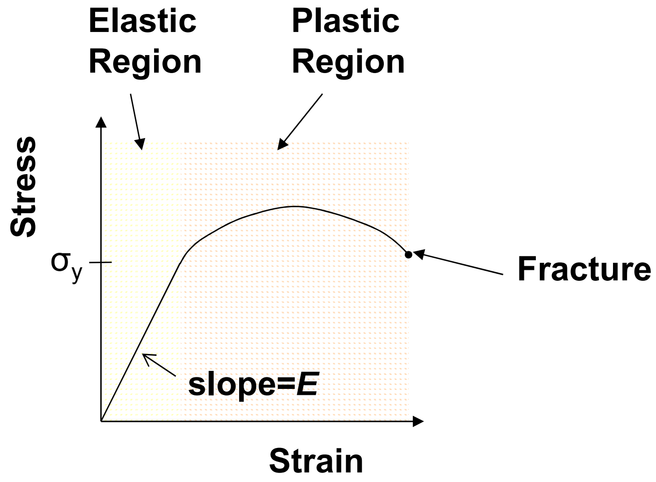

Figure 20: Stress-Strain curve (not to scale): The stress-strain curve is linear in the elastic region. Once the stress-strain relationship becomes nonlinear, the response of the material becomes plastic. The yield stress, σ_y, signifies the stress at which the material transitions from elastic to plastic response.

One empirical relation describing stress and plastic strain is the Holloman hardening law:

$$\sigma = K\varepsilon^n , \tag{3.10}$$

where K is the strength index, ε is the plastic strain and n is the strain hardening coefficient. Various yield models will be discussed in Section 4.4.3 in relation to hydrodynamic simulations.

3.1.3 Fracture and Griffith criterion

Fracture is the separation of material into multiple pieces upon a stress. It is considered to be a more catastrophic failure than plastic deformation. Intergranular fracture is shown by cracks that follow along grain (solid state matter with single crystal structure) boundaries. Transgranular fracture is observed by cracks that occur within a grain. Ductile fracture presents plastic deformation which takes place before fracture while brittle fracture does not. These various fracture modes will be discussed in the context of experimental results in Section 5.2.

The Griffith model is an energy based fracture criterion applicable for brittle materials. In this model, fracture occurs when the crack extension force and crack resistant force are equal. The surface energy created in a crack is $4c\gamma$, where $2c$ is the interior crack length and γ is the surface energy per unit area. The elastic strain energy per unit volume is $\frac{\sigma^2}{2E}$, where E is Young's modulus and σ is the applied stress. The stability criterion for stable crack growth is:

$$\frac{d}{dc}\left[4c\gamma - \frac{\pi\sigma^2 c^2}{E}\right] = 0 \quad (3.11)$$

Rearranging this for the fracture stress yields the Griffith criterion.

$$\sigma_F = \left(\frac{2\gamma E}{\pi c}\right)^{1/2} \quad (3.12)$$

3.2 STRENGTHENING MECHANISMS AND THEIR ROLE IN YIELD STRENGTH

In the last section, I described the onset of plasticity specifically in reference to single crystals. In this section, I discuss multiple mechanisms for increasing the material resistance to plastic deformation. In Section 3.5, the effects that these mechanisms play in the role of spall fracture are discussed.

3.2.1 Grain Boundary Strengthening

By making a material's average grain size smaller, the grain boundaries are able to keep dislocations (crystallographic defects) from moving through the material. Dislocations in a grain will tend to stack up at grain boundaries, resulting in a greater stress needed to move the dislocation. In this manner, grain boundaries strengthen a material because it limits additional plastic flow (dislocation motion). Figure 21 illustrates the concept of dislocations stacking at grain boundaries.

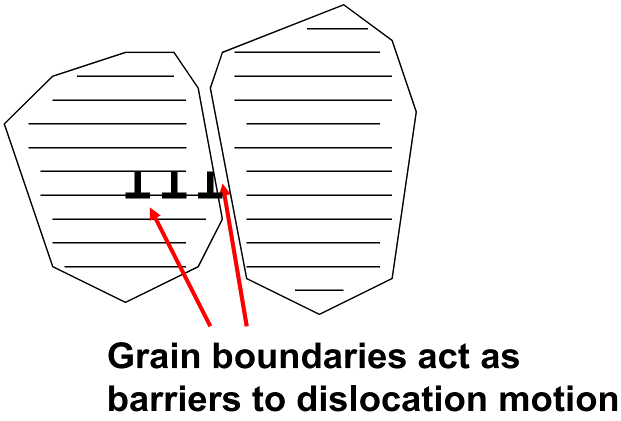

Figure 21: Edge dislocations (⊥) tend to stack at grain boundaries therefore grain boundaries inhibit dislocation motion.

The Hall-Petch equation relates the yield stress (stress at onset of plastic deformation) to the grain size as given by:

$$\sigma_y = \sigma_0 + k_y d^{-1/2}, \tag{3.13}$$

where σ_y is the yield stress, k_y is the strengthening coefficient, and d is the material grain size. This relationship, which has been shown to be true for many materials, shows that as the material grain size decreases the material's yield strength increases. Table 1 shows several k_y values for various materials. For aluminum the k_y value is 0.068 MN/m$^{3/2}$, whereas for copper the k_y value is 0.112 MN/m$^{3/2}$. Thus, grain size refinement results in a greater strengthening effect for copper than for aluminum.

Table 1: k_y values for various materials with their crystal structure. (Courtney 1990)

Material	Crystal structure	k_y (MN/m$^{3/2}$)
Low-carbon steel	bcc	0.307
Armco iron	bcc	0.583
Molybdenum	bcc	1.768
Zinc	hcp	0.220
Magnesium	hcp	0.279
Titanium	hcp	0.403
Copper	fcc	0.112
Aluminum	fcc	0.068

3.2.2 Solid-Solution Strengthening

By adding impurity atoms to a metal, an alloy is created with a greater resistance to plastic flow thus resulting in strengthening of the material. If the impurity atoms are similar in size to those present in the crystal, then they occupy the lattice positions (substitutional alloy). If the impurity atoms are much smaller, they fill the interstitial positions (interstitial alloy). Figure 22 shows an impurity atom within a surrounding matrix of atoms.

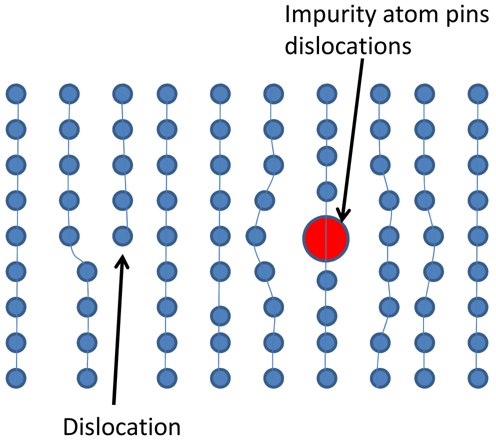

Figure 22: Planes of atoms with a dislocation (the extra half-plane of atoms) towards the left which is attempting to move to the right. The impurity atom creates a stress field around it which inhibits the dislocation from moving to the right.

The presence of the impurity atom produces a stress field in the surrounding atomic matrix. This stress field impedes the progression of the dislocation (the extra half plane of atoms) from propagating from one side of the matrix to the other. Thus, this addition of impurity atoms raises the yield stress and the level of the stress-strain curve by increasing the amount of shear stress (τ) needed to move the dislocation:

$$\Delta \tau \approx \frac{G\sqrt{c}}{1000}, \qquad (3.14)$$

where G is the shear modulus (GPa or kbar) and c is the solute concentration (represented as an atomic fraction).

3.2.3 Work-hardening

The method of strengthening known as work-hardening (or cold-working) increases a material's dislocation density. Figure 23 shows a cross section of a thin plate being rolled to a smaller thickness.

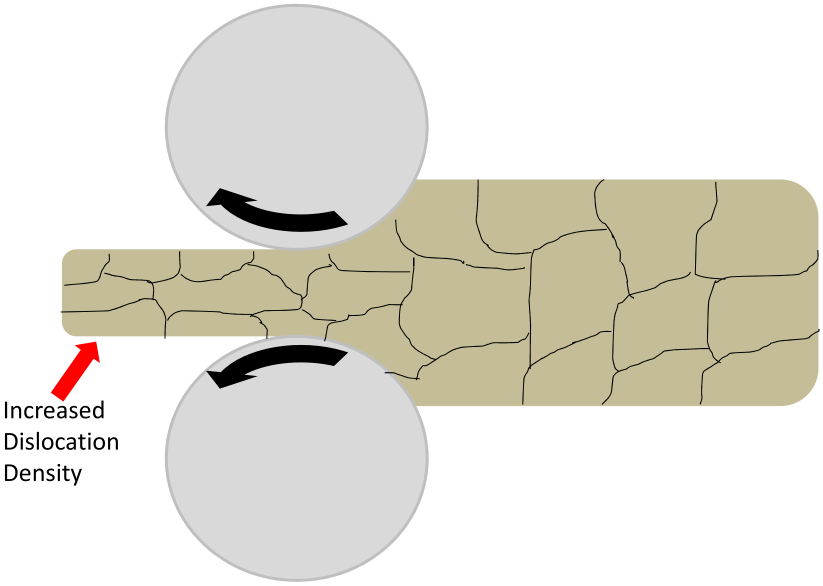

Figure 23: Planar specimen with polycrystalline structure rolled through a rolling mill which results in a higher dislocation density in the material.

The rolling of the specimen results in the grains being elongated, and increasing the dislocation density. The dislocations pin other dislocations thereby inhibiting additional plastic flow. This results in an increase in material hardness, but a decrease in material ductility.

3.3 MELT

To this point, several preliminary engineering concepts and strengthening mechanisms have been introduced. Now, I will discuss the concepts of shock induced melt and fast rate fracture.

3.3.1 Melt

Understanding the time scales necessary for shock induced melting is a fundamental problem. The temperature-pressure phase diagram of aluminum is shown in Figure 24. This figure illustrates two different thermodynamic pathways to melt the material.

1) Shocking to a pressure of ~ 1.4 Mbar (following the Hugoniot curve) compresses the aluminum into a liquid state.
2) Shocking to ~ 0.6 Mbar, which is still below the melt curve, and following isentropic release (release to zero pressure, indicated by the dashed curve) causes the solid to become a liquid.

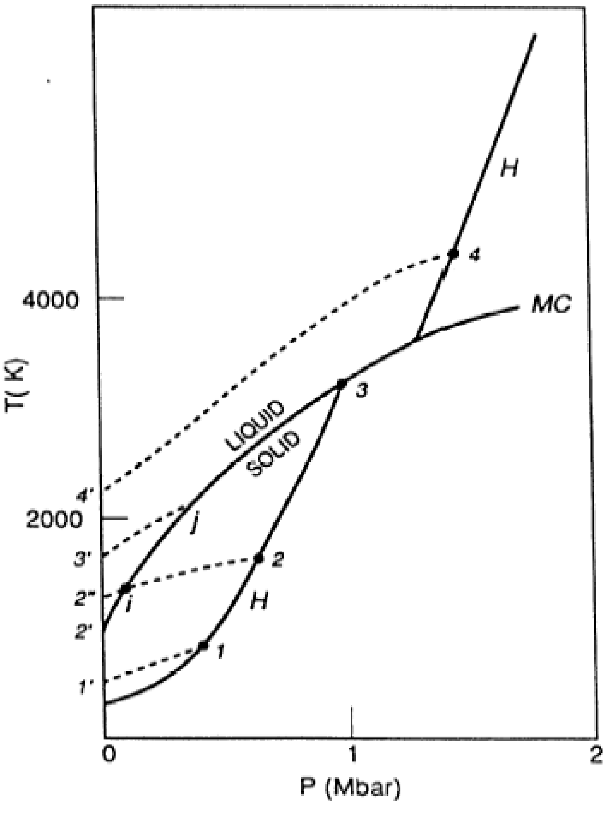

Figure 24: Phase diagram of aluminum in terms of temperature versus pressure. The melt curve (MC) separates the solid and liquid states. The curve, H, shows the shock Hugoniot of aluminum. The dashed curves show isentropic release paths. Reprinted figure with permission from Henis, Z. and Eliezer, S. "Melting phenonmenon in laser-induced shock waves." Physical Review E. 48 (1993):

2094. Copyright (1993) by the American Physical Society.
http://prola.aps.org/abstract/PRE/v48/i3/p2094_1

Experiments involving melting upon compression typically will have aluminum backed on a lithium fluoride, LiF, window (Figure 25a). Because these materials are impedance matched (Section 2.1.6), a shock propagating through aluminum will continue to propagate across the Al-LiF interface into LiF. The aluminum at that interface will not drop to zero pressure, so melting is achieved only by compressing to a point on the Hugoniot above the melt curve (method 1 in Figure 24). Aluminum specimens which are not backed with LiF can also melt as the shocked surface isentropically releases across the melt curve (method 2 in Figure 24).

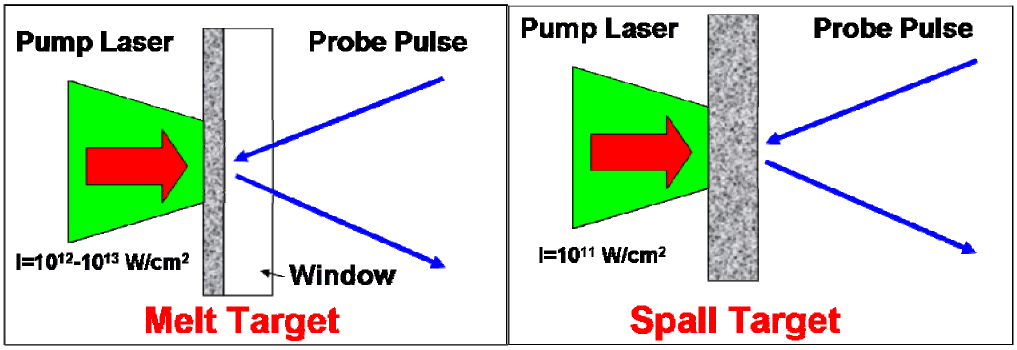

Figure 25: (a) General melt (on compression) target layout illustrates pump laser from left impacting a thin metal layer bonded to an impedance matched window. Probe pulses track the interface motion between metal and LiF. (b) General spall target impacted by laser on left side and probe pulses image the rear surface of these targets. This type of target can melt upon release.

3.4 SPALL

Spall is the planar fracture of material due to a tensile stress such as that generated by shock dynamics initiated by explosives, plate impacts, or pulsed laser irradiation. How materials react to impulsive loads depends on their microstructural characteristics and rate at which strain is introduced to the material (strain rate).

3.4.1 Spall

Figure 25b illustrates the typical pump-probe geometry for laser-induced spall experiments. The target is typically free standing. For example, when an intense laser

(I ~ $10^{11\text{-}12}$ W/cm^2) irradiates a solid target, an ablation-driven shock-wave propagates through the material, reflects off the rear (free) surface at zero pressure and produces a rarefaction wave traveling back into the target. The material is put into tension as this reflected rarefaction wave encounters the rarefaction from the decay of the still forward-going shock. When the material tension surpasses the material spall strength at the given loading conditions, it will separate, or spall. It is important to note that the laser pulse must be temporally short enough to allow the wave decay to encounter the reflected wave inside the material.

Figure 26a shows a schematic representation of interacting rarefactions that result in spall of the material. Figure 26b illustrates a stress wave interaction with a free surface which puts the material into tension and causes spall fracture once the required tensile stress (σ_F) has been met.

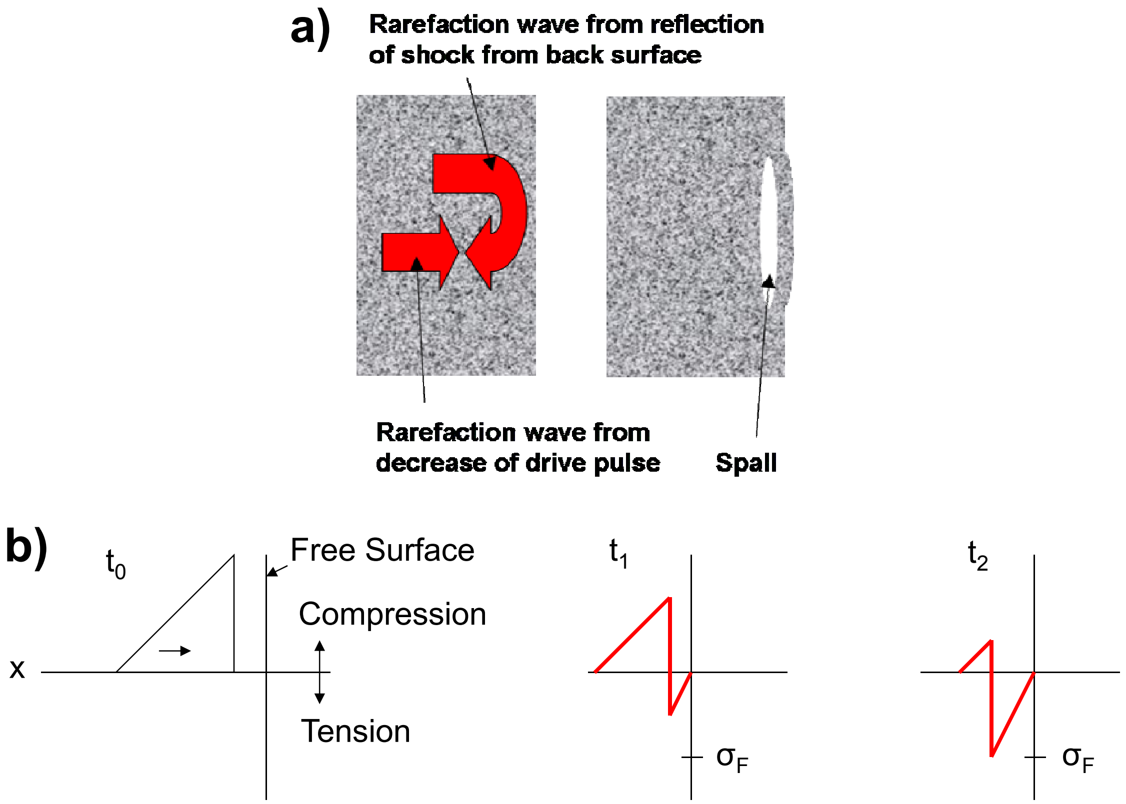

Figure 26: (a) Cartoon illustrating fact that interacting rarefactions results in large amplitude tensile stress resulting in planar fracture (spall). (b) Evolution of an initially compressive triangular pulse at time t_0. At time t_1 part of the compressive pulse has reflected from the free surface, resulting in tension. The red curve shows the net stress. At time t_2 more of the pulse is in tension and the net stress reaches the fracture threshold.

In ductile materials, spallation proceeds through stages of nucleation, growth, and coalescence of voids that may lead to complete fracture, whereas in brittle materials spall occurs from the development and propagation of cracks (Shockey, Seaman and Curran 1973). Figure 27 illustrates the multi-step process of spall for ductile materials.

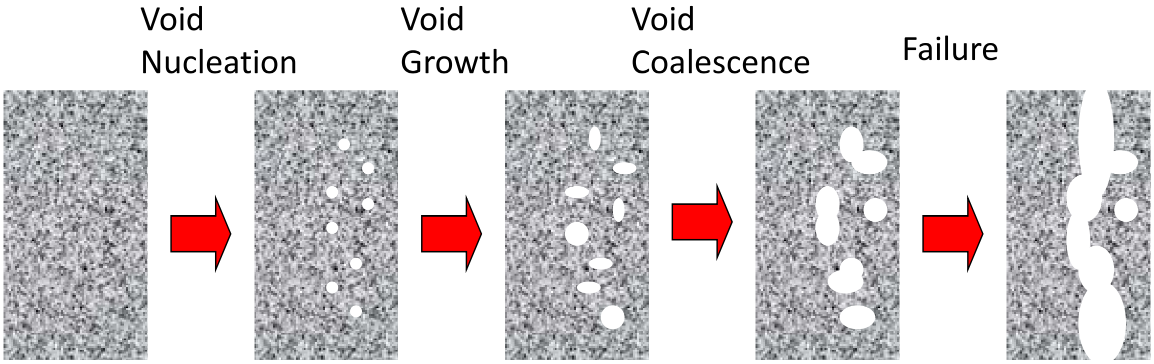

Figure 27: Step by step illustration of the spall process in ductile materials which starts as void nucleation, and continues with void growth, coalescence, and failure (fracture).

3.4.2 Theoretical Spall Strength

Dennis Grady (D.E. Grady, 1988) described a way to estimate the maximum tensile stress that can be supported in a material. The description starts from the Morse potential, *U(V)*, which is a potential for a diatomic molecule (Figure 28):

$$U(V) = U_{coh}\left[\exp\left(\frac{-2(V-V_0)}{a}\right) - 2\exp\left(\frac{-(V-V_0)}{a}\right)\right], \tag{3.15}$$

where U_{coh} is the cohesive energy, V is the specific volume and V_0 is the specific volume at zero pressure. The parameter a is constrained by the material's bulk modulus and is equal to:

$$a = \left(\frac{2V_0U_{coh}}{B_0}\right)^{\frac{1}{2}}, \tag{3.16}$$

where B_0 is the bulk modulus of the material.

The pressure curve of the material is the negative of the derivative of the potential curve.

$$P(V) = -\frac{dU}{dV} = \frac{2U_{coh}}{a}\left[\exp\left(\frac{-2(V-V_0)}{a}\right) - \exp\left(\frac{-(V-V_0)}{a}\right)\right] \tag{3.17}$$

The maximum tension that can be supported in the material is the minimum value of the pressure curve.

$$\frac{dP}{dV} = -\frac{2U_{coh}}{a^2}\left[2\cdot\exp\left(\frac{-2(V-V_0)}{a}\right) - \exp\left(\frac{-(V-V_0)}{a}\right)\right] = 0 \tag{3.18}$$

Solving for *V-V₀* yields:

$$
\begin{aligned}
&2\cdot\exp\left(\frac{-2(V-V_0)}{a}\right)-\exp\left(\frac{-(V-V_0)}{a}\right)=0\\
&\ln(2)-\frac{2(V-V_0)}{a}=\frac{-(V-V_0)}{a} \qquad (3.19)\\
&V-V_0=a\ln(2)
\end{aligned}
$$

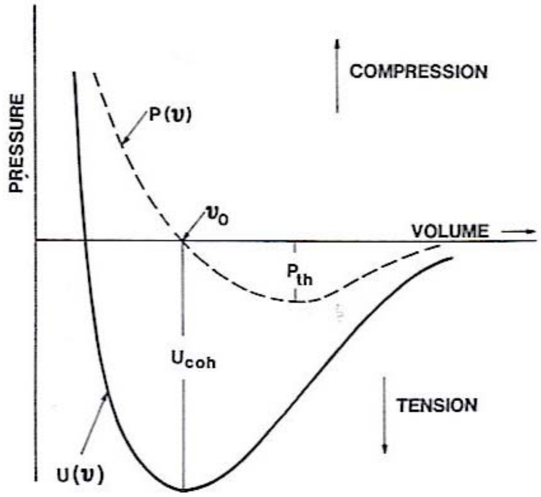

Figure 28: Pressure versus volume cold compression along with curve for a Morse potential. Above the volume axis is compression and below the volume axis is tension. The minimum of the pressure curve gives the maximum tensile stress supported by the material. Reprinted from "The Spall Strength of Condensed Matter, 36, D.E Grady, 353 (1988) with permission from Elsevier.

The theoretical spall strength, P_{th}, (via Eqs. 3.16, 3.17 and 3.19) then becomes an expression that depends on the cohesive energy, bulk modulus, and material density:

$$P_{th}=\sqrt{\frac{U_{coh}B_0\rho}{8}}\,. \qquad (3.20)$$

Inputting reasonable values for aluminum (B_0 = 72.2 GPa, ρ = 2710 kg m^{-3}, U_{coh}=11.9 MJ kg^{-1}) one gets P_{th} of 17.1 GPa or 171 kbar. This gives an upper limit to the expected spall strength in aluminum. Data from Moshe, et al. suggests that at ultrahigh strain rates (>10^8-10^9 s^{-1}) this derived theoretical spall strength limit may be approached (Moshe, Eliezer and Henis, et al. 2000).

3.4.3 Spall Strength

The tensile stress that causes a material to fracture at fast strain rates can be calculated by looking at free surface velocity profiles. One method of calculating this stress, also called the spall strength, is by an acoustic wave approximation (Novikov, Divnov and Ivanov 1966), (Chen, et al. 2005). Figure 29 shows an x-t diagram of a plate (1) impacting a target specimen (2) that is in contact with a low impedance buffer (3). The C^+ characteristics represent release waves from the release of the drive pulse and the C^- characteristics represent release waves from the reflection of the drive pulse off the target-buffer interface.

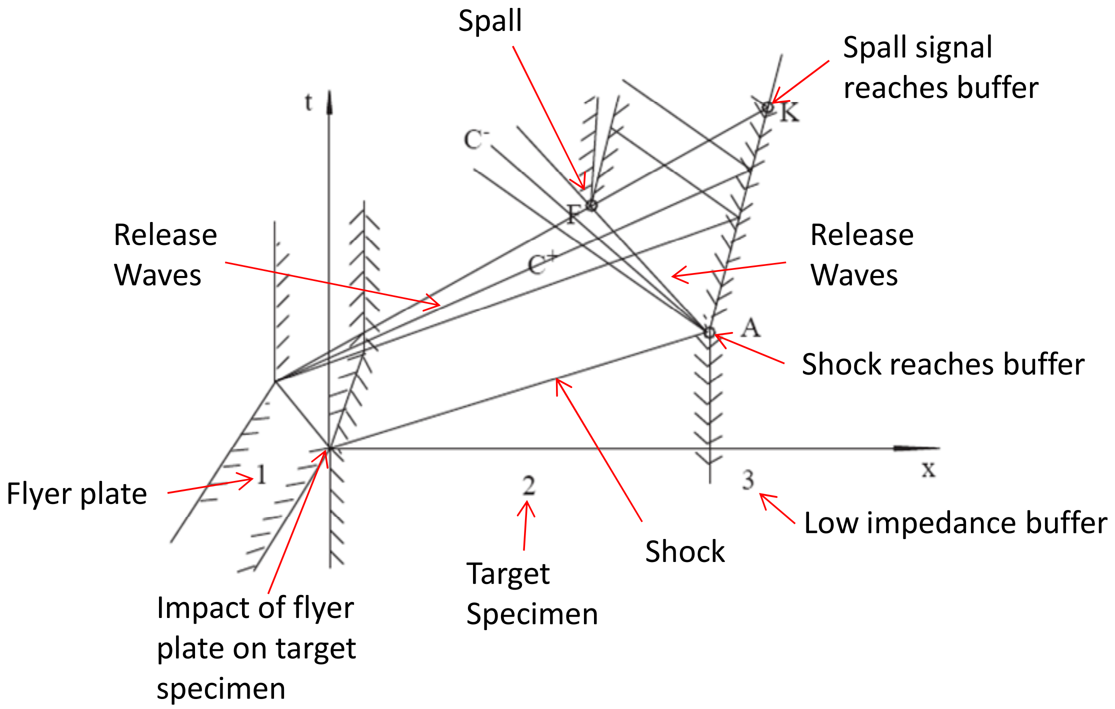

Figure 29: x-t diagram of plate (1) impact on a target (2) with a low impedance buffer (3). The point A is where the interface first moves, F is where fracture is initiated and K is where the spall pulse reaches the interface between 2 and 3 (figure adapted from Chen, et al. 2005). Reprinted from "On the validity of the traditional measurement of spall strength." Chen, D., Y. Yu, Z. Yin, H. Wang, and G. Liu., International Journal of Impact Engineering, 31 (2005): 811 with permission from Elsevier.

The characteristics, C^+ and C^-, are given by:

$$C^+ : \int_{P_K}^{P_F} dP = -\int_{u_K}^{u_F} \rho C du \qquad (3.21)$$

$$\mathrm{C}^{-}: \int_{P_A}^{P_F} dP = \int_{u_A}^{u_F} \rho C du$$

where the spall pulse (point F to K) follows a C^+ characteristic and the release isentropes due to free surface reflection (point A to F) follow the C^- characteristics. The Hugoniot of the target material (subscript 2) in *P*-*u* space is given by:

$$P(u) = \rho_{02} U_S u = \rho_{02}(C_{02} + S_2 u)u \tag{3.22}$$

Differentiating Eq. 3.22 with respect to *u* yields:

$$\frac{dP}{du} = \rho_{02}(C_{02} + 2S_2 u) \tag{3.23}$$

Substituting Eq. 3.23 into Eq. 3.21 yields:

$$\begin{aligned} P_F - P_K &= -\rho_{02}\left[C_{02} + S_2(u_F + u_K)\right](u_F - u_K) \\ P_F - P_A &= \rho_{02}\left[C_{02} + S_2(u_F + u_A)\right](u_F - u_A) \end{aligned} \tag{3.24}$$

where it was assumed that the release isentrope (C^- characteristic) is also represented by the Hugoniot. This assumption is valid for low pressures. In the acoustic approximation ($S_2 u^2 << C_{02} u$), so Eq. 3.24 yields:

$$\begin{aligned} P_F - P_K &= -\rho_{02} C_{02}(u_F - u_K) \\ P_F - P_A &= \rho_{02} C_{02}(u_F - u_A) \end{aligned} \tag{3.25}$$

Adding the two parts of Eq. 3.25 and implementing the boundary condition at the free surface (p_A=p_K=0, u_K=W_K, u_A=W_A), yields:

$$P_F = \frac{1}{2}\rho_{02} C_{02}(W_K - W_A), \tag{3.26}$$

where W_K and W_A are free surface velocities. The spall strength P_{spall}, from the acoustic approximation, is:

$$P_{spall} = \frac{-1}{2}\rho_0 \cdot c \cdot (u_{\max} - u_{\min}), \tag{3.27}$$

where $u_{\max} - u_{\min} = \Delta u$ is the pullback velocity (Figure 30). Thus, the spall strength of a material can be determined from measurements of the rear surface velocity record.

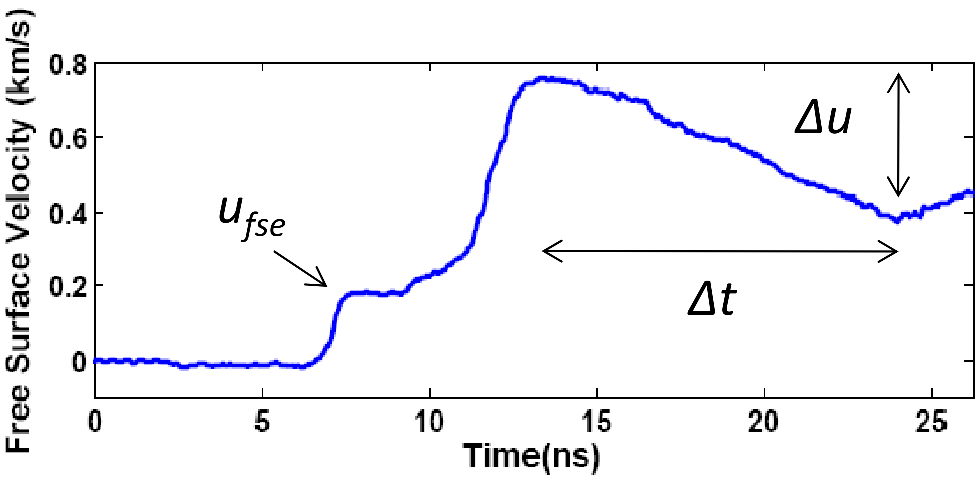

Figure 30: Free surface velocity versus time in the case of spall with u_{fse}, Δt and Δu.

The velocity u_{max} is the peak velocity of the free surface and u_{min} is the first minimum in free surface velocity. There are numerous corrections to this spall strength derivation including the effects of elastic-plastic waves. Stepanov derived the relationship:

$$P_{spall} = \rho_0 c_l \Delta u \frac{1}{1 + c_l / c_b}, \qquad (3.28)$$

to account for differences in wave speeds near the spall pulse (Stepanov 1976). The spall pulse front should propagate at the longitudinal wave speed (c_l) whereas the rarefaction wave before it is traveling at the bulk sound speed (c_b). Kanel et al. derived the expressions for the tensile stress prior to spall (Kanel, Razorenov and Utkin, 1996):

$$P_{spall} = \frac{1}{2} \rho_0 c_b \left(\Delta u + \delta \right), \qquad (3.29)$$

and δ is a correction for the wave profile that accounts for elastic and plastic waves

$$\delta = \left(\frac{h}{c_b} - \frac{h}{c_l} \right) \frac{|\dot{u}_1 \dot{u}_2|}{|\dot{u}_1| + \dot{u}_2}, \qquad (3.30)$$

where h is the spall thickness, and $\dot{u}_1$ and $\dot{u}_2$ are velocity derivatives with respect to time for the pulse ahead of spall and in the spall pulse, respectively.

3.4.4 Strain Rate

Strain rate is defined as the derivative of strain with respect to time:

$$\dot{\varepsilon} = \frac{d\varepsilon}{dt} = \frac{1}{l}\frac{dl}{dt} . \tag{3.31}$$

The strain rate from a particular shot can be calculated from the free surface or particle velocity profiles and is given by (Dekel, et al. 1998):

$$\dot{\varepsilon} = \frac{du_p}{dt}\bigg|_{t=t_{spall}} \frac{1}{c} \approx \frac{\Delta u}{\Delta t}\frac{1}{2c} , \tag{3.32}$$

where *Δu* is the pullback velocity and *Δt* is the difference in corresponding times of these velocities (Figure 30).

3.4.5 Dynamic Yielding

The longitudinal stress of the elastic precursor, also known as the Hugoniot elastic limit (σ_{HEL}) is given by:

$$\sigma_{HEL} = \rho_0 U_{elastic} \frac{u_{fse}}{2} = \frac{(1-\nu)Y}{1-2\nu} , \tag{3.33}$$

where Y is the dynamic yield strength, u_{fse} is the free surface velocity (Figure 30) associated with the elastic precursor, and $U_{elastic}$ is approximately the longitudinal wave speed, c_l. The HEL stress is the maximum stress that can be supported by the material upon compression before failure due to a plastic wave. Poisson's ratio, ν, is taken to be ~0.33 for most metals.

3.5 MATERIAL AND WAVE EFFECTS ON SPALL

In this section I will explore the role that both material properties and pressure wave profiles have on the spall strength of materials such as copper, aluminum and steel. Grain size and orientation, alloy effects and strain hardening are all material properties to explore in spall strength studies. Changes in wave profiles such as impact pressure and strain rate are potential variables that affect spall strength. Spall stress and fracture mode observations are in general not the same for all materials. In this section I will explore how different factors affect the response of materials with varying microstructures to impulsive loading.

3.5.1 Effect of Strain Rate on Spall

Moshe, *et al.* were able to study spall strength over a range of very fast strain rates. They showed that laser-driven foils of aluminum and copper exhibited spall strengths that dramatically increased with strain rate above 10^6 s^{-1} as shown in Figure 31. This result implied a change in spall failure mechanism at strain rates of about 10^7 s^{-1} (Moshe, Eliezer and Henis, *et al.* 2000).

Some have used variables such as threshold irradiance and spall thicknesses to estimate spall stress. These are insightful estimates for spall strength, but they do not measure the dynamic response of the loaded materials.

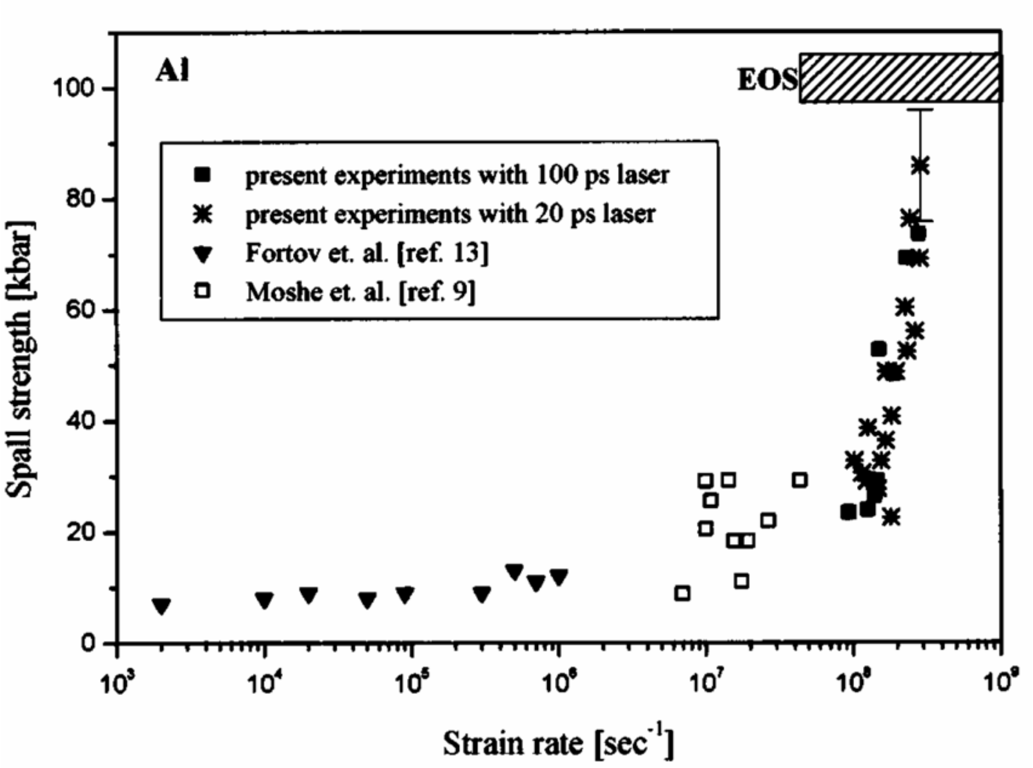

Figure 31: Spall strength versus strain rate on a log scale. Reprinted with permission from Moshe, E. et al. "Experimental measurement of the strength of metals approaching the theoretical limit predicted by the equation of state." Applied Physics Letters 76 (2000): 1555. Copyright 2000, American Institute of Physics.

The Grady spall criterion (Grady 1988), (Grady 1982) is an energy based spall criterion in which the kinetic energy and elastic energy must be as high as the fracture energy,

$$KE + U \geq \Gamma \, , \tag{3.34}$$

where *KE* is kinetic energy, *U* is elastic energy, Γ is the energy spent during fast rate fracture.

The average tension in an expanding material depends on strain rate and time:

$$P = \rho {c_0}^2 \dot{\varepsilon} t \tag{3.35}$$

Another condition needed for spall to occur is the horizon criterion. In order for a volume of ~$(c_0t)^3$ to fail independently, the communication horizon must be no more than c_0t. The horizon condition is thus given as:

$$s \leq 2c_0 t \tag{3.36}$$

where s is the fragment size. The local kinetic energy density within a mass element for fragmentation is given by:

$$KE = \frac{1}{120}\rho\dot{\varepsilon}^2 s^2 . \tag{3.37}$$

In order to derive the equation for kinetic energy density one considers a spherical mass element of radius r. For the shell of mass, dm, the local kinetic energy KE' is:

$$d(KE') = \frac{1}{2}r^2 dm , \tag{3.38}$$

where the shell mass and rate of radius change, $\dot{r}$, are:

$$\begin{gathered} dm = 4\pi\rho r^2 dr \\ \dot{r} = -\left(\frac{\dot{\rho}}{3\rho}\right) r . \end{gathered} \tag{3.39}$$

The kinetic energy is then found by substitution and integrating from $r=0$ to $r=a$:

$$\begin{gathered} KE' = \int_0^a \frac{4\pi}{2\cdot 9}\rho\left(\frac{\dot{\rho}}{\rho}\right)^2 r^4 dr \\ KE' = \frac{2\pi}{45}\rho\left(\frac{\dot{\rho}}{\rho}\right)^2 a^5 \end{gathered} . \tag{3.40}$$

The kinetic energy density then becomes:

$$KE = \frac{KE'}{\frac{4}{3}\pi a^3} = \frac{1}{120}\rho\dot{\varepsilon}^2 s^2 , \tag{3.41}$$

where $\dot{\varepsilon}$ is the strain rate ($\dot{\rho}/\rho$) and s is particle diameter.

The elastic energy density available as the material is put into tension is:

$$U = \frac{1}{2}\frac{P^2}{\rho c_0^{\,2}} . \tag{3.42}$$

For brittle spall, the fracture surface energy density depends on the fracture toughness, K_c, and is given by:

$$\Gamma_B = \frac{3{K_c}^2}{\rho {c_0}^2 s} . \tag{3.43}$$

This model does not take into account the variation of the fracture toughness with strain rate. For brittle spall to occur, the sum of the kinetic and elastic energy densities must be at least as high as the fracture surface energy density:

$$\frac{1}{120}\rho\dot{\varepsilon}^2 s^2 + \frac{1}{2}\frac{P^2}{\rho {c_0}^2} \geq \frac{3{K_c}^2}{\rho {c_0}^2 s} . \tag{3.44}$$

Using this energy condition with the horizon criterion allows for determination of spall strength for brittle spall (neglecting the smaller kinetic energy term):

$$P_{sp,brittle} = \left(3\rho c_0 {K_c}^2 \dot{\varepsilon}\right)^{1/3} \tag{3.45}$$

This equation for brittle spall strength does have strain rate dependence.

The ductile spall fracture energy criterion assumes that all energy is dissipated in the form of plastic deformation. While the energy for brittle spall can be described using the fracture toughness of a material, the energy for ductile spall, Γ_d, can be described using the material's flow stress, Y, and the critical strain ε_c. The critical strain is interpreted as the strain needed for coalescence of voids. This model also does not take into account the changing of the flow stress with strain rate.

$$\Gamma_d = Y\varepsilon_c \tag{3.46}$$

Using the same kinetic and elastic energies as for brittle spall (Equations 3.37 and 3.38), the energy criterion for ductile spall is:

$$\frac{1}{120}\rho\dot{\varepsilon}^2 s^2 + \frac{1}{2}\frac{P^2}{\rho {c_0}^2} \geq Y\varepsilon_c \tag{3.47}$$

Using this condition along with the horizon criterion (and neglecting the smaller kinetic energy term) gives the ductile spall strength:

$$P_{sp,ductile} = \left(2\rho c_0^{\ 2} Y \varepsilon_c\right)^{1/2} \quad . \tag{3.48}$$

This equation for ductile spall strength does not have strain rate dependence. Setting the brittle and ductile spall strengths equal (Equations 3.41 and 3.44) and rearranging yields the critical strain rate transition from brittle to ductile spall:

$$\dot{\varepsilon}_{crit} = \sqrt{\frac{8}{9}\frac{B_0^{\ 2}\left(Y\varepsilon_c\right)^3}{\rho K_c^{\ 4}}} \tag{3.49}$$

For Al 6061-T6 (Table 2) Grady predicted that the critical strain rate to transition from brittle spall to ductile spall is $\dot{\varepsilon}_{crit}$ =4 x 10^5 s^{-1}. Gilath et al. stated that their observation of ductile spall in laser shocked foils above this critical strain rate was direct evidence of Grady's theory; however, there was no observation of a brittle to ductile transition (Gilath, et al. 1988).

Table 2: Parameters for determining the critical strain rate of Al 6061-T6.

B_0	Y	K_c	P	ε_c	$\dot{\varepsilon}_{crit}$
7×10^{10} N/m^2	3×10^8 N/m^2	3×10^7 N/m$^{3/2}$	2710 kg/m^3	0.15	4×10^5 s^{-1}

Buchar et al. measured spall strength versus strain rate for various steels (Buchar and Hrebebicek 1993). The authors attempted to explore the effect that strain rate had on fracture toughness, which is not attempted by Grady's spall model. They found that at low strain rates, the spall strength agreed with the brittle spall strength equation (Eq. 3.41), but was then constant beyond the critical strain rate (Eq. 3.45). They observed ductile fracture at all strain rates investigated. For at least one fracture toughness (~50 MPa $m^{1/2}$), the critical strain rate was increased. In another paper, Buchar et al. measured spall strength versus strain rate for copper of different grain sizes: 94 μm, 130 μm, 185 μm (Buchar, Elices and Cortez 1991). They observed different critical strain rates for the different grain sizes and different constant spall values once the critical rates were reached.

3.5.2 Effect of Grain Size/Orientation on Spall

The effect of grain size on spall strength has not been well established in the literature. Some groups have found that spall strength increases with larger grain sizes (Minich, et al. 2004), while others have found that spall strength increases with smaller grain sizes ((Buchar, Elices and Cortez 1991), (Christy, Pak and Meyers 1986)). Minich, *et al.,* for example, performed spall experiments on copper with flyer-plates over a pressure range of 5-45 GPa (Minich, et al. 2004). The authors reasoned that with a larger grain, there is a smaller surface area per unit volume at the grain boundary, which is a preferential site for fast fracture, thus reducing the total area for possible microvoids to nucleate. They conclude that reducing the grain size to increase the flow stress of a material lowers the spall strength. On the other hand Christy, *et al.* reported the opposite trend, where three grain size copper specimens (250 μm, 90 μm and 20 μm) were impacted with flyer plates at 3.8 GPa (Christy, Pak and Meyers 1986). The authors found that the large and intermediate grained materials exhibited intergranular fracture whereas the small grain and rolled specimens showed transgranular spall. They suggested that void nucleation was likely initiated at grain boundaries in the large and medium grains but grain interiors for small grains. Similarly, Buchar, *et al.* discovered that smaller grain size copper specimens had larger spall strength over the strain rate range of 10^4 to 10^6 s^{-1} (Buchar, Elices and Cortez 1991). Brandon, et al. also observed that the lowest spall strength occurred in largest grain size material (Brandon, Boas and Rosenberg 1984). The authors also reported that spall fracture for the coarse grained specimens occurred not only at grain boundaries but also had areas of transgranular fracture (mixed mode). It is surprising to see such differences in spall strength for similar studies in copper.

For single crystal materials which can be thought of in these kinds of experiments as an “infinite” sized grain, crystal orientation also has an effect on spall strength.

Minich, *et al.* showed a difference in spall strengths between the [100], [110], and [111] orientations of copper single crystals, with the highest spall strength corresponding to the [100] orientation (Minich, et al. 2004). Similarly, Chen, *et al.* determined that [100] aluminum single crystals had the highest spall strength (Chen, Asay and Dwivedi 2006). These results also suggest a preferential direction for a crystal to be strained. Kanel, *et al*. showed that single crystal copper had about 3-4 times higher spall strength than polycrystalline copper of commercial purity. They attributed this to the smaller defect concentration in single crystal samples (Kanel, Razorenov and Fortov 1992).

3.5.3 Effect of Alloying and Cold Rolling on Spall

Garushkin et al. discovered that aluminum D16T (both hardened and annealed) exhibits a lower spall strength than single crystal aluminum (Garkushin, Razorenov and Kanel 2008). The authors also state that the single crystals have a lower yield stress. Brandon et al. observed that high purity [102] copper had lower spall strength than the [110] commercial purity copper. It was reasoned that grain boundaries were the primary cause of fracture in the high purity material whereas oxide inclusions were the cause of spall in the commercial alloy (Brandon, Boas and Rosenberg 1984).

Using a laser-driven mini-flyer system, Robbins, *et al*. showed that cold-rolled copper targets had lower spall strength than annealed copper; however in that study specimen purity may have been a contributing factor (Robbins, *et al*. 2004).

3.5.4 Effect of Temperature on Spall

Kanel *et al.* found that the spall strength of Al single crystals are independent of temperature up to ~ 630 °C and then decreases at temperatures up to 648 °C (G. Kanel, S. Razorenov and K. Baumung, et al. 2001). The HEL stresses were determined to increase with temperature. The authors reason that phonon drag on dislocation motion results in an increase of the flow stress with temperature. The authors also observed that Al AD1 exhibited much lower spall strengths over the same temperature range (at rates of ~ 4 x 10^4 s^{-1}).

3.6 INITIAL TARGET SPECIMENS AND PLAN OF RESEARCH

These studies summarized in the previous section present a backdrop for investigating the role of microstructural defects on fast rate fracture. We wanted to determine the maximum tensile stress (spall strength) of materials with various length scale defects (grain size, impurities, etc.) at the fast strain rates that are achievable with pulsed lasers. As a base case material, we used high purity recrystallized aluminum (denoted Al-HP RX) which is heat treated to produce large equiaxed grains. We also wanted to study the effect of alloying by producing aluminum + 3 wt.% magnesium recrystallized (denoted Al+3Mg RX). Finally, we wanted to study the effect of adding two strengthening mechanisms: first alloying aluminum with magnesium and secondly cold working to produce aluminum + 3 wt.% magnesium cold-worked (denoted Al+3Mg CW).

CHAPTER 4. EXPERIMENTAL SETUP

In this chapter I will describe the two laser systems used in these experiments and I will discuss in detail the various optical diagnostics and special equipment needed. At the conclusion of this chapter I will give an introductory description of the hydrodynamic code HYADES which is vital in understanding the relevant time and pressure scales in our experiments.

4.1 LASER SYSTEMS

The two laser systems that I will describe are both solid state lasers; however, their physical scales are very different. The Z-Beamlet laser is a large scale system contained within a warehouse, whereas the THOR laser is a table top system contained within a university lab. The shot frequency of these two lasers are also very different as Z-Beamlet is available to shoot every three hours, while the repetition rate of THOR is 10 Hz. Z-Beamlet also has three orders of magnitude more energy, which is more ideal for solid target shock experiments.

4.1.1 Z-Beamlet

The Z-Beamlet Laser (ZBL) is a Nd:Glass laser (1ω=1054 nm, 2ω=527 nm) with a long temporal pulse width (up to 1.8 ns) and very high energies (up to 1.2 kJ at 2ω) (Rambo 2005). The Z-Beamlet Laser is located at Sandia National Laboratories in Albuquerque, NM. Figure 32 shows the Z-Beamlet Laser facility. It was built as a prototype beamline for the National Ignition Facility (NIF). ZBL's primary mission is to serve as an x-ray backlighter source for the Z-machine (Z in short), which is a Z-pinch machine used for inertial fusion energy research (Hammer, et al. 1999). ZBL also serves as a platform for developing x-ray diagnostics and for performing other HEDP experiments (Edens, et al. 2005).

Figure 32: Z-Beamlet Laser facility

Figure 33 shows a schematic of the Z-Beamlet Laser system. The front end of ZBL is comprised of a multi-stage oscillator with typical output energies of 0.25-2.5 nJ at 1054 nm. A regenerative amplifier in a ring cavity design contains two Nd:phosphate rods pumped by flashlamps and outputs a typical amplified energy of 250 μJ. The beam is then shaped via a birefringent lens and polarizer which gives the central section of the beam a flat intensity profile. The beam passes through a square serrated aperture which creates a resultant beam that is approximately constant in intensity over a square spatial region. A 4-pass Nd:phosphate rod amplifier (5 cm dia., 48 cm long) is then used to amplify the energies up to 50-400 mJ. The beam is then input to the flashlamp pumped, 4-pass main amplifier slabs. One of the key design components is the Plasma Electrode Pockels Cell (PEPC) which switches out the large aperture beam to continue through the rest of the laser chain. The 1ω light goes through a frequency doubling crystal, where it is partially converted to 527 nm. The $1\omega/2\omega$ light hits a dichroic beamsplitter where 1ω is transmitted and then blocked and 2ω is reflected into the experimental chamber.

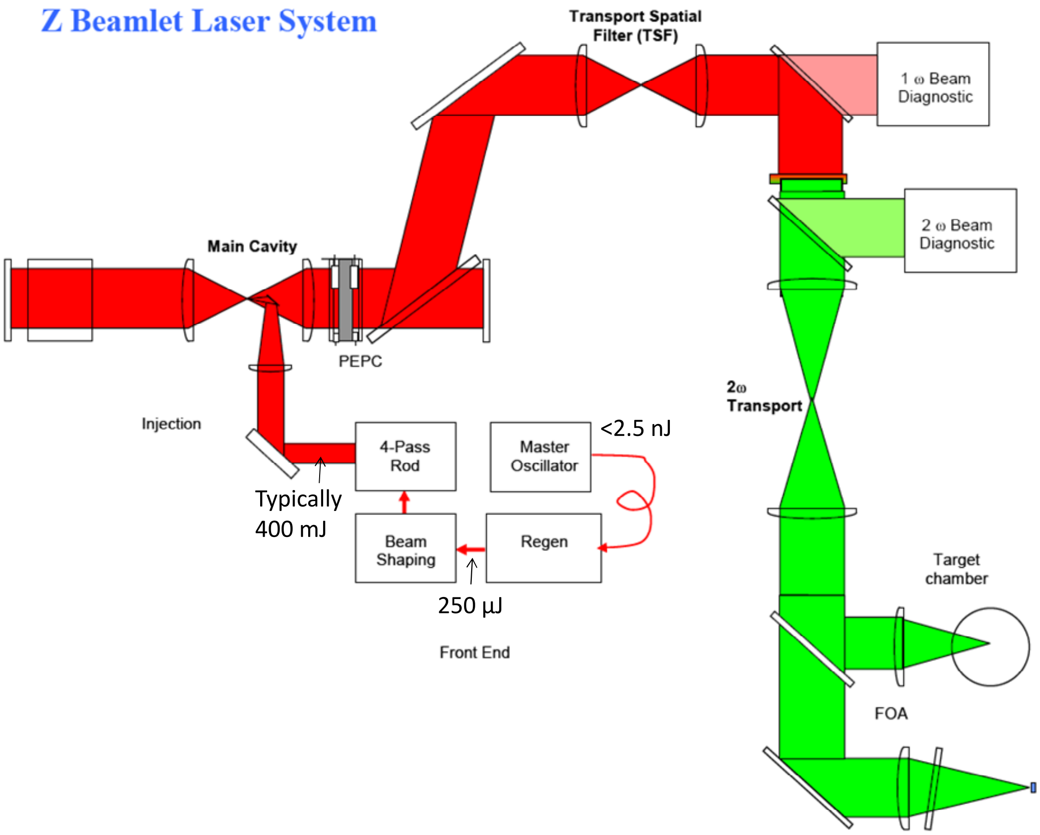

Figure 33: Schematic of the Z-Beamlet Laser. Figure is courtesy of Ian Smith.

The beam is focused with an f/8 lens and directly images the beam from the square aperture to the focal plane. Figure 34 shows a typical near field spatial profile as well as a typical temporal profile from ZBL.

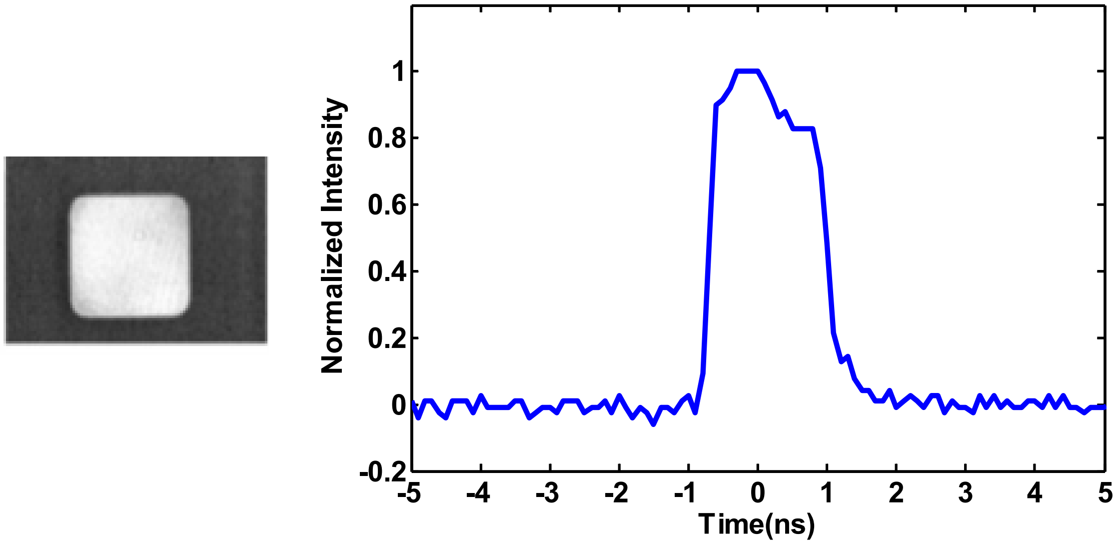

Figure 34: Near-field 1*ω* spatial profile (Rambo 2005) and temporal profile of a ZBL pulse.

A CW 2ω beam is used for ZBL (pump beam) alignment and for determination of the pump spot size. Typically, for most experiments performed in the target chamber, two alignment cameras are used with crosshairs to locate the target chamber center (TCC). The pump beam spot size is determined by the type of experiment and the energies (intensities) needed. Since our shock experiments generally require high energies but low intensities, large area beams are desired. Generally, the lowest energy ZBL can conceivably shoot is ~200 J in the 1.8 ns pulse range, which places a lower limit on the energy. Since we use the beam before it is focused to the center of the chamber, we cannot use the alignment cameras that are focused onto TCC. We set a calibration target (e.g. USAF reference target) inside the chamber in order to determine the spatial calibration. We then image the target to a camera using a photographic lens (Figure 35a). The CW 2ω does not fill the full lens aperture as does the pulsed beam. The size of the box defined by the crosshair is 25 cm, whereas the actual beam is 32 cm. Figure 35b shows the CW 2ω beam with crosshair. The large aspect ratio of the beam is due to viewing the scattered beam off-axis.

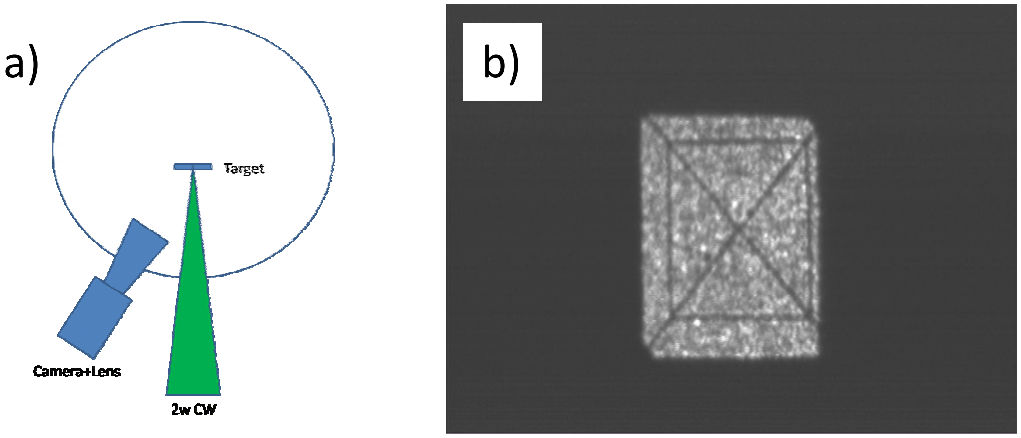

Figure 35: (a) Beam size measurement technique and (b) image of green CW alignment beam with crosshair.

4.1.2 THOR Laser

The Texas High-Intensity Optical Research (THOR) Laser is a ~1 J, 40 fs, 10 Hz laser capable of reaching a peak power of 20 TW. This system is based on chirped pulse amplification technology (Strickland and Mourou 1985), which takes a low energy, temporally short pulse, stretches it in time, amplifies the pulse to higher energies and then re-compresses to a short pulse. Amplifying a stretched pulse allows the pulse to be amplified to higher peak energies while keeping the pulse intensity sufficiently low to avoid damaging the amplification media. Figure 36 shows a schematic of the chirped pulse amplified THOR laser.

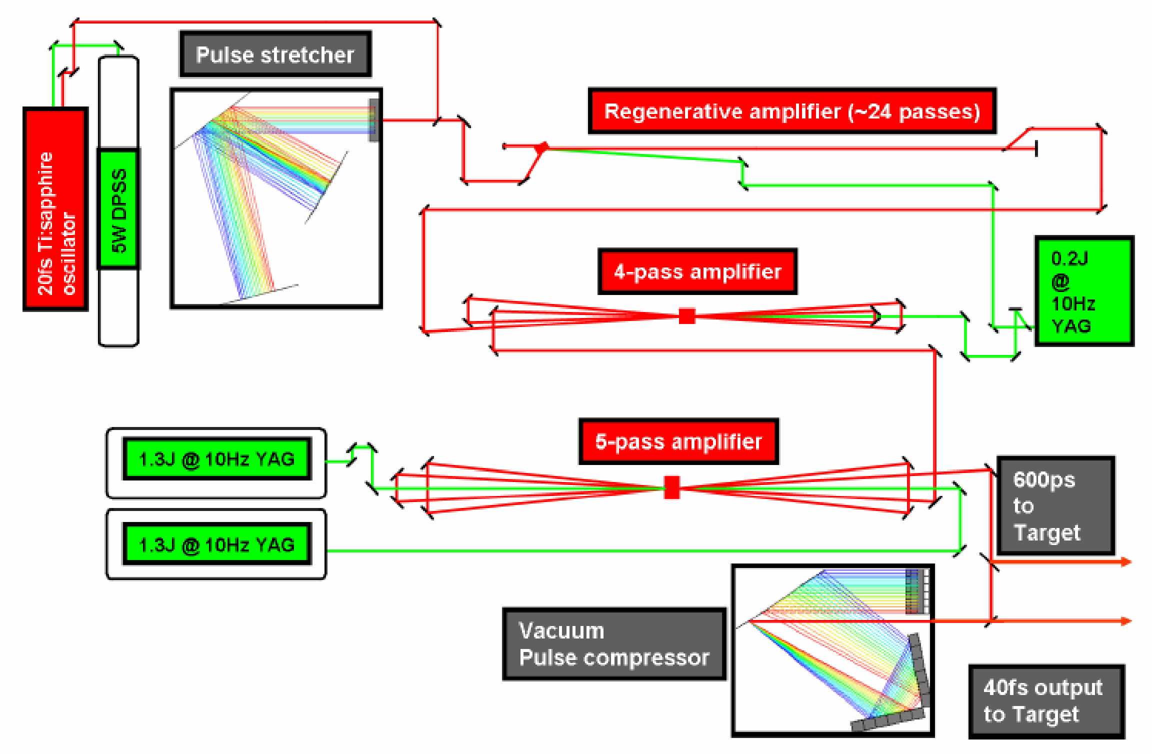

Figure 36: Schematic of the THOR Laser. (Grigsby 2007)

The oscillator is a mode locked Ti:Sapphire laser (Femtosource Scientific 20) which is pumped by an Nd:YVO_4 laser at second harmonic (Spectra Physics Millenia Vs DPSS, 4.5 W). This laser, with 45 nm bandwidth, produces ~8 nJ pulses of 20 fs pulse width. The 73 MHz oscillator output is converted via a Pockels cell to a 10 Hz signal. The pulses then go into the pulse stretcher (Banks, Perry et al. 2000) which chirps the pulse (red edge of the pulse leads the blue edge of the pulse) to 600 ps in duration. After exiting the stretcher the pulse goes through 5 m of a single mode, polarization maintaining fiber which adds dispersion for best recompression. The pulse then enters a regenerative amplifier that includes two cavity mirrors, a Brewster-cut Ti:sapphire crystal, a Pockels cell, and a thin film polarizer. The pulse is switched in/out of the cavity by the Pockels cell/thin film polarizer combination, where it traverses the cavity ~24 times. The Ti:Sapphire crystal is pumped by ~45 mJ from a Nd:YAG laser at second harmonic (BigSky CFR-400). Upon exiting the regen, another Pockels cell/polarizer pair increases the contrast ratio between the desired main pulse and any pre- or post-pulses arsising from the regenerative amplifier. The post-regen pulse again is amplified in a 4-pass bowtie amplifier which contains another Brewster-cut Ti:sapphire crystal. The 4-pass amplifier is pumped with ~100 mJ of energy from the same BigSky laser. The relative energies that pump the regenerative and the 4-pass amplifiers are adjusted with a waveplate and a thin film polarizer. Upon exiting the 4-pass, the seed pulse is spatially filtered and then proceeds into the 5-pass bowtie amplifier. The 5-pass crystal (Ti:sapphire) is pumped by two 1.3 J, 10 Hz, frequency doubled Nd:YAG lasers (Spectra Physics Pro Series). At this point the energy of the seed beam has reached ~1 J and can be used as a high energy 600 ps chirped pulse or sent into a vacuum pulse compressor where it is compressed down to ~40 fs. Much more detail about the design of this laser system can be found in Will Grigsby's dissertation (Grigsby 2006).

4.2 DIAGNOSTICS

In this section I will describe two target diagnostics used in our shock experiments. The two main types of diagnostics involve the displacement interferometer and the velocity interferometer. Figure 37 illustrates the conceptual differences of these types of inteferometers. In the case of the displacement interferometer (Figure 37a), the probe beam is split by a beamsplitter before hitting the shocked target and then recombines at the output beamsplitter, producing a 2D spatial inteferogram. In the case of the velocity interferometer (Figure 37b), the probe beam hits the target and then one portion of the beam is temporally delayed with respect to itself and then recombined.

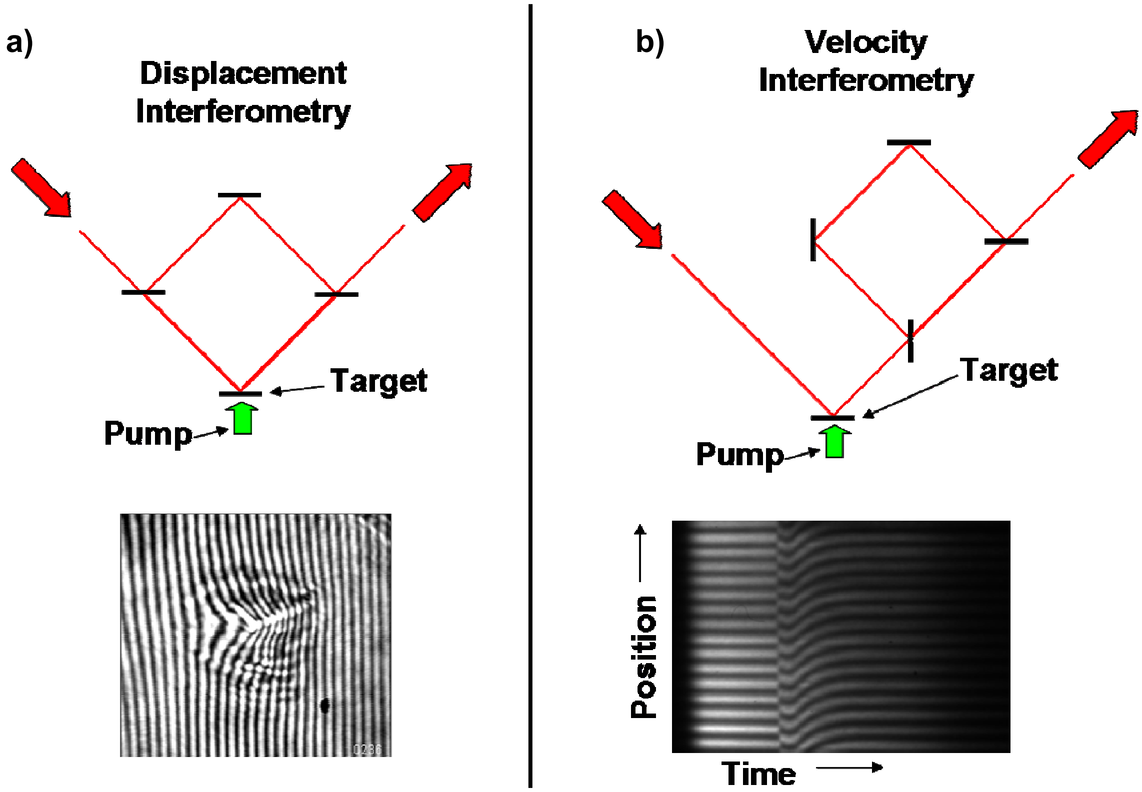

Figure 37: Illustration of the diagnostic concepts and example interferograms for the (a) shortpulse 2D interferometer and the (b) velocity interferometer.

4.2.1 2D Interferometer

In cases where a velocity interferometer does not have sufficient temporal resolution or when a costly streak camera is not a viable option, one may use a short pulse displacement interferometer. A short pulse 2D interferometer provides both high spatial and temporal resolution. By mapping peak displacement versus temporal delay, one may derive particle velocity versus time.

Light collection is of primary concern as we want to design a system that allows us to collect as much light as possible. Originally we had an ~f/16 optic, but we decided to use instead an f/3 collection optic since it would allow for collecting light from a scattering shocked surface. Figure 38 shows a 2D displacement interferogram and a reflectivity image from a Al/LiF shocked specimen using an ~f/16 collection optic.

There are several points that need to be kept in mind when designing a short pulse 2D interferometer for use in shock experiments.

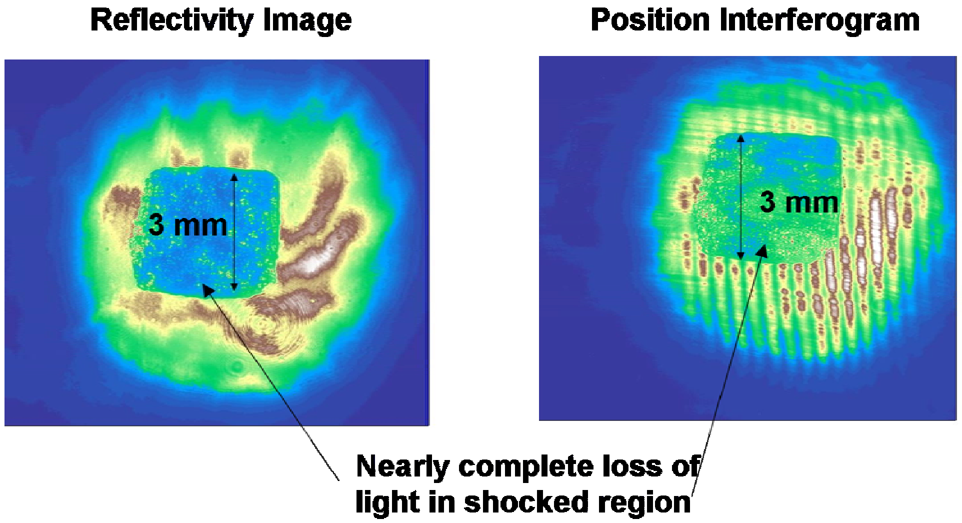
Reflectivity Image

Position Interferogram

Nearly complete loss of light in shocked region

Figure 38: 2D Reflectivity and interferometry showing nearly a complete loss of light in the shocked region when an ~f/16 collection optic is used. We decided to use an f/3 optic.

First, we want a short pulse in order to take a fast snapshot of the rear surface displacement of the target specimen. Too long of a pulse will result in fringe blurring. By using a femtosecond scale pulse, we can easily time resolve shock rise times that are on the order of hundreds of picoseconds. Secondly, we want to illuminate a large enough area of the target. We planned on using a phase plate in the pump beam which would give us a shock spot of ~1.5 mm. So we wanted to illuminate an area of the target ~3x this size and aimed to image a 4 mm spot to our CCD camera.

We wanted to focus the beam in order to illuminate the appropriate size of the target. However, we needed to make sure that the focus was in vacuum and that it did not occur in an optic since the intensity of the beam at a focus is sufficiently high to ionize air or damage an optic. We also chose to use a 2 lens imaging system instead of a 1 lens system because the 2 lens imaging system allowed us to put the image almost anywhere we wanted it and get the desired target magnification. We also needed to make sure that there were no undesired nonlinear focusing effects. The B-integral, or the accumulated nonlinear phase, is given by:

$$B = \frac{2\pi}{\lambda}\int_0^L n_2 I(z)dz \tag{4.1}$$

where I is intensity and n_2 is the nonlinear index of refraction. The accumulated system B-integral is 0.49, which is sufficiently low to ensure no damage in the system.

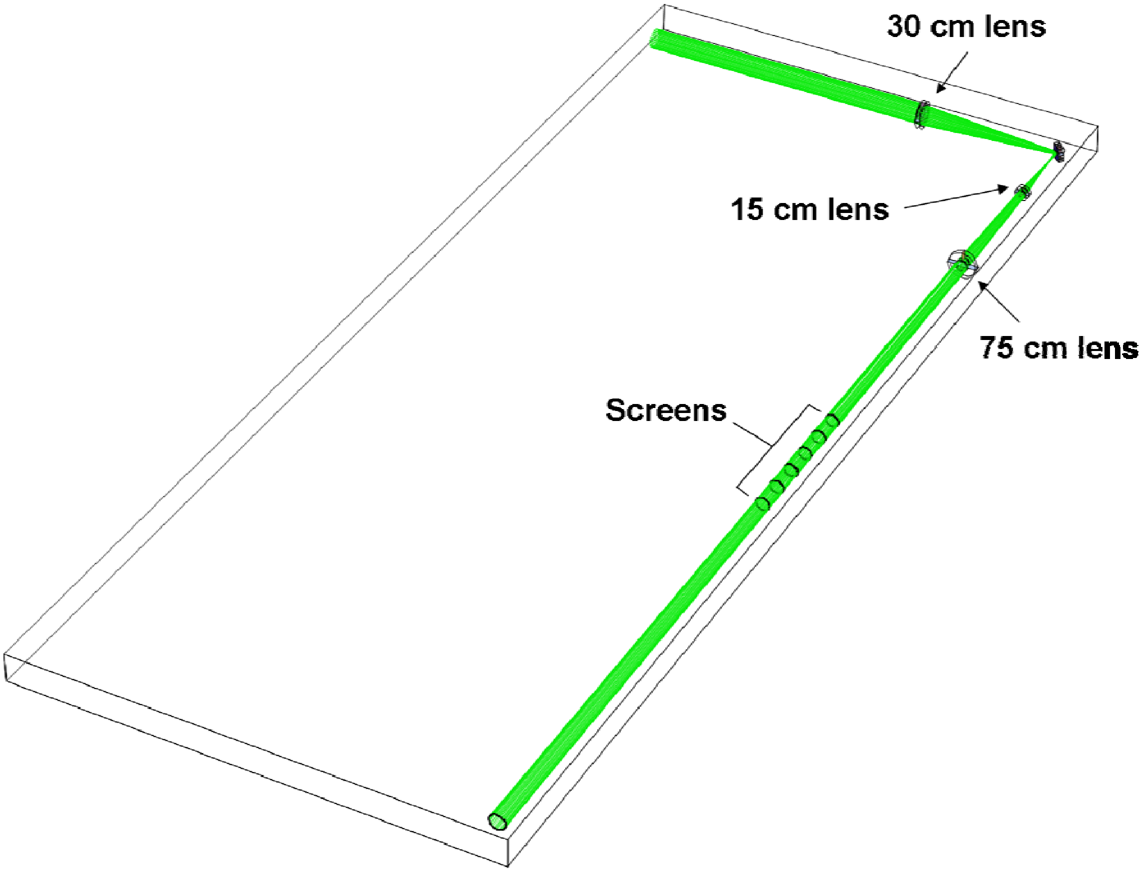

Figure 39: Ray trace results illustrate a focusing lens which illuminates the target and produces a focus shortly after the target. A 2 lens system after the target shows the propagation of the beam at six intermediate screens, allowing us to calculate the beam size and divergence.

The 2D interferometer consists of a target arm and a reference arm. The target arm hits the target and is then later recombined with the reference arm which does not go into vacuum. Figure 39 shows the ray trace results for the target arm of the interferometer. Figure 40 shows the ray trace results for the reference arm of the interferometer.

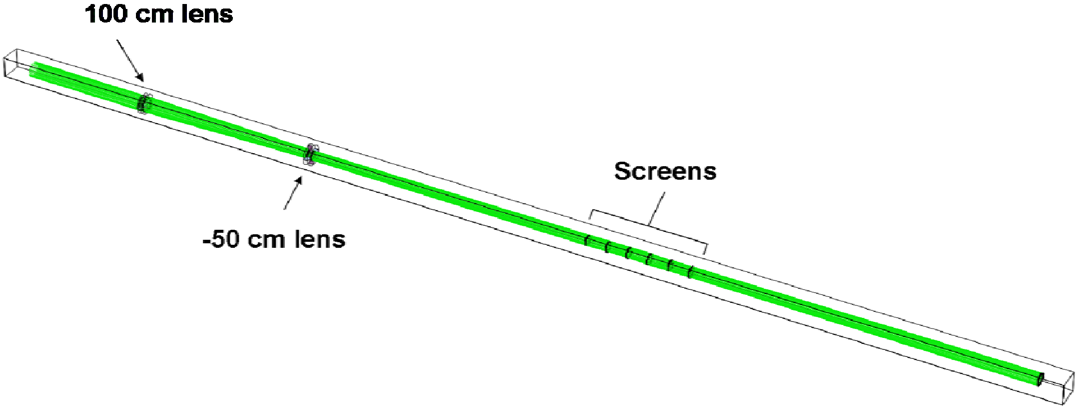

Figure 40: Ray trace results from +/- lens system with six intermediate screens which allows us to calculate beam size and divergence in the reference arm of interferometer.

By choosing the correct +/- lens pair and the corresponding distance between them, we determine the divergence and beam size needed to match that of the target arm. Figure 41 shows several values of the beam diameter versus screen position calculated for the target arm and the reference arm via ray tracing.

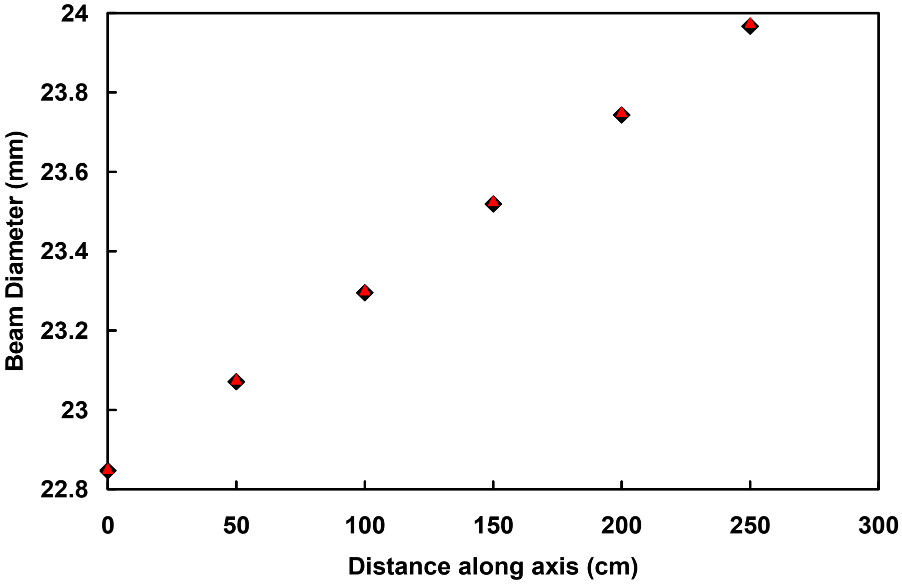

Figure 41: Beam sizes calculated from the target arm (red triangle) and the reference arm (black diamond) versus location of the intermediate screens.

Figure 42 is a schematic of the short pulse diagnostics.

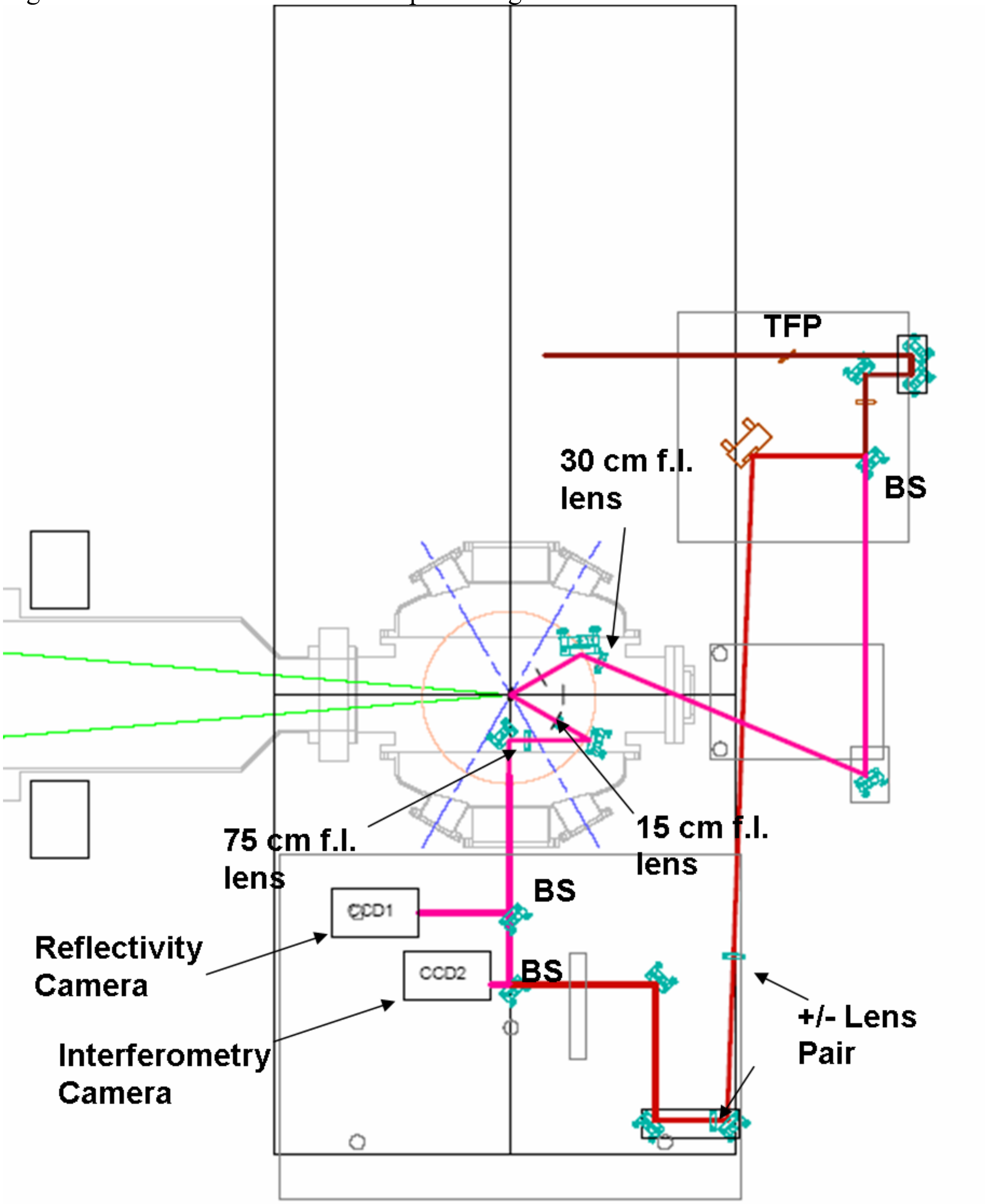

Figure 42: Schematic of short pulse diagnostic in relation to ZBL beam and target chamber. (--- SP, --- SP target arm, --- SP reference arm, --- ZBL)

Figure 43 shows two 2D interferograms for different aluminum specimens at shock breakout. Note that there are several spots (circled in red), that were present from shot to shot in various materials. We thusly inferred these damage spots must come from the non-uniformity of the beam.

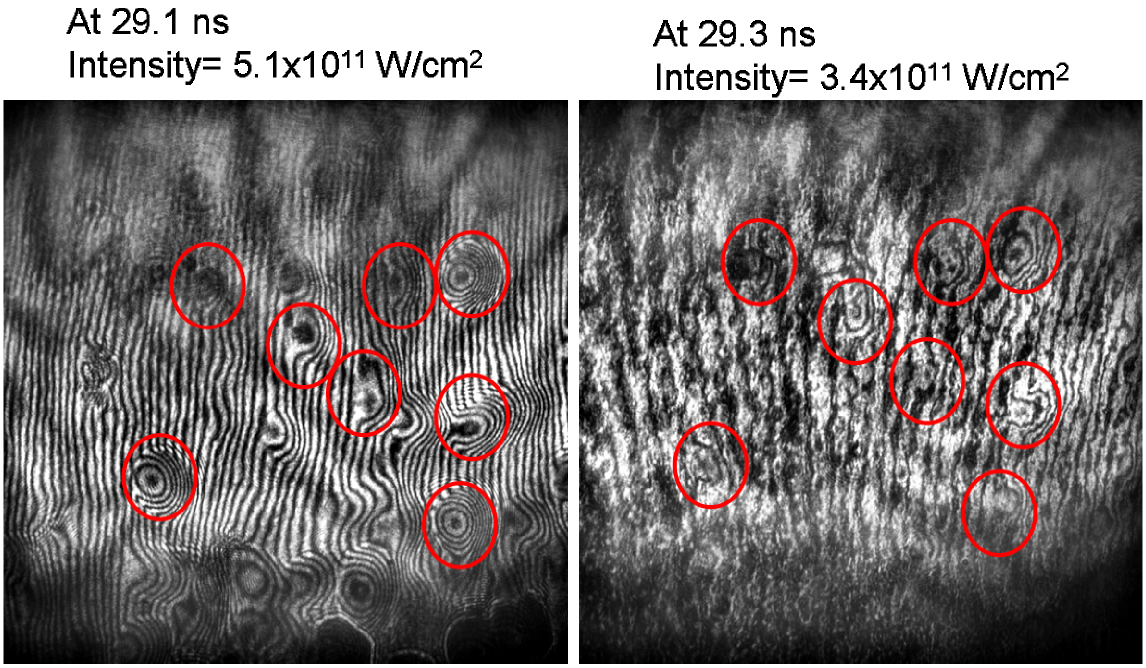

At 29.1 ns
Intensity= 5.1x10^{11} W/cm^2

At 29.3 ns
Intensity= 3.4x10^{11} W/cm^2

Figure 43: 2D interferograms showing many of the same breakout spots.

The displacement of the rear surface (Eq. 4.2) is determined from the unwrapped phase $\varphi(x,y)$ via:

$$d = \frac{\lambda \cdot \varphi(x,y)}{4\pi n \cdot \cos(\theta)} \tag{4.2}$$

where λ is laser wavelength, n is index of refraction and θ is the angle of incidence. In Chapter 6, I will describe in more detail the use of the 2D interferometer for measuring particle velocity of shocked specimens.

4.2.2 Velocity Interferometry

The velocity measurement of fast moving rear target surfaces allows one to determine the relevant stresses and strain rates that are important in shock experiments.

The original Velocity Interferometer System for Any Reflector (VISAR) was designed by Barker and Hollenbach (Barker and Hollenbach 1972). This system allows for velocity determination of fast moving surfaces (e.g. particle velocity, free-surface velocity or shock velocity).

The rear target expansion velocity is measured using a line-VISAR diagnostic designed specifically for Z-Beamlet and closely follows the features of the VISAR published by Celliers, *et al.* (Celliers, et al. 2004). The VISAR interferes the probe pulse reflecting from a moving surface with itself at a relative delay, to produce interference fringes, where their deflection is proportional to velocity. A 1-D lineout of the fringe-pattern is sent into a streak camera, where it is streaked to obtain velocity versus time. Figure 44 shows a schematic of the basic elements of the VISAR.

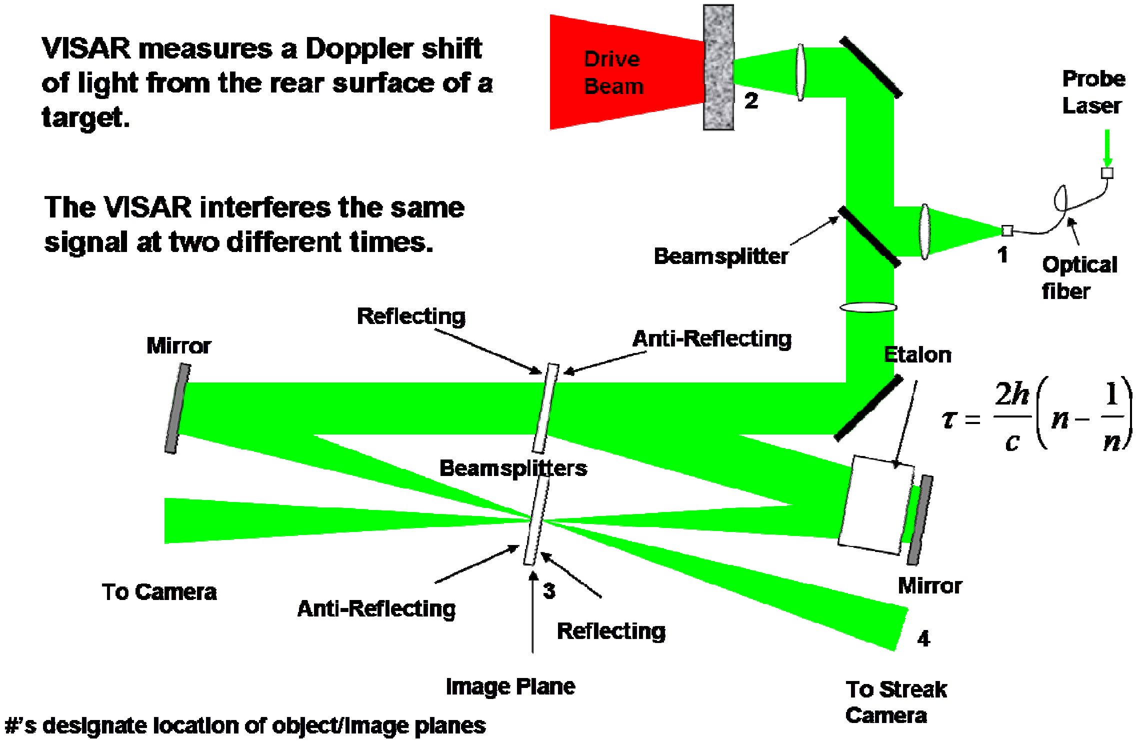

Figure 44: Schematic of the VISAR (based on (Celliers, et al. 2004)).

Figure 45 shows an example interferogram and resulting particle velocity lineout.

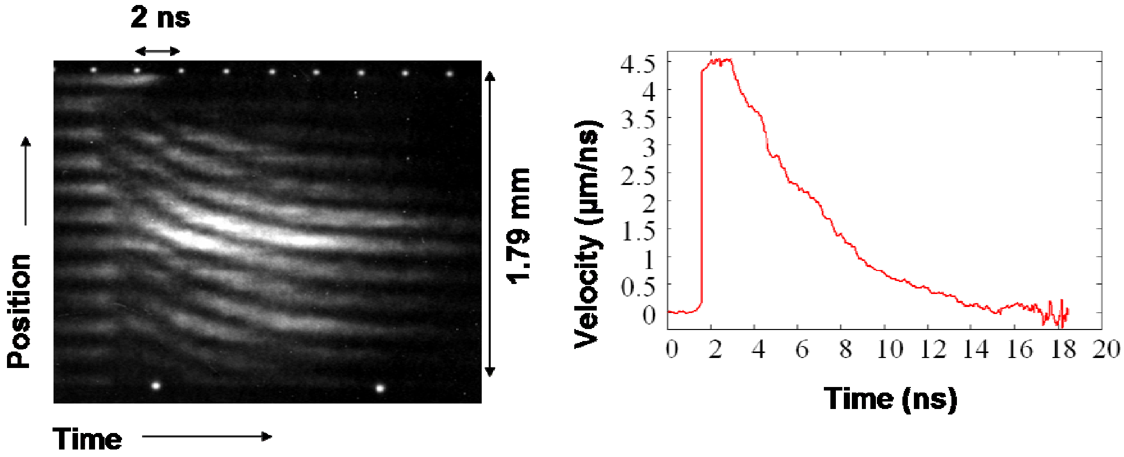

Figure 45: VISAR interferogram of a shock melt experiment and a lineout of particle velocity.

The remainder of this section outlines the vital aspects for VISAR implementation. Those aspects are listed below.

1. Diagnostic Laser
2. Light collection
3. Fiber transport
4. Point to Point Imaging
5. Interferometer
6. Streak Camera
7. Analysis

These aspects are now discussed in detail.

1. Diagnostic Laser

Since the VISAR is interfered with itself at two different points in time, a laser with a long coherence length must be used. The equations that describe linewidth (Δv), coherence time (τ_c) and coherence length (L_c) are:

$$
\Delta\nu = \frac{c}{\lambda^2}\Delta\lambda
$$
$$
\tau_c = \frac{1}{\Delta\nu} \tag{4.3}
$$
$$
L_c = c\tau_c
$$

A single longitudinal mode, or seeded, laser is one that has a single axial mode. A seeded Nd:YAG laser with a linewidth of 130 MHz corresponds to a coherence length of ~2.3 m, whereas for the unseeded case (or multimode) with a linewidth of 120 GHz the corresponding coherence length is ~ 2.5 mm. On several occasions, we found that poor seeding (i.e. multimode laser operation) gave rise to a disappearance in fringes on the streak camera. Figure 46 shows temporal lineouts of seeded and unseeded Nd:YAG performance.

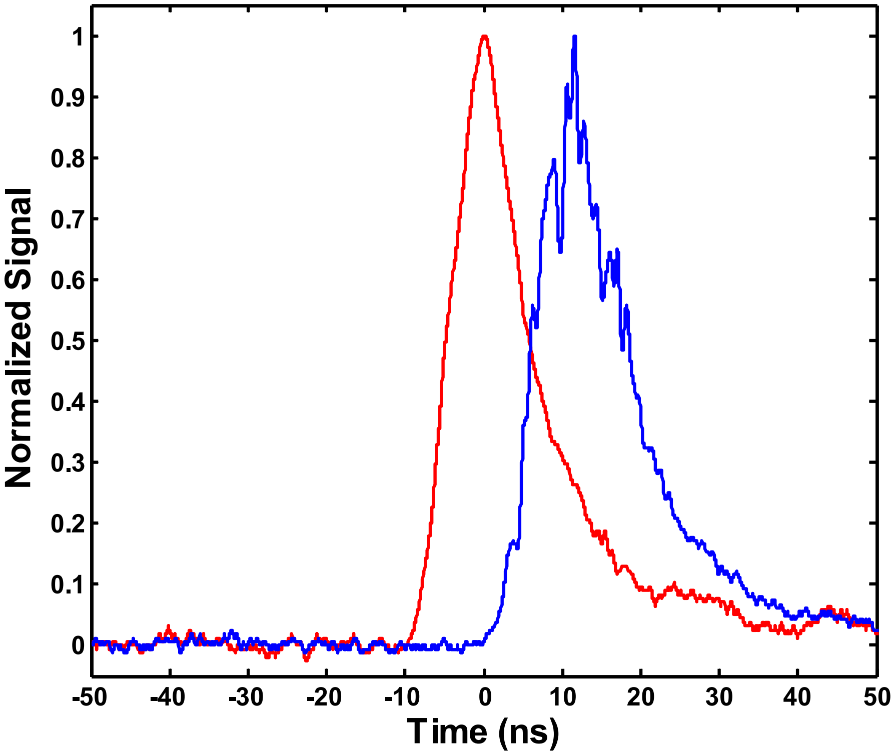

Figure 46: Seeded (red curve) versus unseeded (blue curve) laser performance. The seeded pulse has a cleaner temporal profile, whereas the unseeded (multimode) pulse has temporal structure.

2. *Light Collection*

In our early shock experiments we implemented a line-VISAR for probing the particle velocity at an impedance matched interface. This diagnostic used a cylindrical lens to place a line on the target interface and a second spherical lens to collect light from the moving specimen. We discovered that there was not enough light collected by the streak camera as the surface was set in motion by the shock (Figure 47).

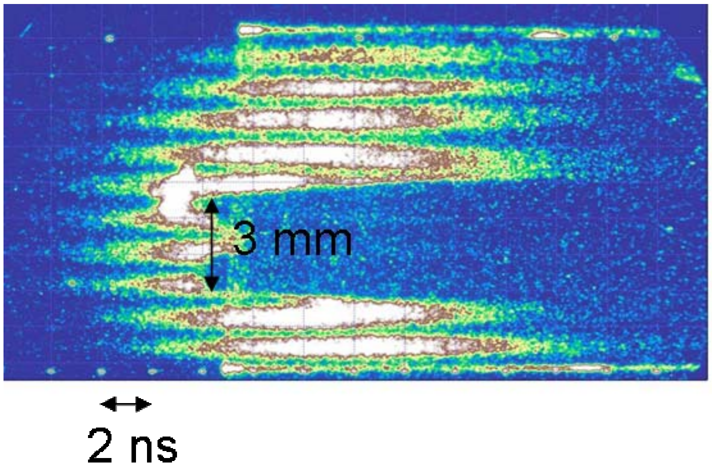

Figure 47: VISAR interferogram showing the disappearance of fringes in the shocked region. Notice that the fringes cover a larger area than the shocked region.

One weakness of the original imaging system is that the collection optic after the target was an ~f/30 optic. In order to prevent overcrowding of the target chamber and also to keep the optics pristine from target debris, we kept all diagnostic optics outside of the chamber. However, this severely limited the speed of our collection optics. Since sufficient light collection is essential in shock experiments, we were forced to redesign our imaging system. Upon redesign, we changed the two optic design (for delivery and collection) to a single f/3 optic.

3. *Fiber Transport*

To transport the probe beam from a remote location to the target we used a large core multimode fiber. In choosing an appropriate fiber for use in our diagnostic we kept several factors in mind. To avoid losing light from clipping at the fiber input, we want to make sure the numerical aperture of the fiber was at least equal to or greater than the numerical aperture of the lens immediately preceeding the fiber input:

$$NA_{lens} \geq NA_{fiber} , \tag{4.4}$$

In order to image small features from the target specimen, we require a large number of small speckle. Having a large number of small speckle on the target requires the use of a large core, high mode fiber. The number of modes is proportional to V^2, where V is given by:

$$V = 2\pi a \frac{NA_{fiber}}{\lambda} , \tag{4.5}$$

where a is the fiber core radius and λ is the laser wavelength. Table 3 summarizes various fiber option details. The fiber that we often chose was the Ocean Optics fiber since it has more modes than the Omega VISAR fiber (Celliers, et al. 2004), but did not require a f/1 lens for light collection.

Table 3: Table shows various multimode fibers, core diameter, numerical apertures, corresponding f/#, and corresponding V^2.

Vendor/Reference	Thorlabs	Thorlabs	Ocean Optics	Omega VISAR
Core diameter (mm)	1	0.6	1	1
NA	0.37	0.37	0.22	0.16
f/#	1.35	1.35	2.27	3.13
V^2	4.8×10^6	1.7×10^6	1.7×10^6	0.9×10^6

One problem that we have had in the past is damaging the fiber near the input. This occurred when the lens immediately preceeding the fiber input was accidentally positioned in such a way that it focused the beam to a spot in the fiber. It is necessary to make sure that the light is focused to a spot just before the fiber entrance. If a fiber is damaged it is highly recommended that one cleaves and repolishes the fiber. Thorlabs sells a fiber repair kit and guide that is pretty easy to use; however, the time needed to repair the fiber is quite lengthy.

4. Point to Point Imaging

In choosing the imaging optics for the VISAR, we kept several key points in mind. As discussed previously in this section, we knew that a fast imaging optic (~f/3) at the target is needed to capture the most light. We also have a 1 mm core fiber to image to the target, which was chosen based on previous considerations. We wanted to image the fiber to the target using at least two lenses, the first of which collects light from the rapidly diverging fiber. We chose to use a 15 cm f.l. lens (5.08 cm dia.). This would give us roughly a 1 mm spot on target (M=1), due to imaging the 1 mm core to the target. We then want to image this 1 mm spot onto a 2.54 cm dia. beamsplitter, the 2nd beamsplitter in our interferometer. All the optics inside the interferometer were also 2.54 cm, so at some point we would need to get the beam size down to ~2.54 cm. Also, we needed to take into consideration that the slit on the streak camera is ~2.54 cm. Using these constraints, we magnified the spot on the target to the streak camera by down collimating the 5.08 cm beam to a 2.54 cm beam before going into the interferometer. The first lens system consists of the 15 cm f.l., 5.08 cm dia. lens (fast lens for light collection) to 150 cm f.l., 5.08 cm dia. lens which magnifies the image to an intermediate plane. The second two lens system is a pair of 75 cm f.l., 2.54 cm dia. lenses which 1:1 image the intermediate image to the 2nd beamsplitter but results in down collimation of the beam. We then 1:1 image the 2nd beamsplitter to the streak camera. Figure 48 shows a summary of the optics chosen for the VISAR system used on ZBL experiments. More information on the VISAR alignment is provided in Appendix E.

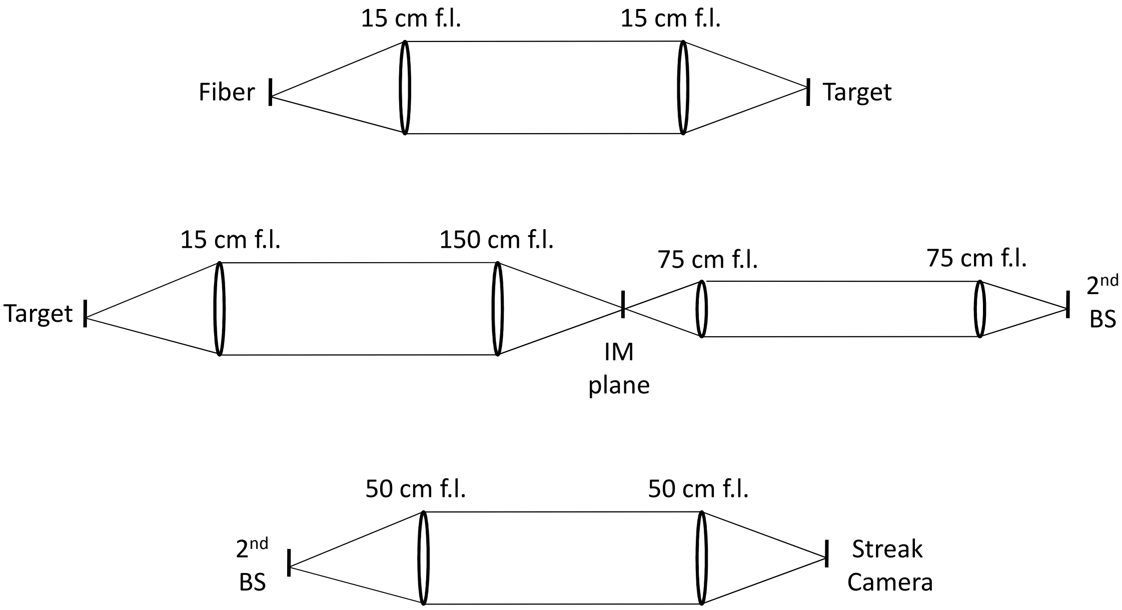

Figure 48: Break down of imaging system. The optical fiber is imaged to the target. The target is imaged to an intermediate plane (IM) and then imaged to the 2nd beamsplitter (BS) in the interferometer. The 2nd beamsplitter is finally imaged to the streak camera.

5. *Interferometer*

The Mach-Zehnder interferometer has the advantage in that adjustments in image overlap and fringe orientation/spacing are completely decoupled. The Mach-Zehnder interferometer consists of two beamsplitters and two end mirrors where one end mirror is on a translation stage. The translation stage holds the temporal delay element (etalon). The fringe visibility depends on the overlap of images on the beamsplitter, which can be adjusted by the end mirrors, whereas the fringe orientation and spacing are controlled by small tilt adjustments in the output beamsplitter. More information on interferometer alignment is provided in Appendix E.

A white light source is used to determine the zero-delay (with the etalon removed) of the interferometer. We used white light since it has the greatest bandwidth and thus the shortest coherence length (~10 microns). When white light fringes are found, note the micrometer settings as it will be necessary to come back to these setting upon changing etalons. At this point, one must decide which etalon is needed for the experiment (i.e velocity resolution) and place it in front of the end mirror on the translation stage. The velocity-per-fringe constant associated with the etalon without a window or target substrate is:

$$VPF_0 = \frac{\lambda}{2\tau(1+\delta)} = \frac{\lambda c}{4h\left(n - \frac{1}{n}\right)(1+\delta)} \tag{4.6}$$

where λ, τ, h, n, and $(1+\delta)$ are, respectively, probe beam wavelength, probe-beam temporal delay introduced by the etalon, etalon thickness, index of refraction, and dispersion (Barker and Schuler 1974). This equation is derived in detail in Appendix E. The velocity-per-fringe constant with a window (i.e. glass substrate) is:

$$VPF_w = VPF_0\left(1 + \frac{\Delta\nu}{\nu_0}\right)^{-1} \tag{4.7}$$

where $\Delta\nu/\nu_0$ is a frequency correction term that is related to the strain dependence of a shocked window's refractive index (e.g. LiF). The temporal delay, τ, related to the double passed etalon is given by:

$$\tau = \frac{2h}{c}\left(n - \frac{1}{n}\right). \tag{4.8}$$

After putting the etalon into the interferometer, one will no longer have white light fringes since the coherence length of white light is on the order of microns; however, you will have fringes if you send in the seeded pulse of the frequency doubled Nd:YAG. The end mirror is then offset a distance *d* which compensates for the etalon thickness and still allows the images in both arms of the interferometer to overlap. The offset distance is given by:

$$d = h(1 - \frac{1}{n}), \tag{4.9}$$

where *h* is the etalon thickness and *n* is its index of refraction.

Table 4 shows typical values for a fused silica etalon and the frequency correction term for a LiF window.

Table 4: Etalon parameters

λ (nm)	n	Δ	$\Delta\nu/\nu_0$
532	1.46071	0.0318	0.281

Table 5 shows etalon thicknesses with corresponding temporal delay, velocity-per-fringe and translation distance. This clearly shows the tradeoff between temporal and velocity resolutions which is dictated by the thickness of the etalon. For the ZBL spall experiments, we typically chose the 17 cm etalon which gives a VPF_0 of 0.29 km/s/fringe and a temporal resolution of 880 ps.

Table 5: Summary of various fused silica etalon parameters that are needed to calculate the temporal delay of the etalon, the uncorrected velocity per fringe, the corrected velocity per fringe (for window backed target, i.e. aluminum backed with LiF window), and the translations distance for the etalon.

h (cm)	τ (s)	VPF_0 (km/s/fringe)	VPF_w (km/s/fringe)	d (cm)
1	$5.18\text{x}10^{-11}$	4.98	3.89	0.32
2.54	$1.32\text{x}10^{-10}$	1.96	1.53	0.80
5.08	$2.63\text{x}10^{-10}$	0.98	0.77	1.60
10.16	$5.26\text{x}10^{-10}$	0.49	0.38	3.20
17	$8.80\text{x}10^{-10}$	0.29	0.23	5.36

6. *Streak Camera*

As previously discussed in this section, a high time resolution streak camera is essential in shock based experiments, particularly when using a VISAR diagnostic. A streak camera is used to record the evolution of a 1D profile (spatial or spectral) in time. The original VISAR used various photomultiplier tubes (PMTs); however, PMTs only give temporal information and their temporal resolution is typically on the order of nanoseconds. By using a streak camera, as opposed to PMTs, one can optically record spatial information in addition to temporal information. Also streak cameras typically have a much faster temporal response (10's of picoseconds). I will now discuss the basic ideas behind how streak cameras work. Consider multiple pulses of light at various locations in space and time. The pulses are incident on a slit which is imaged via imaging optics or a fiber array to a photocathode where the photons are converted to electrons. The electrons are then accelerated and passed through an electrode. The voltage of the electrode is swept in time, allowing the electrons associated with different temporal events to be displaced vertically (assuming sweep is in vertical direction). The electrons then impact a phosphor screen where they are converted back to photons. For low light levels, an image intensifier/multichannel plate (MCP) is used to amplify the signal. Figure 49 shows a schematic of a streak camera. Description of the Hamamatsu C7700 and EG&G streak cameras are provided in Appendix E.

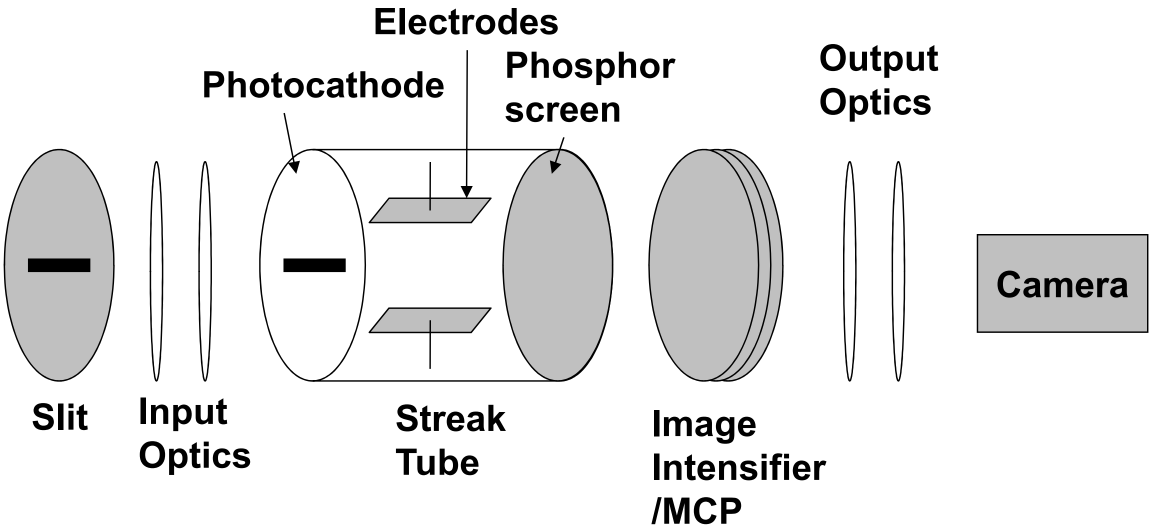

Figure 49: Schematic of a streak camera

7. Analysis

The shock breakout can be observed as a fast shift of fringes in the vertical direction followed by a slower return of the fringes during the material pull back. To obtain the phase as a function of time, lineouts of the raw interferogram are taken along the spatial-axis, Fourier-transformed, spectrally filtered to include only the positive frequency information, and inverse Fourier-transformed. From the inverse Fourier-transformed image, the wrapped phase is calculated. Using a 2D unwrapping algorithm, the phase is unwrapped which results in a phase map (Ghiglia and Pritt 1998). The absolute velocity is calculated by multiplying the phase, $\phi(t)$, by the velocity-per-fringe constant in order to extract a velocity map.

$$Velocity(t-\frac{\tau}{2}) = VPF_0 \cdot \phi(t)\,. \tag{4.10}$$

Figure 50 shows a portion of the multi-step process of analysis. A detailed sample Matlab file is located in Appendix D.

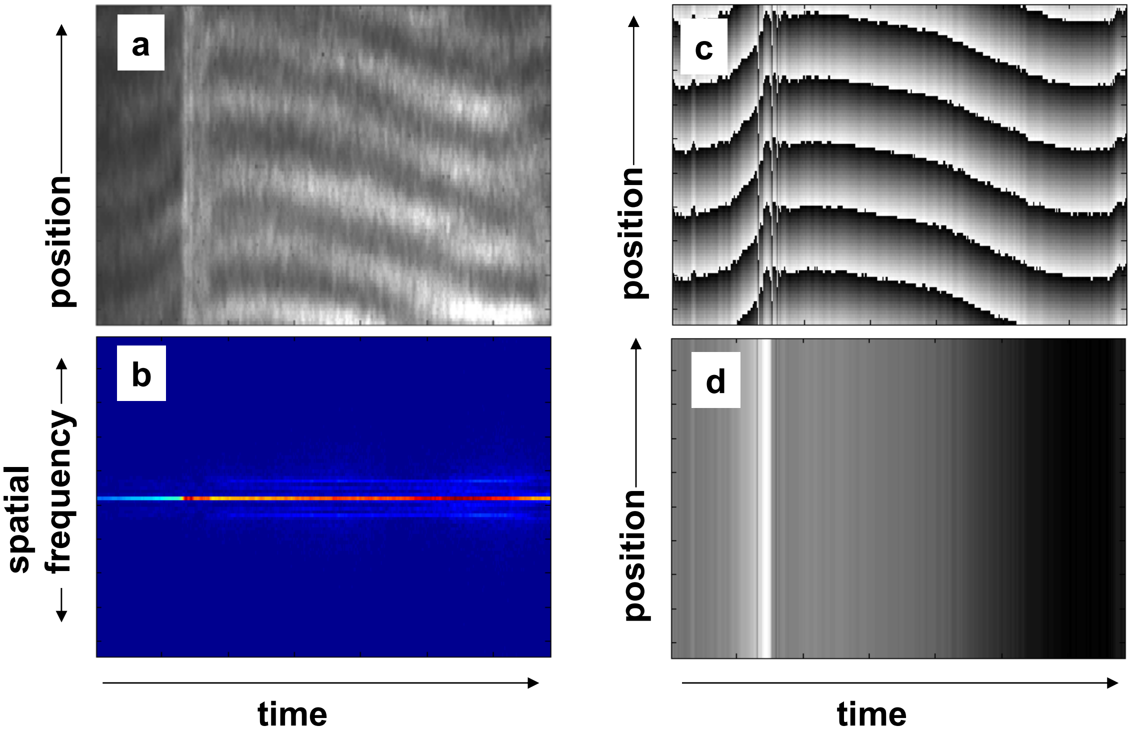

Figure 50: Unwrapped phase map retrieved from Fourier transform analysis of the line-VISAR interferograms: (a) range of interest (ROI) of raw data; (b) Fourier transform of (a) along the spatial axis; (c) wrapped phase; (d) unwrapped phase map

Now I summarize the setup for experiments performed on Z-Beamlet. The rear target expansion was measured using a line-VISAR diagnostic. The line-VISAR probe beam is produced by a single-longitudinal mode laser (532 nm, ~80 mJ, 8 ns FWHM).

The beam is reflected from a wedge to produce a <5 mJ pulse. To derive expansion information on time scales longer than 8 ns required lengthening of the probe pulse. To do this, the beam is transported into a pulse stacker (Section 5.2.2), which elongates the pulse to ~30 ns. The temporally elongated pulse is then injected by a microscope objective (NA=0.25, f.l.=11.0 mm) into a multimode fiber (1 mm core, NA=0.22). The light exiting the fiber is collected and collimated using a 2" dia., 15 cm f.l. achromat lens. The collimated light is injected to the target via a 50/50 beamsplitter. The beam is propagated to chamber height and the fiber is then imaged on the target by a 2" dia., 15 cm f.l. achromat lens. This yields roughly a 1 mm spot on target (M=1). This 15 cm lens then collects and collimates light after reflection from the target, where it goes back through the periscope and through the injection beamsplitter. The target is imaged to an intermediate plane via a 150 cm f.l., 5.08 cm f.l. lens. The intermediate plane is imaged to two Mach-Zehnder interferometers via two 75 cm f.l., 2.54 cm dia. lenses. The light is sent to the two interferometers via a 50/50 beamsplitter. The 2nd beamsplitter of the interferometer is imaged to CCD cameras for alignment and to the streak cameras for dynamic measurement.

Two VISAR's were recently set up to determine the absolute peak velocity. For fast rise time shocks, the breakout can appear as a discontinuity. For this case, the use of two VISAR's with different sensitivities allows for determination of the peak velocity. Figure 51 shows the layout using dual-line VISAR diagnostics that we employed for experiments with ZBL at Sandia.

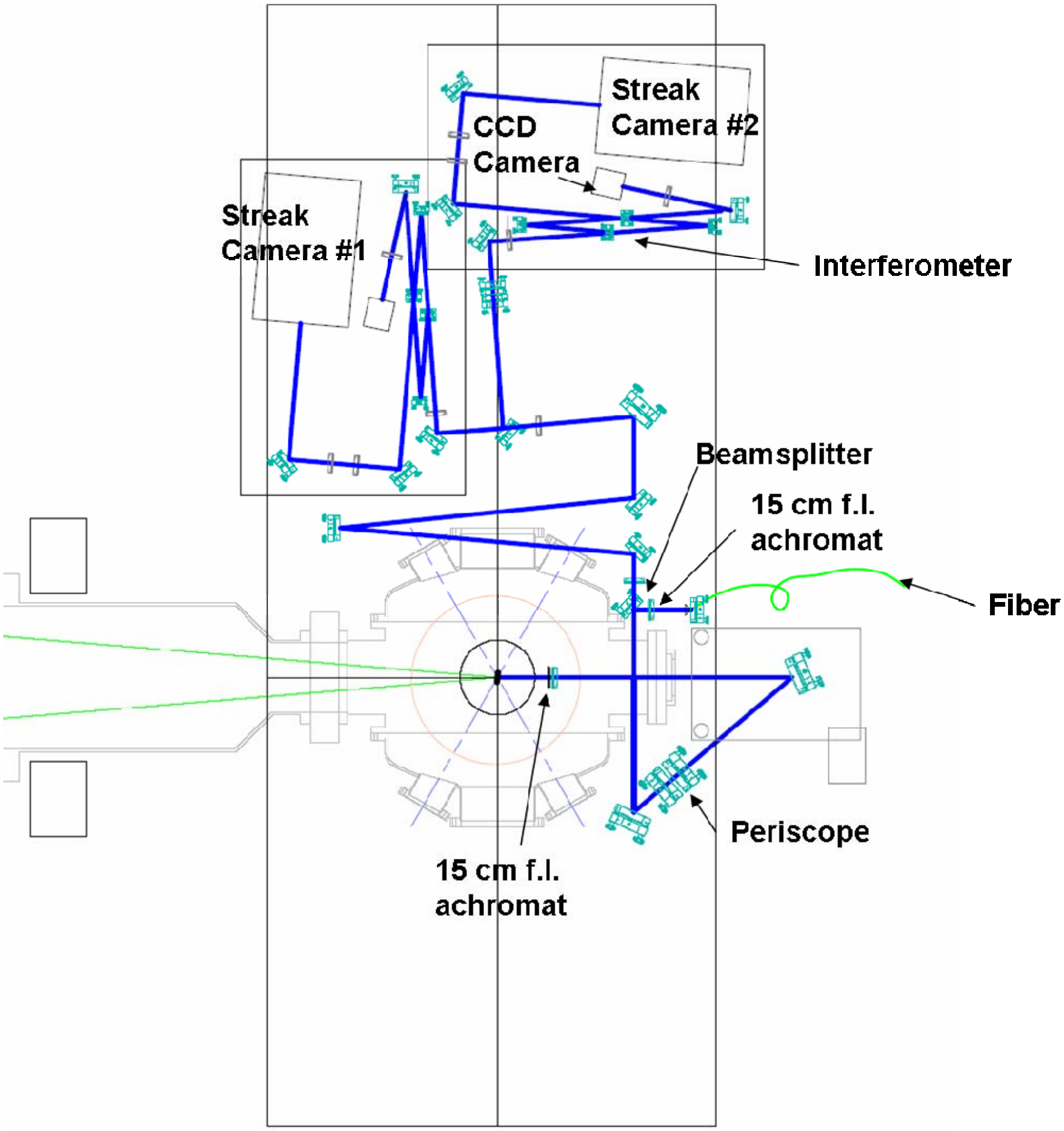

Figure 51: Schematic of dual line-VISAR diagnostics with ZBL beam and target chamber. (--- VISAR, --- ZBL)

4.3 HYADES

4.3.1 HYADES intro

The 1D hydrodynamic code HYADES was used to simulate shocks in different materials under a variety of experimental conditions (Larsen and Lane 1994). It was developed and is administered by Jon Larsen of Cascade Applied Sciences. Scripts are short text files (.inf extension) defined by the user which identify the input parameters to be used by HYADES. There are various versions of HYADES available, some with more capabilities than others. Jon Larsen was a very useful resource while I was trying to get the codes to work properly, by adding additional equations of state and material strength models as needed.

I will now describe some of the basic concepts that are needed in order to successfully run scripts that are applicable to our experimental conditions. Firstly, one must be familiar with the concept of meshes and zones. Mesh points are located at the edges of computational elements. Zones, or regions, define the spatial extent of the computational elements. In other words, regions define the material between the meshes and do not need to be equidistant. Partial differential equations in the form of finite difference equations are used to describe the underlying physics of shock propagation in materials. Some physical quantities are defined at mesh points while other quantities are determined in zones.

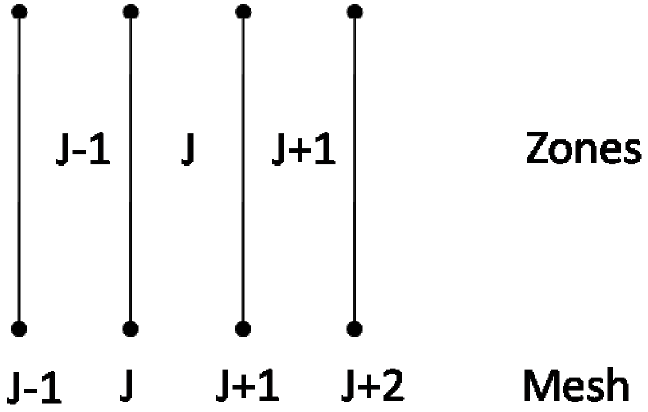

Figure 52: Meshes and zones

I will briefly outline the key features used for input parameters. More details can be found elsewhere (J. Larsen 2007). Since all of our experiments are 1D planar problems, a planar geometry is defined. We then define the mesh and must keep in mind factors such as the skin depth applicable for laser absorption, free surfaces at zero pressure, computing time, etc. Eq. 4.11 is used to determine the feathering, or spacing of adjacent zones:

$$
\begin{gathered}
d = \frac{1 - f^{N}}{1 - f} \Delta x, \\
\Delta x_n = f^{n-1} \Delta x_0,
\end{gathered}
\tag{4.11}
$$

where d is the total thickness, f is the feathering fraction (typically 1.05 for 5% feathering), N is the number of zones, and Δx_0 is the original zone thickness. Since we have performed many simulations with slabs of aluminum, I will use it as an example. Since the skin depth of aluminum at 527 nm (the wavelength of ZBL) is on the scale of nanometers (~5 nm), we want to set up a mesh and corresponding zones where laser energy will be absorbed in a couple of zones on this length scale. In a similar manner, we want surfaces at zero pressure to also have thin zones. If we have a thick material (say hundreds of microns) we set thin zones for laser absorption and increase their thickness towards the center of the bulk material and then taper down the zone size as we approach the free surface (Figure 53).

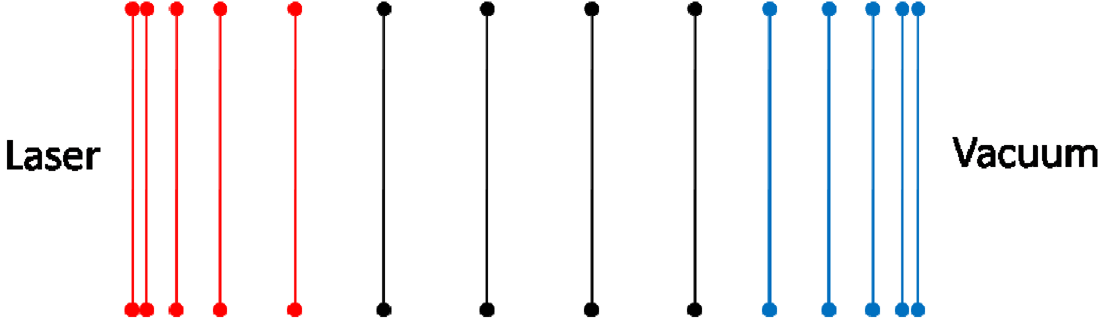

Figure 53: Conceptual illustration of feathering for a spall simulation

The user must also identify the material the material and define the initial mass or density of the zones. The user also supplies an equation of state to be used in the simulation as well as a specific ionization model.

If necessary, the user also defines relevant strength parameters. The strength models include models for melt, yield, shear and spall, some of which we will discuss in more detail in Section 4.3.2 and 4.3.3. It is important to note that Hyades Version 01.06.05 does not incorporate spall modeling; however, HYADES version 01.07.09 does.

The user must also provide information about the cause of the shock. In our case, this means introducing the incident laser pump beam. It is also necessary to define the temporal profile of the source (i.e. pulse width) as well as the output variables of interest (e.g. pressure, velocity, etc.). And then finally, one must input details about the computer system on which the simulation will be run such as the post-processor time step and total run time.

4.3.2 Relevant Spall models

There are two types of commonly used spall models: passive and active. Passive models are those for which no damage variable is accounted. Examples of passive spall models are the Simple Spall Threshold Model, Grady's Spall Model and the Tuler-Butcher Model. Active models are those in which a damage variable is calculated. This damage is then used to alter the properties of the material (i.e. stress) and accordingly alters the relationship between stress and strain (pressure and volume). One example of an active model is the Cochran-Banner model.

The Simple Spall Threshold Model uses a constant value for the critical stress, σ_{sp}, which defines the maximum value at which spall in a material occurs. At stresses above this critical value, $\sigma \geq \sigma_{sp}$, the strength function, F, is set to zero. At this location in the material, tension can no longer be applied hence a void is created and all pressures thusly come to zero at this newly created free surface. This then results in spallation.

The Tuler-Butcher Model (Tuler and Butcher 1968) takes into account the time needed for damage to occur. When the condition for damage is exceeded at a certain plane, fracture occurs. In the Tuler-Butcher model cumulative damage takes the integral form,

$$\int_0^{t_f} (\sigma_0 - \sigma)^\lambda \, dt = K \,. \tag{4.12}$$

The stress, σ_0, is the tensile stress below which fracture would not occur. The symbols λ and K are material dependent constants while t_f is the fracture time. In this equation, tensile stresses are negative valued.

The Cochran-Banner Model is an example of an active spall model. It first considers when the spall strength is exceeded and then the material undergoes nucleation and growth of microcracks. The growth of the microcracks is calculated using a damage variable, *D(x,t)*, that is the volume of microscopic cracks at a particular location and time. In 1D hydrocodes, the damage is given by the actual crack volume per unit area:

$$D(x,t) = \frac{V_c}{A} \,. \tag{4.13}$$

It should be noted that this model assumes that damage occurs only after the spall threshold has been reached

$$D(x,t) = \int_0^t \frac{dV}{A} \,. \tag{4.14}$$

The strength function, *F*, for the Cochran-Banner model is given by:

$$F = 1 - \left(\frac{D}{D_0} \right)^{2/3} , \tag{4.15}$$

where this function can be seen as the factor that reduces the cross-sectional area over which the stress acts. Therefore, when damage occurs, the stress that acts on the material is given by:

$$\sigma = F\Sigma \,, \tag{4.16}$$

where Σ is the spall stress. The values for D_0 and Σ are varied until a good fit to experimental data is found.

4.3.3 Relevant Yield Models

I will discuss here several yield and sheer models that will be relevant for comparison to experimental results in Chapter 5. In the von-Mises model, the yield stress and the shear modulus are both constant.

$$\begin{aligned} Y &= Y_0 \\ G &= G_0 \end{aligned} \tag{4.17}$$

The Steinberg-Guinan model (Steinberg, Cochran and Guinan 1980) is effective at fast strain rates, yet it is a rate independent model. In the Steinberg-Guinan model, the shear modulus has a positive pressure dependence (*A*) and negative temperature dependence (*B*) and is given by:

$$G = G_0\left[1 + A\frac{P}{\eta^{1/3}} - B(T - T_0)\right], \tag{4.18}$$

where η is compression. The yield stress is dependent on the shear modulus and contains a strain hardening term ($[1+\beta(\varepsilon+\varepsilon_i)]^n$):

$$Y = Y_0[1+\beta(\varepsilon+\varepsilon_i)]^n \frac{G(P,T)}{G_0}, \tag{4.19}$$

where is ε_i is the initial plastic strain, and β and n are strain hardening parameters. It is subject to the condition that the strain hardening is less than Y_{max}, the saturation stress.

The Steinberg-Lund rate dependent yield model (Steinberg and Lund 1989) contains both a thermal and an athermal term:

$$Y = \left(Y_t(\dot{\varepsilon}^p, T) + Y_A f(\varepsilon^p)\right)\frac{G(P,T)}{G_0} \tag{4.20}$$

The athermal term is given by the Steinberg-Guinan Model and a thermally activated term is given by:

$$\dot{\varepsilon} = \left\{\frac{1}{C_1}\exp\left[\frac{2U_K}{kT}\left(1-\frac{Y_T}{Y_P}\right)^2\right] + \frac{C_2}{Y_T}\right\}^{-1} \tag{4.21}$$

where $2U_k$ is the formation energy of a kink pair, C_1 and C_2 are constants defined in the reference, Y_T is the thermally activated yield stress, and Y_p is the Peierls stress.

The Johnson-Cook rate dependent model (Johnson 1983) includes effects for strain hardening, strain rate hardening, and thermal softening and is given by:

$$Y = Y_0\left[1 + B\left(\varepsilon^p\right)^n\right]\left[1 + C\ln\left(\frac{\dot{\varepsilon}^p}{\dot{\varepsilon}_0}\right)\right]\left[1 - D\left(\frac{T - T_r}{T_m - T_r}\right)^m\right] \tag{4.22}$$

where B, C, D, n *and* m are constants, ε^p is plastic strain, $\dot{\varepsilon}^p$ is plastic strain rate, T_m is a reference melt temperature, and T_r is a reference temperature. I will discuss the specific use of these various yield and spall models in Chapter 5 to compare with the experimental results.

CHAPTER 5. EXPERIMENTAL RESULTS, SIMULATIONS, AND ANALYSIS

In this chapter I will briefly discuss the primary findings from our aluminum melt experiments on the Janus laser and on the Z-Beamlet Laser (ZBL). I will then describe results from spall experiments performed on ZBL. This section will include discussions of the spall strength dependence on grain size, shock pressure, material purity and strain rate. I will also describe the hydrodynamic simulations performed and discuss how they compare to the experiments.

5.1 MELT EXPERIMENTS

5.1.1 Aluminum Melt on Janus and Z-Beamlet

In an attempt to look at the dynamics of shock melting, we designed an experiment that used VISAR to determine the peak pressure at an aluminum/LiF interface, in addition to measuring linear reflectivity and harmonic signals. While we were able to retrieve some linear reflectivity data, we were unable to generate harmonic data from these experiments. There are several likely reason for this. Aluminum is not a strong source for harmonic generation, whereas a semiconductor such as silicon may be a better choice for reproducible harmonic generation (Burns and Bloembergen 1971). This will be discussed further in Chapter 6. Grain size and orientation may have also been a complicating factor since various crystal orientations will produce different harmonic signals.

Figure 54 shows VISAR interferograms and the resulting interface velocities versus time for the case of 56 μm aluminum on 2 mm LiF at intensities of 2.5 x10^{12} W/cm^2 and 6.5 x10^{12} W/cm^2. The peak particle velocities are 3.1 μm/ns and 4.8 μm/ns. Spatially the shock breakout appears to be very 1D due to the use of a phase plate.

However, after the initial breakout, there is clearly some spatial structure in the material response. In the high intensity case, it is worth noting that there is a second kick in velocity. After some discussions with Jeff Colvin of LLNL, it was concluded that this feature may be due to melt on release. This may be due to a slight impedance mismatch at these pressures or incomplete bonding between aluminum and lithium fluoride. The low intensity case (2.5 x10^{12} W/cm^2) shows approximately a 20% decrease in reflectivity over ~ 2 ns. The high intensity case (6.5 x10^{12} W/cm^2) shows a more sudden drop in reflectivity from ~80% to ~60% in less than 1 ns.

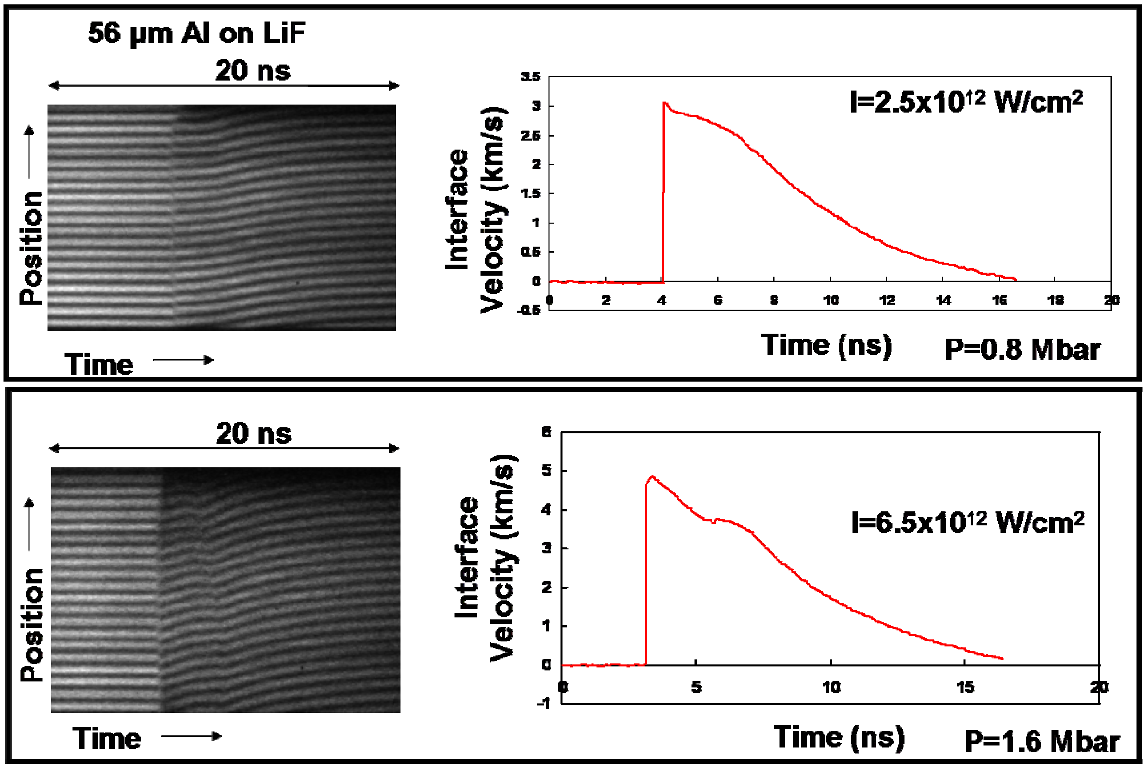

Figure 54: Interferograms for 56 μm Aluminum backed with LiF with resulting interface velocity lineouts. The timescale of the interferograms is 20 ns. The peak pressure in each case was 0.8 Mbar and 1.6 Mbar. Notice the small bump in interface velocity at ~6 ns. The 2nd bump may be an indication of melt upon release. Figure courtesy of Aaron Bernstein.

Figure 55 shows hydrodynamic simulation results for 56 μm Al on LiF at laser intensities of 2.5x10^{12} W/cm^2 and 6.5x10^{12} W/cm^2. For the case of laser intensity of 2.5x10^{12} W/cm^2, the temperature profile versus target depth shows that the last ~30 μm of target depth is unmelted. The peak particle velocity at the Al/LiF interface is 2.8 µm/ns. For the case of laser intensity of 6.5×10^{12} W/cm^2 the temperature profile versus target depth shows that the material temperature at the Al/LiF interface is at about the melt threshold. The peak particle velocity at the Al/LiF interface is 4.2 µm/ns. This velocity profile also shows a hint of a second bump around 9 ns. The particle velocities from the simulations compare favorably to our experimental findings.

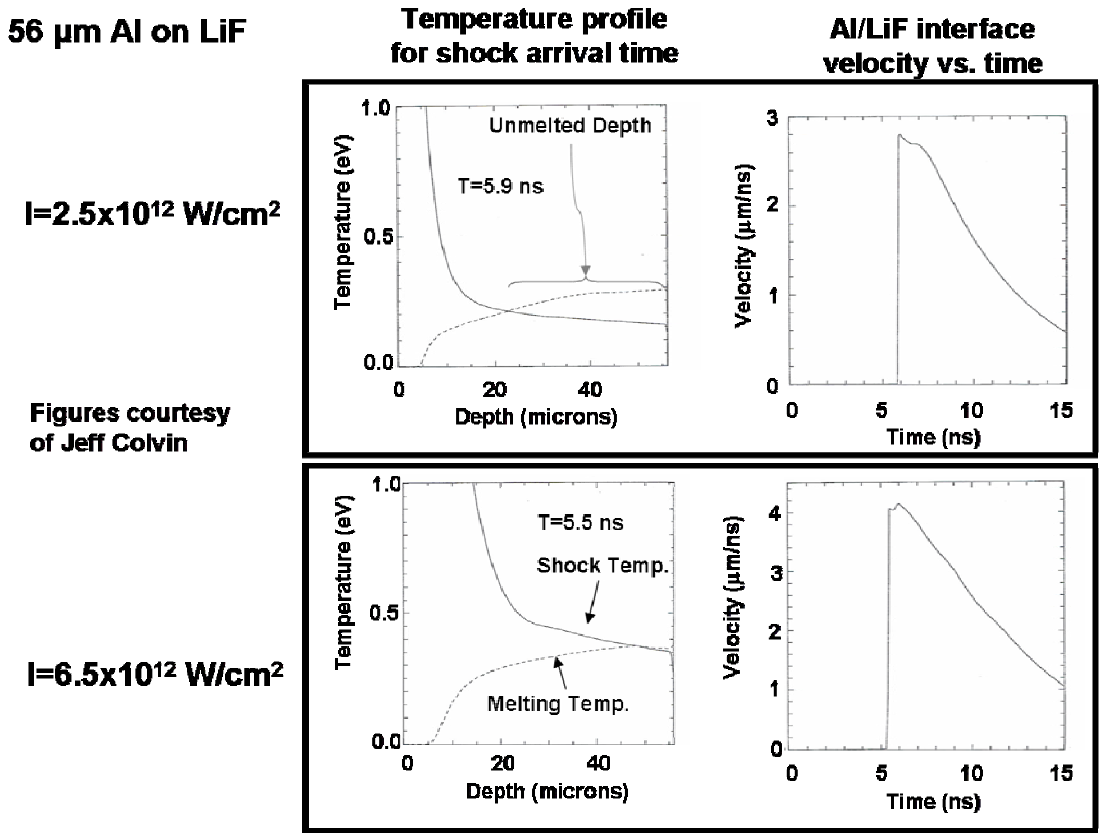

Figure 55: Simulations figures of material temperature versus target depth and particle velocity versus time for 56 µm Al on LiF for the case of laser intensities of 2.5×10^{12} W/cm^2 and 6.5×10^{12} W/cm^2. Simulation figures are courtesy of Jeff Colvin.

In a similar manner, we explored shock induced melting of aluminum on LiF using ZBL as the shock driver. We used the re-designed VISAR to measure the peak particle velocities of the Al/LiF interace. The equation for aluminum was used to determine the peak pressure (Eq. 2.15) and the peak compression (Eq. 2.16). Figure 56 shows a line-VISAR record for 50 µm Aluminum on LiF impacted at ~5x10^{12} W/cm^2. The maximum pressure was determined to be 1.4 Mbar and the maximum compression was 1.7. While we were unable to measure the timescale on which melt occurred we were able to measure the peak velocities relevant to melting.

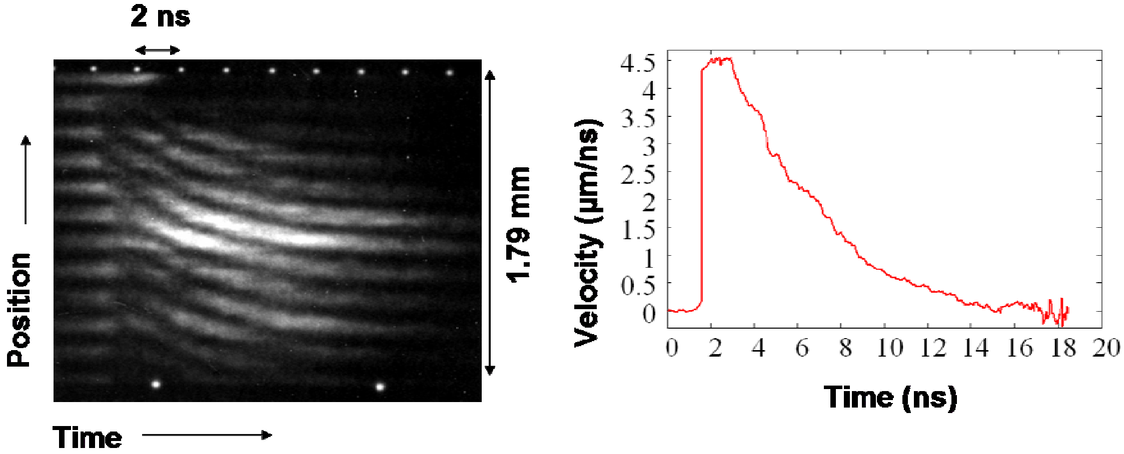

Figure 56: Interferograms for 50 µm Aluminum on LiF wafers along with a resulting particle velocity lineout showing a peak particle velocity of 4.5 µm/ns.

5.2 SPALL EXPERIMENTS

5.2.1 Preliminary Spall Experiments

Upon successfully redesigning a VISAR for use in the shock experiments, we began looking at laser induced spall of aluminum.

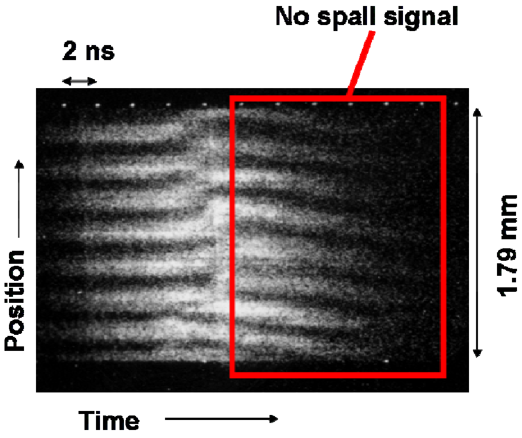

Figure 57: VISAR interferogram for aluminum spall experiments illustrating that the probe pulse is too short of observe the entire spall event.

When we first started shock experiments at ZBL we were studying relatively short time scale events (i.e. shock melting experiments on Aluminum) where a single 10 ns pulse would allow us to measure the event of interest. However, when we started to consider spall experiments it was noticed that the probe pulse was not long enough to see both the straight fringes before shock breakout and the spall event itself. Figure 57 shows a VISAR interferogram for an aluminum spall experiment. Therefore, another diagnostic laser with a longer temporal pulse width or a method to temporally elongate the pulse would be needed to observe the entire fracture event.

5.2.2 Pulse Stacker

In an effort to produce a temporally longer pulse to investigate spall on aluminum, we started to research pulse stackers. Stacking pulses is not a particularly novel idea; however, our approach to pulse stacking is unique in its simplicity and we benefited from several key features in the VISAR. Pulse stackers are useful for creating long probe pulses, seeding high energy laser systems, and quasi-isentropic experiments.

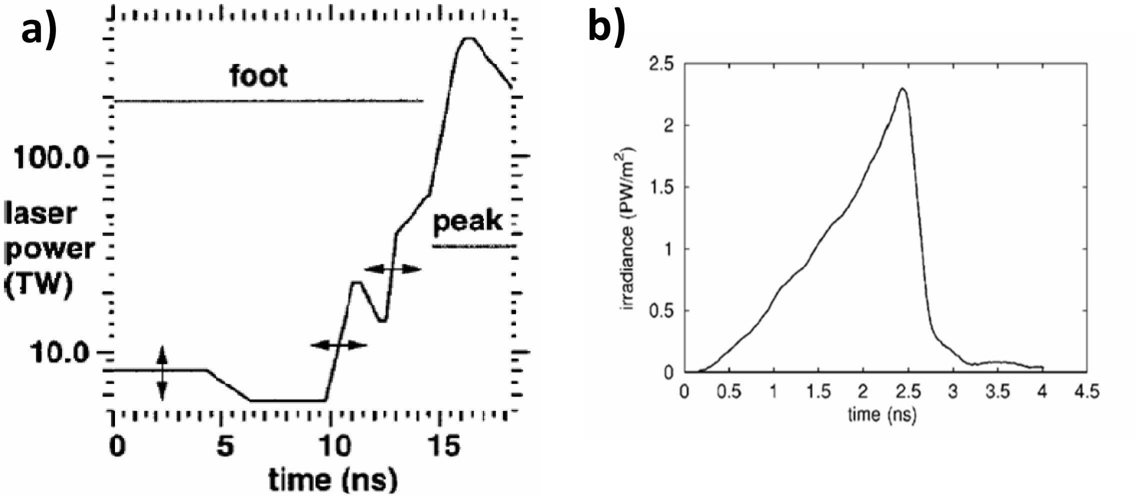

Figure 58: Example of a shaped laser pulse used for (a) ICF studies (Munro 2001) and for (b) quasi-isentropic compression experiments (Swift 2005). Reprinted with permission from Munro, D.H., et al. "Shock timing technique for the National Ignition Facility." Physics of Plasmas, 8, (2001): 2245. Copyright 2001. American Institute of Physics. Reprinted figure with permission from Swift, D.C. and R.P. Johnson. "Quasi-isentropic compression by ablative laser loading: Response of materials to

dynamic loading on nanosecond time scales." Physical Review E, 71, (2005): 066401. Copyright (2005) by the American Physical Society. http://prola.aps.org/abstract/PRE/v71/i6/e066401

Figure 58 shows two examples of temporally shaped pulses. The first example is a Haan pulse which is the ideal temporal pulse shape used for creating ignition in indirect-drive inertial confinement fusion (Munro 2001). The second pulse is a ramp pulse, which is used for quasi-isentropic compression experiments (Swift 2005). Isentropic compression is a way to reach high pressures without significantly heating the specimen.

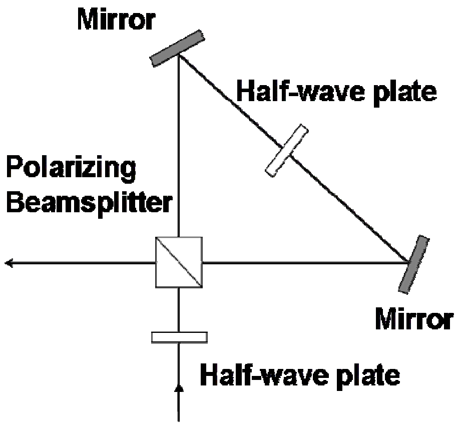

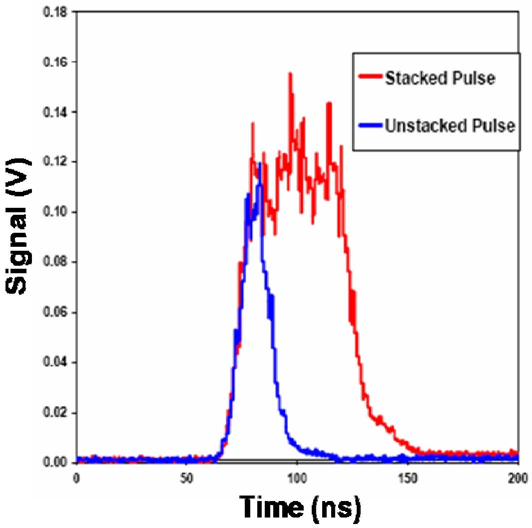

Figure 59: Schematic of our pulse stacker design.

Our pulse stacker is based on the design shown in Figure 59. The design consists of two half-wave plates, a polarizing beamsplitter, and a cavity which delays the pulse with respect to itself. An incoming beam of some linear polarization passes through a λ/2 waveplate. The beam then hits the polarizing beamsplitter where the S polarization reflects away from the cavity and the P polarization passes through the beamsplitter into the ring cavity. The P polarization beam then passes through a second half waveplate, again inducing S and P polarizations. The beam then approaches the polarizing beamsplitter, but along an orthogonal trajectory to that of the previous pass. This time the P polarization passes through and out of the cavity while the S polarization reflects back into the cavity. This process is repeated for many passes until all the beam energy is dissipated. Figure 59 also shows a photodiode trace of a single pulse with the cavity blocked (blue) and a trace with the cavity unblocked (red).

Using a Jones Matrix formulation we start with an incident field, $\widetilde{E}_i$, which proceeds through a λ/2 waveplate with some arbitrary rotation, producing a transmitted field, $\widetilde{E}_t$:

$$\widetilde{E}_t = A(\theta)\widetilde{E}_i, \tag{5.1}$$

where $A(\theta) = R(-\theta)AR(\theta)$

$$\widetilde{E}_t = \begin{bmatrix} \cos(\theta) & -\sin(\theta) \\ \sin(\theta) & \cos(\theta) \end{bmatrix} \begin{bmatrix} 1 & 0 \\ 0 & -1 \end{bmatrix} \begin{bmatrix} \cos(\theta) & \sin(\theta) \\ -\sin(\theta) & \cos(\theta) \end{bmatrix} \begin{bmatrix} 1 \\ 0 \end{bmatrix} \tag{5.2}$$

$$\widetilde{E}_t = \begin{bmatrix} 2\cdot\cos^2(\theta) - 1 \\ 2\cdot\cos(\theta)\cdot\sin(\theta) \end{bmatrix} \tag{5.3}$$

Squaring the transmitted field yields the fraction of intensity distributed into and out of the ring. We desire ~ 27% reflected by the polarizing BS and ~73% distributed into the ring cavity in order to have the relative intensities of the 1st three pulses approximately equal, thus yielding an approximate temporally top hat beam. The S-polarization beam will reflect out first and P-polarization will go into the cavity.

$$\begin{aligned} \left[2\cdot\cos(\theta)\cdot\sin(\theta)\right]^2 &= 0.27 \quad \text{S-polarization} \\ \left[2\cdot\cos^2(\theta) - 1\right]^2 &= 0.73 \quad \text{P-polarization} \end{aligned} \tag{5.4}$$

The angles that satisfy these conditions are 15.7°, 74.3°, 105.7°, and 164.3°. The P-polarization beam now encounters the second waveplate which is used to control the relative intensities of the 2nd and 3rd pulses. For optimum pulse shape we require

$$\begin{aligned} 0.73\cdot\left[2\cdot\cos^2(\theta) - 1\right]^2 &= 0.27 \\ 0.73\cdot\left[2\cdot\cos(\theta)\cdot\sin(\theta)\right]^2 &= 0.46 \end{aligned} \tag{5.5}$$

The angles that satisfy these conditions are 26º, 64º, 116º, and 154º. On the second roundtrip, the P-polarization enters the cavity, whereas on the third roundtrip, the S-polarization enters the cavity. This is due to the pulse being incident on a different face of the beamsplitter.

$$\begin{aligned} 0.46 \cdot \left[2 \cdot \cos^2(\theta) - 1\right]^2 &= 0.17 \\ 0.46 \cdot \left[2 \cdot \cos^2(\theta) - 1\right]^2 &= 0.29 \end{aligned} \tag{5.6}$$

The angles that satisfy this condition must be the same as on the previous pass. Figure 60 shows the relative energy exiting the pulse stacker system against pulse number using the Jones matrix approach. In this case the first three pulses are optimized to have nearly the same intensity. By tuning the angle of the waveplates, one gets independent control of the three pulses.

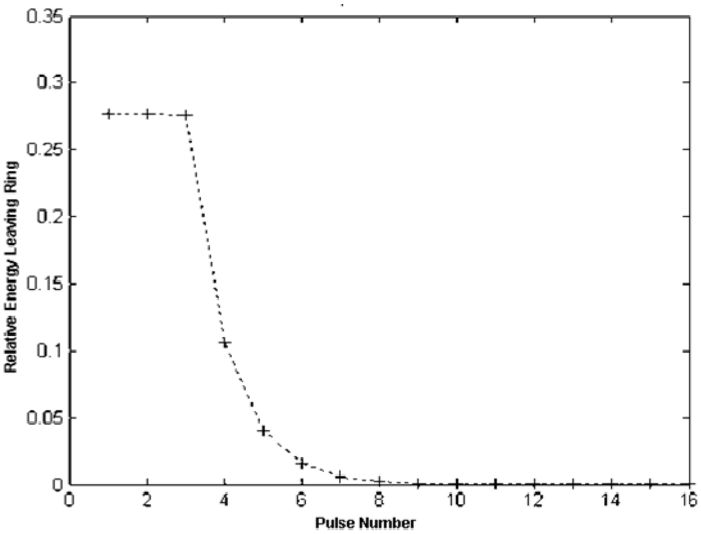

Figure 60: Jones matrix calculation or the relative pulse energy leaving the ring versus the pulse number. The first three pulses have about the same intensities. Figure courtesy of Aaron Bernstein.

Figure 61 shows the unstacked pulse and the stacked pulse for three different temporal profiles. The first pulse (a) is a top-hat pulse which is ideal for the VISAR diagnostic. The second pulse (b) has a pedestal and then a peak, which might be ideal for some types of plasma studies. The final pulse profile (c) is a ramp wave pulse, which is suited for quasi-isentropic experiments.

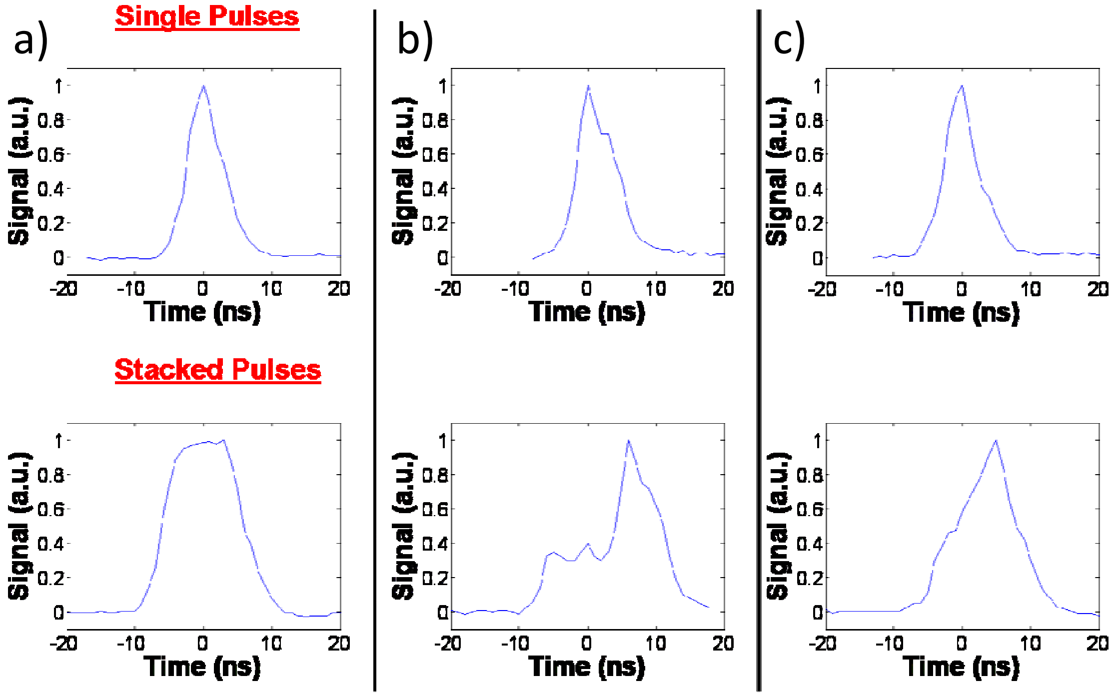

Figure 61: (a)Top-hat, (b)pedestal and (c)ramp pulses compared to the initial pulse used to form those shaped pulses.

One concern in using this type of pulse stacker is that the second, third and subsequent pulses have the same polarization, therefore two pulses can interfere if the coherence length is long enough (i.e. interpulse interference). For our line-VISAR experiments, the laser used is a single longitudinal mode laser, typically has a linewidth of roughly Δν=130 MHz, meaning that the coherence length is ~2.3 m. However, a typical multimode Nd:YAG has an atomic linewidth of Δν=120 GHz which means that the coherence length is ~2.5 mm. Thus one expects greater interpulse interference from a single longitudinal mode laser for our pulse stacker setup.

Given this concern, we set up a Michelson interferometer to observe the effect of interpulse interference with a multimode laser, since a seeded laser was unavailable at the time. First, we placed the laser pulse directly onto a Thorlabs DET210 photodiode with

1-2 interference fringes or ~10 fringes. Secondly, the pulses were sent through a multimode fiber before reaching the photodiode. The results are shown in Figure 62.

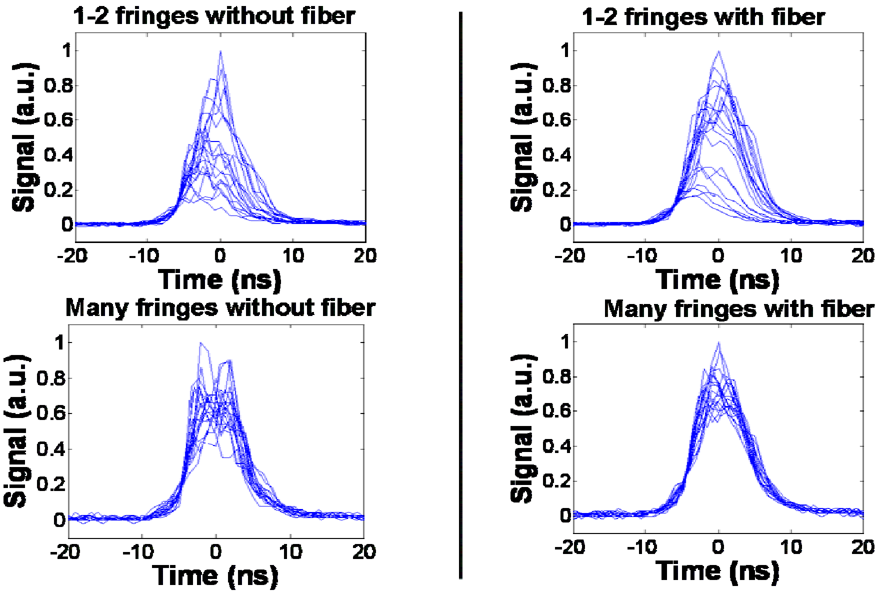
1-2 fringes without fiber

1-2 fringes with fiber

Many fringes without fiber

Many fringes with fiber

Figure 62: Using a Michelson interferometer we explored the effect of interpulse interference for an unseeded Nd:YAG.

It is evident that the cleanest group of pulses comes from using many fringes to average out the peaks and valleys while also putting the pulse through the multimode fiber. Using many fringes and a multimode fiber for averaging appears to alleviate the problem of interpulse interference. Figure 63 shows a reference VISAR interferogram with a stacked pulse. This figure shows that the pulse is sufficient for using with the VISAR.

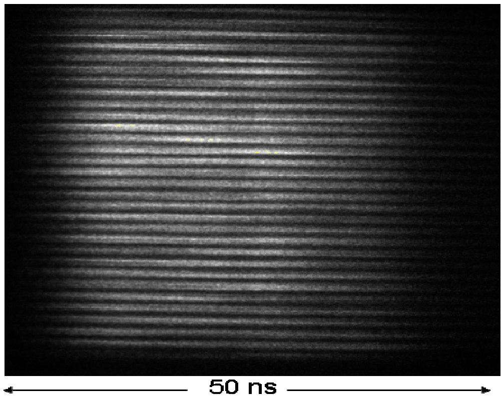

Figure 63: Reference interferogram of a stacked pulse illustrates that the pulse is sufficient for use in a VISAR interferometer.

Our pulse stacker idea is a simple and effective way to create long probe pulses for velocity interferometry measurements. The pulse stacker gives us independent control of three pulses, which can be used to create interesting pulse shapes. With optimized conditions, long pulses can be generated with no interpulse interference. It may be possible to use the pulse stacker to generate energetic temporally shaped seed pulses for amplification without the need of a regenerative amplifier.

5.2.3 Spall Experiments of Polycrystalline Aluminum and Aluminum Alloys at 2-8x10^6 s^{-1}

As previously introduced, we wanted to explore the effect that microstructural imperfections have on spall fracture. Using a high-energy laser to drive shocks in thin slabs, we explored the role that material microstructure plays on the spall strength of high-purity and alloyed aluminum at strain rates of ~ 2–8 x 10^6 s^{-1}. Slabs of pure recrystallized Al and recrystallized or cold worked Al+3 wt % Mg were shock driven using ZBL. Velocity interferometer measurements determined the spall strength of the materials, and postshot target analysis explored the microscopic fracture morphology (Dalton, Brewer, et al. 2008), (Brewer, Dalton, et al. 2007).

Aluminum slab targets of two thicknesses were used in our experiments: 200 μm and 500 μm. The 200 μm targets were irradiated with laser intensities ranging from

3.4×10^{11} to 5.7×10^{11} W/cm^2, producing measured strain rates of ~$6\times10^6 s^{-1}$. The 500 μm targets were irradiated with laser intensities from 1.0×10^{12} to 1.5×10^{12} W/cm^2, producing measured strain rates of ~2×10^6 s^{-1}. This choice of target thickness and corresponding intensity was designed to access different strain rates at the spall plane while roughly maintaining the same peak shock pressure. Our diagnostics did not allow us to measure directly the peak shock pressure due to ambiguity in the number of fringe shifts, but we were able to estimate it using simulations from the hydrodynamic code, HYADES (Larsen and Lane 1994). From these simulations the peak pressure estimated for the 200 μm targets was 65-100 kbar and in the 500 μm targets, the pressure at the rear surface was estimated at 65-80 kbar (Figure 64).

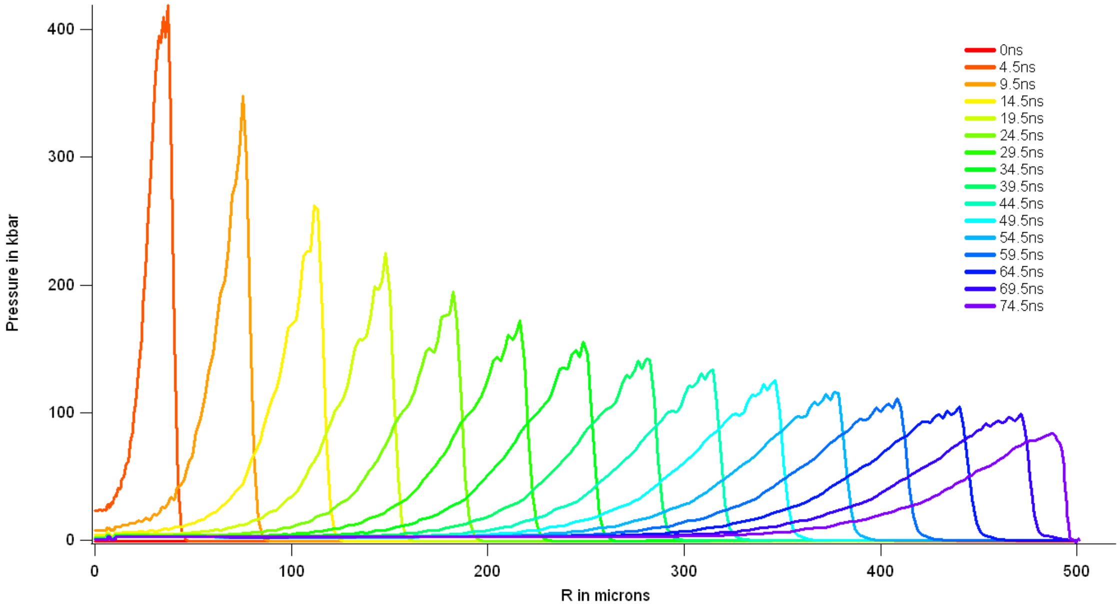

Figure 64: Pressure versus target depth profiles for 500 μm Aluminum impacted at 1.5 x 10^{12} W/cm^2. The peak pressure near the rear surface is ~80 kbar.

1. Materials

Two types of aluminum foil were used for target fabrication: high purity aluminum (99.999% Al, denoted Al-HP) and an aluminum alloy containing 3 wt. % Mg (denoted Al+3Mg). Foils were processed using a rolling technique which is detailed in

Brewer, et al. (Brewer, Dalton, et al. 2007). The Al-HP and Al+3Mg were produced by full recrystallization after rolling (denoted RX). Another set of Al+3Mg samples were cold worked by taking fully recrystallized targets and rolling them to an additional 50% thickness reduction (denoted CW). All foils were then ground and polished to either 200 or 500 μm thicknesses.

Table 6 shows the composition in parts-per-million (ppm) of impurities for the Al-HP and Al+3Mg.

Table 6: Composition of materials in mass ppm (Brewer, Dalton, et al. 2007).

Material	Al	Cr	Cu	Fe	Mg	Mn	Si	Ti	Zn
Al-HP	Bal	0.73	<1	38	1.8	0.33	<200	2.85	0.87
Al+3Mg	Bal.	23.4	16.2	1230	29,900	30.1	<200	134	233

2. *VISAR results*

A battery of these targets were irradiated on Z-Beamlet with slight variations in the peak intensity and line-VISAR traces were recorded on every shot. An example VISAR interferogram and resulting velocity lineout is shown in Figure 65.

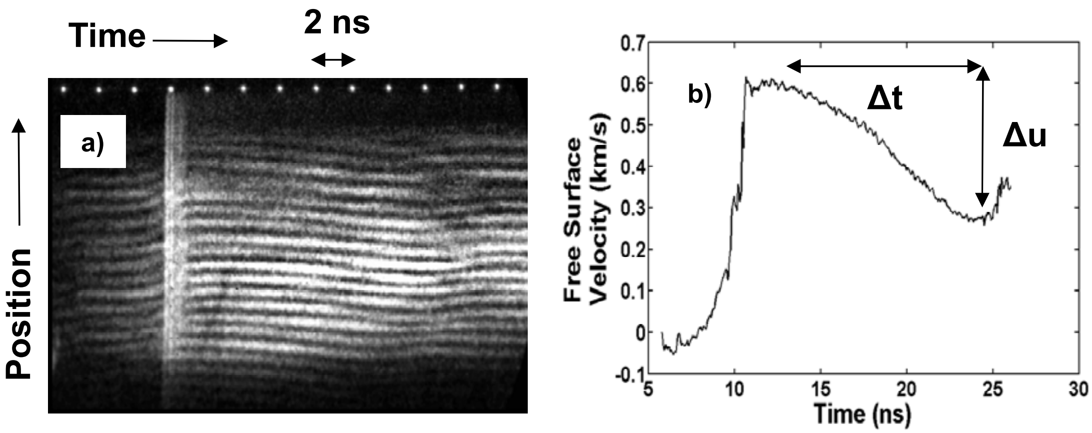

Figure 65: (a) Raw line-VISAR interferogram and (b) Velocity lineout corresponding to a spall experiment of 500 μm, free standing Al+3Mg RX impacted at 1.4 x10^{12} W/cm^{2}. The velocity-per-fringe constant for this shot is 0.29 km/s.

A polynomial fit is applied after shock breakout for four lineouts to get a smooth velocity profile. By extracting the maximum and minimum velocities, a pullback velocity is retrieved from each lineout and the spall strength for the material is calculated. We then averaged the spall strength values for the four lineouts of a given VISAR trace. Figure 66 shows spall strength data versus strain rate found in our experiments for the three target specimens. In all three cases a slight increase in spall strength with increasing strain rate is observed. Most striking, however, is the sizable difference in spall strength between high purity Al and both Al+3Mg foils.

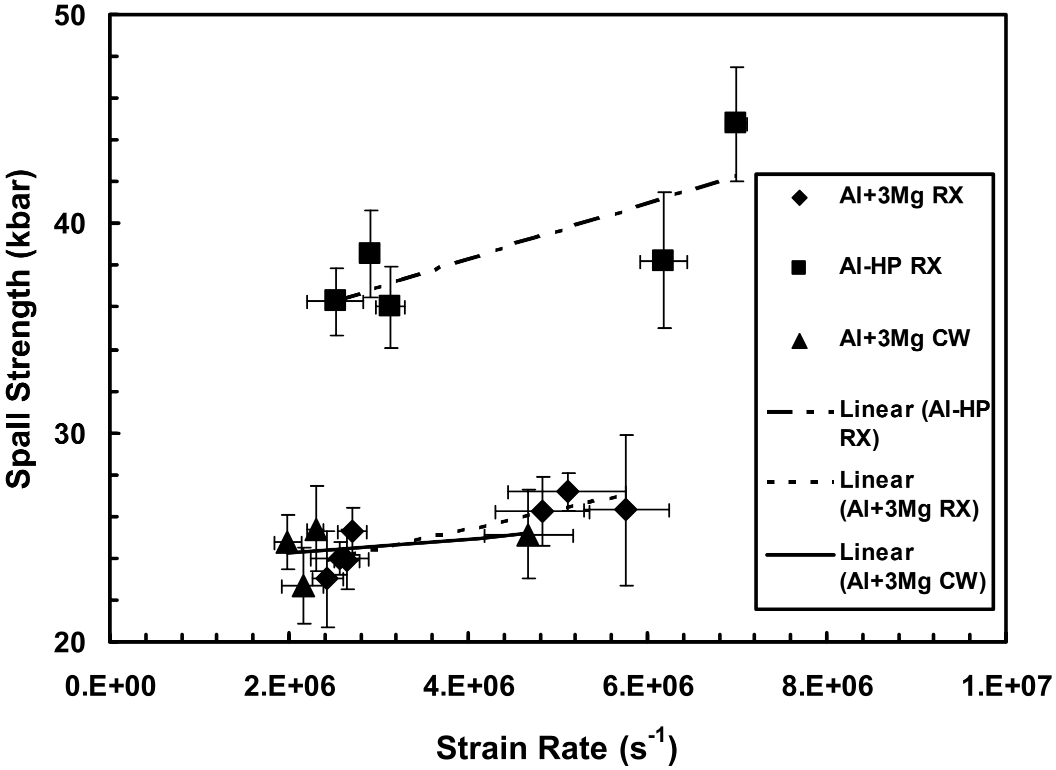

Figure 66: Spall strength versus strain rate for Al-HP RX, Al+3Mg RX, and Al+3Mg CW.

3. *Fracture and Particle Analysis*

In addition to measuring the spall strength and strain rate of these specimens, post shot target analysis was performed to understand the potential causes of fracture.

Table 7 summarizes material thickness, grain size, laser intensity, average tensile strain rate, average spall strength and fracture mode.

Table 7: Material, thickness, grain size, laser intensity, tensile strain rate, average spall strength, and failure mode. (TG means transgranular and IG means intergranular)

Material	**Thick-ness (µm)**	**Longi-tudinal Grain size (µm)**	**Transverse Grain Size (µm)**	**Laser Intensity ($x10^{11}$ W/cm^2)**	**Strain Rate (µs^{-1})**	**Spall Strength (kbar)**	**Failure mode**
Al-HP RX	500	233±113	252±130	11	2.9	37	TG
	200	378±69	200	4.6	6.6	42	TG
Al+3Mg RX	500	23±3	23±3	10	2.6	24	IG
	200	52±6	32±6	4.8	5.2	27	IG+20%TG
Al+3Mg CW	500	56±16	16±1	14	2.1	24	IG
	200	40±15	10±2	3.4	4.7	25	IG

The grain sizes and shapes of the foils in each target group were determined by cross-sectioning the foil and then examining the cross section with optical and scanning electron techniques. Digital images of foil cross sections of Al-HP RX and Al+3Mg RX are illustrated in Figure 67. Both the Al-HP and the Al+3Mg RX samples exhibited nearly circular grains. The average grain size of the 500 µm Al-HP foils was 230±110 µm and the average grain size in the 200 µm thick Al+3Mg RX samples was 50±6 µm. The cold worked Al+3Mg samples exhibited elongated grains with a transverse average size of 56±16 µm and longitudinal size of 16±1 µm.

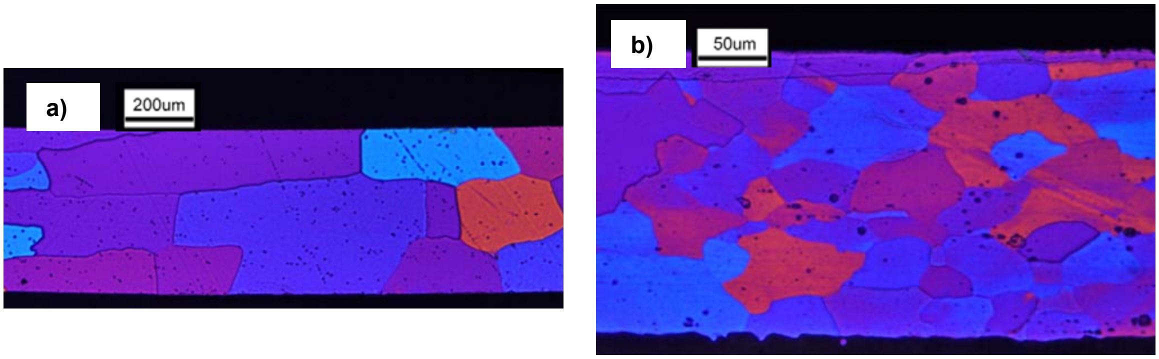

Figure 67: Cross section of (a) Al-HP RX (500 µm) and (b) Al+3Mg RX (200 µm) targets illustrate the differences in grain size. Figures are courtesy of Jonathan Brewer.

The morphology of the fracture surface was also investigated to determine the potential causes of fracture. Figure 68 shows scanning electron microscope (SEM) images of the fracture surface of the (a) Al+3Mg CW (b) Al+3Mg RX and (c) Al-HP RX.

The prominent feature for both 200 μm and 500 μm thick Al-HP RX slabs is transgranular dimpling indicating predominantly ductile failure. However, we see from the fracture surfaces that in Al+3Mg CW the dominant failure modes are both brittle intergranular and brittle transgranular. For Al+3Mg RX foils of 500 μm thickness, we find that the dominant feature is brittle intergranular failure; however, in the thinner 200 μm targets the failure is a mixture of brittle intergranular fracture with areas of ductile transgranular fracture. The areas contribute to ~20% of the total fracture area. This mixed-mode feature is unique among the target specimens.

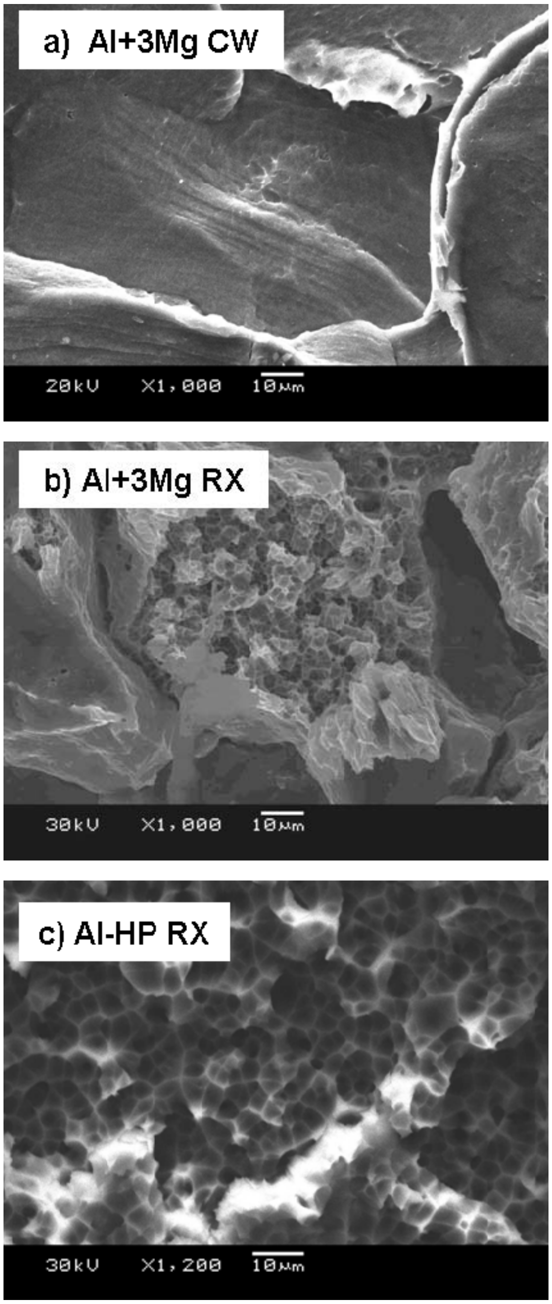

Figure 68: Scanning-electron microscope image showing the exposed spall plane of (a) Al+3Mg CW: the sharp edges and score marks indicate that the fracture is brittle, (b) Al+3Mg RX (200 µm) showing brittle intergranular fracture with regions of ductile dimpling and (c) Al-HP RX: the dimpling is indicative of ductile fracture. Figures are courtesy of Jonathan Brewer.

4. HYADES simulations

As stated earlier, HYADES is a Lagrangian hydrodynamic code that is used to simulate our shock conditions. Using our initial laser conditions for target thicknesses of 200 and 500 μm, HYADES was used to determine pressure versus target depth profiles near the rear surface. The simulations are shown in Figure 69 as time slices of a pressure wave profile reflecting off the free surface and back into the target as a tensile stress wave.

These simulations predict a shallower spall plane with a steeper pressure gradient in the fast strain rate case when compared to the slow strain rate case. The breadth of the pressure wave and the growth rate of its amplitude are two parameters which may control, along with grain size, the transition from brittle intergranular to ductile transgranular fracture. We define a length scale γ which is the spatial expanse of the half maximum tensile stress in the simulated pressure profile.

Figure 69a shows the lower strain rate case ($4x10^{6}$ s^{-1}) of the 23 μm grain size Al+3Mg with 500 μm thickness. When the simulated pressure profile reaches the average measured spall strength of 24 kbar (horizontal dashed line) its spatial expanse is γ=25 μm and it has propagated a distance of 30 μm from the free surface (vertical dotted line). These are both approximately the same as the average measured specimen grain size of *d*=23 μm. The fracture morphology observed in this case is brittle.

Figure 69b simulates the higher strain rate case ($8x10^{6}$ s^{-1}) of the 32 μm grain size Al+3Mg with 200 μm thickness. In Figure 69b, the simulated pressure profile reaches the average spall strength measured for the Al+3Mg RX 200 μm specimen when its spatial expanse is γ=14 μm and has propagated 15 μm from the free surface. This is less than the *d*=32 μm grain size in this specimen. Under these conditions, the mixed mode fracture was observed.

When comparing the results of these simulations it seems evident that when the grain size, *d*, is small compared to length scales such as the width of the tensile pulse, γ, and the spall depth that fracture will statistically be more likely at grain boundaries. In contrast, when the grain size is large compared to the tensile width and the spall depth, the possibility for transgranular fracture statistically increases.

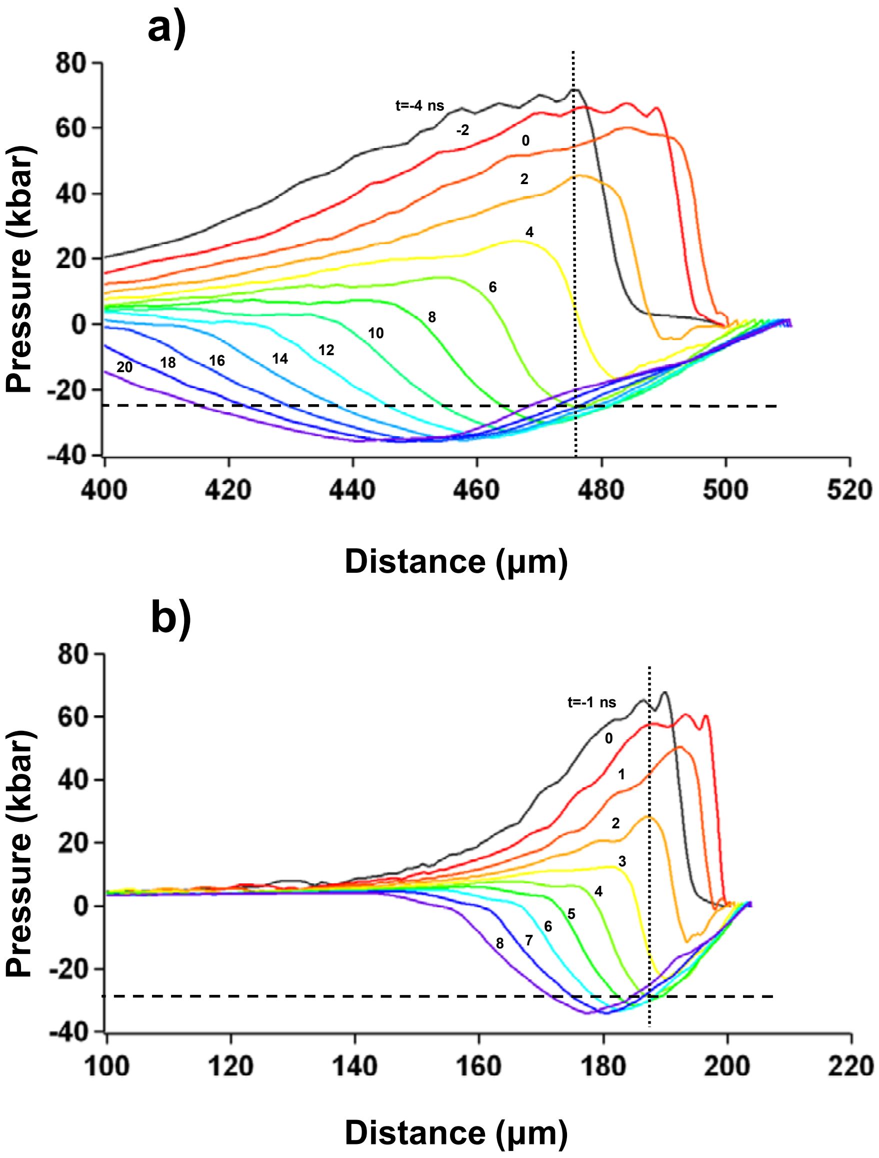

Figure 69: HYADES simulations illustrate the pressure vs. position profiles for strain rates of (a)~4x10^{6} s^{-1} and (b) ~8x10^{6} s^{-1}. The dashed line corresponds to the average measured spall strength and the dotted line corresponds to the spatial location at which the spall threshold is reached.

It is possible to observe the transition in fracture mode (intergranular versus transgranular) by varying grain size and strain rate. The issue is that the spatial scale of the wave must be on the order of the grain size. Since shorter impulsive loads are needed to access faster strain rates, the observed transition in fracture mode can occur in smaller grains.

5. Analysis and Conclusions

Upon analysis, the Al-HP RX specimens showed large average grain size (~200 μm), which seems to correlate to our larger measured spall strength when compared to the aluminum alloy that had smaller (~50 μm) grains. The grain size was smaller and similar in size for both the recrystallized and cold-worked Al+3Mg. The spall strength of the alloys was likely lowered by the fact that there was more surface area at grain boundaries at which voids could form, as suggested by Minich, et al. at the lower strain rates of their experiment (Minich, et al. 2004).

These spall strength measurements are compared in Figure 70 with spall strength measurements performed in aluminum over a range of strain rates from data collected from other sources. The Al-HP RX spall strength values are higher than those of Moshe, et al. at faster strain rates of 10^7–10^8 s^{-1}. It is an open question as to whether the spall strength for Al-HP RX would follow a similar trend to that observed by Moshe, et al., where spall strength dramatically increases with increasing strain rates above 10^7 s^{-1} (Moshe, Eliezer and Dekel, et al. 1998), (Moshe, Eliezer and Henis, et al. 2000). The single datum taken from Robinson at a strain rate similar to ours, approximately 5×10^6 s^{-1}, is consistent with our measurements of Al-HP RX (Robinson 2002). However, we measured a spall strength for Al-HP RX which is 15% greater than the spall strength Robinson measured for aluminum at slower strain rates. These discrepancies may be explained by differences in material composition and microstructure, but further exploration of these parameters requires detailed characterization of the materials investigated. Neither Moshe, et al. nor Robinson specified elemental material composition or microstructure of their aluminum materials, making direct comparison with their results difficult.

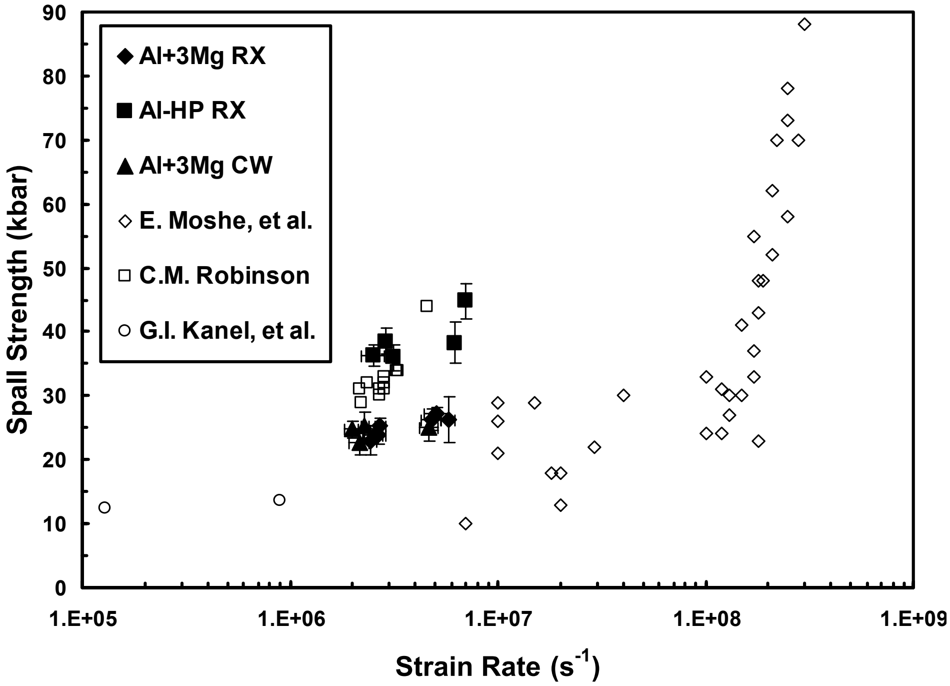

Figure 70: Experimental data of spall strength versus strain rate of Al-HP RX, Al+3Mg RX, and Al+3Mg CW superimposed on other aluminum data (Moshe, Eliezer and Dekel, et al. 1998), (Moshe, Eliezer and Henis, et al. 2000), (Robinson 2002), and (G. Kanel, B. A. Razorenov, et al. 1996) for aluminum AD1. Error bars represent a standard deviation in spall strength and strain rate over multiple equally spaced lineouts.

As this study shows, at fast strain rates, grain size parallel to the shock direction seems to be the dominant force in determining spall strength. Another feature of our data is that, on average, the time scale between the maximum and minimum velocities was longer for the recrystallized aluminum, indicating that it took longer for the spall to occur. Evidently this material takes more time to spall because it undergoes more plastic flow. For smaller grains, there are more restrictions and less slip systems available for plastic flow, allowing spall to occur on a shorter time scale. The ductile fracture for the recrystallized aluminum targets tend to agree with this explanation. Similarly, since the Al+3Mg RX and Al+3Mg CW took a shorter time to occur it makes sense that they had more features indicative of brittle fracture.

At the strain rates studied, it appears that fracture stress and initiation mechanisms are weakly affected by alloy content and instead dominated by grain size and strain rate. We showed that the large grain size of Al-HP RX specimens produced ductile transgranular fracture and the highest spall strength, while the smaller grain sizes of the Al+3Mg RX and CW resulted in mostly brittle intergranular fracture and a low spall strength. These findings are consistent with Minich *et al.*, who showed that spall strength increases with grain size in copper at strain rates of 10–100 times slower than in our laser-driven shock experiments. At engineering strain rates, solid-solution alloying and cold work are known to play critical roles in strengthening materials (Dieter 1976). However, at the much faster strain rates of our experiments, it is unknown what effect these mechanisms have on spall strengthening. The preliminary evidence of Gilath *et al.* showed that, at a strain rate of $2\text{x}10^7$ s^{-1}, aluminum alloy 6061-T6 had a higher spall threshold than did pure aluminum; however, little microstructural detail was provided for these materials (Gilath, et al. 1988).

In conclusion, we measured spall strength in three Al slab preparations, at strain rates approaching 10^7 s^{-1}. On average, we measured the highest spall strength values at strain rates of 10^6-10^7s^{-1} for pure aluminum. One possible explanation for these values is that we have nearly single crystal foils since for some samples the grains grow almost through the thickness of the foil. We find that the spall strength and failure mechanism seem to be correlated to grain size, with the larger grain samples exhibiting significantly higher failure strength. We find that engineering approaches to increase strength, such as alloying and cold working do not increase the strength at these fast strain rates.

5.2.4 Dependence of Pressure on Spall Fracture and Yielding

In addition to looking at microstructural effects, we wanted to study the dependence of drive pressure on the spall strength. In order to do this study, we wanted to perform these experiments using the phase plate that was acquired for our shock experiments. A phase plate serves to smooth out beam inhomogeneities. We planned to use the same laser intensity for all shots, while varying the target thickness which would result in thinner targets experiencing greater pressure near the rear surface.

The shock breakout that was induced in the material after using the phase plate was much smoother. However, due to the beam profile being Gaussian (rather than top hat) and the beam size to target ratio approaching ~3:1 meaning that radial release waves would become more of an issue and the experiment is not one dimensional. Figure 71 shows Al+3Mg RX impacted at 6×10^{12} W/cm^2 which gives a spall strength of ~30 kbar. The shock breakout is clearly very smooth; however the resulting pressures are too great where energy jitter and variations in specimen thickness may result in melt on release.

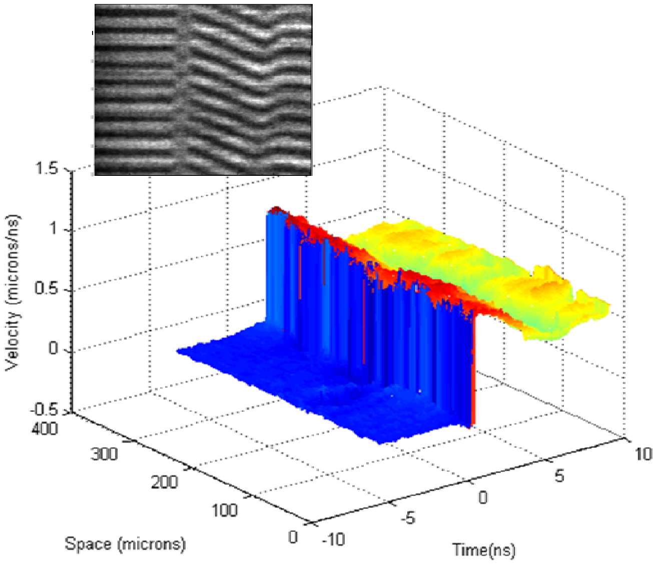

Figure 71: Line-VISAR interferogram for 290 µm Al+3Mg RX showing smoother shock breakout, but also not quite one-dimensional breakout. The laser intensity of 6×10^{12} W/cm^2 produced a strain rate of 8×10^6 s^{-1}, a spall strength of 30 kbar.

After several shots with the phase plate, the data strongly suggested that the pressure near the rear surface induces melt (Figure 72). We decided to remove the phase plate and gather as much spall data versus impact pressure (or target thickness) as possible.

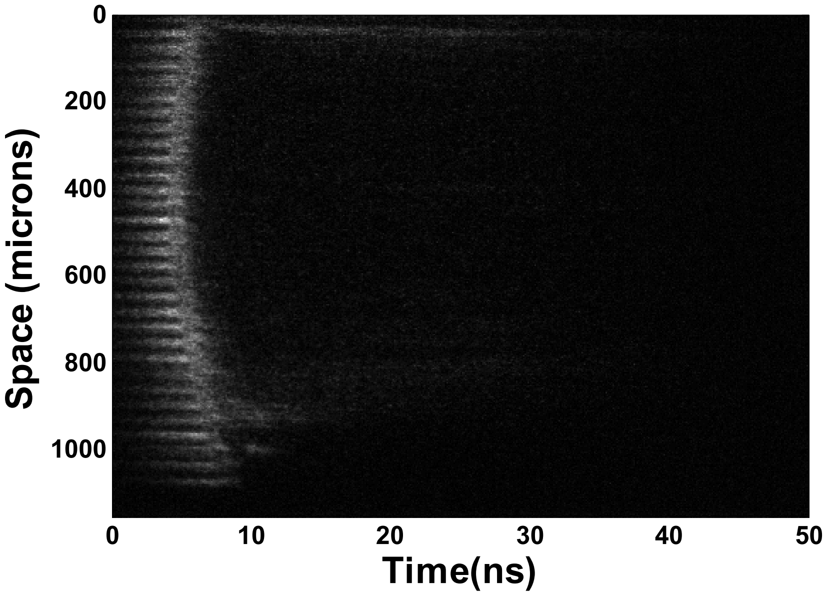

Figure 72: Melt on release of 295 µm Al-HP RX impacted at a laser intensity of 1.5x10^{13} W/cm^2.

The spall strength versus target thickness data (for Al-3Mg RX & CW) suggests that the spall strength has no significant pressure dependence at least in the regime in which we are not close to melting. The data plotted in Figure 73 shows targets impacted at a laser intensity from 1.4-2.3x10^{12} W/cm^2. Notice that there are only two data points for the Al-HP RX, so we can not make any conclusive statement regarding the dependence of spall strength on pressure (or target thickness). We did have several shots with the phase plate in which reflectivity disappeared, fringes disappeared, or there was no spall signal. These are not plotted in the figure.

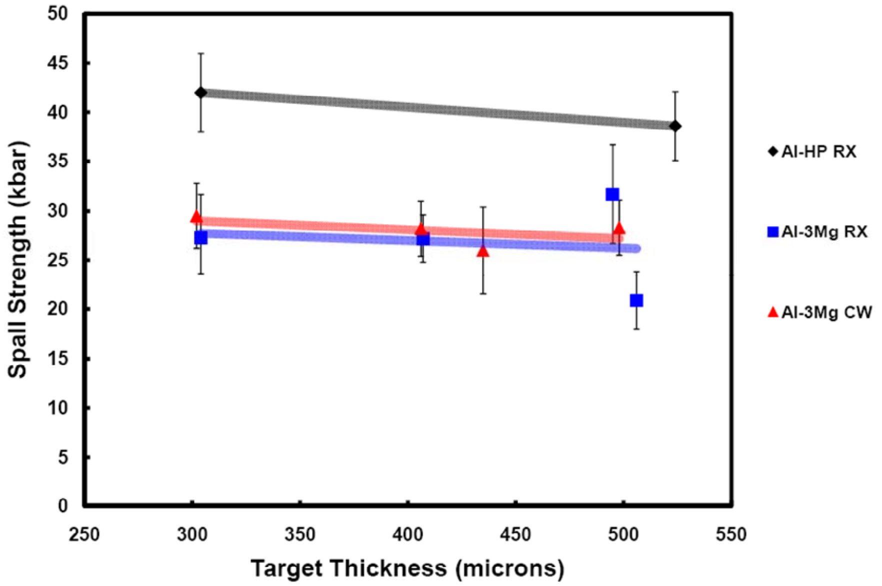

Figure 73: Graph of spall strength versus target thickness showing negligible change of spall strength with target thickness or synonymously shock pressure.

Typically, strengthening mechanisms such as grain size reduction, solid-solution alloying, and cold-working are mechanisms that decrease the plastic deformation (or increase yield strength) of a material and not a material's fracture toughness. Thinking along the same lines, we might expect these mechanisms to increase the threshold plastic deformation due to a shock. In other words, we might expect an increase in the material's Hugoniot Elastic Limit (HEL), or hence the dynamic yield stress.

At the 2007 SCCM Conference, I had a very helpful conversation with James Stolken from Livermore. One important piece of information that we discussed was the effect of our strengthening mechanisms on the HEL. For our preliminary experimental runs, we did not observe the presence of an elastic wave. After our discussion, it seemed informative that we try to quantitatively measure this feature and compare with the fracture results. In a later shot run, we discovered that an elastic precursor was present in some Al+3Mg RX shots, but not in Al-HP or Al+3Mg CW. Figure 74 shows inteferograms of shocked Al+3Mg RX and Al+3Mg CW, with the CW at slightly higher intensity. We see that the elastic precursor does exist before the Al+3Mg RX; however, we do not observe the elastic precursor in front of the Al+3Mg CW. We find this to be odd since hardness measurements suggests that CW has a higher static yield stress. From our measurements, it looks like the CW has a lower dynamic yield stress. The higher laser intensity for the Al+3Mg CW may have shocked the specimen too hard to see the elastic precursor, as the shock may be riding on the precursor. This is a continued area of interest and more results are presented in the next section.

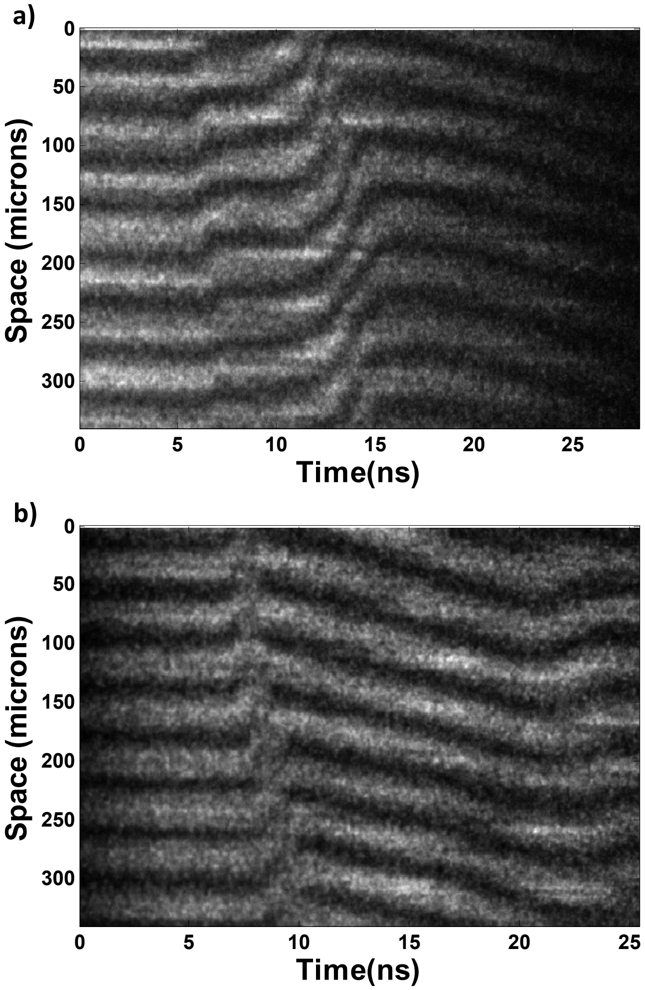

Figure 74: VISAR interferograms of (a) 407 µm Al+3Mg RX impacted at 1.4 x10^{12} W/cm^2 and (b) 406 µm Al+3Mg CW impacted at 2x10^{12} W/cm^2.

5.2.5 Single Crystal Aluminum and Polycrystalline Al+3Mg Spall and Yield Experiments

Spall experiments on single crystal aluminum foils were performed in an effort to eliminate the effect of grain size. By eliminating grain boundaries, we can measure the inherent strength of the crystalline material rather that the strength of grain cohesion. The single crystal materials of interest were a single crystal high-purity aluminum (Al-HP) and a single crystal 1100 series aluminum (Al-1100). In addition to the single crystal specimens, we investigated Al+3Mg at three different grain sizes.

The various specimens were ablatively driven by Z-Beamlet at intensities of 9±2 x 10^{11} W/cm^2 for the 350 μm targets and 1.5±0.4 x 10^{12} W/cm^2 for the 500 μm targets. Using the line-VISAR, we measured the free surface velocity of the various shocked specimens. In these experiments, we were able to use a second VISAR with a different sensitivity to determine the peak shock pressures. We used the first VISAR to measure the spall strength, strain rate and the HEL stress.

1. Sample Specimens

The Al-HP is a 99.999% high purity aluminum. The Al-1100 is a 99% Al with moderate amounts of iron and silicon impurities. The Al+3Mg specimens have a large concentration of magnesium atoms and a fairly large amount of iron impurities.

Table 8 shows detailed impurity analysis of the various aluminum alloys.

Table 8: Particle Analysis of Al-1100 and Al+3Mg in ppm.

Material	Al	Cu	Fe	Mn	Si	Zn	Cr	Mg	Ti
Al 1100	Bal.	1000	5100	55	1400	52			99
Al+3Mg	Bal.	16.2	1230	30.1	<200	233	23.4	29,900	134

Single crystal specimens of aluminum were grown to determine the influence of crystallographic orientation on laser-induced spall fracture. Although several methods exist to make single crystals of metal, the *Fujiwara process* (Fujiwara and Koizume 1952) was chosen for its amenity to lab-scale production. High-quality crystals were grown without the need to purchase expensive equipment or melt the specimen.

The Al+3Mg sheet was cut into strips which were rolled to ~50% strain. The samples were then annealed. Further rolling was done as necessary to a final desired thickness. The rolling stages after annealing used stainless steel mirror polished packs to maintain a flat, smooth surface finish. Grain size variations were made in Al+3Mg by varying rolling strain. The average grain size of the Al+3Mg specimens are given in Table 9.

Table 9: Grain sizes for Al+3Mg in microns.

Al+3Mg LG	Al+3Mg IG	Al+3Mg SG
295	44	29

2. *Single Crystal Results*

In this section I describe dynamic results and post-portem findings for the single crystal specimens. Figure 75 shows an interferogram and free surface velocity lineout for 510 μm single crystal Al-HP which exhibited a peak elastic wave speed of 0.04 km/s corresponding to an HEL stress of 3.7 kbar and a spall strength of 36 kbar.

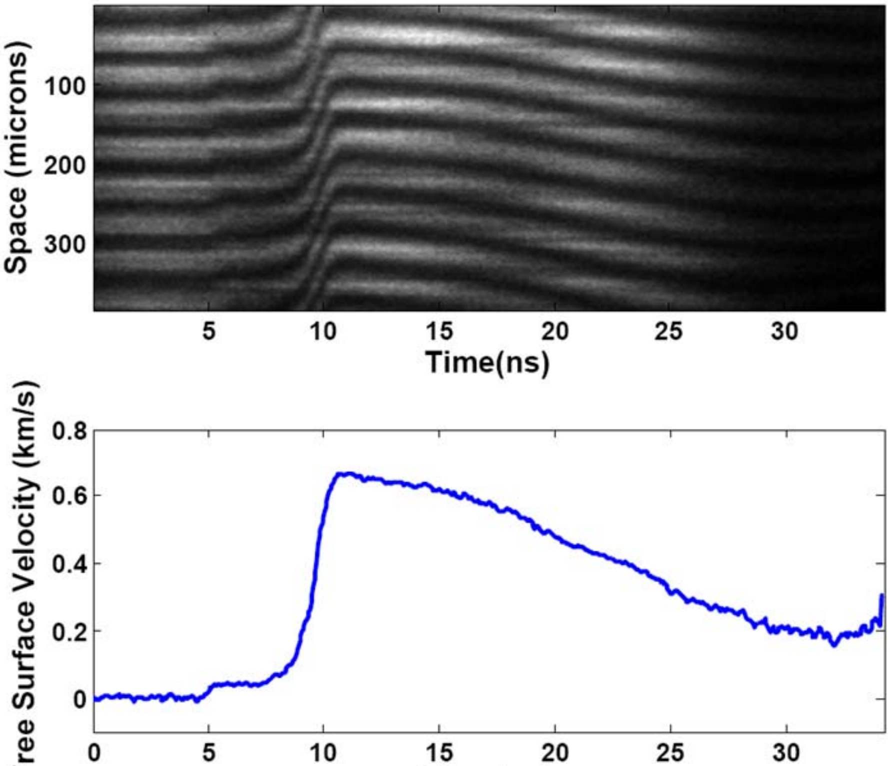

Figure 75: 510 µm single crystal Al-HP impacted at 9x10^{11} W/cm^2 gives a spall strength of 36 kbar with a tensile strain rate of 2x10^6 s^{-1}. The HEL stress is 3.7 kbar.

Table 10 shows a summary of the spall strength, tensile strain rate, HEL stress and dynamic yield stress for the various materials. Both thicknesses of the Al-HP have the same average spall strength of ~35 kbar; however, the Al-1100 has a lower spall strength of ~29 kbar. In contrast the Al-1100 and Al-HP have roughly the same HEL stress.

Table 10: Material, thickness, grain size, laser intensity, tensile strain rate, average spall strength, and failure mode.

Material	Thickness (µm)	Spall Strength (kbar)	Strain Rate (x10^6 s^{-1})	σ_{HEL} (kbar)	Y (kbar)
Al HP	350	35	3.5	1.7	0.8
	500	35	2.6	2.1	1.1
Al 1100	350	29	3.7	1.1	0.6

Figure 76 shows the standard triangle with grain orientations and a key for the specific material specimens. Table 11 shows a summary of the spall strength and HEL stress with grain orientation for the Al-HP and Al-1100. From this data, there are no clear differences in spall strength. The only trend that seems to come from this data is that orientations near the (100) family of directions has the lowest HEL while specimens away from that orientation have a higher HEL stress.

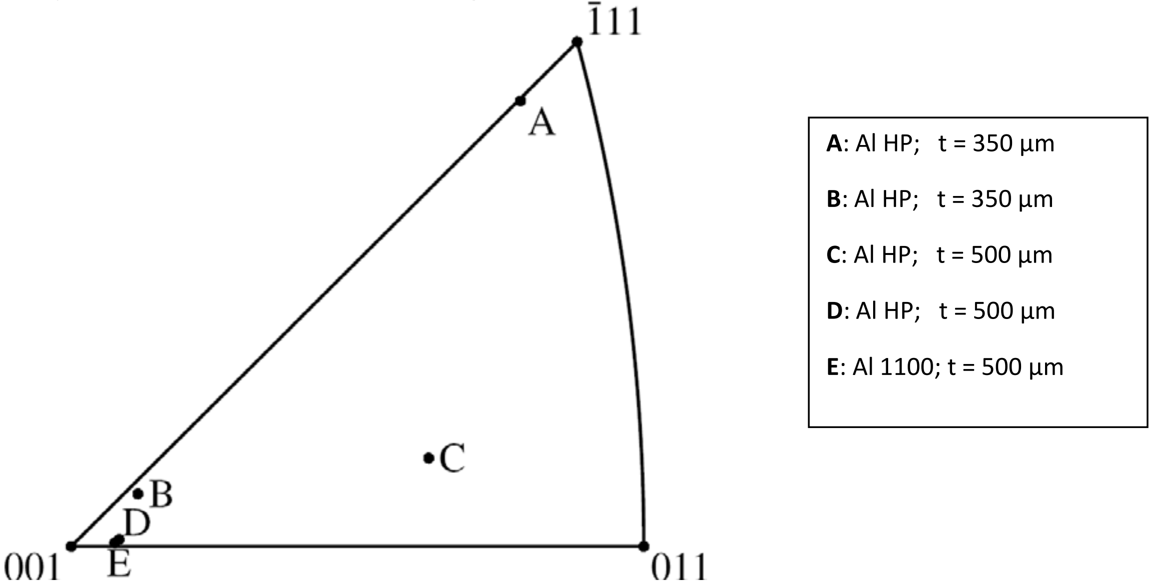

Figure 76: Single crystal orientation for Al-HP and Al-1100. Figure is courtesy of Daniel Worthington.

Table 11: Single crystal orientation with spall strength and HEL stress.

Material	Thickness (μm)	Orientation	P_{sp} (kbar)	σ_{HEL} (kbar)
Al-HP	350	A	36	2.5
	350	B	33	0.5
	500	C	35	3.3
	500	D	36	0.9
Al-1100	350	E	29	1.1

In the fracture analysis, various features from the targets were observed. In the single crystal Al-HP, we observed the presence of ductile dimples (Figure 77a). In the single crystal Al-1100, ductile dimples were also observed; however, at the center of these dimples were iron-rich impurity particles (Figure 77b).

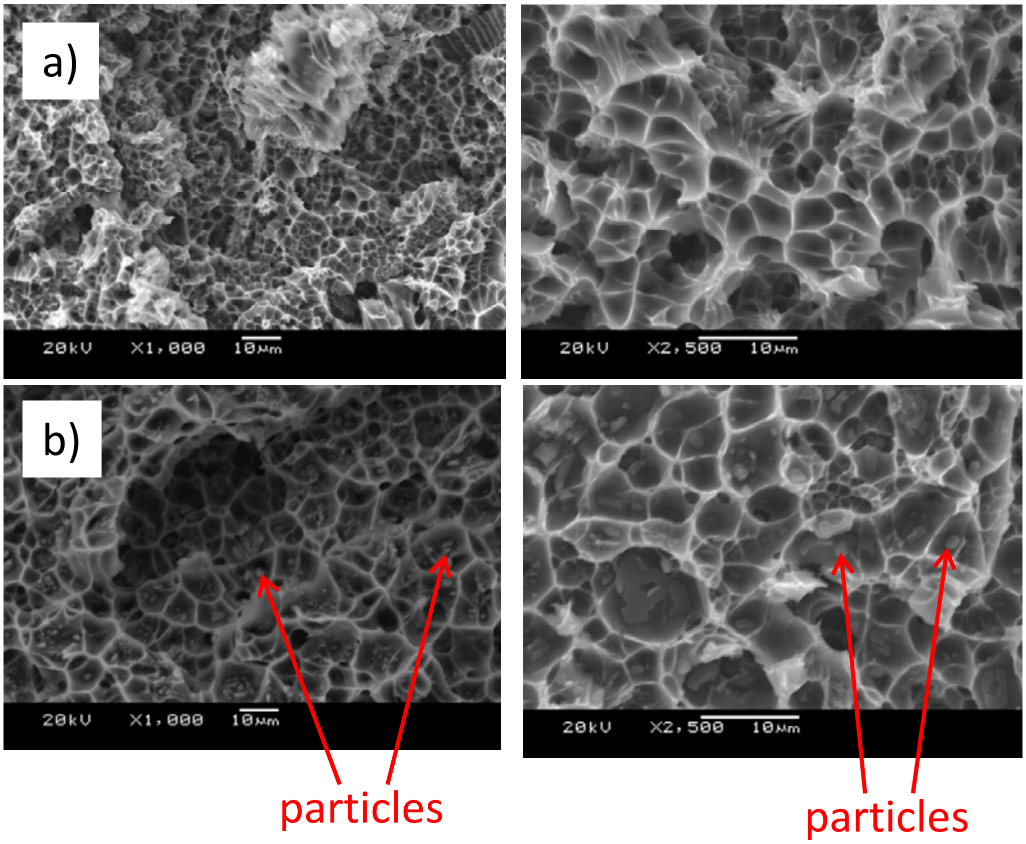

Figure 77: (a) SEM images showing ductile transgranular fracture of high purity, single crystal aluminum. (b) SEM images showing ductile transgranular fracture of Al-1100, single crystal. At the pits of the ductile dimples, iron rich impurity particles are present.

From this figure it is clear that in single crystal Al-1100, microvoid nucleation takes place at iron rich particles. In contrast, for the single crystal Al-HP nucleation does not take place at grains or impurity particles. Figure 78 shows the average particle spacing and average dimple spacing for Al-HP and Al-1100. For the Al-1100, the ratio of average particle spacing to average dimple spacing is ~1, meaning that iron rich impurity particles are likely initiating fracture in this material. For the Al-HP, the ratio of average particle spacing to average dimple spacing is ~8, meaning that impurity particles are not readily available to initiate fracture in materials at these strain rates.

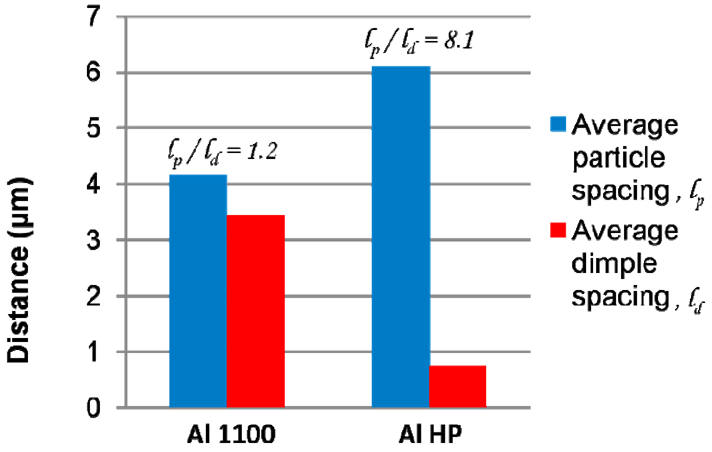

Figure 78: Particle spacing and ductile dimple spacing of Al 1100 and Al HP. The ratio of particle spacing to dimple spacing is ~1 in Al-1100 and ~8 in Al-HP. Figure is courtesy of Daniel Worthington, Nick Pedrazas, and Paul Sherek.

Comparison of the post shot fracture analysis and VISAR results leads to conclude that iron rich particles in Al-1100 yields smaller spall strength; however, these particles do not contribute to any significant compressive yield strengthening.

3. *Al+3Mg Results*

In this section I show VISAR and fracture analysis results for the polycrystalline Al+3Mg. Figure 79 shows a VISAR interferogram and the free surface velocity lineout for 359 µm Al+3Mg Large Grain. It has a peak elastic wave velocity of 0.16 km/s which corresponds to an HEL stress of 14 kbar and a spall strength of 25 kbar.

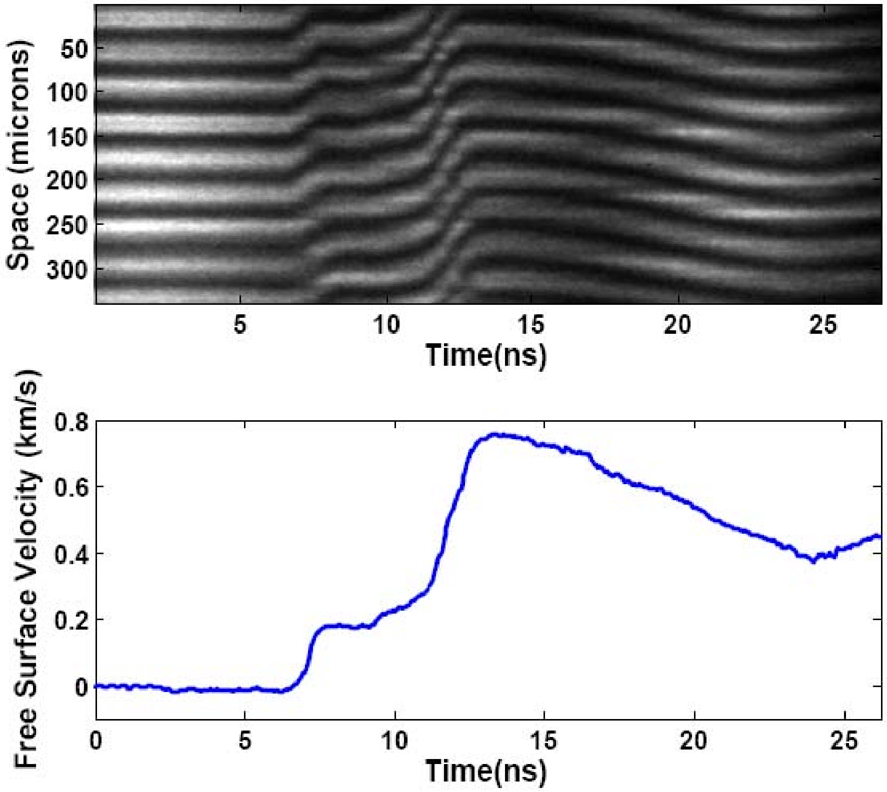

Figure 79: Interferogram and a resulting velocity lineout for 359 µm Al+3Mg Large Grain impacted at $9x10^{11}$ W/cm^2 resulting in a spall strength of 25 kbar and tensile strain rate of $3x10^6$ s^{-1}. The HEL stress was determined to be 14 kbar.

Table 12 shows a summary of results for Al+3Mg. The average spall strength for the various grain sized specimens is ~25-26 kbar. The HEL stress is also about the same for these samples at ~15-18 kbar.

Table 12: Properties of Al+3Mg

Material	Thickness (µm)	Grain Size (µm)	Spall Strength (kbar)	Strain Rate (x10^6 s^{-1})	HEL (kbar)	Y (kbar)
Al-3Mg	350	29	25	3.4	15.5	7.9
	350	44	26	3.2	17.6	8.9
	350	295	26	3.0	14.8	7.5

Two distinct fracture modes were observed in the Al+3Mg. In the large grained material (295 µm), or quasi-single crystal material, the fracture was predominantly transgranular and ductile in nature (Figure 80a). For the small grained material, the fracture was mostly brittle intergranular but with some areas of ductile dimpling (Figure 80b). We have seen much of this evidence before (Section 5.2.3). Also present at the pits of the ductile dimples are iron-rich particles which were not observed before in Section 5.2.3. This observation has a profound effect on our conclusions.

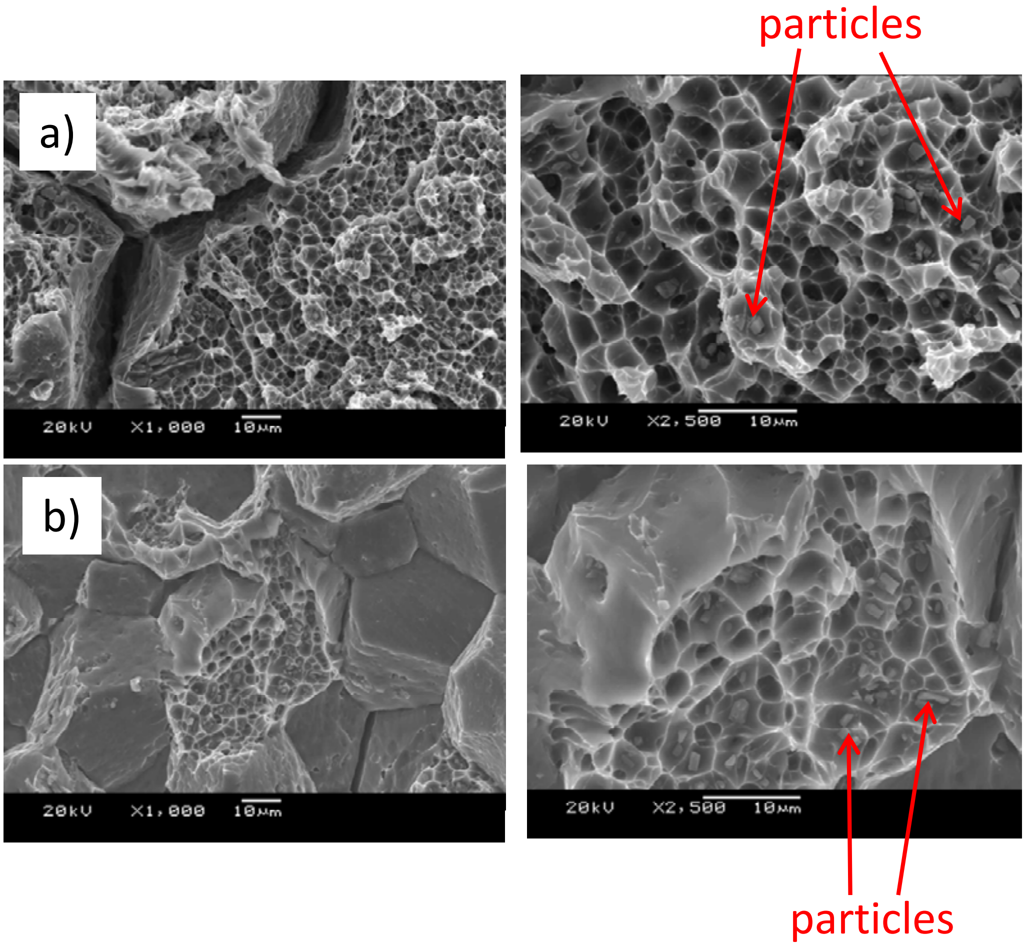

Figure 80: (a) SEM images showing primarily ductile transgranular fracture for coarse-grained Al+3Mg. At the pits of the ductile dimples are iron-rich particles. (b) SEM images showing primarily brittle fracture with islands of ductile transgranular fracture for fine-grained Al+3Mg. At the pits of the ductile dimples are iron-rich particles.

We postulate that in fine grained polycrystalline materials the nucleation sites for spall are initiated at grain boundaries which are the longer length scale imperfections. Secondly, fast fracture is initiated in the grains at particles which are micron scale imperfections. In the quasi-single crystal (coarse-grained) Al+3Mg, the nucleation sites for spall are at secondary particles. Figure 81 shows the area fraction of ductile fracture versus grain size for this study and the studies from Sections 5.2.3 and 5.2.4. This is consistent with our previous results that smaller grains (or slower strain rate) enable more grain boundaries to be available for fracture, resulting in brittle intergranular fracture.

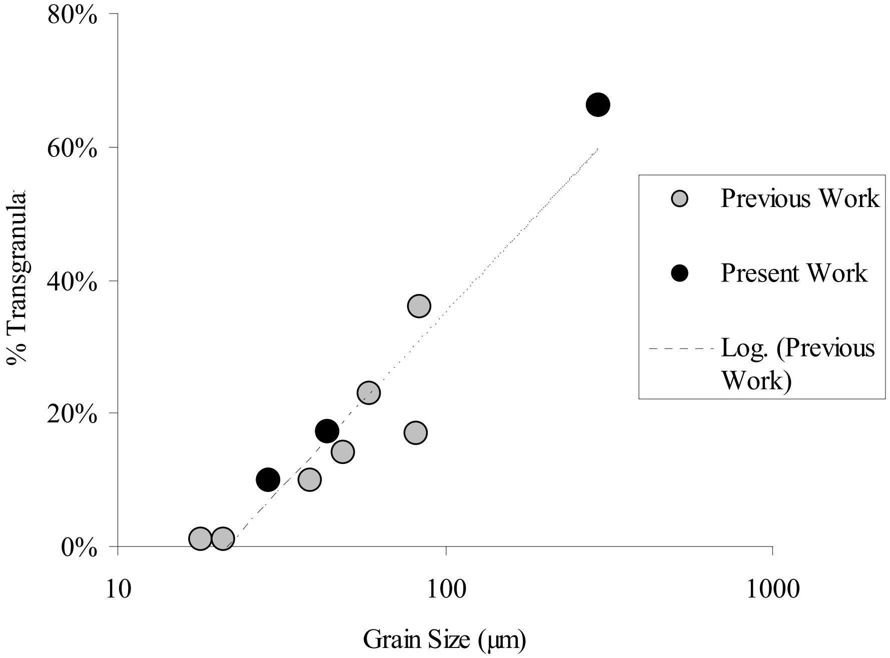

Figure 81: Ductile area fraction versus grain size of Al+3Mg. Figure is courtesy of Daniel Worthington, Nick Pedrazas, and Paul Sherek.

The surprising result in this section is that there is an apparent dependence of fracture mode on grain size, but the spall strength and HEL stress results show no clear dependence with grain size.

4. HYADES Simulation Results

In this section, I discuss how HYADES simulations compare to experiment. HYADES is used to look at the development of the pressure wave profile versus time and to determine the free surface velocity profiles. Figure 82 shows a velocity lineout of 510 μm single crystal Al-HP impacted at $9\text{x}10^{11}$ W/cm^2 which yields a HEL stress of 3.7 kbar and a spall strength of 36 kbar with a tensile strain rate of $2x10^6$ s^{-1}. The von-Mises and Steinberg-Guinan yield models are also included. It is found that lower intensities are needed to approach the measured peak velocities; however, there is some dependence on the peak pressure when the particular yield model is changed. For example in the figure, when using the von-Mises yield model, which is a constant value model, the laser intensity of $6x10^{11}$ W/cm^2 gives a free surface velocity just above the experimental data. In contrast, when using the Steinberg-Guinan yield model, a laser intensity of $7x10^{11}$ W/cm^2 is needed to approach the experimental peak free surface velocity. In using the simple spall model, the von-Mises yield threshold of 33 kbar is closer to the measured data compared to the Steinberg-Guinan model. The spall value of 33 kbar is used in the simulation compared to 36 kbar for the experimental data which is measured using the acoustic approximation. There appears to be good agreement in the level of the HEL stress between the experimental data and the simulations, although the arrival in time of the pulse does not completely match the simulated values.

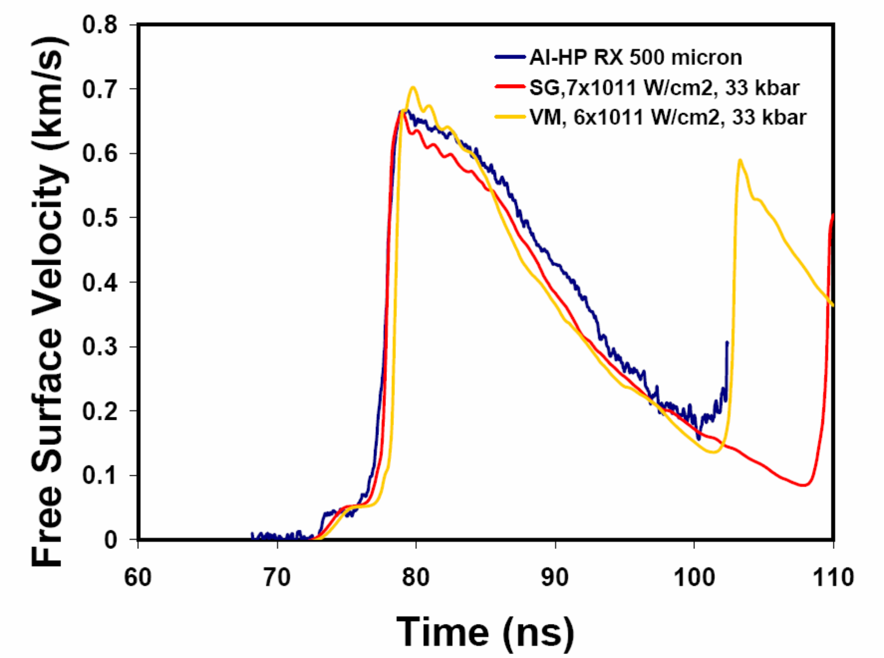

Figure 82: HYADES simulation results showing free surface velocity versus time.

The values used for the Steinberg-Guinan model (Eq. 4.18 and 4.19) are found in Table 13 (Steinberg, Cochran and Guinan 1980).

Table 13: Steinberg-Guinan shear and yield model parameters for Aluminum.

G_0 (GPa)	A (TPa^{-1})	B (kK^{-1})	Y_0 (GPa)	β	ε_0	n	Y_{max} (GPa)
27.6	65	0.62	0.29	125	0	0.10	0.68

Since the Steinberg-Guinan model does not have strain rate dependence we also explored using the Johnson-Cook Model (Eq. 4.22) which does include strain rate dependence. Figure 83 shows the Johnson Cook yield model versus strain for Al. As the strain rate is increased, the level of the flow stress curve increases. Table 14 shows the parameters used for the Johnson-Cook model.

Table 14: Johnson-Cook yield model parameters for aluminum.

Y_0(GPa)	B	n	C	ε_0	D	m
0.152	1.329	0.35	0.015	1.0	0.01	1

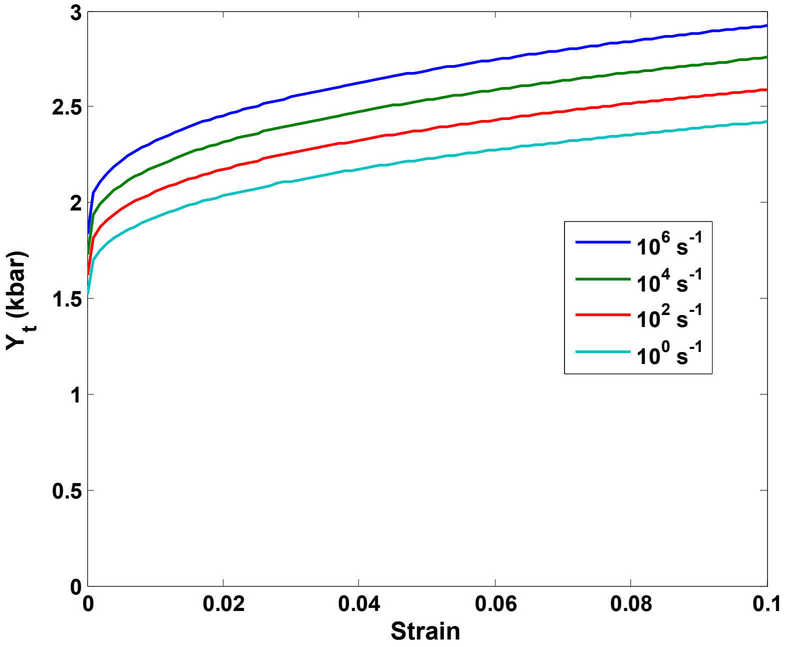

Figure 83: Flow stress of Al for the Johnson Cook model versus strain for several strain rates.

Figure 84 shows the same Al-HP lineout with free surface velocity using the Johnson-Cook yield model. Note that the model underestimates the amplitude of the elastic precursor

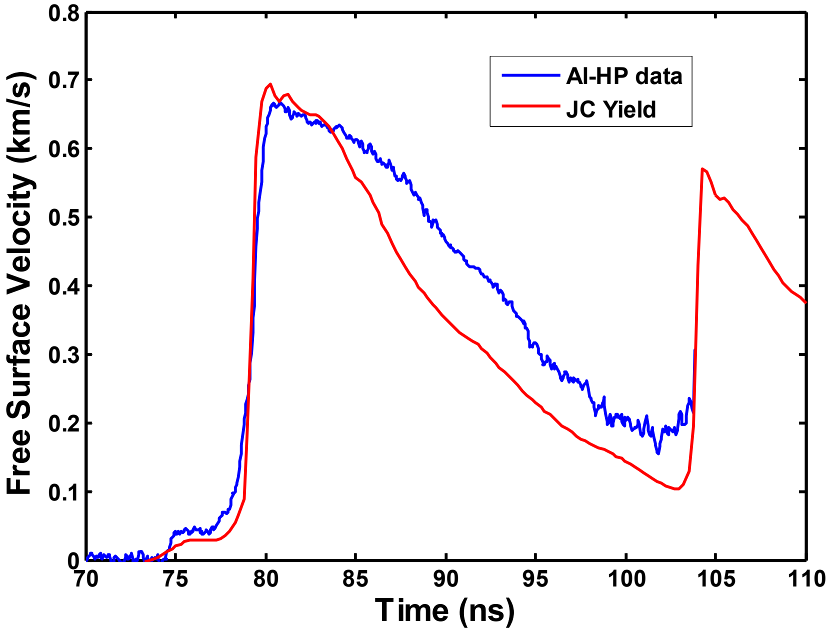

Figure 84: Johnson-Cook Yield Model

In addition to investigating various yield models, we also include a model for spall. Values for the Tuler-Butcher model (Eq. 4.12) for aluminum are given in Table 15. We tested this model for our experimental conditions and found that the parameters (TB1) do not yield spall fracture (Tuler and Butcher 1968). We can find a new set of parameters which do yield spall (TB2) under laser drive conditions (de Resseguier, et al. 1997). Figure 85 shows the Tuler-Butcher model for both sets of parameters. These parameters to not fit our data, but do suggest parameters which help to identify the correct fit parameters (TB3). Notice that the values for K were decreased several orders of magnitude due to strain rate being greatly increased.

Table 15: Tuler-Butcher coefficients

	λ	K ($Pa^{2.02}$ s)	σ_0 (GPa)

TB1	2.02	3.98×10^{11}	1.0
TB2	2.02	3.5×10^{8}	1.6
TB3	2.02	3.5×10^{8}	3.0

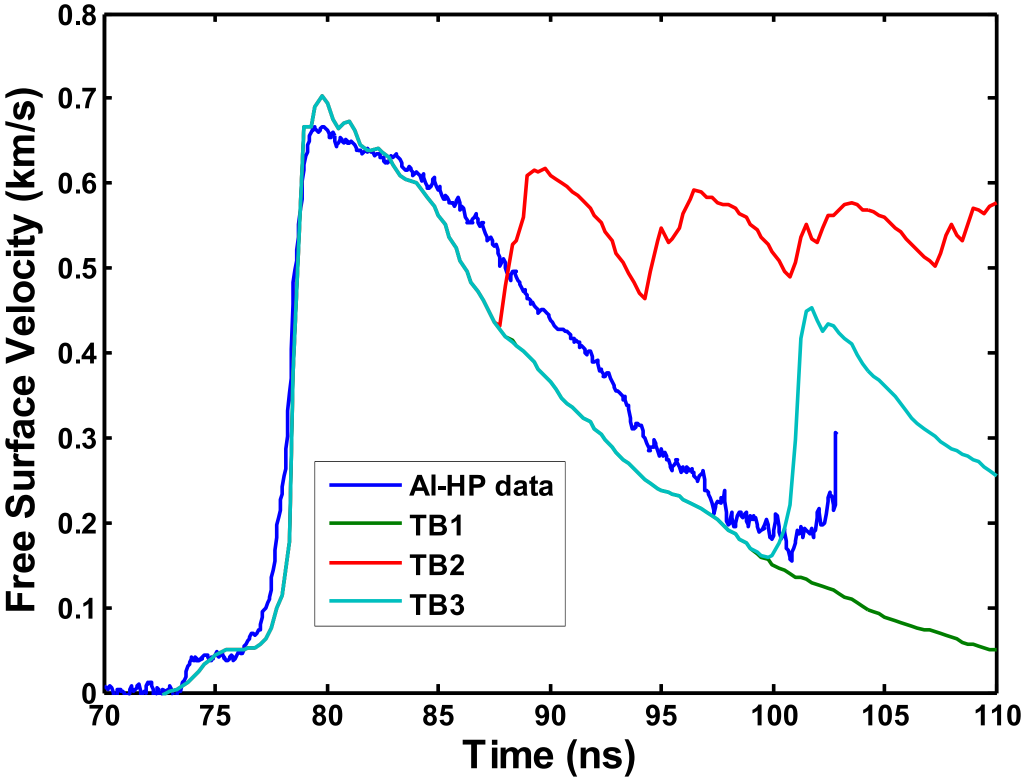

Figure 85: Tuler-Butcher models with data. The values for TB1 do not yield spall, whereas the values for TB2 and TB3 do yield spall.

In conclusion, various yield and spall models were investigated; however, the constant yield and constant spall models seem sufficient for modeling Al-HP in this strain rate regime. The other yield and spall models include various considerations for strain hardening, strain rate, etc. and this section showed that while many input parameters were needed for these models, the fit to data was not significantly better or necessarily predictive.

5. *Acoustic Analysis*

As similar to the analysis performed by Moshe, et al. (Moshe 1998), we decided to perform an acoustic wave analysis using our free surface velocity profiles. By using this simple analysis we could gauge the development of the tensile stress in time and determine the time to spall and spall thickness. The momentum conservation equation in Lagrangian coordinates is given by:

$$\frac{\partial u}{\partial t} + \frac{1}{\rho_0} \frac{\partial P}{\partial h} = 0 \qquad (4.20)$$

The general solution to two waves moving in opposite directions is give as:

$$P(h,t) = f_1\left(\frac{h}{c} + t\right) + f_2\left(\frac{h}{c} - t\right). \qquad (4.21)$$

The boundary condition at the free surface (*h*=0) is that the pressure is zero, which provides the following condition:

$$0 = f_1\left(\frac{h}{c} + t\right) + f_2\left(\frac{h}{c} - t\right). \qquad (4.22)$$

Using the free surface velocity profile, the pressure is then given by:

$$P(h,t) = \frac{-\rho_0 c}{2}\left[u_{fs}\left(\frac{h}{c} + t\right) - u_{fs}\left(\frac{-h}{c} + t\right)\right]. \qquad (4.23)$$

Figure 86a shows the free surface velocity profile for 510 µm single crystal Al-HP impacted at $9\text{x}10^{11}$ W/cm^2 with a 30th order polynomial fit to this data. Figure 86b shows 359 µm Al+3Mg impacted at $9\text{x}10^{11}$ W/cm^2 along with a polynomial fit. The time corresponding to the peak free surface velocity was 6.5 ns for the 500 µm Al-HP and 6.9 ns for the 350 µm Al+3Mg.

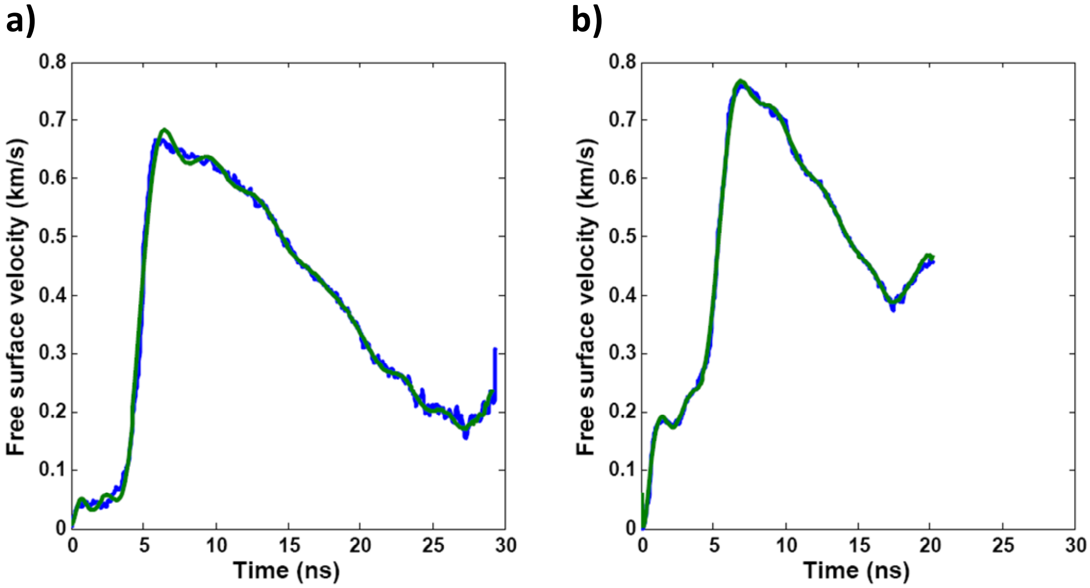

Figure 86: Lineout of free-surface velocity versus time with 30th order polynomial fit.

Figure 87 shows the pressure versus time at the plane of maximum tensile stress which can be used to determine the time to spall. The times coordinating to maximum tensile stress are 16.8 ns and 12.2 ns meaning that the time from peak velocity to fracture initiation onset are 10.3 ns and 5.3 ns.

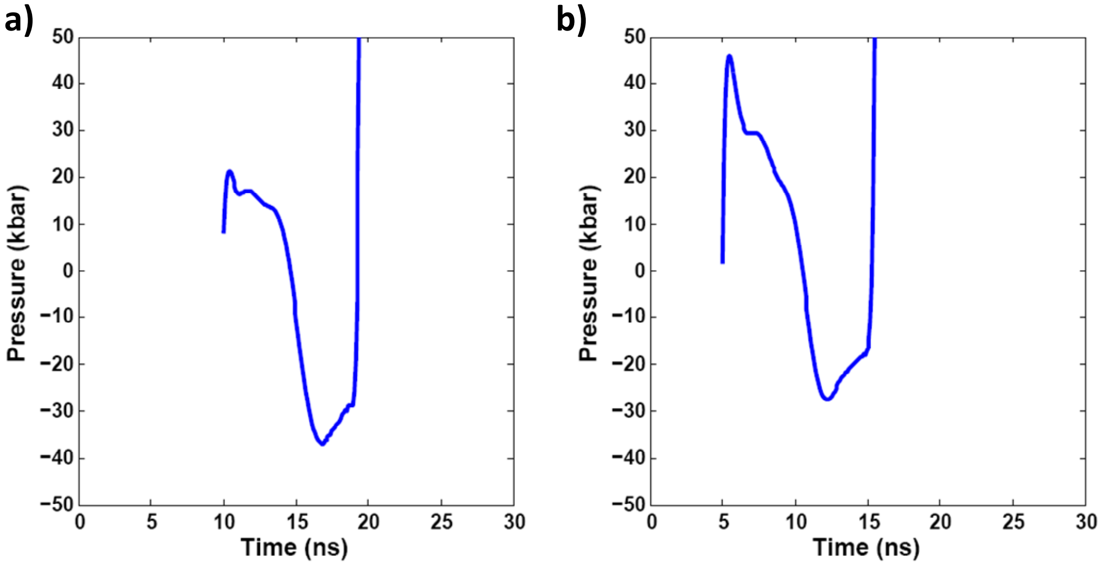

Figure 87: Pressure versus time at the plane of maximum tensile stress.

Figure 88 shows the development of pressure versus Lagrangian coordinate, which is used to determine the location of minimum stress (i.e. spall plane).

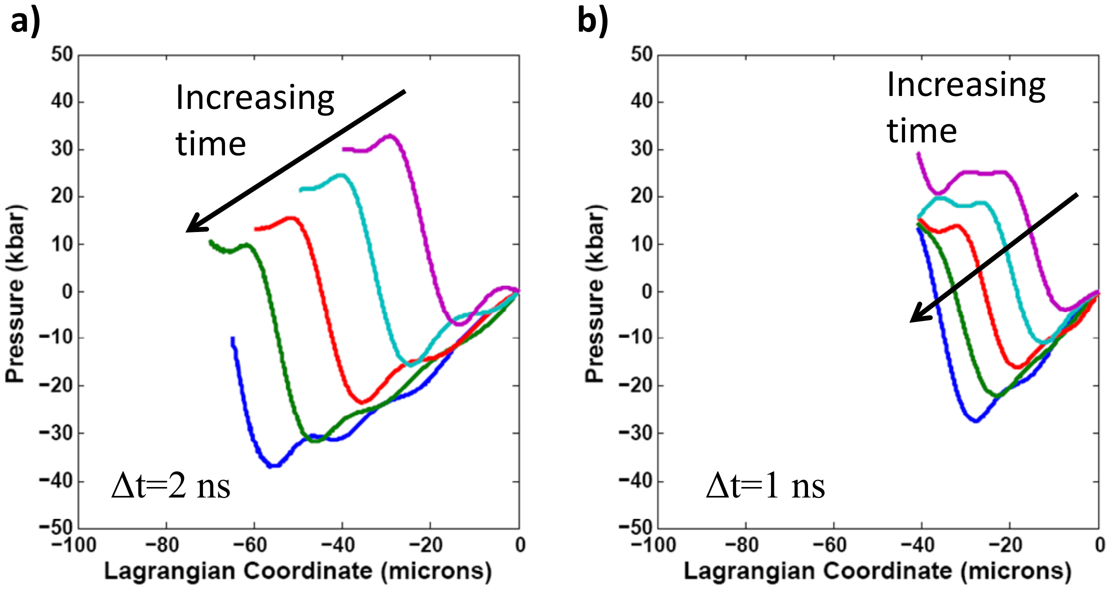

Figure 88: Pressure versus Lagrangian coordinate for various times (2 ns and 1 ns increments respectively) showing the building of tensile stress.

For the 510 μm thick Al-HP RX, the predicted spall thickness is 56 μm and the spall strength is 37 kbar. In a similar manner, we perform the same analysis for 359 μm thick coarse grained Al+3Mg. The predicted spall thickness is 28 μm and the minimum pressure is 27 kbar.

6. *Analysis*

The single crystal Al-HP exhibited the highest spall strength, whereas the single crystal Al-1100 exhibited the second highest spall strength and the Al+3Mg specimens possessed the smallest spall strength. The fracture of the Al-HP was limited by the strength of the crystal. The Al-1100 fracture stress was inititated by iron rich particles. There was no obvious trend in the spall strength data among the different grain sizes of Al+3Mg. The fracture of Al+3Mg was initiated by both impurity particles and grain boundaries.

In general we observed that the Al+3Mg had the highest dynamic yield stress and showed no dependence with grain size. This is likely due to the magnesium atoms within the matrix of aluminum. The size of the magnesium atoms compared to the aluminum atoms likely yielded a stress field which inhibits dislocations from moving through the grains. We did not observe any trend with grain size, which is surprising, considering that smaller grains should inhibit the movement of dislocations. One must keep in mind that yield strengthening due to the grain size effect does not greatly affect aluminum compared to other metals like copper, even at engineering strain rates (Table 1).

In contrast, we saw that the Al-HP RX had a much lower dynamic yield stress. This is likely due to the absence of an alloying element, which allows dislocations to move freely. The Al-1100 showed very little evidence of an elastic precursor and in some cases exhibited no precursor at all. The absence of a precursor in some cases may be due to a slightly higher energy shot.

Figure 89 shows a graph of the spall strength of the various materials versus the Hugoniot Elastic Limit (HEL) stress. The general trend shows that the higher spall strength materials have the lowest HEL stress, while the materials with the highest HEL stress have the lowest spall strength.

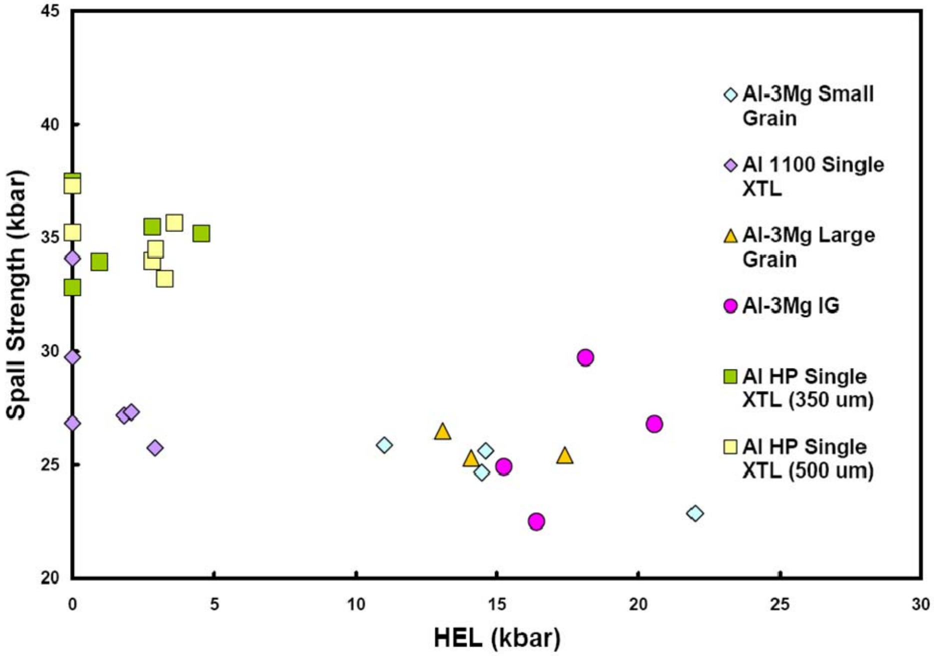

Figure 89: Graph of spall strength versus HEL stress for single crystal Al-HP, single crystal Al-1100, Al+3Mg of 3 grain sizes.

At strain rates of 10^6 to 10^7 s^{-1}, spall fracture is determined by imperfections in the material. The length scales of the imperfections are vital to the type of fracture and to the maximum stress that can be supported in these materials. The low strengthening effect due to grain size is consistent with there being no difference in HEL stress.

The HEL stresses found in these shots were not well defined, meaning the free surface velocities did not come to a sharp peak, decay and then increase again. This is consistent with what G.I. Kanel found previously (G. Kanel, S. Razorenov and K. Baumung, et al. 2001). The authors also determined that when heated to higher temperatures, the HEL stress does become better defined. This is due to the dislocation drag mechanism being increased at higher temperatures.

With respect to single crystal orientation, Chen, et al. reported that single crystal [100] Al had the highest spall strength and that it consistently had 40% higher spall strength than polycrystalline aluminum (Chen, Asay and Dwivedi 2006). The authors also observed an increase in pullback velocity with impact stress. They also saw that pullback signals for polycrystalline Al differs by a large amount at 40 kbar but were similar at 220 kbar. This is in contrast with our finding that the Al orientation has no strong preference in spall strength.

5.2.6 Fast Strain Rate Spall experiments on THOR

In order to investigate the dependence of the Al fracture stress at faster strain strain rates we needed to look at thinner target specimens and shorter drive pulses. We performed experiments on the THOR laser using a 600 ps chirped pulse. There were a variety of foils used: 50 μm Al, 10 μm Al and 10 μm copper. We designed and implemented a VISAR similar to that discussed in Section 4.2.2. The velocity-per-fringe constant in these experiments was 0.496 km/s/fringe. Figure 90 shows a VISAR interferogram and resulting free surface velocity temporal profile for 10 μm thick copper.

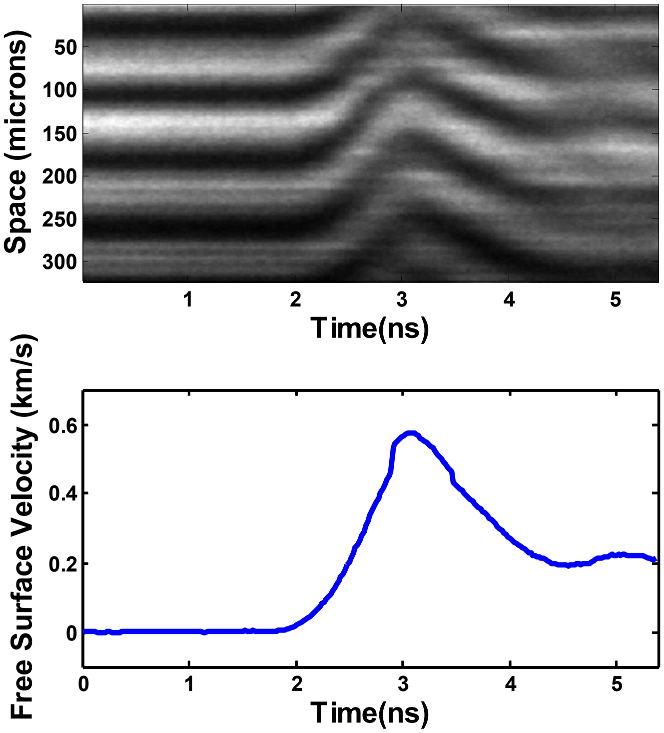

Figure 90: Fast rate fracture of Copper.

Table 16 shows the average spall strength and strain rate for various thicknesses of aluminum and copper.

Table 16: Ultrafast fracture of Copper and aluminum

Material	Spall Strength (kbar)	Strain Rate (x10^7 s^{-1})
Al 50 µm	40±2	2.3±0.9
Al 10 µm	35± 3	2.2±1.3
Cu	66±5	3.4±0.2

The spall strengths for the Al specimens are no higher than what we have measured before in the Sandia experiments. Although these specimens are prepared in a different manner, these experiments do not suggest an increase in spall strength with strain rate for aluminum. However if the data is compared to that of Moshe, et al. it actually follows better with their data for both Al and Cu (Moshe, Eliezer and Henis, et al. 2000).

5.3 SUMMARY

In this chapter results for shock induced melt and fast rate fracture were discussed. The melt experiments of aluminum on LiF showed evidence of melt via higher particle velocities and loss of reflectivity. Preliminary spall experiments on aluminum motivated our need for a pulse stacker. The pulse stacker that we developed was well suited for use as a long pulse VISAR probe.

Primary findings of the spall experiments note that grain size and strain rate were factors that played an important role in the fracture mode observed and in the spall strength results. This was best evidenced by the transition from brittle intergranular fracture to ductile transgranular fracture in Al+3Mg. Follow-up experiments on single crystal specimens showed that iron rich impurity particles significantly lowered the maximum tensile stress of Al-1100, but did not affect the compressive yielding of the material. A grain size study of Al+3Mg specimens showed that while grain size along with impurity particles certainly played a role in the fracture mode, there was no evidence of a grain size dependence on spall strength or HEL stress. The high HEL stress exhibited by Al+3Mg was likely initiated by magnesium impurity atoms.

Spall experiments on THOR showed that the spall strength in aluminum is very comparable to the values that we have previously measured using thicker specimens on ZBL and thus exhibits no appreciable increase with strain rate up to strain rates of $\sim 2 \times 10^7$ s^{-1}.

CHAPTER 6. SHOCKED SILICON EXPERIMENTS ON THOR

In his dissertation, Will Grigsby presented preliminary evidence for a drop in third harmonic generation (THG) signal of a probe beam on the rear surface in silicon shocked to pressures above the elastic limit (Grigsby 2007). However, it is not well understood why this decrease in third harmonic signal occurs. In order to investigate these results further, we added linear reflectivity as a diagnostic for comparison with third harmonic generation.

6.1 INTRODUCTION AND MOTIVATION

Silicon is known to possess a very complicated phase diagram, with many solid phases. Several groups have used diamond anvil cells to generate high pressures and x-ray diffraction to investigate the various phases of silicon (Duclos, Vohra and Ruoff 1987), (Crain, et al. 1994). These polymorphs have different crystalline and electronic properties. Additionally, various groups have measured absorption coeffections via transmission experiments over various wavelengths and elevated temperatures (Weaklien and Redfield 1979). Grigsby showed preliminary evidence (Figure 91) of no drop in third harmonic signal at shock pressures < 100 kbar, below the Hugoniot elastic limit (HEL); however, at higher pressures (>HEL) the third harmonic signal fell dramatically, indicating fast crystalline disordering (Grigsby 2007).

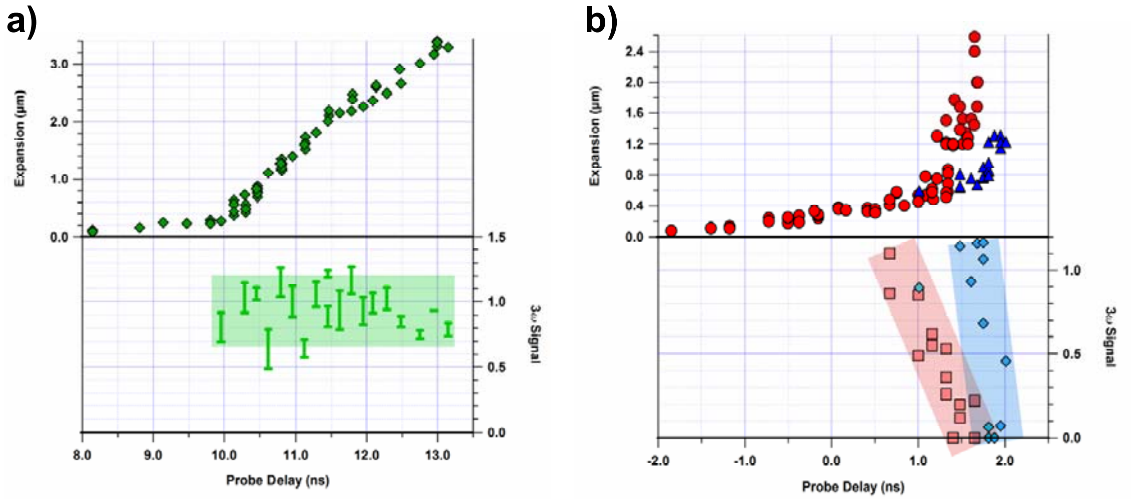

Figure 91: Peak expansion and third harmonic signal versus probe delay for shock pressures of (a) 100 kbar and (b) 300 kbar (Grigsby 2007).

In order to diagnose the cause in THG drop we used several diagnostics. Using short pulse 2D interferometry, we were able to determine the elastic and plastic wave velocities, and therefore the associated pressures. We also measured time resolved linear reflectivity at 800 nm and third harmonic generation at 266 nm. Unexpectedly, in contrast to Grigsby's results, we observed decay of the linear reflectivity upon shock breakout, while third harmonic generation remained roughly constant. This result suggests that the silicon remains crystalline, yet the drop in linear reflectivity indicates a change in electronic structure.

6.2 EXPERIMENTAL SETUP

We use both linear and nonlinear optical diagnostics to probe the material dynamics of shocked silicon. Pump-probe shock experiments on [100] orientation Si crystals were carried out using the Ti:Sapphire, chirped pulse amplified THOR laser (800 nm, 1 J, 600 ps-chirped pump, 40 fs-compressed probe). After amplification the beam is split sending 90% of the energy into the pump arm and 10% of the energy to the probe arm. Both beams are spatially filtered and the probe arm is then temporally compressed to 40 fs using a single grating compressor. The pump beam energy delivered to the chamber is typically 550-600 mJ and remains chirped at 600 ps. Two-dimensional interferometry was used to map the temporal history of the rear surface displacement in order to infer a peak shock pressure. Third harmonic generation is used to probe the bulk material's long range order, while a linear reflectivity diagnostic is used in conjunction with the THG diagnostic to determine its validity.

The target specimens were made from silicon-on-insulator (SOI) wafers. This material consists of three parts: device, oxide, and handle. The device is the part of the material that is used for the shock experiments and is 20 μm thick. The oxide layer is the thinnest layer and typically only a few microns thick. The handle is the thickest part of the wafer. In preparing the target specimens, the handle and oxide layers are etched away, leaving only the device. Upon etching the appropriate number of targets per wafer, the wafers are coated with 1000 angstroms of Al. The Al layer serves as an absorbing layer for the silicon. By ablating the aluminum layer a shock is formed and transmitted into the silicon.

6.2.1 2D Interferometer

Two-dimensional interferometry was used to measure the displacement of [100] silicon at discrete time intervals. The interferograms are analyzed by selecting a range of interest. A one-dimensional lineout is taken and Fourier transformed. A filter is applied to the Fourier transform to select only the positive frequencies. The inverse Fourier transform is then taken. The wrapped phase is calculated and a 2D phase unwrapping algorithm is applied to determine the phase map. The phase map is then converted to a displacement map. The displacement is determined from the unwrapped phase $\varphi(x,y)$,

$$d = \frac{\lambda \cdot \phi(x, y)}{4\pi n \cdot \cos(\theta)} \tag{6.1}$$

where λ is laser wavelength (800 nm), n is the index of refraction and θ is the angle of incidence (60 degrees). Figure 92 shows an example interferogram and corresponding phase map. For each probe delay, 5-7 shots were taken and we then plotted maximum displacement. Additional fringe shifts were added in the analysis when fringes appeared as a discontinuity. The analysis is very similar to that performed for the VISAR interferograms, which is included in Appendix D.

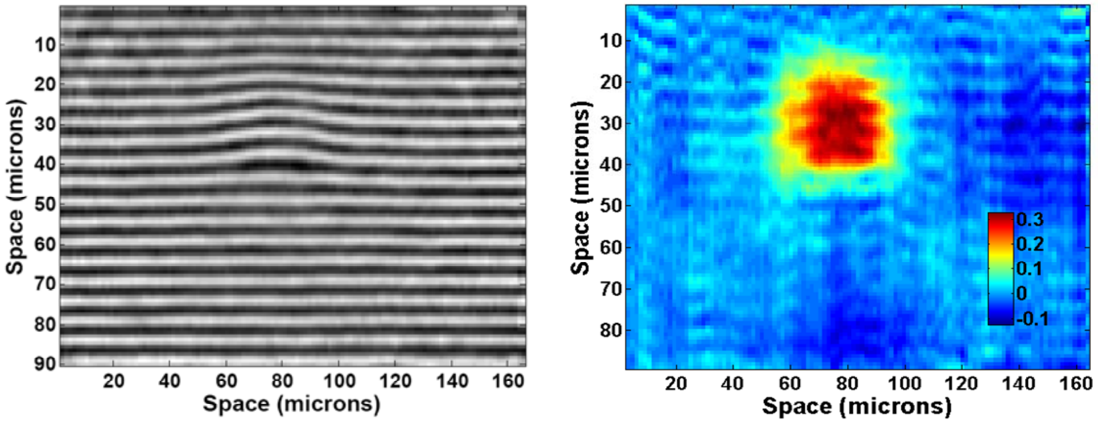

Figure 92: Raw displacement interferogram and phase map for shocked silicon.

6.2.2 Linear Reflectivity

By measuring surface reflectivity we expect to gain insight into the electronic structure of silicon at high pressures. Following the derivation of Adachi ((Adachi 1989) (Adachi 1988)), the dielectric function can be derived from the band structure of silicon shown in Figure 93.

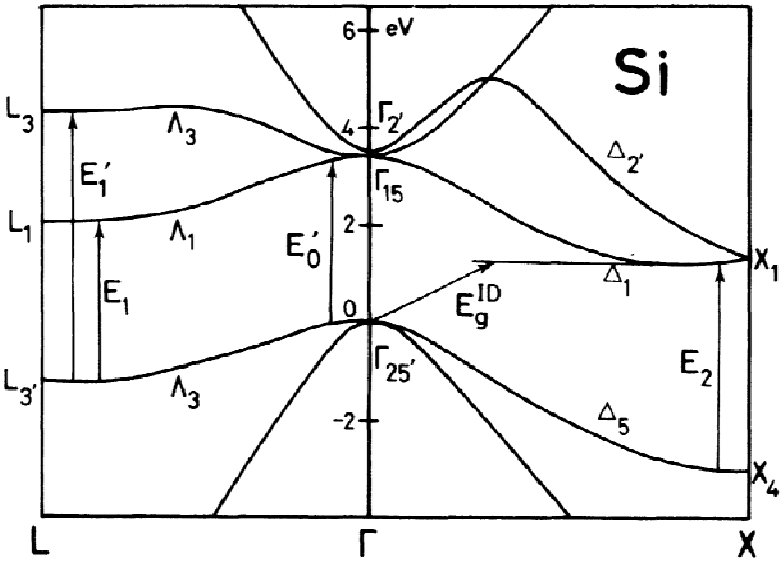

Figure 93: Energy band structure of silicon (Adachi 1988). Reprinted figure with permission from Adachi, S. "Model Dielectric Constants of Si and Ge", Physical Review B, 38, (1988): 12966. Copyright 1988 by the American Physical Society. http://prola.aps.org/abstract/PRB/v38/i18/p12966_1

The complex index of refraction, $\tilde{n}(\omega)$, is related to the dielectric function, $\varepsilon(\omega)$, by

$$\tilde{n}(\omega) = n(\omega) + ik(\omega) = \varepsilon(\omega)^{1/2}, \tag{6.2}$$

where n and k are the real and imaginary parts of the refractive index respectively. These quantities can be calculated from the dielectric function:

$$n = \sqrt{\frac{\sqrt{\varepsilon_1{}^2 + \varepsilon_2{}^2} + \varepsilon_1}{2}} \qquad k = \sqrt{\frac{\sqrt{\varepsilon_1{}^2 + \varepsilon_2{}^2} - \varepsilon_1}{2}} \tag{6.3}$$

where ε_1 and ε_2 are the real and imaginary parts of the dielectric function. Figure 94a shows the calculated real and imaginary indices of refraction versus wavelength for cold silicon. The reflectivity, R, for normal angle of incidence is given by

$$R = \frac{(\varepsilon_1 + \varepsilon_2)^{1/2} - \left[2\varepsilon_1 + 2(\varepsilon_1{}^2 + \varepsilon_2{}^2)^{1/2}\right]^{1/2} + 1}{(\varepsilon_1 + \varepsilon_2)^{1/2} + \left[2\varepsilon_1 + 2(\varepsilon_1{}^2 + \varepsilon_2{}^2)^{1/2}\right]^{1/2} + 1}. \tag{6.4}$$

Figure 94b shows the absolute reflectivity versus wavelength for cold silicon, which at 800 nm is ~ 0.3.

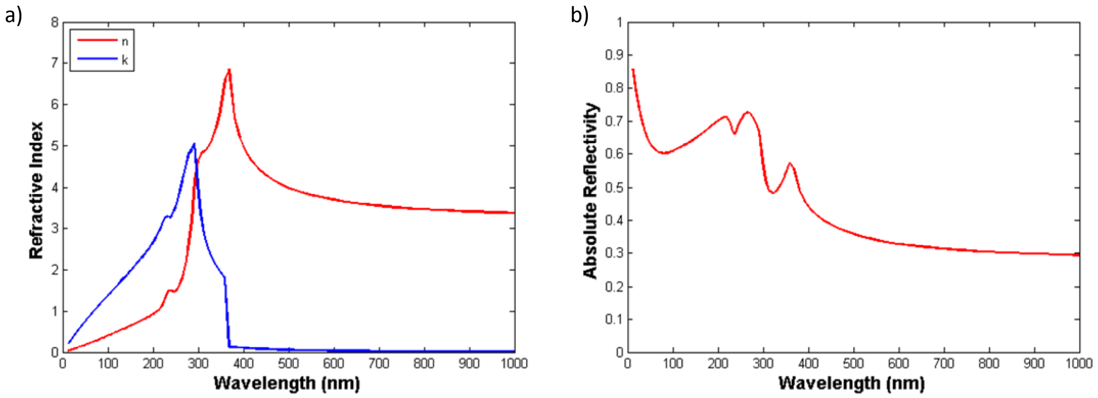

Figure 94: (a) Real and imaginary indices of refraction versus wavelength for cold silicon. (b) Reflectivity versus wavelength for cold silicon.

In contrast to the cold silicon calculations we also wanted to determine how reflectivity would be affected by the shock. We first assume the case treating silicon as a metal. The Drude model describes a material that is dominated by free carriers. The equation for the dielectric function in a free carrier model is given by:

$$\varepsilon(\omega) = 1 - \frac{\omega_p{}^2\tau^2}{1+\omega^2\tau^2} + i\frac{\omega_p{}^2\tau}{\omega\left(1+\omega^2\tau^2\right)} = \varepsilon_1 + i\varepsilon_2 \tag{6.5}$$

Where the plasma frequency, ω_p, or free electron resonant frequency is given by:

$$\omega_p = \sqrt{\frac{N_{e,h}e^2}{\varepsilon_0 m_e}}, \tag{6.6}$$

where $N_{e,h}$ is the number density of free carriers, m_e is electron mass, e is charge, and ε_0 is free space permittivity and τ is the collision time. Using previously published values for τ=212 fs and $\omega_p = 2.523\text{x}10^{16}$ s^{-1}. One can calculate the real and imaginary parts of the index of refraction, as in Eq. 6.3 (Li and Fauchet 1987). Figure 95a shows the real and imaginary indices of refraction for silicon representred by a Drude model. Figure 95b shows the reflectivity for silicon as a Drude metal as a function of wavelength.

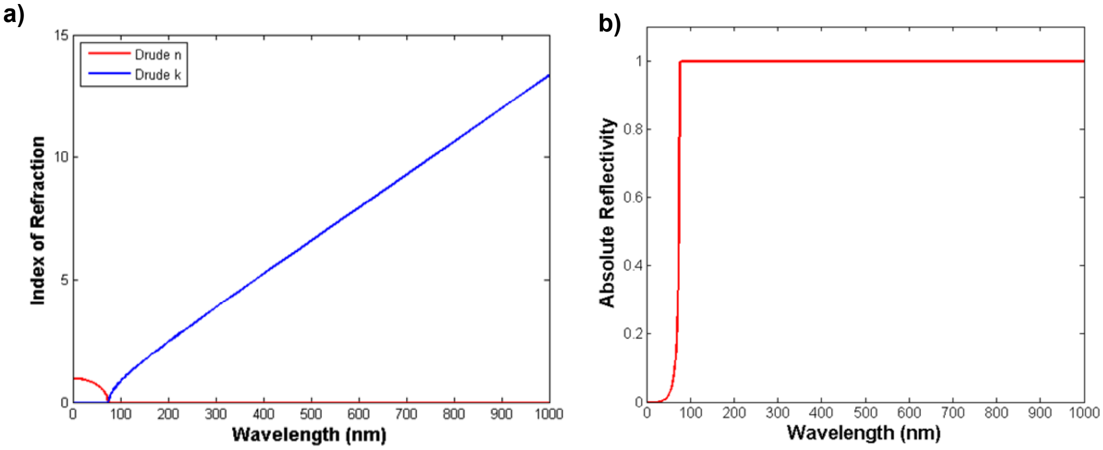

Figure 95: (a) The real and imaginary parts of the index of refraction plotted versus wavelength for a Drude model of Si. (b) Reflectivity versus wavelength for silicon as a Drude metal.

We have presented the cold Si electronic model along with a Drude metal model to determine what we might expect from Si when shocked to higher pressures. Comparing Figure 94b and Figure 95b at 800 nm, one would expect the reflectivity to increase by a factor of ~3.

6.2.3 Harmonic Generation

Third Harmonic Generation (THG) was measured to determine whether the silicon specimen remained crystalline at higher shock pressures. Assuming a cubic crystal with point group symmetry of 432, (-4)3m or m3m (i.e. [100] Si), the third order susceptibility tensor has only two independent elements. For such a crystal, the nonlinear third harmonic polarization components are given by:

$$P_i = 3C_{1122}E_i\left(\vec{E}\cdot\vec{E}\right) + \left(C_{1111} - 3C_{1122}\right)E_i^{\,3}, \qquad (6.7)$$

where $\vec{E}$ is the electric field and i refers to the cubic axes (Burns and Bloembergen 1971). In order to use third harmonic as a potential probe one must consider a circularly polarized field:

$$\vec{E} = E_0\hat{x} + iE_0\hat{y}, \qquad (6.8)$$

where E_0 is the field amplitude. The portion of the first term of the polarization $\vec{E} \cdot \vec{E}$ in Eq. 6.7 disappears, as shown:

$$\vec{E} \cdot \vec{E} = \left(E_0 \hat{x} + iE_0 \hat{y}\right) \cdot \left(E_0 \hat{x} + iE_0 \hat{y}\right) = E_0{}^2 - E_0{}^2 = 0\,. \tag{6.9}$$

For the case of an isotropic material (i.e. melted), the relationship between the elements of the susceptibility tensor is:

$$C_{1111} = 3C_{1122}\,. \tag{6.10}$$

So in the case of a melted material, third harmonic polarization is not allowed. However, for the case of an anisotropic material the susceptibility tensor elements have the relationship:

$$C_{1111} \neq 3C_{1122}\,. \tag{6.11}$$

So the third harmonic polarization simplifies to only the second term in the third harmonic polarization (Eq. 6.7). Using this formulation, it is reasonable to pursue THG as a probe for the dynamics of crystalline disordering. Silicon was chosen as a material of interest since it is a good source THG (Burns and Bloembergen 1971).

6.3 RESULTS

The maximum displacement versus time is shown in Figure 96. It is evident that there are two different regions of interest. The slope of displacement versus time gives the free surface velocity. The smaller slope results in a free surface velocity that coordinates with the elastic response of the material. The sharper slope gives a free surface velocity which coordinates with the plastic wave. Using the equation of state for silicon, we determined the pressures that correspond to elastic and plastic waves (Goto, Sato and Syono 1982), (Gust and Royce 1971). The free surface velocity of the elastic wave is ~0.3 km/s and corresponds to a pressure of ~50 kbar. The free surface velocity of the plastic wave is ~3.4 km/s and corresponds to a pressure of ~250 kbar.

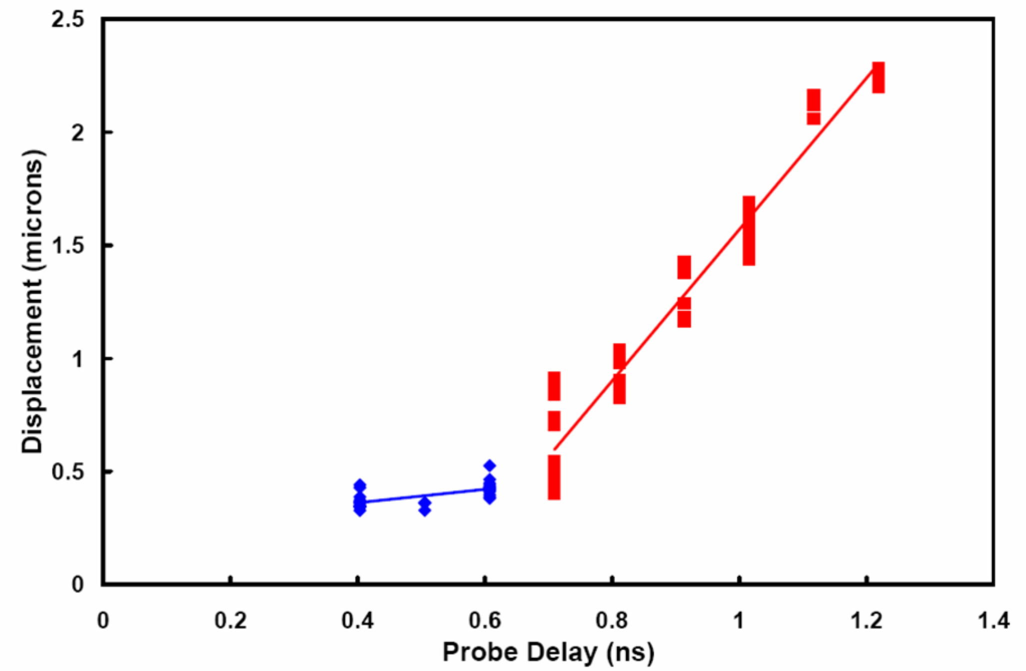

Figure 96: Displacement versus probe delay for (100) silicon shocked at 2x10^{14} W/cm^{2}. The blue data points cover the elastic wave and the red data points cover the plastic or shock wave. The pressure of the plastic wave is 250 kbar.

Figure 97 shows the linear reflectivity and third harmonic signals for the reference (before shot), shot, fit to shot data, and the blackbody emission signals. Blackbody emission is a concern at higher temperatures. One way that we alleviated this issue is by placing a black mask between the target and collection optic. Five shots were averaged for each probe delay. An additional two shots at each probe delay were used to determine the blackbody emission of the shocked material.

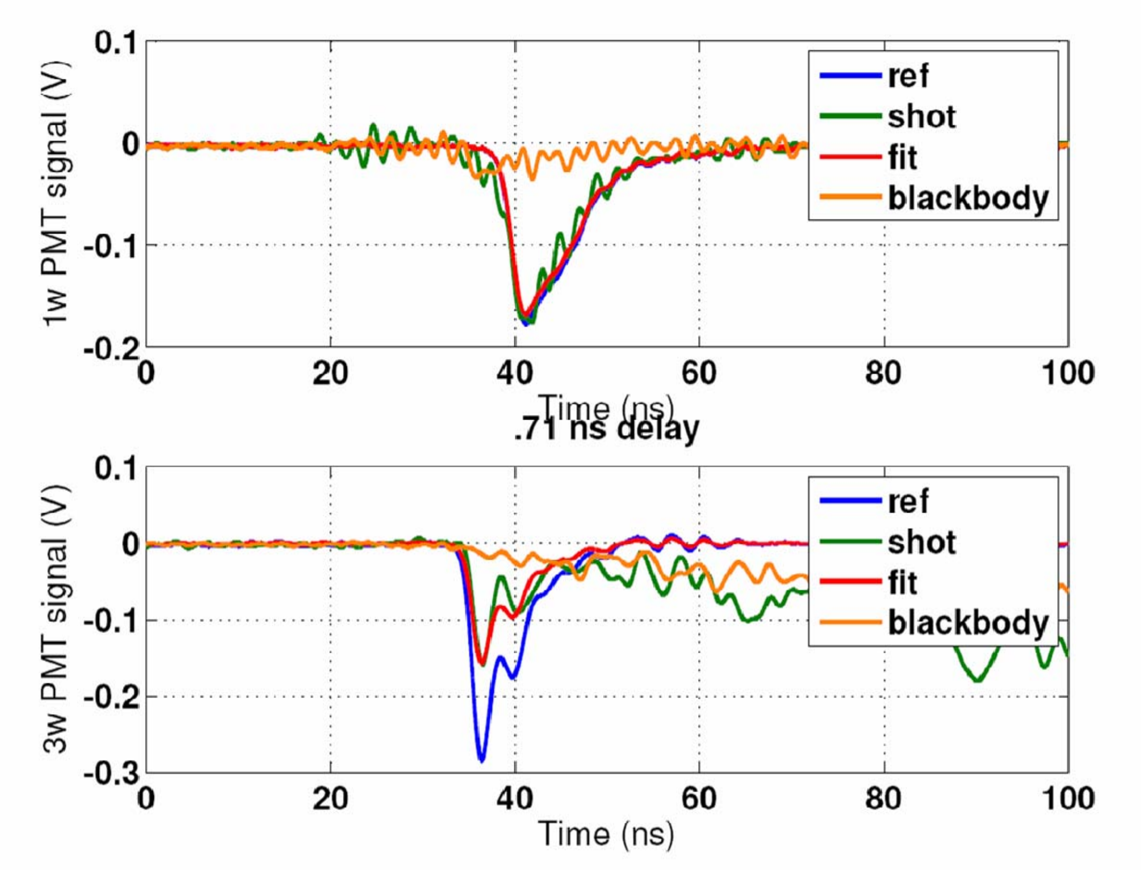

Figure 97: Reflectivity and third harmonic data from PMT signals for a 0.71 ns delay after the pump..

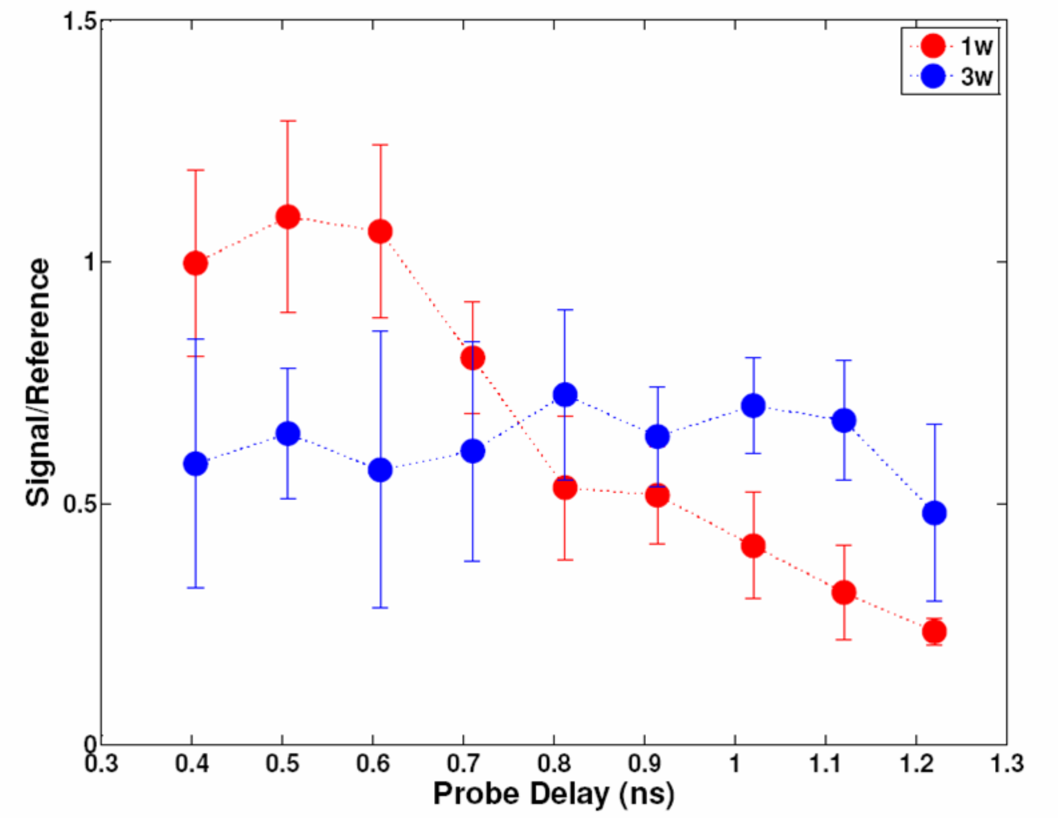

Figure 98: Ratio of signal to reference versus probe delay for linear reflectivity and third harmonic.

Figure 98 shows normalized signal versus probe delay. At probe delay times of ~0.7-0.8 ns there is a sudden drop in linear reflectivity; however, there is no observed change in third harmonic signal. Previous fine scans in probe delay showed trends that appeared to show a preliminary drop in third harmonic generation; however, by using multiple shots at a single time delay the third harmonic generation drop is clearly not evident. These results appear to contradict previous results of Grigsby (Grigsby 2007). It also seems relevant to point out that some 800 nm light (reflectivity) shows up on the interferometer camera at slightly later delays of 1.4 ns which is well after the initial sharp drop in reflectivity.

6.4 DISCUSSION

Using third harmonic generation as a probe allows us to shock materials to high pressures and observe their ability or inability to maintain crystalline order. One would expect a significant decrease in third harmonic signal due to crystal melting; however, our pressure regime is well below this threshold, but higher than the elastic limit. One potential reason for the sharp reflectivity decline is light scattering out of the collection cone of the optics; however, if this were the case one would also expect a significant decrease in the collected THG signal. We also wondered if THG was artificially enhanced by blackbody emission; however, we discount this hypothesis as the most significant cause since we went through great pains to alleviate any of these effects.

In order to understand these results one must consider previous work. Gilev, et al. measured time resolved electrical conductivity of single crystal silicon to shock pressures of 230 kbar (Gilev and Trubachev 2004). Figure 99 shows the electrical conductivity of silicon versus stress.

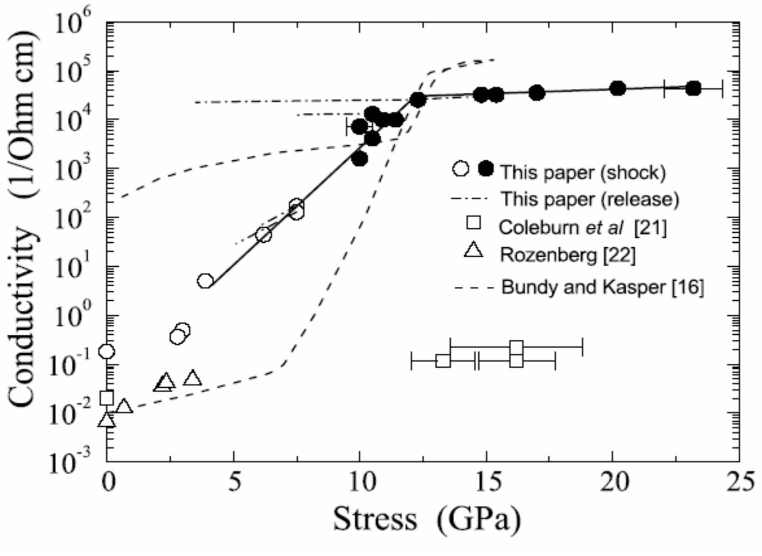

Figure 99: Electrical conductivity versus stress. Reprinted figure from Gilev, S.D., and A.M. Trubachev. "Metallization of silicon in a shock wave: the metallization threshold and ultrahigh defect densities." ***Journal of Physics: Condensed Matter*** **16 (2004): 8139. Copyright (2004) by Institute of Physics.**

The conductivity increased 5 orders of magnitude and then plateaus. From the Fresnel equations, the linear reflectivity is determined from the electrical conductivity of the material. From this data, one would expect an increase in linear reflectivity signal or at least no change in reflectivity, as suggested by the points of low conductivity at high stress (at 15 GPa). This type of expected change would signify a change in the electronic band structure of silicon.

Another reason for the drop in linear reflectivity is that 800 nm light was absorbed since silicon had been shock heated by at least 200 K. Previous literature does not support a drop in reflectivity or hence conductivity. There is overwhelming support that at elevated pressures the reflectivity/conductivity increases due to the more metallic response of silicon. Mintsev et al. has shown that when shocked to high pressures, the reflectivity of 1.06 μm light increases (Mintsev, Zaporoghets and Fortov 1990). The authors stated that the reflectivity of Si remains at ~30% up to pressures of 100 kbar. At pressures of ~150 to 180 kbar the reflectivity increases to the value of ~80%. The authors concluded that this increase in reflectivity puts silicon into a metallic state.

We also looked at static transmission studies of silicon at elevated temperatures. Weaklien reported the absorption coefficient versus photon energy (1.1-2.7 eV) at various temperatures (Weaklien and Redfield 1979). At 1.55 eV (800 nm), as the temperature is increased, the absorption coefficient increases from $\sim 9\times10^{2}$ cm^{-1} at 298 K to $\sim 2\times10^{3}$ cm^{-1} at 473 K. An increasing absorption coefficient certainly suggests a change in reflectivity.

There are various ways in which this experiment can be improved. We have recently designed and implemented a line-VISAR, which allows single shot determination of free surface velocity and the corresponding pressure. Another experimental idea for shocked silicon is to used a CW bright white light source and observe the time resolved absorption at 800 nm. This would involve using a spectrometer coupled to a fast streak camera. Reflectivity could then be performed at two or three wavelengths using a spectrometer coupled to a streak camera.

Germanium has a lower melting point than silicon. One idea is that we could try to look at shock melting germanium, however, there is a real shortage of high pressure shock data for both silicon and germanium. Another idea is that we could look at heating silicon or germanium to a high temperature without melting (via resistive heating or CW laser heating) and then induce the melt phase transition by a shock. It is important to note that third harmonic generation has been used to study femtosecond laser melting of silicon (Gundrum, Averback and Cahill 2007).

Additionally, developing an experiment where 1D shock drive is possible would be more convincing. First if we use a 3-5 times bigger spot, we would create a 1D problem. Currently the geometry is 1:1. Secondly, a higher energy laser, such as Z-Beamlet, would make it possible to create greater pressures. At Z-Beamlet, we have access to 1.2 kJ energy, 1.8 ns temporal width, and could tighten to a spot of 100 μm to give average intensity of 6.7×10^{15} W/cm^2.

Another method that may help alleviate the effects of light scattering is to bond a window, such as LiF to the silicon or germanium. The final pressure determination may require knowledge of the impedances of these materials. Turneaure and Gupta used this technique to measure orientation effects on elastic, plastic and phase transformation waves in single crystal silicon (Turneaure and Gupta 2007).

CHAPTER 7. CONCLUSION

7.1 SUMMARY

In the first chapter, I introduced the concepts of shock induced fast rate fracture and compressive yielding and summarized our experimental findings. Chapter 2 described the introductory shock physics and explained how lasers can initiate shocks yet also potentially complicate the comparison with gas gun and explosive data. Chapter 3 presented an introduction to the mechanical response of materials and included descriptions of our melt and spall experiments. Chapter 4 detailed the experimental setup, which included discussions of the laser systems, diagnostics, and an introduction of the hydrodynamic code, HYADES. In chapter 5, the experimental results were presented, which detailed results from our melt and spall studies. The primary findings of these experiments are that impurities play a significant role in fracture stress and fracture mode, whereas fracture mode was also affected greatly by grain boundaries. Finally, in chapter 6, shocked silicon experiments were motivated and results presented.

7.2 FUTURE WORK

Future work in shocked materials needs to be developed two fronts. Materials development is key to studying and analyzing fast rate shock experiments. Additionally, optical diagnostic development is critical for resolving these experiments both spatially and temporally. I will now describe my suggestions for continuing to perform laser induced shock experiments. In order to continue pursuing spall experiments on ZBL, I have several general recommendations. My first recommendation is to choose a material that melts on release at higher temperature and pressure than aluminum, possibly copper. Aluminum was initially chosen in our experiments since it is a relatively easy metal to process. One must consider the relationship between the Hugoniot curve and the melt curve since isentropic release from the Hugoniot may result in melt. Secondly I would recommend using the available phase plate at Sandia along with thin targets (~300 um) to create 1D shock drive. This is a coupled problem since thicker targets are needed to avoid melting on release, but thinner targets are needed to produce 1D shock propagation.

By using the phase plate on ZBL, one can easily reach pressures to melt metals thereby producing liquid spall. An experiment producing liquid spall would require diagnostics other than a line-VISAR, since melt on release results in a complete loss of reflectivity. One diagnostic idea is to use debris size measurement techniques such as Mie scattering or holography (Arad, et al. 1995), (Werdiger, et al. 1997). Mie scattering is the scattering of electromagnetic radiation from micron scale spherical particles. One issue with a Mie scattering diagnostic is that the particles leaving the free surface need to be spherical. Non-spherical shapes make the analysis of Mie scattering data much more complicated. This consideration most likely requires the material near the free surface to be melted or in a near melted state.

Some material strength experiments could be performed using the YOGA laser. YOGA is an Nd:YAG oscillator with two Nd:Glass amplifiers. This laser is much lower in energy (~5 J) than ZBL and has a longer pulse length (~8 ns). With this laser, lower intensities and hence lower pressures are attainable. Even though high pressures cannot be approached with this system, a well designed material strength experiment can still be tested and developed. YOGA also has unlimited time availability whereas on ZBL one has about one to two experimental runs per year with a maximum of 3 shots per day. In addition to performing more experiments at lower laser intensities, I would also encourage branching out into more materials development (i.e. other metals, ceramics, etc.) and include development of well characterized and controlled thin materials, which are needed for approaching strain rates of ~10^7-10^8 s^{-1}. This would involve even more collaborative efforts toward material development and characterization. The additional benefit of performing these material strength experiments on a dedicated system is that it fosters development of optical diagnostics which can be impeded when working on a lower repetition rate, higher cost system like ZBL. One such suggested diagnostic is the 2D imaging-VISAR which was recently developed by Peter Celliers (Celliers, Erskine, et al. 2009).

It would also be interesting to look at another material that has greater grain boundary strengthening dependence that aluminum. Table 1 showed that metals such as iron and titanium have a greater k_y value, meaning that smaller grains have a greater influence on its yield strength. It would be beneficial to observe if there is a stronger dependence on the HEL stress with grain size than that observed with the Al+3Mg.

Another suggestion is to add a CW heating element to these dynamic material experiments. As mentioned in Chapter 6, preheating semiconductors may allow access to a different part of the phase diagram, thereby more easily accessing melt. With respect to strengthening, Gennady Kanel has performed an extensive amount of work in dynamic response of aluminum and magnesium under the influence of elevated temperatures (G. Kanel, B. A. Razorenov, et al. 1996). The addition of a heating element could further compliment the types of material experiments performed in this thesis.

7.3 CONCLUSION

In conclusion, fast rate material strength experiments were performed on the Z-Beamlet laser at Sandia National Laboratories. In early experiments we determined that grain size was a vital factor in producing different types of fracture. We later measured the dynamic elastic response and fast rate fracture of both high purity aluminum and various aluminum alloys. In these experiments, we found that the high purity aluminum exhibited the highest spall strength and among the lowest dynamic yield strength. An Al-1100 alloy demonstrated a lower spall strength due to the presence of impurities. An Al+3Mg alloy produced lower spall strength, but had the highest resistance to plastic response due to the presence of magnesium atoms. We also confirmed that grain size affects the fracture mode observed, but observed no dependence with grain size on the fracture stress or resistance to dynamic yielding.

Table 17: Table of the various dynamic and static quantities measured along with the various material characteristics studied.

Quantities measured	Material characteristics
HEL stress	Solid solution content
Spall strength	Intermetallic (impurity) particle content
Tensile strain rate	Strain hardening
Fracture character/morphology	Grain size
	Crystal Orientation

Table 17 shows the critical quantities observed and the various types of material characteristics that these experiments were designed to explore. The HEL stress measurements highlighted the role that solid solution alloying had in increasing the dynamic yield strength of materials. The dynamic spall strength measurements evidenced the importance of impurity content, yet showed no dependence on strain hardening or crystal orientation. The effect of grain boundaries with respect to spall strength measurements was no strong trends. The fracture characterization was vital for comparison with spall strength measurements. Fracture determination and strain rate measurements indicated strong differences in fracture type as a function of both grain size and strain rate. Fracture morphology also showed the importance of impurity particle content in lowering the maximum supportable tensile stress. These experiments made advances in isolating the effect of each of these material characteristics on the quantities measured in laser-induced shock experiments of aluminum and aluminum alloys.

APPENDICES

APPENDIX A: PULSE STACKER ALIGNMENT

Pulse stacker alignment

1. Setup a wedge to decrease the energy if needed and setup some irises for daily alignment as slight adjustments are commonly needed.
2. Align the beam normal into and out of the polarizing beamsplitter.
3. Set up at least 2 mirrors after the beamsplitter for alignment into the fiber. The first mirror after the beamsplitter is for alignment to the front of the objective. The second mirror after the beamsplitter is for alignment at the end of the objective. At this point the first pulse is aligned into the fiber.
4. Now put in the first half waveplate since it will give control of the energy into and out of the cavity. Also place the 3 mirrors that form the cavity and put in the second half waveplate. Now choose 2 of the 3 mirrrors to align the pulse stacker. The first or second mirror will be used to align the 2nd pulse with the first pulse. And either the second or third mirror will be used to align the 3rd pulse with the first two pulses.
5. Now check the 1st and 2nd spots at two different planes after the beamsplitter or check the alignment of all 3 spots at one plane. At this point iterate the adjustments between the two mirrors until all spots are aligned.
6. Also, make sure there are ~15 fringes before going into the objective. This is done by slightly misaligning the last mirror in the cavity.

APPENDIX B: HYADES SCRIPT

Example script for running a spall simulation (.inf file)

```
mesh 1 125 0. 0.005 1.05
mesh 125 300 0.005 0.045
mesh 300 424 0.045 0.05 0.95

region 1 423 1 2.7

material 1 13. 26.9815 1.
eos 44 1
ioniz 1 3 1.e-5
strength 1 1 1 1
data shear 1 2.76e+11
data yield 1 2.9e+9
data spall 1 3.3e+10
data tmelt 1 1.05e-4 1.5 1.97

source laser .527 1
tv 0. 0.
tv .1e-9 .1e+20
tv 1.9e-9 .1e+20
tv 2.0e-9 0.

parm flxlem .05
parm temin 2.5e-5
parm timin 2.5e-5
parm trmin 2.5e-5
pparray r rcm pres rho u ucm

parm postdt .5e-9
parm editdt .5e-9
parm tstop 100.e-9
parm itmcyc 5000
parm nstop 1200000
```

APPENDIX C: TIMING DIAGRAMS FOR EXPERIMENT AND NLS

Timing System

The timing system for these experiments is somewhat complex. There are at least 7 or 8 delay generators (DG) used for these experiments. They are labeled in the following manner: Mezz DG #1, Mezz DG #2, Mezz DG #3, Mezz DG #4, Rich's SPLab DG, Mezz Heartbeat DG, Control Room DG, Mezz Shortpulse DG. Figure 100 and Figure 101 show the DG setup and timings.

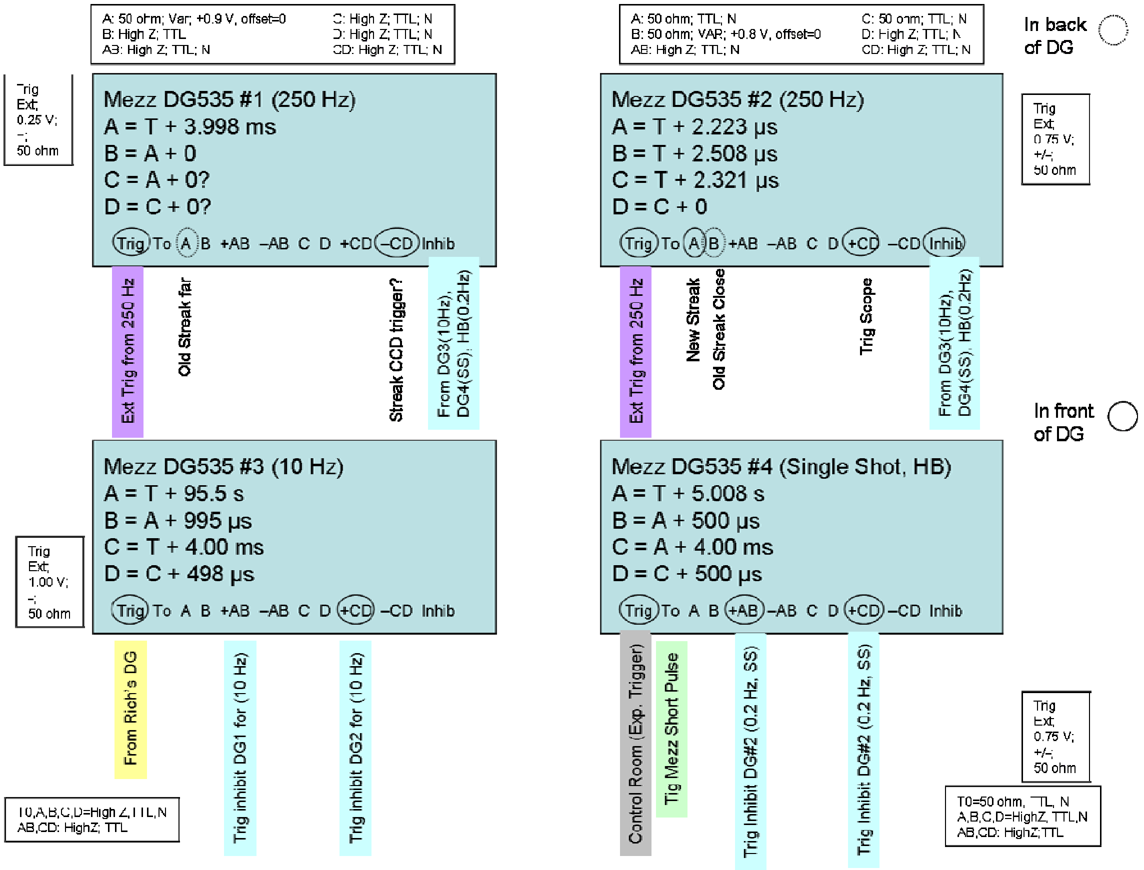

Figure 100: DG boxes on the Mezzanine

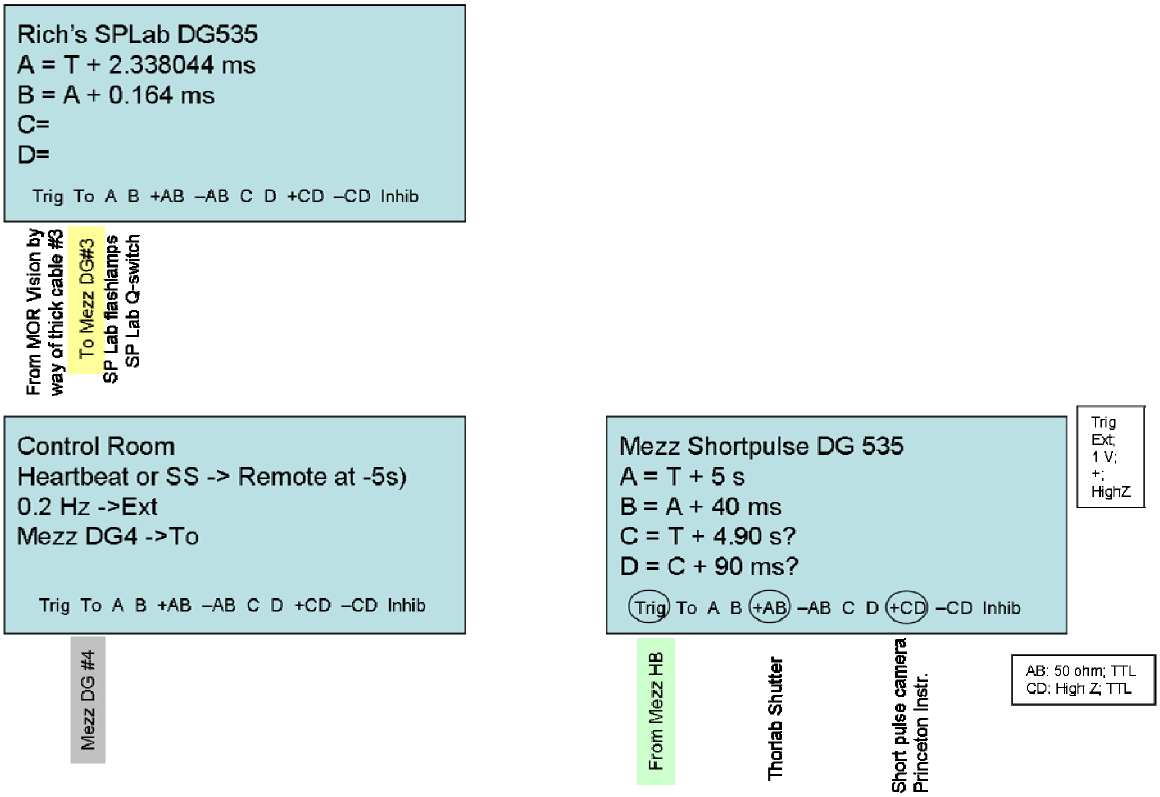

Figure 101: Auxiliary DG boxes

There are several triggers available that we can use for various purposes. First there is a 10 Hz trigger from Rich's DG (originates from MOR Vision clock) that is used for when we are doing a lot of alignment work. Secondly, there is a 250 Hz pulse (a picket fence) which triggers Mezz DG #1 and #2. Thirdly there is a 0.2 Hz signal which can be sent from the control room (referred to as the Heartbeat signal). Finally there is a single shot trigger which is sent from the Cap room via a fiber. This replaces the Heartbeat signal on the shot.

All of our diagnostic timing is initiated at Mezz DG2, where we use the trigger inhibit. DG1 and DG2 are always being triggered at 250 Hz except when we using the trigger inhibit. By using the trigger inhibit, we select out a single pulse from the 250 Hz to trigger everything else. DG1 is used to trigger the streak camera(s), an oscilloscope, and depending on configuration a separate CCD for one of the streak cameras. DG2 is used to trigger DG1 and is the origin of the 250 Hz signal. DG3 is triggered by the 10 Hz signal from Rich's DG (MOR) and is used when we want to trigger inhibit DG2. DG4 is triggered from the Cap room and is used when we want to trigger inhibit DG2 for single shot. Rich's DG is again triggered from the MOR Vision clock. This DG also triggers the Spectra Physics Laser that is used for the VISAR. This DG is located under the mezzanine and coordinating with Rich is usually necessary. This is the DG needed to be adjusted when you want to move the relative timing between the ZBL and the VISAR. The Mezz Heartbeat DG receives the trigger signal from the control room (which comes on 0.2 Hz signal and shots and baselines). This DG has greater than 5 seconds delay which results in trigger at 0.1 Hz. This DG triggers the Mezz Shortpulse DG, the thorlab shutter, and is used to trigger inhibit DG2. The Control Room DG controls the signal that is sent to the Mezz Heartbeat DG. When doing alignments, this DG needs to be in external; however, when getting ready for a shot this DG needs to be in Single shot. The last DG is the Mezz Shortpulse and receives a trigger signal from the Mezz HB DG. It triggers the Thorlabs shutter that is used for the short pulse beam and also triggers the Princeton Instruments cameras used for the short pulse diagnostics.

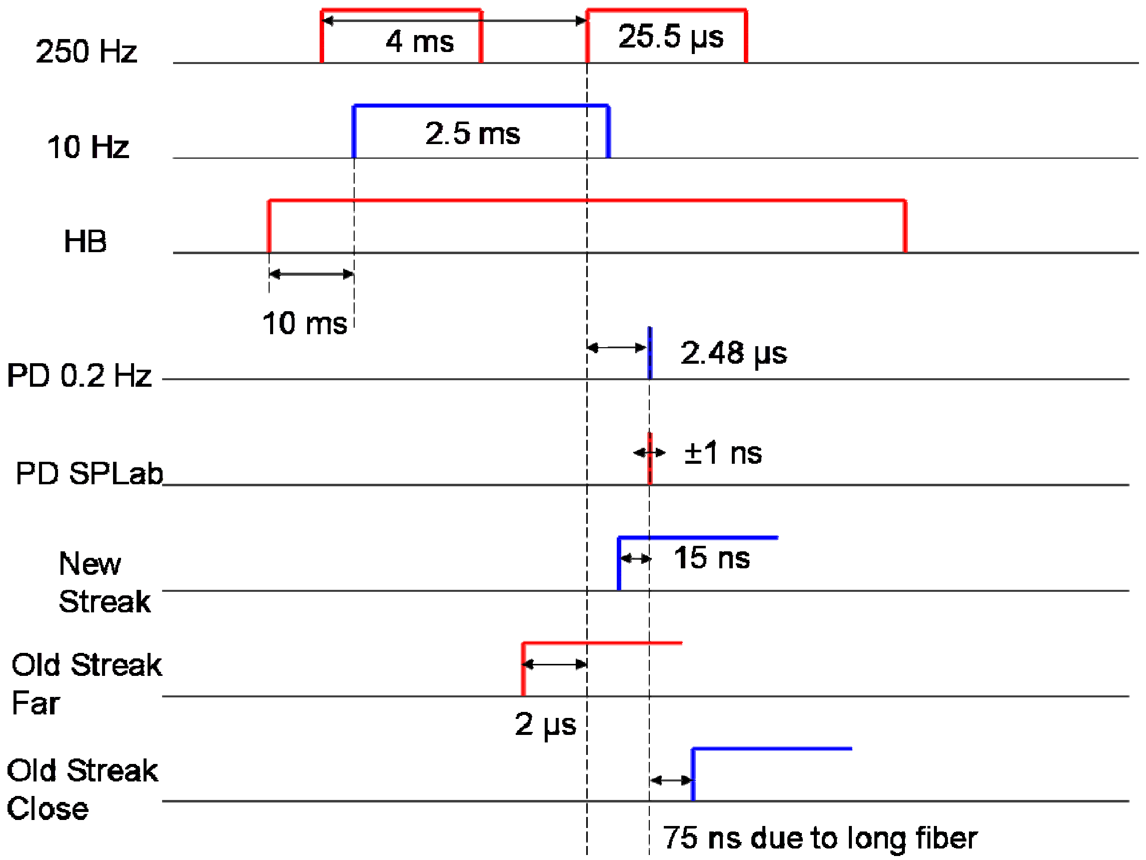

Figure 102: Timing Diagram for spall experiments

We tracked all pulses on an oscilloscope so that we could keep track of where in time pulses were supposed to come and when we expected them to come. The first thing that we did was use a photodiode (Thorlabs DET210) to track determine when we expected Z-Beamlet to come into the chamber. The way that we did this was by using the regen pulse at 1 micron from ZBL. We had to ask for access to this beam since it is not always available. By placing the photodiode at the center of the chamber we can determine when the main ZBL pulse when actually arrive at target chamber center (TCC). Because it is sometimes difficult to see this pulse and because it comes at 0.2 Hz, we externally triggered the oscilloscope at 10 Hz (from Mezz DG #1). We took note of the delay between the trigger and this regen pulse since it would be helpful in keeping track of ZBL's expected arrival time. Setting up another photodiode behind the first beamsplitter after the fiber allowed us to determine when the VISAR pulse arrives. We also needed to take into account the difference in time between this location and the chamber (flip around photodiode measuring regen pulse). Differences in cable length also needed to be taken into account. In a similar manner we were able to track the short pulse 100 TW beam. As a sanity check, we would often check the temporal location of the regen pulse to make sure that that there was very little temporal jitter and no temporal drift over time. On shots, we also set up a lens and photodiode that imaged the target front surface in an attempt to catch plasma light so that we could compare it to the other pulses. We often found that the photodiode would pick up EMP from the target and would thus give us a lot of noise on the oscilloscope.

I have included several timing diagrams that were referred at various times. – is the timing diagram for NLS. In this diagram SRS G is the same as “Rich’s SPLab DG535”.

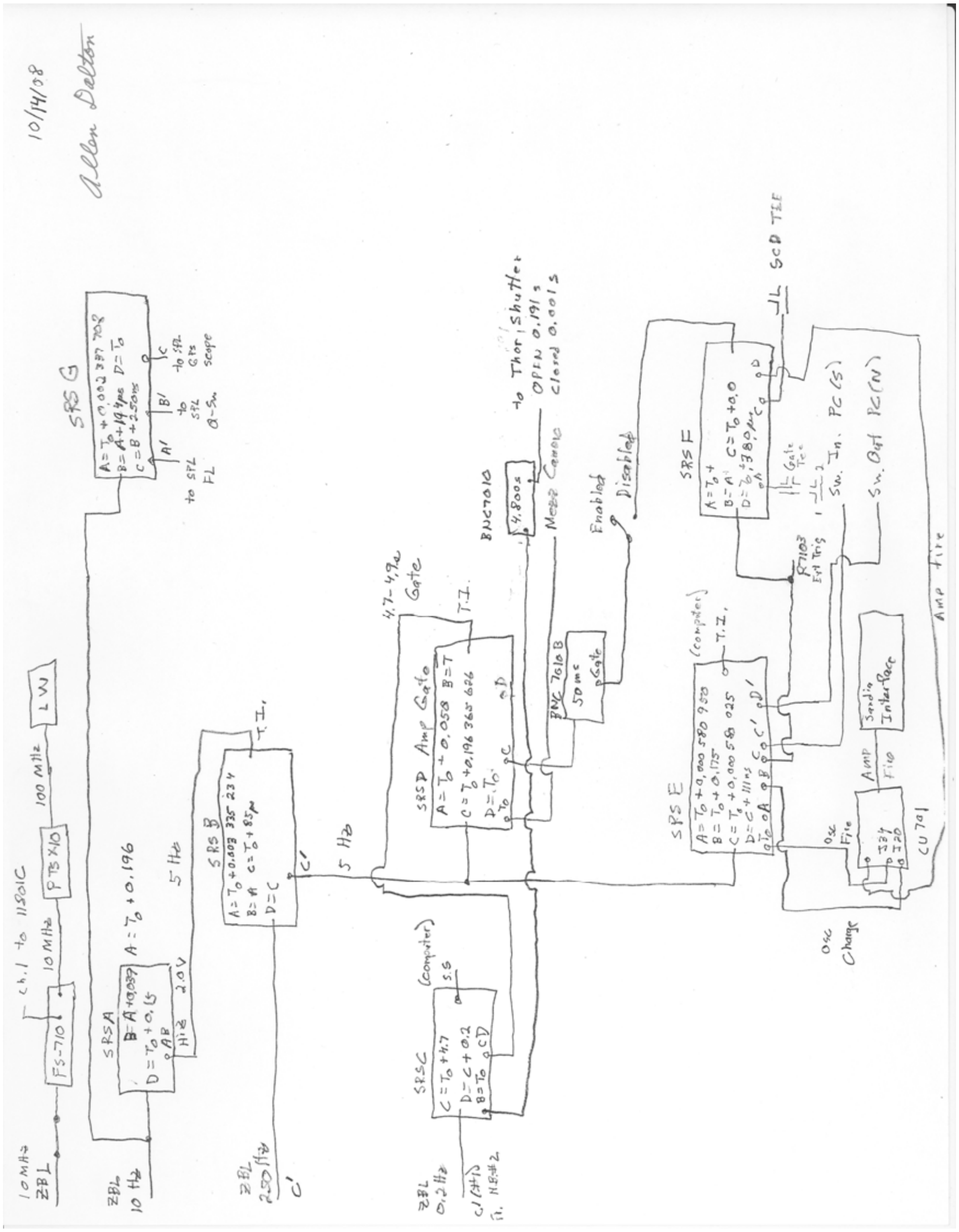

Figure 103: NLS Timing Diagram

APPENDIX D: VISAR SAMPLE ANALYSIS FILE

```
close('all');
clear('all');

%to change on each file (filename, dispos, pxstart, ROI, filter, phase
file
%number)

A=imread('C:\Documents and Settings\Allen\My Documents\AllenWork\Sandia
Experiments\ZBL Final Oct 2008\Final\Visar 1\shot 10.tif');
A=double(A)';
A=fliplr(flipud(A));

vpf=0.29254;
discpos=390;
window=20;
numfringe=0;
figure(1);imagesc(A);colormap(gray);

condition=0;
while condition==0
     %angleentry=input('Enter rotation angle in degrees: ');
     angleentry=180;
     A=imrotate(A,angleentry);
     A=flipud(A);
     aa=size(A);
     B=double(A);
     fine=input('Is this image okay (yes=0,no=1): ');
     fine;
     if condition==fine
         break;
     else
         cond=0;
     end
end

ns_px=50/1024;  %50 ns over 1024 pixels
    for b=1:1024
        b;
        ns(b)=b*ns_px;
    end

figure(5);imagesc(A);colormap(gray);
%%%%%%%%%%%%%%%%%%%%%%%%%%%%%%%%%%%%%%%%%%%%%%%%%%%%%%%%%%%%%%%%%%
%Define region of interest
minx=200   %min(x);
maxx=740  %max(x);
miny=200  %min(y);
maxy=500  %max(y);
```

```
B(miny-2:miny+2,minx:maxx)=250;
B(maxy-2:maxy+2,minx:maxx)=250;
B(miny:maxy,minx-2:minx+2)=250;
B(miny:maxy,maxx-2:maxx+2)=250;
figure(311);imagesc(B);colormap(gray);

%%%%%%%%%%%%%%%%%%%%%%%%%%%%%%%%%%%%%%%%%%%%%%%%%%%%%%%%%%%%%%%%%%%
%Find space and time dimensions
region=A((miny:maxy),(minx:maxx));
regionsize=size(region);
TimeSize=regionsize(2);
SpaceSize=regionsize(1);
figure(51);imagesc(region);colormap(gray);

%Perform 1-D FFT
ftregion=fftshift(fft(fftshift(region)));

%define gaussian matrix
yaxis=-SpaceSize/2:(SpaceSize/2-1);
filter1(1:SpaceSize)=0;
filter1(floor(SpaceSize/2)+3:floor(SpaceSize/2)+20)=rectwin(18);
filters=filter1;
filters=filters';
filters(1:floor(SpaceSize/2)+1)=0;
filtmat=zeros(regionsize);
for j=1:TimeSize
    filtmat(:,j)=filters;
end

%Multiply ftregion by filtmat
filtered=ftregion.*filtmat;

%Take inverse FT
ifftfiltered=fftshift(ifft(fftshift(filtered)));
figure(10);imagesc(real(ifftfiltered));colormap(gray);

figure(91);
subplot(5,1,1); plot(region(1:maxy-miny+1,1))
subplot(5,1,2); plot(abs(ftregion(1:maxy-miny+1,1)))
subplot(5,1,3); plot(filtmat(1:maxy-miny+1,1))
subplot(5,1,4); plot(abs(filtered(1:maxy-miny+1,1)))
subplot(5,1,5); plot(real(ifftfiltered(1:maxy-miny+1,1)))

%Calculate wrapped phase
phase=(angle(ifftfiltered));
figure(13);imagesc(phase);colormap(gray);
size(phase)
fwriteid=fopen('phase10.bin','w');
count=fwrite(fwriteid,phase,'float');
status=fclose(fwriteid);
```

```
%status=dos('qual -input phase10.bin -format float -output
phase10.output -xsize 301 -ysize 451 -mode min_var -debug yes -tsize
3')
status=dos('flyn -input phase10.bin -format float -output
phase10.output -xsize 301 -ysize 541 -mode min_var -debug yes -tsize
3')
%status=dos('gold -input phase10.bin -format float -output
phase10.output -xsize 301 -ysize 451 -mode min_var')
%status=dos('unwt -input phase10.bin -format float -output
phase10.output -xsize 301 -ysize 451')
%status=dos('unmg -input phase10.bin -format float -output
phase10.output -xsize 526 -ysize 381')
%status=dos('fmg -input phase10.bin -format float -output
phase10.output -xsize 301 -ysize 451')
%status=dos('lpno -input phase10.bin -format float -output
phase10.output -xsize 301 -ysize 451')
%status=dos('pcg -input phase10.bin -format float -output
phase10.output -xsize 301 -ysize 451')

fid=fopen('phase10.output','r');
phase10=fread(fid,[SpaceSize TimeSize],'float');
size(phase10)
figure(100);imagesc(phase10);

phase10sum(1:SpaceSize,1)=0;
phase10avg(1:SpaceSize,1)=0;
for i=1:SpaceSize
    for j=1:10
        phase10sum(i,1)=phase10sum(i,1)+phase10(i,j);
    end
end

phase10avg(:,1)=phase10sum(:,1)/10;

figure(199);plot(phase10(:,1));

for k=1:SpaceSize
    phase10(k,:)=phase10(k,:)-phase10avg(k,1);
end

figure(198);plot(phase10avg(:,1));
figure(19);imagesc(phase10);colormap(gray);
figure(299);plot(phase10(50,:));

%%%%%%%%%%%%%%%%%%%%%%%%%%%%%%%%%%%%%%%%%%%%%%%%%%%%%%%%%%%%%%%%%%%%%%%%
%find the discontinuity, please.
phasediff=abs(diff(phase10,1,2));
discont=discpos-minx;
phasediff(:,1:(discont-window))=0;
phasediff(:,(discont+window):end)=0;
```

```
figure(14);plot(phasediff(floor(SpaceSize/2),:));colormap(gray);
maxvector=[];
for m=1:SpaceSize
    gmax(m)=max(phasediff(m,:));
    maxvector(m) = find(phasediff(m,:)==gmax(m));

phase10(m,(maxvector(m):end))=phase10(m,(maxvector(m):end))+2*pi*numfri
nge;
end
%%%%%%%%%%%%%%%%%%%%%%%%%%%%%%%%%%%%%%%%%%%%%%%%%%%%%%%%%%%%%%%%%%%%%%%%%
%create velocity map
velocity=vpf*phase10/(2*pi);
pxstart=275;
polyorder=10;

Lineout=2;
[out(Lineout),out2(Lineout)]=velfunction(velocity,ns,Lineout,minx,maxx,
SpaceSize,pxstart,polyorder);

Lineout=4;
[out(Lineout),out2(Lineout)]=velfunction(velocity,ns,Lineout,minx,maxx,
SpaceSize,pxstart,polyorder);

Lineout=6;
[out(Lineout),out2(Lineout)]=velfunction(velocity,ns,Lineout,minx,maxx,
SpaceSize,pxstart,polyorder);

Lineout=8;
[out(Lineout),out2(Lineout)]=velfunction(velocity,ns,Lineout,minx,maxx,
SpaceSize,pxstart,polyorder);

%%%%%%%%%%%%%%%%%%%%%%%%%%%%%%%%%%%%%%%%%%%%%%%%%%%%%%%%%%%%%%%%%%%%%%%%%
%%%
out %spall strength
SpallStengthAVG=mean(out(1,2:2:8))
SpallStrengthSTD=std(out(1,2:2:8))

out2 %strain rate
StrainRateAVG=mean(out2(1,2:2:8))
StrainRateSTD=std(out2(1,2:2:8))

um_pix=1.1266 %calibration from visar calibration
figure(392);mesh(ns(minx:maxx), um_pix*(miny-miny:maxy-miny),velocity)

xlabel('Time(ns)') %x label name
ylabel('Space (microns)') %y label name
zlabel('Velocity (microns/ns)') %z label name
%%%%%%%%%%%%%%%%%%%%%%%%%%%%%%%%%%%%%%%%%%%%%%%%%%%%%%%%%%%%%%%%%%%%%%%%%
%
phase10avg = sum(phase10,1)/301;
velocityavg=vpf*phase10avg/(2*pi);
```

```
figure(600);plot(velocityavg);

Lineout=1;
[out(Lineout),out2(Lineout)]=velfunction2(velocityavg,ns,minx,maxx,Spac
eSize,pxstart,polyorder);
out(1)
out2(1)

%%%%%%%%%%%%%%%%%%%%%%%%velfunction%%%%%%%%%%%%%%%%%%%%%%%%%%%%%%%%%%%%

function[SpallStrength,StrainRate]=velfunction(velocity,ns,Lineout,minx
,maxx,SpaceSize,pxstart,polyorder)

density=2.707;
soundspeed=5.386;

p=polyfit(ns(minx+pxstart:maxx),velocity(round(SpaceSize*Lineout/10),px
start+1:size(velocity,2)),polyorder);
%p
p2=polyval(p,ns(minx+pxstart:maxx));
figure;plot(ns(minx:maxx),velocity(round(SpaceSize*Lineout/10),:),ns(mi
nx+pxstart:maxx),p2);

%First derivative
p3=polyder(p);
%p3
p4=polyval(p3,ns(minx+pxstart:maxx));
%Second derivative
p5=polyder(p3);
%p5
p6=polyval(p5,ns(minx+pxstart:maxx));
figure;
subplot(3,1,1);plot(ns(minx+pxstart:maxx),p2);
subplot(3,1,2);plot(ns(minx+pxstart:maxx),p4);
subplot(3,1,3);plot(ns(minx+pxstart:maxx),p6);

minv=min(p2(size(p2,2)/2:size(p2,2)));
mini=find(p2==minv);
minti=ns(minx+mini+pxstart);
maxv=max(p2) ;
maxi=find(p2==maxv);
maxti=ns(minx+maxi+pxstart);

deltav=abs(maxv-minv);
deltat=abs(maxti-minti);
SpallStrength=1/2*soundspeed*density*abs(maxv-minv)*10;
StrainRate=abs((maxv-minv)/(maxti-minti))/2/soundspeed/1e-9;
```

APPENDIX E: VISAR AND STREAK CAMERA NOTES

Derivation of Velocity Equation

The derivation of the velocity per fringe constant can be found elsewhere (Barker and Schuler 1974). First consider the interferometer with two arms. The number of waves in the left arm (reference arm) of the interferometer is:

$$N_L = \frac{2L_L}{\lambda}, \tag{E.1}$$

where L_L is the distance from the beamsplitter to the end mirror. The number of waves in the right arm (with etalon) is:

$$N_R = \frac{2L_R}{\lambda} = \frac{2(L_R - L_E)}{\lambda} + \frac{2nL_E}{\lambda}, \tag{E.2}$$

where L_R is the distance from the beamsplitter to the end mirror and L_E is the length of the etalon. The order of interference or fringe order, N, is given by the difference in the right and light arms of the interferometer:

$$\begin{gathered} N = N_R - N_L \\ N = \frac{2(L_R - L_L - L_E)}{\lambda} + \frac{2n(t)L_E}{\lambda(t)} \end{gathered}. \tag{E.3}$$

Where in order to get the best fringe contrast the legs of the interferometer must satisfy the condition:

$$L_R = L_L + L_E\left(1 - \frac{1}{n_0}\right). \tag{E.4}$$

The order of interference then becomes:

$$\begin{gathered} N = \frac{2\left(L_L + L_E\left(1 - \frac{1}{n_0}\right) - L_L - L_E\right)}{\lambda} + \frac{2n(t)L_E}{\lambda(t)} \\ N = \frac{2L_e}{\lambda(t)}\left(n(t) - \frac{1}{n_0}\right) \end{gathered}. \tag{E.5}$$

In the absence of Doppler shifting from the moving target, *N*, is given by:

$$N_0 = \frac{2L_e}{\lambda_0}\left(n_0 - \frac{1}{n_0}\right). \tag{E.6}$$

The wavelength of Doppler shifted light is given by:

$$\lambda(t) = \lambda_0\left[1 - \frac{2v(t)}{c}\right]. \tag{E.7}$$

Since the wavelength varies little (typically v/c ~ 10^{-5}), the index of refraction can be represented as a series expansion in wavelength:

$$n(t) = n_0 + \frac{dn}{d\lambda}|_{\lambda=\lambda_0}\left[\lambda(t) - \lambda_0\right]. \tag{E.8}$$

The fringe count resulting from the velocity of a moving surface is the difference between the fringe order at time t and at time t=0:

$$F(t) = N(t) - N_0$$

$$F(t) = \frac{2L_e}{\lambda(t)}\left(n(t) - \frac{1}{n_0}\right) - \frac{2L_e}{\lambda_0}\left(n_0 - \frac{1}{n_0}\right) \tag{E.9}$$

Substitution along with an expansion of the denominator in terms of v/c yields:

$$F(t) = \frac{4L_e}{\lambda_0}\left(n_0 - \frac{1}{n_0}\right)\left[1 - \left(\frac{n_0}{{n_0}^2 - 1}\right)\lambda_0\frac{dn}{d\lambda}\right]\frac{v(t)}{c} \tag{E.10}$$

Where the second term in brackets accounts for dispersion of the etalon:

$$\delta = -\left(\frac{n_0}{{n_0}^2 - 1}\right)\lambda_0\frac{dn}{d\lambda}|_{\lambda=\lambda_0}. \tag{E.11}$$

The fringe count can then be simplified as:

$$F(t) = \frac{2\tau}{\lambda_0}\left[1 + \delta\right]\cdot v(t), \tag{E.12}$$

where τ is the temporal delay associated with the etalon. This equation can then be rearranged for the velocity of the moving surface:

$$v(t) = \frac{\lambda_0}{2\tau}\frac{F(t)}{(1+\delta)}. \tag{E.13}$$

The velocity-per-fringe constant, VPF_0, is:

$$VPF_0 = \frac{\lambda}{2\tau(1+\delta)} = \frac{\lambda c}{4h\left(n-\frac{1}{n}\right)(1+\delta)} \quad \text{(E.14)}$$

VISAR interferometer alignment

The imaging of the VISAR is critical to getting good resolvable interferograms. First the multimode optical fiber must be imaged to the target plane. Secondly the target plane must be imaged to the correct side of the second beamsplitter. I like to use a scratched target and image it to the beamsplitter. Finally the beamsplitter must be imaged to the streak camera and alignment camera. I typically used slightly frayed lens tissue that was taped to the beamsplitter. Once the system imaging is set, the interferometer can be aligned. I would send white light through the multimode fiber for this alignment. If I had trouble getting white light fringes, I would first start with the CW green.

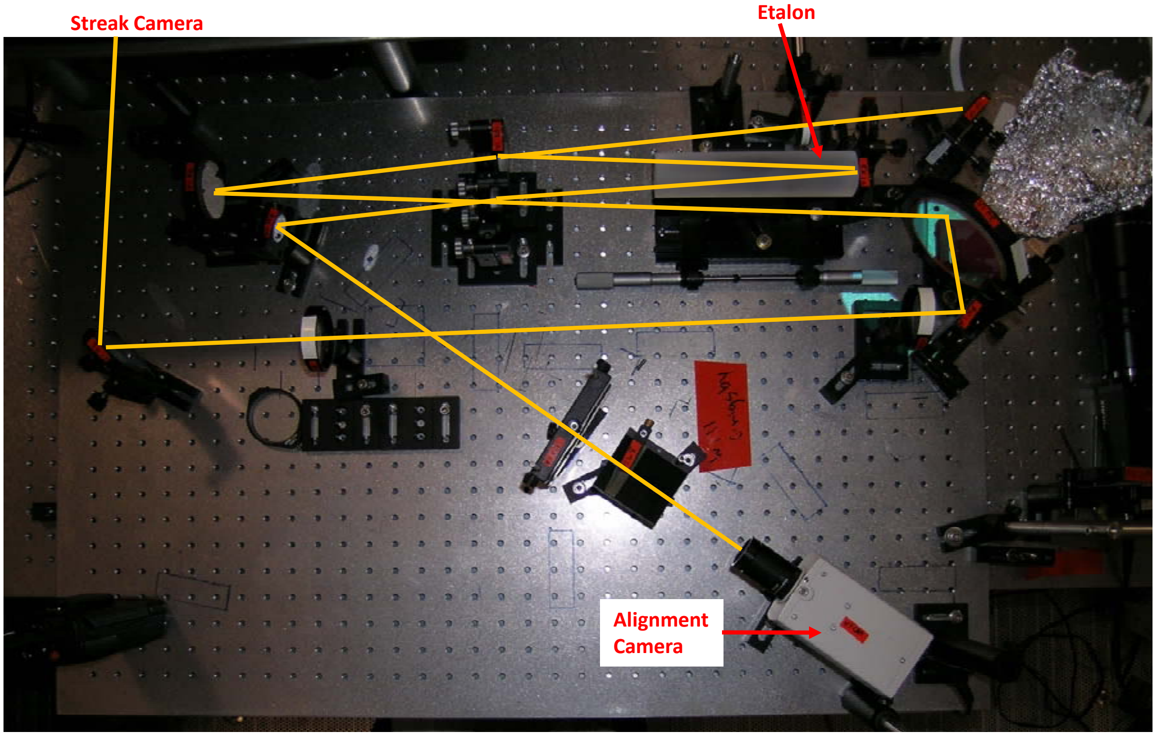

Figure 104: VISAR

The alignment of the interferometer is performed in the following manner:

1. Align the images (of the scratched target) on the camera with the end mirror.
2. Adjust the zero-delay, or translation stage, of the end mirror.
3. Iterate between steps 1 and 2 until fringes are found.
4. Once fringes are found, tip and tilt the second beamsplitter of the interferometer to adjust fringe frequency and fringe orientation.
5. Adjust the zero-delay to maximize contrast.
6. Iterate between steps 4 and 5 until fringe frequency, orientation, and contrast are satisfactory. Typically I want about 25-30 vertical fringes onto the slit of the streak camera.

Hamamatsu C7700 Streak Camera System

The Hamamatsu streak camera several booklets which detail performance parameters of the camera. The booklets are essential for determining the optimum timing settings for a particular sweep. The focus mode of the streak camera is needed to optimize imaging from the beamsplitter of the interferometer to the slit of the streak camera. When using the focus mode, I normally used a white light source or a green CW alignment laser. The streak camera should be set up to image the slit at the input to the CCD camera. Before opening the shutter get the input beam to a low light level. When using focus mode, one must ensure that a lot of ND filters are available. Always start with too many filters and slowly decrease the filters until you see something. The last thing one wants is to damage the photocathode.

Once the pulsed beam is brought into camera, one must select the sweep speed. This dictates the trigger timing needed for the pulsed event to show up on the streak camera.

Figure 105: Hamamatsu C7700 streak camera system

Streak camera software control

1. Ensure that the streak camera is connected correctly with the computer and the CCD controller
2. Open the "HPD-TA 8.2.0" Icon on the Desktop. The program will check for all connections, so if something is not connected correctly, the program will let you know.
3. The "LUT Contol" and "C7700 Control" will be open. The LUT control allows the user to adjust the brightness level on acquire image. By clicking on the asterisk, the image is rescaled.
4. Click on the "C4742-95 Acquisition Control". This controls various parameters of the streak camera.

Options	**Range**	**Comments**
Time Range	0.5 ns-1ms	For most of our experiments, 20 ns or 50 ns
Mode	Focus, Operate	Focus for alignment, Operate to streak
Gate Mode	Normal	Most commonly run in Normal
II Gain	0-63	Image Intensifier Gain
Shutter	Open, Closed	Controls the shutter
Trigger Mode	Cont., Single	Controls the trigger type
Trigger Status	Ready, Fire	

EG&G streak camera

The EG&G streak camera system was lent to use from Larry Ruggles at Sandia National Laboratories, and he is still the best contact regarding info on this system. The bottom section of the unit contains the timing circuits for the system and I generally did not need to change these timing adjustments. The top section contains the streak tube which is in contact with a long fiber array (~150 ft. long). This particular system takes two trigger signals: a 9V "far" trigger, which is a microsecond time scale trigger before the event and a 8V "close" trigger, which is a nanosecond time scale trigger before the event.

There are several options for recording streaked images: directly couple film to the phosphor screen, fiber taper to CCD camera, macrolens to CCD camera, or imaging optics to CCD camera. All of these methods have advantages and disadvantages, but I personally recommend using a macrolens and triggerable CCD unless the output optics and camera are integrated into the streak camera system (as in the Hamamatsu C7700 system) which was used in later experiments. Figure 106 shows a picture of the EG&G streak camera system also used in our experiments.

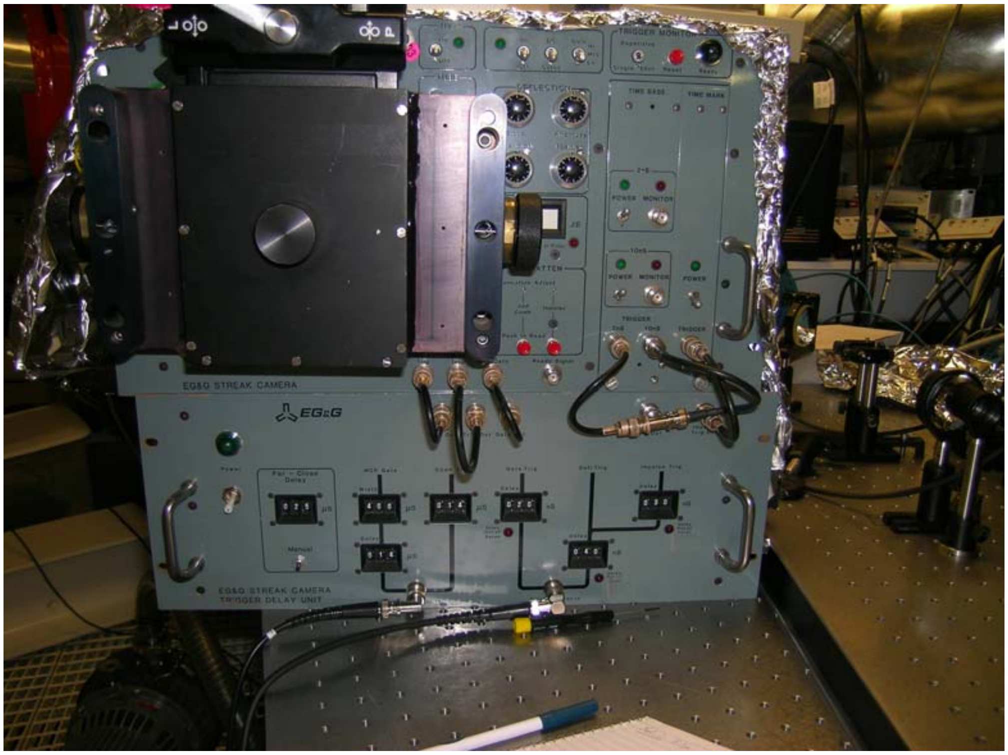

Figure 106: EG&G streak camera system for the first couple of VISAR experiments.

One important note regarding this system is that at some point the streak tube got rotated to a point where the streak is neither vertical or horizontal. Because of this the coupling of the fiber array into the streak camera is very delicate. On several occasion, I have needed to open the streak system and rotate the fiber array until it was again aligned with the streak tube. One must be sure that the system is off when making these adjustments because there is high voltage access due to the MCP.

REFERENCES

Adachi, Sadao. "Model Dielectric Constants of Si and Ge." *Physical Review B* 38 (1988): 12966.

Adachi, Sadao. "Optical Dispersion Relations for Si and Ge." *Journal of Applied Physics* 66 (1989): 3224.

Arad, B., et al. "A New Method for stuyding debris from laser-induced spall in metals." *Review of Scientific Instruments* 66 (1995): 5590.

Banks, P.S., and M.D. Perry. "Novel all-reflective stretcher for chirped-pulse amplification of ultrashort pulses." *IEEE Journal of Quantum Electronics* 36, no. 3 (2000): 268-274.

Barker, L.M., and K.W. Schuler. "Correction to the velocity-per-fringe relationship for the VISAR interferometer." *Journal of Applied Physics* 45 (1974): 3692-3693.

Barker, L.M., and R.E. Hollenbach. "Laser interferometer for measuring high velocities of any reflecting surface." *Journal of Applied Physics* 43 (1972): 4669-4675.

Barker, L.M., and R.E. Hollenbach. "Shock Wave Studies of PMMA, Fused Silica, and Sapphire." *Journal of Applied Physics*, 1970: 4208-4226.

Boslough, M.B., and J.R. Asay. "Basic Principles of Shock Compression." In *High-Pressure Shock Compression of Solids*, by J.R. Asay and M. Shahinpoor, 7-42. New York: Springer-Verlag, 1993.

Brandon, D.G., M. Boas, and Z. Rosenberg. "Effect of grain boundaries on ductile fracture under planar impact." *3rd Conf. Mech. Prop. High Rates of Strain.* 1984. 261-268.

Brewer, J.L., et al. "Influence of Microstructure on the Spall Failure of Aluminum Materials." *Metallurgical and Materials Transactions A* 38 (2007): 2666.

Buchar, J., and J. Hrebebicek. "The Dynamic (Spall) Strength of Steels." *Czechoslovak Journal of Physics* 43 (1993): 73-85.

Buchar, J., M. Elices, and R. Cortez. "The Influence of Grain Size on the Spall Fracture of Copper." *Journal de Physique IV* 1 (1991): C3-623.

Burns, W.K., and N. Bloembergen. "Third-Harmonic Generation in Absorbing Media of Cubic or Isotropic Symmetry." *Physical Review B* 4 (1971): 3437-3450.

Celliers, P.M., D.K. Bradley, G.W. Collins, D.G. Hicks, T.R Boehly, and W.J. Armstrong. "Line-imaging velocimeter for shock diagnostics at the OMEGA laser facility." *Review of Scientic Instruments* 75 (2004): 4916.

Celliers, P.M., et al. "Observations of intrinsic shock front anisotropy in diamond." *Shock Compression of Condensed Matter.* 2009.

Chen, D., Y. Yu, Z. Yin, H. Wang, and G. Liu. "On the validity of the traditional measurement of spall strength." *International Journal of Impact Engineering* 31 (2005): 811-824.

Chen, J., D.J. Weidner, and M.T. Vaughan. "The Strength of MgFeSiO3 perovskite at high pressure and temperatue." *Nature* 419 (2002): 824-826.

Chen, X., J.R. Asay, and S.K., Field, D.P. Dwivedi. "Spall behavior of aluminum with varying microstructures." *Journal of Applied Physics* 99 (2006): 023528.

Christy, S., H.-R. Pak, and M.A. Meyers. *Metallurgical Applications of Shock-Wave and High-Strain-Rate Phenomena.* New York: Marcel Dekker, 1986. 835.

Collins, G.W., et al. "Measurements of the Equation of State of Deuterium at the Fluid Insulator-Metal Transition." *Science* 281 (1998): 1178-1181.

Cottet, F., and M. Boustie. "Spall measurements in metallic targets using shock waves induced by short duration laser pulses." Edited by S.C. Schmidt, J.N. Johnson and L.W. Davison. *Shock Compression of Condensed Matter-1989.* New York: Elsevier Science, 1990. 425.

Cottet, F., and M. Boustie. "Spallation studies in aluminum targets using shock waves induced by laser irradiation at various pulse durations." *Journal of Applied Physics* 66 (1989): 4067-4073.

Courtney, T.H. *Mechanical Behavior of Materials.* Long Grove, IL: Waveland Press, 2000.

Crain, J., G.J. Ackland, J.R. Maclean, R.O. Piltz, G.S. Hatton, and G.S. Pawley. "Reversible pressure-induced structural transition between metastabel phases of silicon." *Physical Review B* 50 (1994): 13043.

Da Silva, L.B., et al. "Absolute Equation of State Measurement on Shocked Liquid Deuterium up to 200 GPa (2 Mbar)." *Physical Review Letters* 78 (1997): 484-486.

Dalton, D.A., et al. "Laser-induced spallation of aluminum and Al alloys at strain rates above 2x106 s-1." *Journal of Applied Physics* 104 (2008): 013526.

de Resseguier, T., S. Couturier, J. David, and G. Nierat. "Spallation of metal targets subjected to intense laser shocks." *Journal of Applied Physics* 82 (1997): 2617.

Dekel, E., S. Eliezer, Z. Henis, E. Moshe, and Ludminsky. "Spallation model for the high strain rates range." *Journal of Applied Physics* 84 (1998): 4851-4858.

Dieter, G.E. *Mechanical Metallurgy.* New York: McGraw-Hill, 1976.

Ditmire, T. "Plasma II Lecture Notes." 2004.

Duclos, S.J., Y.K. Vohra, and A.L. Ruoff. "hcp-to-fcc Transition in Silicon at 78 GPa and Studies to 100 GPa." *Physical Review Letters* 58 (1987): 775.

Duvall, G.E., and R.A. Graham. "Phase transitions under shock-wave loading." *Review of Modern Physics* 49 (1977): 523-579.

Edens, A.D., et al. "Measurement of the Decay Rate of Single-Frequency Perturbations on Blast Waves." *Phys. Rev. Lett.* 95 (2005): 244503.

Eliezer, S., I. Gilath, and T. Bar-Noy. "Laser-induced spall in metals: Experiment and simulation." *Journal of Applied Physics* 67 (1990): 715.

Fujiwara, T., and K. Koizume. "The Method Partially Improved to Produce Aluminum Single Crystal Wire and Palte Having Any Desired Crystallographic Orientations." *Journal of Science of the Hiroshima University* , 1952.

Garkushin, G.V., S.V. Razorenov, and G.I. Kanel. "Submicrosecond Strength of the D16T Aluminum Alloy at Room and Elevated Temperatures." *Physics of the Solid State* 50 (2008): 839-843.

Ghiglia, D.C., and M.D. Pritt. *Two-Dimensional Phase Unwrapping Theory, Algorithms and Software.* New York: Wiley-Interscience, 1998.

Gilath, I., S. Eliezer, M.P. Dariel, and L. Kornblit. "Brittle-to-ductile transition in laser-induced spall at ultrahigh strain rate in 6061-T6 aluminum alloy." *Applied Physics Letters* 52 (1988): 1207.

Gilev, S.D., and A.M. Trubachev. "Metallization of silicon in a shock wave: the metallization threshold and ultrahigh defect densities." *Journal of Physics: Condensed Matter* 16 (2004): 8139.

Goto, T., T. Sato, and Y. Syono. "Reduction of shear-strength and phase transition in shock loaded silicon." *Japanese Journal of Applied Physics* 21 (1982): 369.

Grady, D.E. "Local inertial effects in dynamic fragmentation." *Journal ofApplied Physics* 53 (1982): 322.

Grady, D.E. "The Spall Strength of Condensed Matter." *Journal of the Mechanics and Physics of Solids* 36 (1988): 353.

Grigsby, W. "Experimental Studies of High Energy Density Silicon Using Ultrafast Lasers." PhD Dissertation, Austin, TX, 2007.

Gundrum, Bryan C., Robert S. Averback, and D.G. Cahill. "Time resolved measurement of melting and solidification in Si using third harmonic generatiion of light." *Applied Physics Letters* 91 (2007): 011906.

Gust, W.H., and E.B. Royce. "Axial Yield Strengths and Two Successive Phase Transition Stresses for Crystalline Silicon." *Journal of Applied Physics* 42 (1971): 1897.

Hammer, J.H., et al. "High yield inertial confinement fusion target design for a z-pinch-driven hohlraum." *Physics of Plasmas* 6 (1999): 2129.

Henis, Z,, and S. Eliezer. "Melting phenomenon in laser-induced shock waves." *Physical Review E* 48 (1993): 2094.

Hixson, R.S., J.E. Vorthman, R.L. Gustavsen, A.K. Zurek, W.R. Thissell, and D.L. Tonks. "Spall wave-profile and shock-recovery experiments on depleted uranium." *Conference on Shock Compression of Condensed Matter.* AIP, 1998. 479-482.

Johnson, G.R. "Response of Various Metals to Large Torsion Strains Over a Large Range of Strain Rates: Part I: Ductile Metals." *Journal of Engineering Materials and Technology* 105 (1983): 42-47.

Kanel, G.I., Bogatch, A. Razorenov, A.V. Utkin, V.E. Fortov, and D.E. Grady. "Spall fracture properties of aluminum and magnesium at high temperatures." *Journal of Applied Physics* 79 (1996): 8310.

Kanel, G.I., S.V. Razorenov, and A.V. Utkin. "Spallation in Solids Under Shock-Wave Loading: Analysis of Dynamic Flow, Methodology, of Measurements, and Constitutive Factors." In *High Pressure Shock Compression of Solids II*, by L. Davison, D.E. Grady and M. Shahinpoor, 1-23. Berlin: Springer, 1996.

Kanel, G.I., S.V. Razorenov, and V.E. Fortov. *Shock-Wave and High Strain-Rate Phenomena in Materials.* New York: Marcel Dekker, 1992. 775.

Kanel, G.I., S.V. Razorenov, K. Baumung, and J. Singer. "Dynamic yield and tensile strength of aluminum single crystals at temperatures up to the melting point." *Journal of Applied Physics* 90 (2001): 136-143.

Knudson, M.D., D.L. Hanson, J.E. Bailey, C.A. Hall, J.R. Asay, and W.W. Anderson. "Equation of State Measurement in Liquid Deuterium to 70 GPa." *Physical Review Letters* 87 (2001): 225501.

Kruer, W.L. *The Physics of Laser Plasma Interactions.* Redwood City: Addison Wesley, 1988.

Larsen, J. *HYADES User's Guide.* Cascade Applied Sciences, Inc. 2007.

Larsen, J.T., and S.M. Lane. "Hyades-a Plasma Hydrodynamics Code for Dense-Plams Studies." *J. Quant. Spect. Rad. Trans.* 51 (1994): 179.

Li, K.D., and P.M. Fauchet. "Drude Parameters of Liquid Silicon at the Melting Temperature." *Applied Physics Letters* 51 (1987): 1747.

Minich, R.W., J.U. Cazamias, M. Kumar, and A.J. Schwartz. "Effect of microstructural length scales on spall behavior of copper." *Metallurgical and Materials Transactions A* 35 (2004): 2663.

Mintsev, V.B., Yu.B. Zaporoghets, and V.E. Fortov. "Laser Beam Reflection from Shock Waves in Xenon and Silicon." *AIP Conference Proceedings.* 1990. 549-555.

Moshe, E., et al. "An increase of the spall strength in aluminum, copper, and Metglas at strain rates larger than 107 s – 1." *Journal of Applied Physics* 83 (1998): 4004.

Moshe, E., et al. "Experimental measurements of the strength of metals approaching the theoretical limit predicted by the equation of state." *Applied Physics Letters* 76 (2000): 1555.

Munro, D.H., et al. "Shock timing technique for the National Ignition Facility." *Physics of Plasmas*, 2001: 2245.

Novikov, S.A., I.I. Divnov, and A.G. Ivanov. "The Study of Fracture of Steel, Aluminum, and Copper under Explosive Loading." *Phys. Metals Metal Science (USSR)* 21 (1966): 608-615.

Phipps, Jr.,C.R., et al. "Impulse coupling to targets in vacuum by KrF, HF, and CO2 single-pulse lasers." *Journal of Applied Physics* 64 (1988): 1083-1096.

Rambo, P.K. et al. "Z-Beamlet: a multikilojoule, terawatt-class laser system." *Applied Optics* 44 (2005): 2421-2430.

Robbins, D.L., et al. "Laser Driven Miniflyer System." Los Alamos Technical Report No. LA-14150, 2004.

Robinson, C.M. "Modeling of Laser Spall Experiments of Aluminum." Edited by M.D. Furnish, N.N. Thadhani and Y. Horie. *Shock Compression of Condensed Matter-2001.* Melville, NY: American Instittute of Physics, 2002. 1359.

Shockey, D.A., L. Seaman, and D.R. Curran. In *Metallurgical Effects at High Strain Rates*, by R.W. Rohde, B.M. Butcher, J.R. Holland and C.H. Karnes, 473. New York: Plenum, 1973.

Steinberg, D.J., and C.M. Lund. "A constitutive model for strain rates from 10^-4 to 10^6 s^-1." *Journal of Applied Physics* 65 (1989): 1528.

Steinberg, D.J., S.G. Cochran, and M.W. Guinan. "A constitutive model for metals applicable at high-strain rate." *Journal of Applied Physics* 51 (1980): 1498-1504.

Stepanov, G.V. "Spall Fracture of Metals by Elastic-Plastic Loading Waves." *Problemy Prochnosti* 8 (1976): 66-70.

Strickland, D., and G. Mourou. "Compression of Amplified Chirped Optical Pulses." *Optics Communications* 55 (1985): 447.

Swift, D.C., and R.P. Johnson. "Quasi-isentropic compression by ablative laser loading: Response of materials to dynamic loading on nanosecond time scales." *Physical Review E* 71 (2005): 066401.

Trunin, R.F. *Experimental Data on Shock Compression and Adiabatic Expansion of Condensed matter.* SAROV, RFNC-VNIIEF, 2001.

Tuler, F.R., and B.M. Butcher. "A Criterion for the Time Dependence of Dynamic Fracture." *International Journal of Fracture Mechanics* 4 (1968): 431.

Turneaure, S.J., and Y.M Gupta. "Inelastic deformation and phase transformation of shock compressed silicon single crystals." *Applied Physics Letters* 91 (2007): 201913.

Veeser, L.R. et al. *Subcritical plutonium experiments at the Nevada Test Site.* Los Alamos Natioinal Laboratory report LA-13606-PR, 1997-1998 Physics Division Progress Report, May 1999, pp. 94-101.

Weaklien, H.A., and D. Redfield. "Temperature dependence of the optical properties of silicon." *Journal of Applied Physics* 50 (1979): 1491.

Werdiger, M., et al. "Off-axis holography of laser-induced shock wave targets." *Applied Physics Letters* 71 (1997): 211.

Zel'dovich, Ya.B., and Yu.P. Raizer. *Physics of Shock Waves and High-Temperature Hydrodynamic Phenomena.* New York: Academic, 1966.

VITA

Douglas Allen Dalton was born November 16, 1978 in Lynchburg, VA. His parents are Doug and Barbara Dalton. He attended Lynchburg College, a liberal arts college in Lynchburg, VA and earned a B.S. with a double major in physics and chemistry. He graduated *summa cum laude* and finished with highest honors in physics.

Permanent address: 309 Laguna Seca Lane, #2703, Austin, TX, 78664

This dissertation was typed by Douglas Allen Dalton.